Imperial College London

Photo-Electrochemical Reactors with Hematite Photo-anodes for Water and Hydrogen Sulfide Splitting

Franky Esteban Bedoya-Lora

Department of Chemical Engineering
Imperial College London
South Kensington Campus
London SW7 2AZ, UK

A thesis submitted to Imperial College London in partial fulfilment of the requirements of the degree of Doctor of Philosophy

August 2017

Declaration

I confirm that this thesis is my own work and all references made to other researches are referenced in the text.

Copyright Notice

Imperial College of Science, Technology and Medicine

Department of Chemical Engineering

Photo-Electrochemical Reactors with Hematite Photo-anodes for Water and Hydrogen Sulfide Splitting

The copyright of this thesis rests with the author and is made available under a Creative Commons Attribution Non-Commercial No Derivatives license. Researchers are free to copy, distribute or transmit the thesis on the condition that they attribute it, that they do not use it for commercial purposes and that they do not alter, transform or build upon it. For any reuse or redistribution, researchers must make clear to others the license terms of this work.

Franky Bedoya-Lora

August 2017

Dedicated to my five mothers

Aura, Herminia, Elena, Martha and Ana Benilda

"The first principle is that you must not fool yourself,

and you are the easiest person to fool."

Richard Feynman

Acknowledgements

I would like to thank my supervisor Prof. Geoff Kelsall, for welcoming me to the Electrochemical Engineering Group and giving me the opportunity to live probably one of the most unique journeys of my life. I cannot acknowledge enough all the help and company of my co-supervisor Anna Hankin, thanks for being an amazing lab-mate and friend. Thanks to Fola, Lisa and Nick for filling with fun and adventures the day by day in the lab.

Special thanks to the *ChemEng PhD Group*: Claudia, Diego, Florence, Mark, Manu, Marie, Marine, Saul and Selene, and the newest member Assen. It was fun to share the good times and live through real-life soap operas with the people I considered not only my friends but also my family in the UK. While living in London, I met incredible people that were there for me in one way or another. Thanks to Catherine, Naima, Clarence, Ivan, Maria, the people in the Latin-American Society and many other people with whom I have shared terrific experiences.

Also, I would like to acknowledge the academic discussions (and maybe not just academic) with Isaac, Faye, the people in the Durrant Group, Alessandra (Raman) and Anna Regoutz (XPS). And the departmental staff that made all this a nice experience, Susi, Sarah, Anusha, Camille, Ben and Keith.

Thanks to my family back in Colombia, my mum, Victor, my dad, aunts, uncles, brothers and cousins. I know that the distance is still far but you all were there when I needed you the most. Thanks to my old friends *Armario*, *Gabeta*, and Maritza, and all my friends from the '*mesitas de cemento*', we all started together, it only took me a bit longer to finish. Thanks to all the people in my former research group for their unconditional support during the early stages of my PhD, specially to Carolina, Jorge, Paula, Esteban and Franklin.

Finally, I acknowledge greatly the Government of Colombia, Colciencias and Colfuturo, for the financial support with the scholarship for PhD studies abroad (568). And, the UK Solar Fuels Network for allowing me to attend numerous conferences and laboratories around the world.

As Gustavo Cerati would say: Gracias… totales!

List of publications

[1] F. Bedoya-Lora, A. Hankin, G.H. Kelsall, Photo-electrochemical hydrogen sulfide splitting using Sn^{IV}-doped hematite photo-anodes, *Electrochem. Commun.*, 68 (2016) 19-22.

[2] A. Hankin, F. Bedoya-Lora, C.K. Ong, J.C. Alexander, F. Petter, G.H. Kelsall, From millimetres to metres: the critical role of current density distributions in photo-electrochemical reactor design, *Energy Environ. Sci.*, 10 (2017) 346-360.

[3] F. Bedoya-Lora, A. Hankin, I. Holmes-Gentle, A. Regoutz, M. Nania, D.J. Payne, J.T. Cabral, G.H. Kelsall, Effects of low temperature annealing on the photo-electrochemical performance of tin-doped hematite photo-anodes, *Electrochim. Acta*, 2017. doi.org/10.1016/j.electacta.2017.08.090

[4] F. Bedoya-Lora, A. Hankin, G.H. Kelsall, *En route* to a unified model for photo-electrochemical reactor optimisation. I - Photocurrent and H_2 yield predictions, *J. Mater. Chem. A*, 2017. doi.org/10.1039/C7TA05125E

[5] F. Bedoya-Lora, A. Hankin, G.H. Kelsall, *En route* to a unified model for photo-electrochemical reactor optimisation. II - Up-scaled validation and geometrical optimisation, *submitted*.

[6] F. Bedoya-Lora, A. Hankin, G.H. Kelsall, *In situ* determination of polysulfides in alkaline hydrogen sulfide solution, *in preparation*.

[7] F. Bedoya-Lora, A. Hankin, G.H. Kelsall, Solar-driven hydrogen sulfide splitting using Sn^{IV}-doped hematite photo-anodes, *in preparation*.

Table of Contents

List of figures **15**

List of tables **21**

Abstract **23**

Nomenclature **25**

Chapter 1
Introduction and literature review **29**

1.1 Introduction 29
1.2 Hydrogen production from solar energy 31
1.2.1 Photo-biological processes 33
1.2.2 Photo-electrochemical processes 33
1.3 General considerations about semiconductors 36
1.4 Efficiency of PEC systems 38
1.5 Economic aspects of solar hydrogen production 42
1.6 Hydrogen sulfide splitting 42
1.6.1 Thermochemical and thermal decomposition 43
1.6.2 Electrolysis 43
1.6.3 Photocatalytic 45
1.6.4 Photo-electrochemical 46
1.7 Semiconductor materials for photo-electrochemical processes 46
1.7.1 Water splitting 47
1.7.2 Hydrogen sulfide splitting 49
1.7.3 Initial screening of semiconductors for hydrogen sulfide splitting 50
1.8 Standard methods and reporting protocols for material and PEC assessment 51
1.9 Modelling of photo-electrochemical devices 53
1.10 Thesis outline 56
1.10.1 Project objectives 56

Chapter 2
Effects of annealing on the performance of tin-doped hematite photo-anodes 59
2.1 Introduction 59
2.2 Experimental 61
2.2.1 Photo-anode fabrication 61
2.2.2 Photo-electrochemical characterization 61
2.2.3 Optical and morphological characterization 62
2.3 Theoretical treatment 63
2.3.1 Mott-Schottky (MS) analysis 63
2.3.2 Photo-electrochemical impedance spectroscopy (PEIS) 64
2.4 Results and discussion 65
2.4.1 Effect of doping 65
2.4.2 Effect of the substrate - FTO vs. Titanium 65
2.4.3 Annealing effect 67
2.4.4 Incident photon-to-current efficiencies (IPCE) 68
2.4.5 Interfacial charge transfer efficiencies 69
2.4.6 Mott-Schottky analysis 69
2.4.7 Flat band potential 71
2.4.8 Photo-electrochemical impedance spectroscopy 72
2.4.9 Morphology and optical properties 73
2.4.10 XPS Analysis 75
2.5 Conclusions 76

Chapter 3
Model of PEC systems: photocurrent and hydrogen yield predictions 79
3.1 Introduction 79
3.2 Theoretical treatment 80
3.2.1 Definition of bulk and surface electron-hole recombination 80
3.2.2 Photocurrent density prediction 81
3.2.3 Dark (anodic and cathodic) current 83
3.2.4 Ionic current 83
3.2.5 Bubble formation and gas desorption 84
3.2.6 Diffusion of dissolved species 87
3.2.7 Boundary conditions 88
3.3 Experimental 89
3.3.1 Photo-anode fabrication and characterization in a PEC 89
3.3.2 Numerical considerations 90
3.4 Results and discussion 90
3.4.1 Photo-anode characterization 90
3.4.2 1D Model 93
3.4.3 2D Model 97
3.5 Conclusions 99

Chapter 4
Model of PER systems: up-scaled validation and geometrical optimisation.....101
4.1 Introduction.....101
4.2 Theoretical description of reactor in 3D.....102
4.2.1 Geometrical definitions.....102
4.2.2 Target definitions.....103
4.3 Experimental.....103
4.3.1 Photo-anode fabrication.....103
4.3.2 Photo-electrochemical reactor.....104
4.3.3 Numerical considerations.....105
4.4 Preliminary considerations.....105
4.4.1 Effects of temperature on the performance of the cell.....105
4.4.2 Photon flux distribution of solar simulator.....106
4.5 Results and discussion.....106
4.5.1 3D reactor model validation.....106
4.5.2 3D (symmetrical) model optimisation.....110
4.5.3 Sensitivity analysis.....115
4.6 Conclusions.....117

Chapter 5
In situ determination of polysulfide ions in alkaline hydrogen sulfide solution.....119
5.1 Introduction.....119
5.2 Polysulfide disproportionation.....120
5.2.1 Polysulfide concentrations at equilibrium.....120
5.2.2 Effect of electrode potential on polysulfide concentration.....121
5.2.3 Decomposition of polysulfide ions to sulfoxides.....124
5.3 Experimental.....125
5.3.1 Polysulfide ions alkaline solutions.....125
5.3.2 Absorbance measurements.....126
5.3.3 Generation of polysulfides ions in PERs.....127
5.4 Results and discussion.....127
5.4.1 Calibrations curves.....127
5.4.2 Estimation of molar attenuation coefficient.....129
5.4.3 Validation via electrochemical generation of polysulfides.....130
5.5 Conclusions.....133

Chapter 6
Photo-assisted hydrogen sulfide splitting using tin-doped hematite.....135
6.1 Introduction.....135
6.1.1 Water splitting in photo-electrochemical cells.....135
6.1.2 Hydrogen sulfide treatment.....136
6.1.3 Hydrogen sulfide splitting.....137

6.2 Experimental 138
6.2.1 Photo-anode fabrication 138
6.2.2 Photo-electrochemical cell (PEC) and reactor (PER) 139
6.2.3 Electrochemical measurements 139
6.2.4 Quantification of polysulfide concentrations and hydrogen fluxes 140
6.2.5 Light sources 140
6.2.6 Numerical considerations 141
6.3 Results and discussion 142
6.3.1 Hydrogen sulfide splitting vs. water splitting 142
6.3.2 Stability of Sn^{IV}-doped α-Fe_2O_3 photo-anodes 145
6.3.3 Mechanism of hydrogen sulfide splitting 147
6.3.4 Long term electrolysis and charge yields 157
6.3.5 Model predictions for hydrogen sulfide splitting 159
6.4 Conclusions 160

Chapter 7
Conclusions and future work 163
Future work 165

References 167

List of figures

Figure 1-1. Scheme of hydrogen sulfide splitting vs. typical water splitting on hematite photo-anodes (SEM image). 30

Figure 1-2. Relative emissions of greenhouse gases (expressed in carbon units per km) for vehicles with internal combustion engines or fuel cells [20]. 31

Figure 1-3. Technologies for hydrogen production using renewable sources of energies [24]. 32

Figure 1-4. Processes for solar hydrogen production [26]. 33

Figure 1-5. Schematic of PEC water splitting in alkaline solution using a photo-anode [30]. Potentials on the physical scale. 34

Figure 1-6. Schematic of a monolithic bi-pole for water splitting [31]. Potentials on the physical scale. 34

Figure 1-7. Schematic band diagram showing the phenomena of photo-absorption, band bending, charge separation, and hydrogen and oxygen evolution for a PEC with two photo electrodes [25] 38

Figure 1-8. ASTM G173-03 reference solar spectrum terrestrial direct normal + circumsolar, and absorption edges of three photo-electrodes compared against the energy level for H_2O decomposition 38

Figure 1-9. E-pH diagram for S-H_2O system, 0.1 MPa, 298 K and total dissolved sulfur activity 0.5 and sulfoxides species excluded. 44

Figure 1-10. Mechanism of liquid-phase photocatalytic hydrogen production from water and H_2S streams [75]. 45

Figure 1-11. Solar-to-hydrogen (STH) conversion efficiencies for integrated systems as a function of year of report [31]. 48

Figure 1-12. E-pH diagram for Fe-S-H_2O system, 0.1 MPa, 298 K and total dissolved iron and sulfur activities 0.01 and 0.1, respectively. 51

Figure 1-13. PEC characterization flow chart for a single-absorber material for water splitting [44] 52

Figure 1-14. Different electrode geometries and configurations of PEC(a) directly illuminated photo-anode surface (hematite film on a Ti foil substrate) facing away from counter electrode; (b) photo-anode surface facing towards the counter electrode mesh, which is interposed between the photo-anode and light source; (c) directly illuminated photo-anode surface (hematite film on a perforated Ti foil substrate) facing away from counter electrode; (d) directly illuminated hematite film, which is a part of a wireless 'photo-bipole' type electrode assembly. The current paths of OH^- anions, corresponding to each scenario, are shown with dotted arrows. The photo-inactive sides of the photo-anodes were covered with insulating varnish, so were not electrochemically active. 55

Figure 2-1. Cyclic voltammograms of Sn^{IV}-doped α-Fe_2O_3 films deposited on FTO and Ti, without and with annealing at 500 °C for 60 min. A scan rate of 10 mV s^{-1}, 1 mol dm^{-3} NaOH electrolyte and irradiation of 3 500 W m^{-2} by a Xe arc lamp were used. Dashed lines represent corresponding dark current densities. 66

Figure 2-2. Interfacial charge transfer efficiency of Sn^{IV}-doped α-Fe_2O_3 films deposited on FTO and Ti, unannealed and with annealing at 500 °C for 60 min. Calculated from fitting PEIS to the equivalent electrical circuit shown in the inset. 66

Figure 2-3. Cyclic voltammograms on Ti|Sn^{IV}-doped α-Fe_2O_3 | 1 mol dm^{-3} NaOH at different annealing temperatures and times. A scan rate of 10 mV s^{-1}, and irradiation of 3 000 W m^{-2} by a Xe arc lamp were used. Inset figure shows current densities on log scale. Dashed lines represent dark currents....67

Figure 2-4. Cyclic voltammograms of Ti|Sn^{IV}-doped α-Fe_2O_3 | 1 mol dm^{-3} NaOH + 0.5 mol dm^{-3} H_2O_2 for different annealing temperatures and times. A scan rate of 10 mV s^{-1}, and irradiation of 3 000 W m^{-2} by a Xe arc lamp were used. Inset figure shows current densities on log scale. Dashed lines represent dark currents. 67

Figure 2-5. IPCE spectra for Ti|Sn^{IV}-doped α-Fe_2O_3 | 1 mol dm^{-3} NaOH at (a) 1.51 and (b) 1.71 V vs. RHE....69

Figure 2-6. Effects of potential and annealing temperature and time on interfacial charge transfer efficiencies for Ti|Sn^{IV}-doped α-Fe_2O_3 | 1 mol dm^{-3} NaOH, together with corresponding fitting to equation (2-6) and resistances were extracted from equivalent electric circuit shown in the inset. 69

Figure 2-7. Effects of annealing temperature and time on Mott-Schottky plots on Ti|Sn^{IV}-doped α-Fe_2O_3 | 1 mol dm^{-3} NaOH. Capacitances were extracted after fitting to a circuit as shown in the inset. 70

Figure 2-8. Effects of annealing temperature and time on estimated donor densities from Mott-Schottky plots for Ti|Sn^{IV}-doped α-Fe_2O_3 | 1 mol dm^{-3} NaOH. 70

Figure 2-9. Effect of annealing temperature and time on impedance spectra: 1.21 V vs. RHE (a) Bode and (b) phase plot, and 1.71 V vs. RHE (c) Bode and (d) of Ti|Sn^{IV}-doped α-Fe_2O_3 | 1 mol dm^{-3} NaOH at and 3 000 W m^{-2} Xe arc lamp....73

Figure 2-10. Effects of potential and frequency on phase (colour, y2 scale) of PEIS behaviour of illuminated Ti|Sn^{IV}-doped α-Fe_2O_3 unannealed, and annealed at 400 °C and 500 °C for 60 minutes. 73

Figure 2-11. SEM images (100k ×) of Sn^{IV}-doped α-Fe_2O_3 deposited on FTO and Ti, unannealed and annealed at 400 °C and 500 °C for 60 min. Images recorded with the help of Mr. Isaac Holmes-Gentle....74

Figure 2-12. AFM images of Sn^{IV}-doped α-Fe_2O_3 deposited on FTO and Ti, unannealed, 400 °C and 500 °C annealing for 60 minutes. AFM images were recorded by Ms. Manuela Nania. 74

Figure 2-13. XPS core level spectra of Sn^{IV}-doped α-Fe_2O_3 on FTO and titanium unannealed and after annealing at 500 °C for 60 minutes, including (a) Fe 2p and (b) Sn 3d. Spectra was recorded and analysed by Dr. Anna Regoutz. 76

Figure 3-1. Scheme of recombination processes (in red) happening in the bulk and surface of a photo-anode after charge separation (yellow)....81

Figure 3-2. Scheme of gas evolution on an electrode and in the electrolyte, modified version from Vogt [127]. 85

Figure 3-3. Scheme of boundary conditions for 1D model photo-electrochemical reactor cathode | catholyte | membrane | anolyte | photo-anode and electrodes facing each other. 89

Figure 3-4. Linear sweep voltammograms on Ti|Sn^{IV}-doped α-Fe_2O_3 annealed previously at different temperatures for 1 hour. 1 mol dm^{-3} NaOH electrolyte solution with and without 0.5 mol dm^{-3} H_2O_2 as hole scavenger; 3 000 W m^{-2} irradiation from Xe arc lamp; 10 mV s^{-1} potential scan rate. Dashed lines represent dark current densities. 91

Figure 3-5. Nyquist and Bode-phase plots of Ti|Sn^{IV}-doped α-Fe_2O_3 | 1 mol dm^{-3} NaOH at 1.1 V vs. RHE obtained by PEIS under irradiation of 3 000 W m^{-2} by a Xe arc lamp. Continuous lines represent fitting to an electrical equivalent circuit R(C[R(RC)]). 92

Figure 3-6. Effects of electrode potential and annealing temperature on interfacial charge transfer efficiencies (symbols) and fitted exponential functions (lines, equation (2-6)) for Ti|Sn^{IV}-doped α-Fe_2O_3 | 1 mol dm^{-3} NaOH. 92

Figure 3-7. Calculated bulk recombination for Ti|Sn^{IV}-doped α-Fe_2O_3 samples annealed at different temperatures. 1 mol dm^{-3} NaOH + 0.5 mol dm^{-3} H_2O_2 electrolyte and irradiation of 3 000 W m^{-2} by a Xe arc lamp were used. 92

Figure 3-8. Predicted photocurrent densities according to the Gärtner–Butler equation, after correction for photon absorption, equation (3-2); photon flux limitation, equation (3-4); and surface and bulk recombination, equation (3-6). Ti|Sn^{IV}-doped α-Fe_2O_3 annealed at 400 °C, 1 mol dm^{-3} NaOH electrolyte and 3 000 W m^{-2} irradiation by Xe arc lamp. 94

Figure 3-9. Effect of electrode potential and annealing temperature on predicted (dashed) and experimental (continuous) current densities (photo + dark currents) for Ti|Sn^{IV}-doped α-Fe_2O_3 | 1 mol dm^{-3} NaOH electrolyte solution. 3 000 W m^{-2} irradiation by Xe arc lamp. ... 94

Figure 3-10. Effect of (Ti|Sn^{IV}-doped α-Fe_2O_3 | 1 mol dm^{-3} NaOH) photo-anode potential on predicted charge yields (dashed) and collection efficiencies (continuous) for hydrogen evolution on Ti|Pt. 95

Figure 3-11. Predicted effects on hydrogen fluxes of cathode current density (continuous), photo-anode potentials (dashed) and annealing temperature for Ti|Sn^{IV}-doped α-Fe_2O_3 | 1 mol dm^{-3} NaOH. 96

Figure 3-12. Predicted effects of electrode potential charge yields (dashed) and collection efficiencies (continuous) as a function of potential for hydrogen evolution on Ti|Pt when using a photo-anode Ti|Sn^{IV}-doped α-Fe_2O_3 | 1 mol dm^{-3} NaOH and separated by Nafion® membrane. 96

Figure 3-13. Current density distributions over the length of a hypothetical enhanced photo-anode operating at 1 V vs. RHE in 1 mol dm^{-3} NaOH and without a membrane. Distances are relative to the total length of the electrode varied between 0.01 and 1 m, and the edge at relative distance 0. 98

Figure 3-14. Current density and hydrogen flux (top); charge yields, collection and ASTH efficiencies (bottom) as a function of the electrode length for 'enhanced' photo-anode operating at 1 V vs. RHE in 1 mol dm^{-3} NaOH and without a membrane. 98

Figure 4-1. Schematic view of the up-scaled photo-electrochemical reactor for model validation. 102

Figure 4-2. (a) Square and hexagonal distribution of perforations in the photo-anode, and definitions of lengths and areas of interest. Arrangement of electrodes for geometrical optimisation; (b) photo-anode facing away from cathode ('wired') and (c) monolithic photo-bipole with a single photo-anode ('wireless'). 103

Figure 4-3. Photo-response of planar unannealed Ti|Sn^{IV}-doped α-Fe_2O_3 | 1 mol dm^{-3} NaOH and predicted behaviour using a solar simulator, 497 W m^{-2}. Inset with logarithmic y-axis. 107

Figure 4-4. Average photocurrent density, hydrogen and oxygen molar fluxes evaluated during chronoamperometric operation at a cell potential difference of 1.6 V for 0.1 × 0.1 m^2 Ti|Sn^{IV}-doped α-Fe_2O_3 (planar and perforated) | 1 mol dm^{-3} NaOH irradiated with 497 W m^{-2} from a solar simulator. Dashed lines are model predicted values. 108

Figure 4-5. Molar stoichiometry for H_2:O_2 and (y2) estimated charge yields for hydrogen and oxygen fluxes evaluated during chronoamperometric operation at a cell potential difference of 1.6 V for 0.1 × 0.1 m^2 Ti|Sn^{IV}-doped α-Fe_2O_3 (planar and perforated) | 1 mol dm^{-3} NaOH using a solar simulator and a power density of 497 W m^{-2}. Dashed lines represent predicted values. 108

Figure 4-6. Current density distribution at Ti|Sn^{IV}-doped α-Fe_2O_3 | 1 mol dm^{-3} NaOH photo-anode at 1.51 V vs. RHE with cathode (Ti | Pt | 1 mol dm^{-3} NaOH), and steady state spatial distributions of oxygen and hydrogen concentrations for up-scaled reactor operating at 40 °C. 109

Figure 4-7. Total current densities and (y2) hydrogen fluxes as a function of (a) ld/lp for $lp = 50\,\mu m$ and (b) lp for an optimum ld/lp, in a wired symmetrical 3D model with perforations in a square and hexagonal distribution. Wired cell without membrane in 1 mol dm^{-3} NaOH and 1.51 V vs. RHE. 111

Figure 4-8. Optimisation of ld/lp for 'wired' reactor with Ti|Sn^{IV}-doped α-Fe_2O_3 | 1 mol dm^{-3} NaOH photo-anode at 1.51 V vs. RHE without a membrane (dashed) and with a membrane (solid). (a) Current densities and hydrogen fluxes for $lp = 50\,\mu m$. (b) Collection efficiencies and amount of O_2 collected in the catholyte. (c) Current densities and hydrogen fluxes for different perforation sizes, and (d) current densities and hydrogen fluxes as a function of the ratio of active and geometric areas. 112

Figure 4-9. (top) Effect of inter-perforation distance (ld) on current densities for 'wired' reactor with and without a membrane, with Ti|Sn^{IV}-doped α-Fe_2O_3 | 1 mol dm^{-3} NaOH photo-anode at 1.51 V vs. RHE with a perforation size of $lp = 50\,\mu m, ld/lp = 2\ or\ 10,$ and (bottom) concentration profiles of oxygen and hydrogen in the z-direction in the centre of the perforation ($x = 0$, $y = 0$). 112

Figure 4-10. Effect of ld/lp on current densities for 'wireless' reactor, 1 mol dm^{-3} NaOH | Pt | Ti | Ti | Sn^{IV}-doped α-Fe_2O_3 | 1 mol dm^{-3} NaOH with (solid lines) and without (dashed lines) a membrane, photo-anode at 1.51 V vs. RHE. (a) Current densities and hydrogen fluxes for perforation size $lp = 50\,\mu m$. (b) Collection efficiencies and amounts of O_2 collected in the catholyte. (c) Current densities and hydrogen fluxes for different perforation sizes, and (d) current densities and hydrogen fluxes as a function of the ratio of active and geometric areas. 114

Figure 4-11. (top) Current densities for different perforation distances using a perforation size of $lp = 50\,\mu m$ and (bottom) concentration profiles of oxygen and hydrogen in the z-direction in the centre of the perforation ($x = 0$, $y = 0$) for a 'wireless' reactor, 1 mol dm^{-3} NaOH | Pt | Ti | Ti | Sn^{IV}-doped α-Fe_2O_3 | 1 mol dm^{-3} NaOH with and without a membrane, photo-anode at 1.51 V vs. RHE. 114

Figure 4-12. Hydrogen fluxes relative to maxima achieved as a function of ld/lp for different ranges of donor densities, electrode thicknesses, irradiance and electrolyte conductivity while keeping other parameters unchanged. 'Wired' Ti | Pt | 1 mol dm^{-3} NaOH | Sn^{IV}-doped α-Fe_2O_3 | Ti with and without a membrane, photo-anode at 1.51 V vs. RHE. Dashed lines represent the values used typically in the model. 116

Figure 4-13. Hydrogen fluxes relative to maxima achieved as a function of ld/lp for different ranges of donor densities, electrode thicknesses, irradiance and electrolyte conductivity while keeping the other parameters unchanged. 'Wireless' reactor, 1 mol dm^{-3} NaOH | Pt | Ti | Ti | Sn^{IV}-doped α-Fe_2O_3 | 1 mol dm^{-3} NaOH with photo-anode at 1.51 V vs. RHE and a hexagonal array of perforations. Dashed lines represent the values typically used in the model. 116

Figure 5-1. Predicted (top) concentration and (bottom) molar fraction of S_n^{2-} as a function of zero-valent sulfur in 1 mol dm^{-3} NaOH and 0.5 mol dm^{-3} Na_2S, pH 14, 298 K. 121

Figure 5-2. Potential-pH diagram for a meta-stable S-H_2O system with sulfoxides excluded; total dissolved sulfur activity 0.5, 298 K and 0.1 MPa [74]. 123

Figure 5-3. Effect of electrode potential on polysulfide distribution; dissolved sulfur activity 0.5, pH 14, 298 K and 0.1 MPa. 123

Figure 5-4. Potential-pH diagram for a S-H_2O system excluding sulfate(VI) species 0.01, 298 K and 0.1 MPa. 125

Figure 5-5. Equipment for polysulfide determination as zero-valent sulfur in alkaline solution using an immersion probe and UV-vis spectrophotometer. 126

Figure 5-6. Typical absorbance spectra of different polysulfide solutions expressed as zero-valent sulfur content in 1 mol dm^{-3} NaOH and 0.5 mol dm^{-3} Na_2S. 128

Figure 5-7. Calibration curves of polysulfide solutions for different ranges of concentrations in 1 mol dm^{-3} NaOH and 0.5 mol dm^{-3} Na_2S. (a) Linear regression for low range at 295 nm (b) exponential regression for medium range at 295 nm, affected by polysulfide disproportionation, and (c) linear regression for high range at 420 nm. 129

Figure 5-8. Estimated absorbance of polysulfide ions in 1 mol dm^{-3} NaOH and 0.5 mol dm^{-3} Na_2S and contributions of S_3^{2-} and S_4^{2-} in absorbance at 295 nm, compared to (○) experimental data. 130

Figure 5-9. Time dependences of polysulfide concentrations expressed as zero-valent sulfur in 1 mol dm^{-3} NaOH and 0.5 mol dm^{-3} Na_2S after HS^- oxidation in an 0.1 dm^{-3} electrochemical reactor, (top) short and (bottom) long term current densities for two different anode samples. Electrode potential of 1.15 vs. RHE. 131

Figure 5-10. Time dependences of polysulfide concentrations expressed as zero-valent sulfur in 1 mol dm^{-3} NaOH and 0.5 mol dm^{-3} Na_2S after HS^- oxidation in an 0.8 dm^{-3} electrochemical reactor for two different electrodes (planar and perforated) and applied cell potential difference of 1.226 V. 131

Figure 5-11. Time dependences of charge yields of polysulfide formation expressed as zero-valent sulfur in 1 mol dm^{-3} NaOH and 0.5 mol dm^{-3} Na_2S after HS^- oxidation and hydrogen in an 0.8 dm^3 electrochemical reactor for two different electrodes (planar and perforated) and applied cell potential difference of 1.226 V. 132

Figure 6-1. Equipment for photo-assisted electrolysis of hydrogen sulfide ions in alkaline solution. 141

Figure 6-2. Linear sweep voltammograms for 3 replicates of Ti | Sn^{IV}-doped α-Fe_2O_3 | 1 mol dm^{-3} NaOH ± 0.5 mol dm^{-3} Na_2S (pH = 14) | Pt | Ti under dark and illuminated conditions in a PEC; 10 mV s^{-1} scan rate. Xenon arc lamp irradiance 2 670 W m^{-2}. Inset: semi-log plot. 143

Figure 6-3. (a) Effects of irradiation wavelength and photo-anode potentials on IPCE of Ti | Sn^{IV}-doped α-Fe_2O_3 | 1 mol dm^{-3} NaOH | Pt | Ti (water splitting). (b) IPCE of water splitting and hydrogen sulfide splitting for Ti | Sn^{IV}-doped α-Fe_2O_3 | 1 mol dm^{-3} NaOH + 0.5 mol dm^{-3} Na_2S | Pt | Ti at 1.24 V vs. RHE. (c) interfacial charge transfer efficiencies of Ti|Sn^{IV}-doped α-Fe_2O_3 in presence and absence of hydrogen sulfide ions. 143

Figure 6-4. Linear sweep voltammograms for Ti|Sn^{IV}-doped α-Fe_2O_3 samples, annealed at different temperatures and times, under illumination in 1 mol dm^{-3} NaOH (dashed) and 1 mol dm^{-3} NaOH + 0.5 mol dm^{-3} Na_2S (continuous); 10 mV s^{-1} scan rate. Xenon arc lamp irradiance 3 000 W m^{-2}. 145

Figure 6-5. Time dependences of current densities (continuous, left axis) and admittances at 1 Hz (dashed, right) for Ti | Sn^{IV}-doped α-Fe_2O_3 | 1 mol dm^{-3} NaOH + X mol dm^{-3} Na_2S | Pt | Ti at an applied photo-anode potential of 1.15 V vs. RHE and in the presence of different concentrations of hydrogen sulfide ions. Xenon Arc lamp irradiance 2670 W m^{-2}. 145

Figure 6-6. Phase shift of PEIS spectra as a function of time for Ti | Sn^{IV}-doped α-Fe_2O_3 | 1 mol dm^{-3} NaOH + X mol dm^{-3} Na_2S | Pt | Ti at an applied photo-anode potential of 1.15 V vs. RHE and in the presence of different concentrations of hydrogen sulfide ions. Xenon arc lamp irradiance 2 670 W m^{-2}. 146

Figure 6-7. SEM images and EDX analysis of Ti|Sn^{IV}-doped α-Fe_2O_3 photo-anodes before and after continuous hydrogen sulfide splitting at 1.15 V vs. RHE. 146

Figure 6-8. Cyclic voltammograms (20 cycles) under (a) dark and (b) illuminated conditions and quiescent electrolyte for Ti | Sn^{IV}-doped α-Fe_2O_3 | 1 mol dm^{-3} NaOH + 0.5 mol dm^{-3} Na_2S | Pt | Ti with different upper limits of photo-anode potential and 500 mV s^{-1} scan rate. (c) Linear polarizations for positive-going and negative-going potentials under dark conditions and 1 mV s^{-1} scan rate. Xenon arc lamp irradiance 2 900 W m^{-2}. 149

Figure 6-9. Cyclic voltammograms (20 cycles) under (a) dark and quiescent electrolyte, (b) dark and stirred electrolyte, (c) illuminated and quiescent and (d) illuminated and stirred conditions for Ti | Sn^{IV}-doped α-Fe_2O_3 | 1 mol dm^{-3} NaOH + 1.0 mol dm^{-3} Na_2S | Pt | Ti with different photo-anode potential upper limits and 50 mV s^{-1} scan rate. Xenon arc lamp irradiance 2 900 W m^{-2}. 150

Figure 6-10. (a) Mechanism of hydrogen sulfide oxidation on Ti|Sn^{IV}-doped α-Fe_2O_3 without illumination at different potentials; sulfoxides excluded from consideration, (b) schematic concentration profile of sulfide and polysulfide ions in the diffusion layer assuming fast kinetics for chemical reactions, low current densities (charge transfer controlled process) and quiescent electrolyte..... 153

Figure 6-11. Time dependence of low frequency admittance (EIS spectra) for Ti | Sn^{IV}-doped α-Fe_2O_3 | X mol dm^{-3} NaOH + 1.0 mol dm^{-3} Na_2S | Pt | Ti operating at a photo-anode potential of 1.65 V vs. RHE with different hydrogen sulfide concentrations and with quiescent and stirred electrolytes..... 154

Figure 6-12. Photocurrent densities as a function of potential of Ti | Sn^{IV}-doped α-Fe_2O_3 | 1 mol dm^{-3} NaOH ± X mol dm^{-3} Na_2S (pH = 14) | Pt | Ti at different concentrations of hydrogen sulfide ions in quiescent electrolyte solutions. 10 mV s^{-1} scan rate. Xenon arc lamp irradiance 2 670 W m^{-2}. 154

Figure 6-13. Fitted parameters from PEIS spectra, (a) Charge transfer resistance, (b) semiconductor capacitance, (c) electron-hole recombination resistance and (d) interfacial charge transfer efficiency for Ti | Sn-doped α-Fe_2O_3 | 1 mol dm^{-3} NaOH ± X mol dm^{-3} Na_2S (pH = 14) | Pt | Ti at different concentrations of hydrogen sulfide ions. Xenon arc lamp irradiance 2 670 W m^{-2}. 155

Figure 6-14. Phase shift of PEIS spectra as a function of photo-anode potential for Ti | Sn^{IV}-doped α-Fe_2O_3 | 1 mol dm^{-3} NaOH + X mol dm^{-3} Na_2S | Pt | Ti at different concentrations of hydrogen sulfide ions. Xenon arc lamp irradiance 2 670 W m^{-2}. 156

Figure 6-15. Time dependence of current density for Ti | Sn^{IV}-doped α-Fe_2O_3 | 1 mol dm^{-3} NaOH + X mol dm^{-3} Na_2S (pH = 14) | Pt | Ti at different concentrations of hydrogen sulfide and high and low admittance for photo-assisted electrolysis during 1.5 hours at different photo-anode potentials and stirred electrolyte. Xenon arc lamp irradiance 2 670 W m^{-2}. Legends are the same as Figure 6-13. 157

Figure 6-16. Fitted parameters from PEIS spectra of Ti | Sn^{IV}-doped α-Fe_2O_3 | 1 mol dm^{-3} NaOH + X mol dm^{-3} Na_2S (pH = 14) | Pt | Ti at different concentrations of hydrogen sulfide ions for photo-assisted electrolysis during 1.5 hours at 1.15 V vs. RHE and stirred electrolyte. Xenon arc lamp irradiance 2 670 W m^{-2}. Legends the same as for Figure 6-13. 157

Figure 6-17. Time dependence of (a) hydrogen and elemental sulfur molar flux in the PER for hydrogen sulfide splitting (1 mol dm^{-3} NaOH + 0.5 mol dm^{-3} Na_2S) operating at cell potential difference of 1.23 V, (b) Hydrogen and oxygen molar flux for water splitting (1 mol dm^{-3} NaOH) at 1.60 V. (c) Charge yield for hydrogen sulfide splitting and (d) current density for both hydrogen sulfide and water splitting, in a planar and perforated 0.1×0.1 m^2 photo-anode Ti|Sn^{IV}-doped α-Fe_2O_3. Xenon arc lamp irradiance 457 W m^{-2}. 159

Figure 6-18. Experimental and predicted effects of photo-anode potential on photocurrent densities (total - dark) of Ti | Sn^{IV}-doped α-Fe_2O_3 | 1 mol dm^{-3} NaOH + 0.5 mol dm^{-3} Na_2S (pH = 14) | Pt | Ti in a PEC with Xe arc lamp irradiance 2 670 W m^{-2}..... 160

List of tables

Table 1-1. Comparison of hydrogen properties with other fuels at 25 ° C and 1 atm. 31

Table 1-2. Projected costs (long term) of hydrogen production [24] 42

Table 1-3. Summary of PEC characterization techniques, properties measured and their limitations. 52

Table 1-4. Summary of research gaps, tasks and novelties for each chapter. 58

Table 2-1. Effects of annealing temperature and time on flat band potential vs. RHE (V) for Ti|Sn^{IV}-doped α-Fe_2O_3 | 1 mol dm^{-3} NaOH estimated by different methods. 72

Table 2-2. Summary of phenomena detected. Hypotheses listed first (in bold) for each phenomenon are the proposed explanation with techniques listed for its validation. Subsequent hypotheses are disregarded or assumed to have minimum effect, with techniques listed for validation. 77

Table 5-1. Estimated molar attenuation coefficients of polysulfides ions in aqueous solution. 122

Table 5-2. Calibration curve parameters for different ranges of polysulfide concentration expressed as zero-valent sulfur in 1 mol dm^{-3} NaOH and 0.5 mol dm^{-3} Na_2S 129

Table 5-3. Molar attenuation coefficient of S_3^{2-} and S_4^{2-} ions in aqueous solution derived from experimental data reported here compared to values reported in the literature. 130

Table 5-4. Summary of charge yields obtained by (top) charge integration of current densities and (bottom) averaged currents. 133

Table 6-1. Steps for photo-assisted electrolysis of hydrogen sulfide ions in alkaline aqueous solution. 137

Table 6-2. EDX elemental analysis of Ti|Sn^{IV}-doped α-Fe_2O_3 photo-anodes before and after 18 h of continuous hydrogen sulfide splitting at 1.15 V vs. RHE. 147

Table 6-3. List of electrochemical-chemical reactions for hydrogen sulfide splitting at different potentials in absence of sulfoxide species 154

Abstract

The impact of CO_2 emissions on climate change, human health and local environments are driving the search for more benign sources of energy. The sun is the earth's ultimate energy source, though subject to diurnal and seasonal intermittency. This calls for a technology to effectively store the harvested solar energy, and make it readily available when needed. 'Solar fuels', such as hydrogen, have been proposed as suitable energy carriers. However, due to high costs involved in the production of hydrogen using renewable sources, coupling its production to other processes, such as waste treatment, would be advantageous. Hydrogen sulfide is a toxic and highly corrosive gas which is produced by hydrodesulfurisation processes in petroleum refineries for removal of sulfur from gas and petroleum products. Hence, hydrogen sulfide, which is thermodynamically predicted to be easier to oxidise than water, can be treated while simultaneously producing hydrogen via photo-assisted electrolysis.

The performances of tin(IV)-doped hematite photo-anodes were assessed for hydrogen production using photo-assisted electrolysis of water and hydrogen sulfide in photo-electrochemical reactors. Initially, photo-electrochemical, optical and morphological properties were measured as a function of post-deposition annealing. Using these parameters, a semi-empirical model was developed for the prediction of photocurrent densities and the performance of bench-scale (< 0.1 dm^3) and up-scaled (0.8 dm^3) reactors for water splitting. The model was also implemented to predict optimised geometric properties of photo-anodes with the aim to decrease (H_2-O_2) cross-over losses and minimise inhomogeneities in current density distributions.

Lastly, a comparison between conventional water splitting and hydrogen sulfide splitting indicated that interfacial electron-hole recombination rates are diminished effectively in presence of hydrogen sulfide ions, and the photo-anode potentials could be decreased by ca. 0.5 V. Charge yields for hydrogen and polysulfide ions were also estimated, typically as 0.9 and 1.0, respectively. A customised UV/vis absorption technique was required for *in situ* quantification of polysulfide ions at low concentrations in hydrogen sulfide alkaline solution. A mechanism was proposed for hydrogen sulfide oxidation to polysulfide ions on tin(IV)-doped hematite photo-anodes, on which electrodeposition of elemental sulfur occurred and polysulfide ions accumulated; this needs to be considered when selecting operating conditions for hydrogen production via photo-assisted hydrogen sulfide splitting.

Nomenclature

Symbol	Name/description	Units
A	Area	m^2
A_a	Tafel slope for oxygen evolution at the anode	V dec^{-1}
a	Area of transfer per unit volume	m^{-1}
$a_{G,i}$	Kwie parameter (a) for gas evolution of species i	-
c_i	Concentration of species i	mol m^{-3}
$c_{\mathrm{sat},i}$	Concentration of species i at saturated conditions	mol m^{-3}
D_i	Diffusion coefficient of species i	m^2 s^{-1}
D_p	Diffusion coefficient of holes	m^2 s^{-1}
d_B	Sauter diameter of bubbles	m
d_i	Electrolyte path length	m
e	Electron charge, 1.6022×10^{-19}	C
E^0	Standard equilibrium potential	V
E_g	Band gap	eV
$E_{\mathrm{H_2}}$	Energy per mole of hydrogen, 236000	J mol^{-1}
F	Faraday constant, 96484.6	C mol^{-1}
f_G	Efficiency of gas evolution	1
G^0	Standard Gibbs free energy of formation	kJ mol^{-1}
I	Current	A
I_0	Incident photon flux	m^{-2} s^{-1}
I_x	Transmitted photon flux at thickness x	m^{-2} s^{-1}
j	Current density	A m^{-2}
$j_{0,a}$	Exchange current density at the anode	A m^{-2}
$j_{0,c}$	Exchange current density at the cathode	A m^{-2}
j_{ph}	Photocurrent density	A m^{-2}
K_i	Dissociation constant of species i	-
$K_{i,m}$	Partition coefficient at membrane | electrolyte interface	1
k_{B}	Boltzmann constant, 1.3806×10^{-23}	J K^{-1}
k_L	Mass transfer coefficient of gas dissolved in liquid	m s^{-1}
k_La	Volumetric mass transfer coefficient of gas in liquid	s^{-1}
k_r	Rate constant of *e-h* recombination	s^{-1}
k_t	Rate constant of charge transfer in semiconductor	s^{-1}
$L_{\mathrm{D,eff}}$	Effective diffusion length of charge carriers	m^2 s^{-1}
L_p	Diffusion length of holes	m
l_a	Anolyte length	m
l_{a-c}	Distance between anode and cathode surfaces	m
l_c	Catholyte length	m
l_d	Distances between perforations	m
l_e	Electrode thickness	m
l_p	Perforation size (diameter)	m
N_A	Avogadro's number, 6.022×10^{23}	mol^{-1}
N_{bulk}	Flux of dissolved gas transferred by diffusion	mol m^{-2} s^{-1}
N_D	Total flux of gas evolving at the electrode surface	mol m^{-2} s^{-1}
$N_{\mathrm{desorption}}$	Flux of gas evolving by desorption	mol m^{-2} s^{-1}
N_G	Flux of gas evolving as bubbles at the electrode	mol m^{-2} s^{-1}
N_i	Flux of species i	mol m^{-2} s^{-1}
n_0	Charge carrier concentration / Donor density	m^{-3}
$n_{g,i}$	Kwie parameter (n) for gas evolution of species i	-
$\dot{n}_{\mathrm{H_2}}$	Molar flow rate	mol s^{-1}

P^0	Photon power density	W m^{-2}
p_i	Partial pressure of gas i	Pa
p_0	Equilibrium concentration of holes in the dark	m^{-3}
Q_r	Constant phase element associated with e-h recombination	F m^{-2}
Q_{SC}	Constant phase element of the semiconductor depletion layer	F m^{-2}
R	Gas constant, 8.31445	J mol^{-1} K^{-1}
R^2	Coefficient of determination	1
R_a	Resistance associated to sulfur deposition on the electrode	ohm m^2
Re	Reynolds number	1
R_i	Volumetric reaction rate of species i	mol m^{-3} s^{-1}
R_r	Resistance of *e-h* recombination at the electrode	ohm m^2
R_t	Resistance of charge transfer at the electrode	ohm m^2
Sc	Schmidt number	1
T	Temperature	K
U	Electrode potential	V
ΔU_{bias}	Applied potential cell difference (bias)	V
$U_{H_2O\|H_2}$	Hydrogen evolution (HER) equilibrium potential	V
$U_{O_2\|H_2O}$	Oxygen evolution (OER) equilibrium potential	V
$u_{m,i}$	Mobility of species i	m^2 V^{-1} s^{-1}
$\mathbf{v}$	Velocity of fluid	m s^{-1}
v_B	Bubble slip velocity relative to the liquid	m s^{-1}
x_{SC}	Thickness of thin film semiconductor / depth from interface	m
z_i	Charge of species i	-

Greek symbols		
α_λ	Absorptivity coefficient at wavelength λ	m^{-1}
$\alpha_{ox,c}$	Anodic transfer coefficient at the cathode	1
$\alpha_{red,c}$	Cathodic transfer coefficient at the cathode	1
ε_0	Vacuum permittivity, 8.85×10^{-12}	F m^{-1}
ε_r	Relative permittivity	1
ε_G	Gas holdup	1
η_a	Overpotential (for oxygen evolution) at the anode	V
η_c	Overpotential (for hydrogen evolution) at the cathode	V
θ	Fractional surface coverage by bubbles	1
λ	Wavelength	nm
μ	Chemical potential	J mol^{-1}
ν_i	Stoichiometry coefficient of species i	-
$\nu_{e,i}$	Electron stoichiometry or charge number for reaction i	-
σ	Electrical conductivity	S m^{-1}
υ	Kinematic viscosity	m s^{-1}
Φ_{bulk}	Electron-hole recombination ratio in the bulk of the SC	1
$\Phi_{collection,}$	Collection efficiency of species i	1
Φ_{device}	Overall device efficiency	1
Φ_{e^-/h^+}	Electron-hole separation efficiency	1
Φ_i^e	Charge yield of species i	1
$\Phi_{photo-elec}$	Photo-electrode efficiency	1
$\Phi_{surface}$	Interfacial charge transfer efficiency	1
$\Phi_{transport}$	Charge transport efficiency	1
$\Delta\phi_{SC}$	Band bending of semiconductor	V
χ	Electronegativity	-

Abbreviations

ABPE	Applied bias photo-to-current efficiency	1
AB-STH	Applied bias solar-to-hydrogen efficiency	1
ASTH	Assisted solar-to-hydrogen efficiency	1
CB	Conduction band	-
CPE	Constant phase element	-
EIS	Electrochemical impedance spectroscopy	-
FTO	Fluorine-doped tin oxide	-
HER	Hydrogen evolution reaction	-
IPCE	Incident to photocurrent conversion efficiency	1
ITO	Indium tin oxide	
OCP	Open circuit potential	-
OER	Oxygen evolution reaction	-
PEC	Photo-electrochemical cell (characterisation only)	-
PEIS	Photo-electrochemical impedance spectroscopy	-
PER	Photo-electrochemical reactor (H_2 production)	-
RHE	Reversible hydrogen electrode	-
SC	Semiconductor	
SCE	Saturated calomel electrode	-
STH	Solar-to-hydrogen efficiency	1
VB	Valence band	-

Chapter 1

Introduction and literature review

1.1 Introduction

Growing concerns about climate change and energy security has promoted efforts to harness energy from renewable sources, which could be accessed readily and by means that place minimal environmental burdens on the planet. Combustion of fossils fuels produces greenhouse gases, such as carbon dioxide, so contributing to global warming and localised pollution in urban areas. Even bio-ethanol, regarded as a clean fuel, has a significant effect on the production of ozone [1], another undesirable and pollutant gas.

New sources of clean energy have been investigated in recent decades. The sun is one of the most promising and ubiquitous sources of energy since it provides the earth with 1.2×10^{17} W [2] in photons, which was four orders of magnitude higher than the global energy demand (1.8×10^{13} W) in 2014 [3]. However, the total consumption of energy worldwide has grown by 48% and electrical energy generation by 76% since 1993, in comparison with world population growth by only 27% [4]. It is evident that such solar energy needs to be stored in order to be used when the incident radiation is limited, e.g., winter season or night. Presently, photovoltaic cells are the most developed and deployed technology for solar energy harvesting. However, even with the available highly efficient and stable photovoltaic cells [5], solar electricity cannot be used as a primary source of energy without solving the issues related to the storage and distribution of large quantities of electrical energy [6]. When medium (hours) to long term (days) storage is needed for large quantities of solar energy, or any other intermittent renewable energy source, conventional options include mechanical storage such as pumped hydro (PHES) and compressed air (CAES), electrochemical storage (flow batteries) and thermal energy storage (TES) [7, 8]. These technologies are relatively mature, but are centralised in nature due to their low energy densities. Chemical energy carriers, or fuels, can also be produced from renewable sources and can be stored for extended periods, but easily distributed and available decentralised manner use; hydrogen, ammonia and syngas, are promising 'solar fuel' candidates.

Hydrogen is a popular candidate for such chemical energy storage, because of its facile oxidation in fuel cells without formation of harmful by-products [9]. Splitting liquid water to produce hydrogen (and oxygen) using solar energy requires a minimum of 1.48 eV under thermoneutral conditions. Prospectively, photo-electrochemical reactors could produce hydrogen directly using solar energy, but photo-electrode materials are yet to be adequately efficient, durable, and fabricated by economic and scalable processes. Thermodynamically less energy intensive processes, such as hydrogen sulfide splitting that requires a minimum of only 0.3 eV, remain largely as a concept for lack of suitable semiconductors, though its feasibility has been reported [10-14]. Hydrodesulfurisation processes in the world's oil refineries use hydrogen to remove sulfur from oil products such as (highly toxic and corrosive) H_2S, which must be oxidised subsequently to elemental sulfur at a scale of > 70 Mt per year (2015) by Claus processes [15]. Using hydrogen sulfide to produce hydrogen and polysulfide ions (S_n^{2-}) with solar energy could achieve the same result without the need to produce hydrogen from fossil fuels effectively emitting CO_2.

The following chapters report results of a study of Sn^{IV}-doped Fe_2O_3 photo-anodes used in photo-electrochemical reactors for hydrogen production via photo-assisted electrolysis of water and hydrogen sulfide. The properties of photo-anode materials, including superficial and bulk electron-hole recombination rates, flat band potentials, donor densities, photocurrent responses, photon absorptivities and band gaps, were measured and used to predict the performance of bench-scale and up-scaled reactors. The advantages and disadvantages of typical water splitting and hydrogen sulfide splitting in photo-assisted electrolysis needs to be considered, and how to achieve a better understanding of these processes in photo-electrochemical reactors to improve their performances. Figure 1-1 shows a simplistic scheme of water and hydrogen sulfide oxidation using a photo-anode of Sn^{IV}-doped Fe_2O_3, semiconducting film on a titanium substrate. Though the flower-like structure appears beautiful, it was actually a defect due to the growth of hematite near to the edges of the titanium during spray pyrolysis.

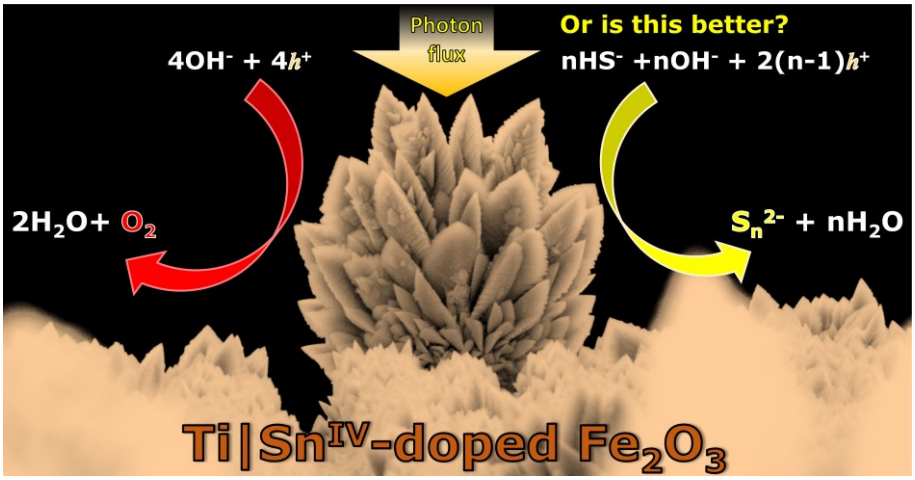


Figure 1-1. Scheme of hydrogen sulfide splitting *vs.* typical water splitting on hematite photo-anodes (SEM image).

1.2 Hydrogen production from solar energy

Hydrogen is considered the fuel of the future. Its uses as an energy carrier and properties are well-known [16]. The hydrogen economy has been proposed as a possible hydrogen-based energy system to obviate the negative effects associated with the combustion of traditional fossil fuels. Several roadmaps with a positive outlook for the use of hydrogen to provide heating [17], storage [18] and motive power [19] have been reported. The energy density of hydrogen is the highest in mass compared to other fuels; however, by volume is the lowest as shown in Table 1-1. This constitutes an issue for safe and inexpensive storage [16]. Nevertheless, the combustion of hydrogen is cleaner compared to traditional fuels, that is assuming the hydrogen source is also carbon-free, Figure 1-2 [20]. Hydrogen gas is not found on Earth naturally, due to its high escape velocity from Earth's gravitational field, so it must be produced from other natural resources. Currently, the most economical and most widely used method to obtain hydrogen is via steam reforming of methane [21], by which more than 95% of the hydrogen in United States is produced by reactions (1-1), (1-2) and (1-3) [22]:

$$CH_4 + H_2O \rightarrow CO + 3H_2 \tag{1-1}$$

$$CO + H_2O \rightarrow CO_2 + H_2 \tag{1-2}$$

$$CH_4 + 2H_2O \rightarrow CO_2 + 4H_2 \tag{1-3}$$

Table 1-1. Comparison of hydrogen properties with other fuels at 25 ° C and 1 atm.

	Hydrogen	Methane	Gasoline	Diesel	Methanol
Density / kg m^{-3}	0.0838	0.71	702	855	799
Energy density / kWh m^{-3}	3.0	9.1	8680	10090	4030
Energy density / kWh kg^{-1}	33.3	12.8	12.4	11.8	5.0

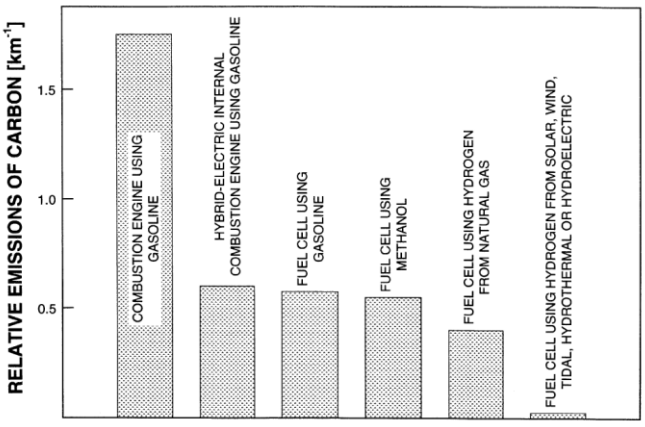


Figure 1-2. Relative emissions of greenhouse gases (expressed in carbon units per km) for vehicles with internal combustion engines or fuel cells [20].

Despite pollutant-free combustion, hydrogen production by steam reforming has associated CO_2 emissions, so cannot qualify as a clean energy carrier. On the other hand, electrolysis of water is also a very well-established technology. However, the use of expensive electrodes containing noble metals, e.g. platinum, and the use of electricity (60% generated worldwide by combustion of fossil fuels [23]) as the source of energy make electrolysis of water unpopular in the industry due to high costs compared to other technologies such as steam reforming [24, 25].

Hence, it is important to find an alternative way to produce hydrogen from carbon-free fuels and using a renewable source of energy, such as solar energy. Figure 1-3 shows a scheme of the main technologies proposed to date to produce hydrogen from renewable energies and their relation to each other [24]. It is worth noting that even when several renewable sources such as solar, wind or biomass are used, hydrogen can be obtained only via electrolysis, pyrolysis, thermochemical decomposition or gasification. Figure 1-3 does not include photobiological and photo-electrochemical processes, which are technologies still in early stages of development.

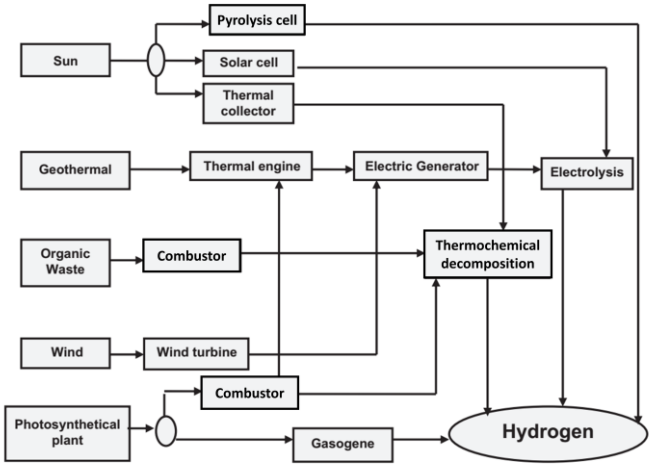


Figure 1-3. Technologies for hydrogen production using renewable sources of energies [24].

Figure 1-4 shows a more detailed scheme of the technologies used for hydrogen production exclusively using solar energy [26]. Bio-photolysis and photo-electrolysis are the only processes capable of producing hydrogen directly from water and light. It has also been proposed to use a renewable energy source (solar, wind and hydro) + electrolyser for the production of hydrogen [27]. The former technologies, although mature on their own, require an initial conversion of energy to electrons which incurs in efficiency losses and increased capital costs. Photovoltaics powering an electrolyser are predicted to have the lowest exergy efficiency while a hydro-electricity powered electrolyser has the highest [27].

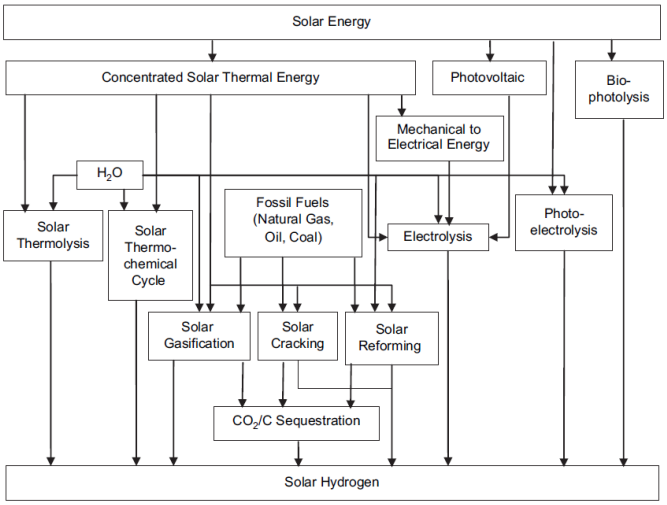


Figure 1-4. Processes for solar hydrogen production [26].

1.2.1 Photo-biological processes

In photo-biological processes, hydrogen is produced through photosynthesis using a suitable living organism (algae, cyanobacteria or photosynthetic bacteria), which can produce hydrogen in the presence of an irradiated mixture of water and enzymes. These processes are usually carried out at ambient temperature. However, typical efficiencies are ca. 1% and low rates of H_2 production have been achieved [28]. Currently, the research on this systems is focused on the improvement of efficiencies; an overall efficiency as high as 10% can be achieved with this type of system [29].

1.2.2 Photo-electrochemical processes

Photo-electrochemical water splitting is a process in which solar energy is converted to hydrogen (H_2) and oxygen (O_2) from water at the surface of photo-electrodes, cathode and anode respectively, where one or both of them can be irradiated with light [20].

Water splitting is an endothermic reaction with a Gibbs free energy of $\Delta G^0_{H_2O} = +238\ \mathrm{kJ\ mol^{-1}}$, see reaction (1-4).

$$\mathrm{H_2O_{(l)}} \rightarrow \mathrm{H_{2(g)}} + \frac{1}{2}\mathrm{O_{2(g)}}\ ,\Delta G^0_{H_2O} = +238\ \mathrm{kJ\ mol^{-1}} \tag{1-4}$$

Semiconductors can be used as photo-active materials in order to generate the required driving force after absorbing photons with greater energy than their band gap, generating electrons in its conduction band and highly oxidising 'holes' in its valence band by reaction (1-5):

$$\mathrm{Semiconductor} + h\nu \underset{\text{recombination}}{\overset{\text{absorption}}{\rightleftharpoons}} \mathrm{Semiconductor}(e^-_{\mathrm{CB}}, h^+_{\mathrm{VB}}) \tag{1-5}$$

Photo-electrolysis of water may be effected with photo-anodes (n-type semiconductors), chosen judiciously so that holes at their valence band edges are sufficiently energetic ($E_{\mathrm{VB}} < E_{\mathrm{O_2/H_2O}}$ on the physical scale) to oxidise water (or hydroxide ions at high pH) in the anolyte by reaction (1-6), coupled to photocathodes with photogenerated electrons at their conduction band edges having

sufficient energy ($E_{CB} > E_{H_2O/H_2}$ on the physical scale) to reduce water to hydrogen in the catholyte by reaction (1-7):

$$2H_2O + 4h^+_{VB} \rightarrow O_2 + 4H^+ \quad (1\text{-}6)$$

$$2H^+ + 2e^-_{CB} \rightarrow H_2 \quad (1\text{-}7)$$

A scheme of a typical photo-electrochemical cell (PEC) used for water splitting in alkaline solution with a single photo-anode can be seen in Figure 1-5 [30], and a PEC with a monolithic bi-pole in neutral or acidic conditions in Figure 1-6.

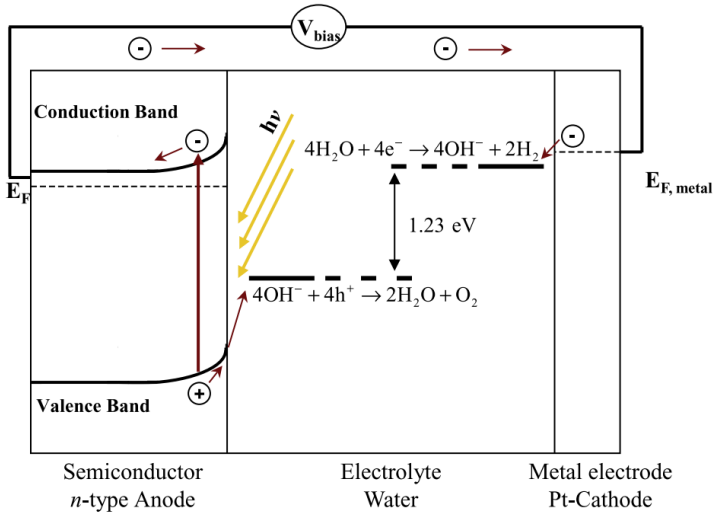


Figure 1-5. Schematic of PEC water splitting in alkaline solution using a photo-anode [30]. Potentials on the physical scale.

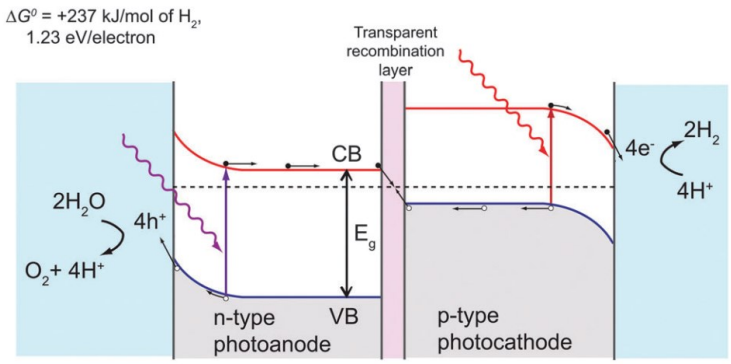


Figure 1-6. Schematic of a monolithic bi-pole for water splitting [31]. Potentials on the physical scale.

The main mechanism for the photo-assisted electrolysis of water involves the following steps [20]:

- Light-induced intrinsic ionization of the semiconductor, resulting in the formation of electronic charge carriers (electrons and holes);
- Oxidation of water at the photoanode by holes;
- Transport of H^+ from the anolyte or OH^- from the catholyte through the electrolyte towards the opposite electrode, and transport of electrons from the anode to the cathode through an

external circuit;

- Reduction of H^+ or H_2O at the cathode by photo-generated electrons.

In the case in which a photo-anode is used, the electrons and holes are formed according to equation (1-8).

$$2hv \rightarrow 2e^-_{CB} + 2h^+_{VB} \tag{1-8}$$

Then, the required energy to split water is $237.2\ \mathrm{kJ\ mol^{-1}}$ [32] can be expressed as the minimum potential difference to drive the reaction, equation (1-9).

$$E^0 = \frac{\Delta G^0_{H_2O}}{2eN_A} \tag{1-9}$$

Where, $\Delta G^0_{H_2O}$ is the standard Gibbs energy change of reaction (1-4), 2 the electron stoichiometry, N_A the Avogadro's number and e is the electron charge. Thermodynamically, 1.229 V is the minimum electrical potential required to split water spontaneously, or 1.48 V under thermoneutral conditions after considering the enthalpy change for water formation ($\Delta H^0_{H_2O} = 285.8\ \mathrm{kJ\ mol^{-1}}$) [32]. For finite reaction rates at current density *j*, the operating potential difference will be greater due to overpotentials and additional potential losses introduced by ohmic resistances in the electrolyte and electric contacts. However, few photo-absorbers can in theory harvest enough solar energy and supply enough energy to drive the reaction spontaneously. A combination of photo-anodes and photo-cathodes or stacked photo-absorbers have been proposed to achieve water splitting spontaneously [31].

Hence, a photo-electrochemical system for water splitting, that does not fulfil the energy requirements, needs an electrical or chemical bias in order to perform the photo-electrolysis, or in this case photo-assisted electrolysis. To date, there is no report of a photo-electrochemical cell with only one photoelectrode capable of achieving this process in satisfactorily with high efficiency [33] and using a wide range of visible light. Consequently, most of the reported systems require an electrical or chemical bias to produce hydrogen at an acceptable rate. When an electrical bias is applied, the electricity can be obtained from the burning of fossil fuels or, preferably, from renewable sources such as hydro, wind or solar energy, e.g. photovoltaic cell. In the latter, a photovoltaic cell is integrated with a PEC system, buried or external, to harvest the rest of the energy required [29]. Few systems requiring zero external bias have been reported. Until now, $SrTiO_3$ is considered the only semiconductor capable of supplying sufficient energy for water splitting without a bias [34]; however high intensity of UV light was required [20].

A chemical bias is also an option if an ion exchange membrane is used to separate the anolyte and catholyte, enabling a differential pH to be achieved. For every unit of difference in the pH between both solutions, the required bias is decreased 0.059 V at 298 K [35]. The major drawback of these systems is that acid and alkali must be supplied constantly to the electrolytes in order to maintain the bias.

Systems with more than one absorber (stacked semiconductors) could be used to supply enough energy to achieve spontaneous water splitting. This configurations are sometimes referred as an internally biased systems [33] or integrated photo-electrochemical devices [31, 36]. Photo-absorbers can be tailored to absorb photons in a wide range of the solar spectrum [37-39], and could potentially increase conversion efficiencies of solar to electrical energy from 12 to 16% for a single photo-absorber, 30-38% for two photo-absorbers, or even 72% for a hypothetical solar cell with 36 different band gaps [38]. However, as it is evident from these studies, systems involving stacked photo-absorber tend to be complex and large-scale implementation would not be practical [39] or economical.

1.3 General considerations about semiconductors

Electrons in solids are arranged in energy levels which can contain at most two electrons, they also form wide orbital energy bands of bonding (valence band), nonbonding and antibonding (conduction band) character [40]. When a material has an odd number of valence electrons (e.g., sodium), the valence band is not fully occupied and the electrons can move freely, causing conductive material. There are also materials with an even number of valence electrons and a fully occupied valence band; hence, the conduction band is completely empty. Electrons from the valence band can be excited into the conduction band after a certain amount of energy is applied, corresponding to the semiconductor band gap. The band gap (E_g) is the forbidden band that separates the valence band (VB) and conduction band (CB).

An insulator is defined as a material that needs large amount of energy (large band gap) to promote electrons from the valence to the conduction band. Insulators have low electrical conductivity, i.e., materials with band gaps greater than 3 or 4 eV [40, 41]. However, there are some materials with a band gap low enough that photons can excite the electrons and be transferred to the conduction band; these are the so-called semiconductors. Generally, a material with a band gap between 1 and 3 eV is considered a semiconductor [40]. TiO_2 and other materials with a band gap slightly higher than 3 eV are also usually considered semiconductors.

The electrons, a type of fermions, are distributed in energy levels as described by the Fermi-Dirac distribution, equation (1-10):

$$f(\varepsilon_i) = \frac{1}{\exp\left[\frac{\varepsilon_i - \mu}{k_B T}\right] + 1} \tag{1-10}$$

Where, $f(\varepsilon)$ is the occupation probability of a single-particle state ε_i, k_B is Boltzmann's constant, μ is the chemical potential, and T is the temperature. At 0 K, the chemical potential is defined as the Fermi energy. In the case of metals, this level is almost the same at room temperature, but for a pure semiconductor, the Fermi energy level lies halfway between the energies of the conduction and valence band edges and it depends on temperature. The Fermi level is a function of the electronegativity, $-\chi$. Semiconductors can be doped with impurities so that the Fermi level can be displaced towards the valence or conduction band due to a new allowed level between both

bands. Semiconductors with no allowed electron levels in the band gap are called intrinsic, e.g. pure silicone, while those with impurity atoms and allowed levels inside the band gap are called extrinsic.

The addition of impurities into semiconductors is usually referred to as doping. For example, if an atom of the group V in the periodic table, e.g., phosphorus (P^{V}), is added to a silicon (Si^{IV}), a surplus of valence electrons will displace the Fermi level to lie closer the conduction band. This defines an n-type semiconductor, where n stands for 'negative'. On the other hand, if an element of the group III, such as aluminium (Al^{III}), is added to silicon (Si^{IV}), a lack of electrons in the valence band will displace the Fermi level towards the valence band. These materials are called p-type semiconductor, where p stands for 'positive'.

When an electron is excited, thermally or by a photon with an energy larger than the band gap, a hole (i.e. absence of electron) is left in the valence band, creating an electron-hole pair (exciton). Electrons and holes are called charge carriers; holes, virtual species, are considered to have a positive charge. For a n-type semiconductor, the majority of the carriers are electrons (donor states), and for a p-type semiconductor they are holes (acceptor states) [41]. Consequently, photo-anodes should be n-type and photo-cathodes p-type semiconductors. Figure 1-7 shows a schematic representation of the interaction between photons and two semiconductors in order to split water in a PEC system.

As mentioned previously, only photons of energy larger than the band gap can promote electrons from one band to another. Then, the spectrum of the light source is of main importance. Figure 1-8 shows the solar spectrum as a function of the band gap and corresponding wavelength of three semiconductors: TiO_2, Fe_2O_3 and FeS_2. The thermo-neutral potential for water splitting (1.48 eV) is also shown as a reference [42]; however, the required potential difference could be as high as 2.0 eV after accounting for other losses [20]. After normalization of the power density, it can be seen how much energy an electrode of certain band gap can absorb from the solar spectrum. For example, TiO_2 can absorb only in the ultraviolet region, so only a small portion ($< 2.6\%$) of the total irradiance is used in the photo-absorption process.

However, a semiconductor's band gap is not the only parameter that needs to be considered for PEC systems. The energy levels of the bands or band edges, as shown in Figure 1-7, must be appropriate so that the electrons or holes have the adequate energy to drive the oxidation and reduction reactions. These properties can be estimated using the band gap and electronegativity of a pure semiconductor, according to equations (1-11) and (1-12). Also, the flat band potential, defined as the potential that needs to be applied to the electrode | electrolyte interface in order to make the bands flat, must be considered [43]. As mentioned before, spontaneous photo-electrolysis, zero bias, can be achieved only if this potential is higher (on the physical scale) than the H^+/H_2 redox potential, -4.44 eV [20]; or lower in the electrochemical potential scale, 0 V *vs.* RHE.

$$E_{CB} = -\chi + 0.5E_g \tag{1-11}$$

$$E_{\mathrm{VB}} = -\chi - 0.5E_g \tag{1-12}$$

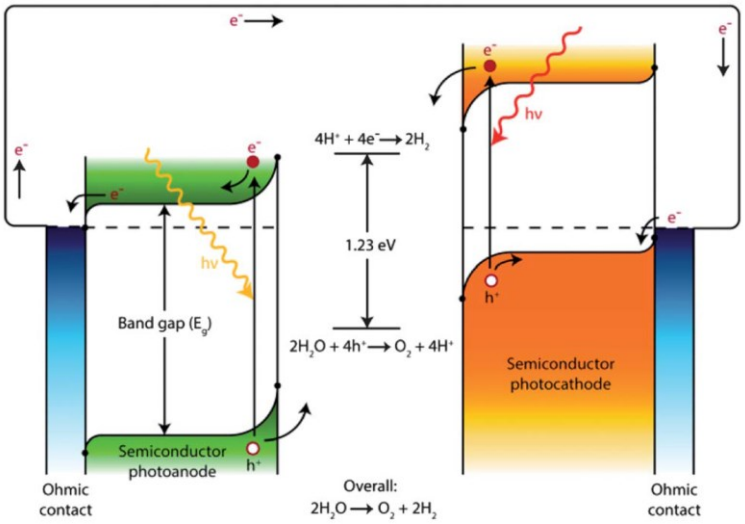


Figure 1-7. Schematic band diagram showing the phenomena of photo-absorption, band bending, charge separation, and hydrogen and oxygen evolution for a PEC with two photo electrodes [25].

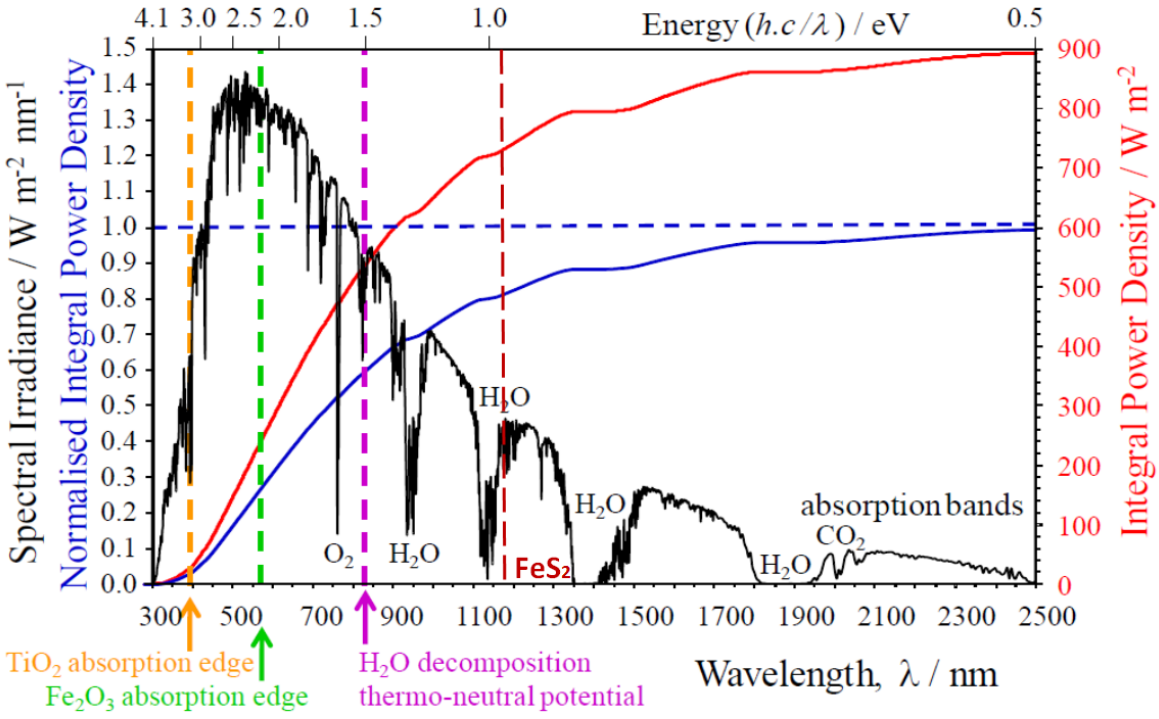


Figure 1-8. ASTM G173-03 reference solar spectrum terrestrial direct normal + circumsolar, and absorption edges of three photo-electrodes compared against the energy level for H_2O decomposition

1.4 Efficiency of PEC systems

The performance assessment, characterisation, optimisation and comparison of photo-electrochemical systems require the definition of suitable efficiencies that encompass whole devices and their more critical components individually.

Most of the definitions for efficiency of photo-electrochemical systems and standard protocols found in literature are focused largely on material and semiconductor development [44, 45].

Commonly referred to as 'diagnostic efficiencies', these are used to assess specifically the performance of photo-electrodes [46]. Among them, the solar to hydrogen conversion (STH) efficiency is the only efficiency that can be used as a representation of the overall efficiency of a PEC. It is also the most widely reported efficiency for systems under zero applied bias.

$$\mathrm{STH} = \left[\frac{E_{\mathrm{H_2}}\dot{n}_{\mathrm{H_2}}}{P^o A}\right]_{\mathrm{AM\ 1.5G}} \tag{1-13}$$

STH is defined as the quotient of the 'rate of chemical energy produced' and the 'rate of solar energy input', where $E_{\mathrm{H_2}}$ is the energy contained per mole of hydrogen, and $\dot{n}_{\mathrm{H_2}}$ is the hydrogen molar flow rate. The Gibbs energy change for water splitting (237 kJ mol^{-1} at 25 °C) is commonly used as $E_{\mathrm{H_2}}$ [44], though it neglects the thermal energy requirement [47]; P^o is the photon power density for standard terrestrial spectra of air mass 1.5 global power density (ca. 1000 W m^{-2}) and A the area of the irradiated photo-electrode. Researchers also use a modified version of STH in terms of the photocurrent (j_{ph}), charge yields for hydrogen production ($\Phi_{\mathrm{H_2}}$) and the equilibrium water-splitting potential difference (ΔU^0) of 1.23 V, though the thermo-neutral potential difference is 1.48 V. However, the estimation of charge yields still requires the measurement of H_2 and O_2 gas volumes or flow rates.

$$\mathrm{STH} = \left[\frac{j_{\mathrm{ph}} \times \Delta U^0 \times \Phi_{\mathrm{H_2}}}{P^o}\right]_{\mathrm{AM\ 1.5G}} \tag{1-14}$$

Little has been defined for PECs under applied bias and the few suggested efficiencies are focused only on material assessment, making them unsuitable for researchers investigating overall system efficiencies.

Applied bias photon-to-current efficiency (ABPE) has been suggested consistently as a way to assess the performance of systems operated under applied bias [44, 46].

$$\mathrm{ABPE} = \left[\frac{j_{\mathrm{ph}}(\Delta U^0 - |\Delta U_{\mathrm{bias}}|)}{P^o}\right]_{\mathrm{AM\ 1.5G}} \tag{1-15}$$

where $|\Delta U_{\mathrm{bias}}|$ is the applied cell bias in a two electrode cell. The principal issue with ABPE is that, under conditions when $\Delta U_{\mathrm{bias}} > \Delta U^0$, negative ABPE values are calculated from equation (1-15) that counter-intuitively become more negative for higher photocurrents. Hence, such values could mislead conclusions on device performance. A material that exhibits the best performance at $\Delta U_{\mathrm{bias}} < 1.23\ \mathrm{V}$ then exhibits the worst performance at $\Delta U_{\mathrm{bias}} > 1.23\ \mathrm{V}$. Of course, in reality the material that generates the higher current density will always lead to better device performance at any given bias. Reports of ABPE in the literature can be found only for the conditions $\Delta U_{\mathrm{bias}} < 1.23\ \mathrm{V}$. A few recent studies report ABPE values for bias-requiring systems, such as p-type Cu^{II}-doped α-Fe_2O_3 ($\Delta U_{\mathrm{bias}} = 0.5\ \mathrm{V}$) [48], Ta_3N_5 ($\Delta U_{\mathrm{bias}} = 0.5\ \mathrm{V}$) [49] and $BiVO_4$ ($\Delta U_{\mathrm{bias}} = 0\ \mathrm{to}\ 1.2\ \mathrm{V}$) [50]. All ABPE values found in these reports are $< 3\ \%$ and for current densities $< 60\ \mathrm{A\ m^{-2}}$. There are no reports of ABPEs for $\Delta U_{\mathrm{bias}} \geq 1.23\ \mathrm{V}$, so it is plausible that the issue discussed above has not been encountered previously or is unpublished.

Despite clear general guidelines set out by Chen et al. [44], which will be discussed below, the applied cell bias ΔU_{bias} in equation (1-15) is often misinterpreted, such that it is not possible to deduce whether a given reported system was in fact operating under or above 1.23 V bias. Misinterpretations include the use of electrode potentials *vs.* RHE instead of the actual cell bias [51-55]. This approximation is only reliable provided the ohmic potential drop across the reactor is negligible and the overpotential at the counter electrode is close to zero. These conditions are rarely met in up-scaled devices. Furthermore, some studies use electrode potentials relative to reference electrodes other than RHE, such as SCE [56], without introducing corrections. Others use an approximated flat band potential value instead of the applied cell bias [57]. These inconsistencies render comparison of device and materials performances most difficult.

Several authors have now noted that ABPE is not an efficiency that describes photonic or electrical conversion properly [58]. Also, it is not an appropriate measure for comparison of device performance because the charge yield and hydrogen flow rates are not considered either implicitly or explicitly [45]. It is also noticeable that recent reviews and systematic studies of photo-electrode materials in biased systems do not use ABPE as an effective way to compare their performances [59-64].

To avoid these issues, Dias et al. [58] proposed two separate definitions: a device efficiency (Φ_{device}) and a photo-electrode efficiency ($\Phi_{\text{photo-electrode}}$).

$$\Phi_{\text{device}} = \frac{j_{\text{ph}} \Delta U^0}{P^o + j_{\text{ph}} \Delta U_{\text{bias}}} \tag{1-16}$$

$$\Phi_{\text{photo-electrode}} = \frac{j_{\text{ph}} (\Delta U^0 - |U_{\text{fb}}|)}{P^o} \tag{1-17}$$

Φ_{device} represents the overall PEC efficiency and $\Phi_{\text{electrode}}$ the actual photoelectrode performance without considering the applied cell bias. These two definitions avoid negative and null efficiencies, but charge yields and hydrogen flow rates are still not considered.

On the other hand, Hisatomi et al. proposed an equivalent expression to STH in biased systems: applied-bias-compensated solar-to-hydrogen efficiency or AB-STH [45].

$$\text{AB} - \text{STH} = \frac{j_{\text{ph}} \times \Phi_{\text{H}_2} \times (E^0 - \Delta U_{\text{bias}})}{P^o} \tag{1-18}$$

This definition accounts for charge yields below unity, but still does not represent a photonic or electronic conversion, as the numerator is still not a representation of the net energy output.

By analogy with the STH efficiency and based on the reports by Dias and Hisatomi, Assisted Solar-to-Hydrogen (ASTH) efficiency was proposed to assess biased photo-electrochemical reactors as a whole [65], which is similar to the graphical circuit analysis proposed by Coridan at al. [66]. In this case, the actual 'rate of chemical energy produced' is divided by the 'total rate of energy input', which comprises contributions from 'solar photons' and 'applied bias'. It also considers ohmic potential losses in the cell and hydrogen flow rates, which implicitly includes the charge yield.

$$\mathrm{ASTH} = \frac{E_{\mathrm{H_2}}\dot{n}_{\mathrm{H_2}}}{(P^o + j_{ph}\Delta U_{\mathrm{bias}})A} \tag{1-19}$$

where ΔU_{bias} is the applied cell potential difference, i.e. the potential applied between the (photo-)anode and (photo-)cathode. This equation requires the measurement of hydrogen gas in a two-electrode cell. The use of ASTH efficiencies allows reasonable comparisons not only between materials, but more importantly between devices operating under different conditions. It is also worth mentioning that the efficiency of a material and device is just one of several parameters that needs to be optimized to minimise the total cost of (photo-assisted) electrolysers for hydrogen production. Focusing solely on efficiency as a key performance indicator has implications for capital costs, which decrease with increasing current densities; technical and economic viabilities of photo-electrochemical reactors also require adequate durability and resilience which limit rates of development and deployment [67]. A more extensive review of efficiencies for comparison of energy-conversion systems can be found elsewhere [66].

The incident photon-to-current efficiency (IPCE), also called the external quantum efficiency, is recently gaining popularity among researches as a diagnostic tool for photo-absorbers. It is defined as the total efficiency that encompasses the three main mechanisms involved in the photo-generation of charge carriers at a semiconductor, equation (1-20), namely the photo absorbance or fraction of electron-hole pairs generated by the incident photo flux, the charge transport to the solid-liquid interface, and the efficiency of interfacial charge transfer at the surface of the electrode [44].

$$\mathrm{IPCE} = \Phi_{\mathrm{e^-/h^+}}\Phi_{\mathrm{transport}}\Phi_{\mathrm{surface}} \tag{1-20}$$

IPCE is a function of the incident wavelength, so a monochromator must be used in order to have the corresponding current density for each wavelength. IPCE can be estimated as:

$$\mathrm{IPCE} = \frac{|\mathrm{j_{ph,\lambda}}| \times 1239.8\ (\mathrm{V\,nm})}{\mathrm{P_\lambda} \times \lambda\ (\mathrm{nm})} \tag{1-21}$$

Where $j_{ph,\lambda}$ is the photocurrent density and P_λ is the incident power density at a given wavelength λ. The constant $1239.8\ (\mathrm{V\,nm})$ is related to the conversion of wavelength to energy according to Planck's constant and the speed of light.

It should be noted that IPCE is significantly different from STH efficiency. STH is described in terms of power (incident power, output power) in the whole solar spectrum, meanwhile IPCE is a function of the wavelength and it describes the relation between incident photons and electrons. However, an estimation of the maximum STH can be made with an integration of the IPCE over the solar spectrum in the absence of a bias. When a bias is applied, IPCE is allowed only as a diagnostic parameter and must be studied very cautiously, but it is still very useful when different sources of light are used.

1.5 Economic aspects of solar hydrogen production

To date, only a few reports on the exergy efficiency and cost analysis of hydrogen production from renewable sources can be found. However, photo-electrolysis, a technology still in development, is usually not properly analysed [26] or not analysed at all [24, 27]. From these reports it is concluded that the electrolysis of water using electricity from hydroelectric power has the highest exergy efficiency (5.6%) and systems using photovoltaic assistance has the lowest (1.0%) [27]. Presently, there are no reports with a proper comparison in terms of the exergy efficiency of a photo-electrochemical cells for hydrogen production.

Several cost analysis studies have been reported, but they also omit PEC and photocatalytic systems. Table 1-2 shows the expected costs of hydrogen production using conventional and already available technologies compared to those still in development [24]. It can be seen how the solar methane steam reforming process is the most economical technology. These values have been also corroborated recently [25], where an estimated cost of hydrogen coming from steam methane reforming is approximately \$1.25 per kg H_2, whereas the cost using photovoltaic technology is higher than \$4.09 per kg H_2. In the same report, an estimated cost for hydrogen obtained from photo-electrolysis in particle-based systems was \$1.60 per kg H_2 assuming 10% of STH efficiency, \$4.10 per kg H_2 for concentrated panel systems with 15% STH efficiency, and as high as \$10.40 per kg H_2 for an integrated PEC system with 10% STH efficiency. It is obvious that the latter systems can barely compete with conventional methods. Improvements in reactor design and efficiency must be made before the systems could be deployed commercially. Nevertheless, it has been stated that the production of hydrogen by photo-electrolysis is a viable option among carbon free processes [25].

Table 1-2. Projected costs (long term) of hydrogen production [24]

Current process designs and small-scale pilot plants	Cost / € $(t\ H_2)^{-1}$
Solar hybrid sulfur cycle	1900
Solar sulfur-iodine cycle	2000
Solar metal/metal oxide cycle	3500
Solar high temperature electrolysis	4667
Solar methane cracking	1767
Solar methane steam reforming	1633
Other future renewable options	
Biomass gasification	1067
Alkaline electrolysis using photovoltaic power	6667
Alkaline electrolysis using solar thermal power	2667
Alkaline electrolysis using wind power	2333

1.6 Hydrogen sulfide splitting

Replacing the energetically demanding oxygen evolution reaction of splitting water with hydrogen sulfide oxidation, coupled to hydrogen evolution, decreases the thermodynamic energy requirement for hydrogen production by ca. 80 %. Such a process could be used to recover sulfur from hydrogen sulfide emissions, e.g. from hydrodesulfurisation processes or sour water treatment.

The main advantages of splitting hydrogen sulfide instead of water are [10]:

- Economical: hydrogen sulfide splitting requires less energy than H_2O splitting;
- Environmental: the removal of H_2S is desirable due to its toxic and corrosive nature. Also, the simultaneous production of an environmentally benign fuel such as H_2 is welcomed;
- Availability: though not as abundant as water, hydrogen sulfide is an intermediate in thermochemical cycles or as a by-product in acid bleaching of sulfides and hydrodesulfurisation of petroleum products ($>$ 70 Mt treated sulfur per year in 2015)[15]. It can also be found naturally in sour gas streams from geothermal sources.

Claus processes are used to remove H_2S from naphthas and petroleum oils, the H_2S being oxidised to elemental sulfur at high temperature in the presence of a catalyst. However, such processes produce tail gases from which hydrogen sulfide has to be depleted to acceptably low concentrations by additional processes [10].

1.6.1 Thermochemical and thermal decomposition

Hydrogen sulfide splitting has been studied extensively using concentrated solar energy in a thermochemical process, also called thermal decomposition [68, 69]. In these processes, hydrogen sulfide can be decomposed to hydrogen and sulfur at high temperatures (around 1000 K) in the presence of metal oxides or sulfides. These processes require greater specific energies than photocatalytic or photo-electrochemical processes.

1.6.2 Electrolysis

Electrolysis of hydrogen sulfide can be achieved in an analogous manner to water electrolysis. The main issue with the electrolysis of hydrogen sulfide is the passivation of the anodes by elemental sulfur [69] by the reaction (1-22). In these processes sulfur is produced on the anode and hydrogen is released at the cathode according to reaction (1-23).

$$HS^- + OH^- \rightarrow 'S' + H_2O + 2e^- \tag{1-22}$$

$$2H_2O + 2e^- \rightarrow H_2 + 2OH^- \tag{1-23}$$

The electrolysis can be achieved in acidic or alkaline conditions. However, alkaline media is preferred because sulfur dissolves readily to form polysulfides ions, S_n^{2-}. Then, the passivation due to elemental sulfur can be minimised:

$$n'S' + HS^- + OH^- \Leftrightarrow S_{n+1}^{2-} + H_2O \tag{1-24}$$

Polysulfides may also be produced directly at the anode:

$$nHS^- + nOH^- \Leftrightarrow S_n^{2-} + nH_2O + 2(n-1)e_{CB}^- \tag{1-25}$$

The solubility of polysulfide ions in aqueous sodium sulfide solutions is very high, between 3.7 to 4.4 S:Na_2S ratio [70-72]. However, if polysulfide ions reach the cathode, an undesirable reaction could take place instead of hydrogen evolution, reaction (1-26). In order to prevent this, cation-permeable membrane, e.g. Nafion® can be placed between both electrodes to prevent the diffusion of polysulfides to the cathode.

$$S_n^{2-} + 2(n-1)e^- + nH_2O \rightarrow nHS^- + nOH^- \quad (1\text{-}26)$$

Figure 1-9 shows a potential-pH (Pourbaix) diagram for a meta-stable sulfur-water system, from which all sulfoxy species had been excluded in its calculation, to allow for the large activation barriers for their formation. Such diagrams are useful in predicting the (meta-) stability regions of different species as functions of electrode potential and pH according to the thermodynamic predictions of the reactions presented above. These diagrams are computed using the standard potentials of each redox reaction and the required potential from the Nernst equation as follows [73].

$$U = U^0 + \ln 10 \frac{RT}{\nu_e F} \log \prod [i]^{\nu_i} \quad (1\text{-}27)$$

Where U^0 is the standard equilibrium potential calculated from the standard Gibbs energy of formation, ν_i is the stoichiometry constant of species i, negative for reactants and positive for products, and ν_e is the charge number for the reaction. The Nernst equation can be rewritten as:

$$U = U^0 - 0.0591 \frac{\nu_{H^+}}{\nu_e} pH + 0.0591 \frac{\nu_{red}}{\nu_e} \log[red] + 0.0591 \frac{\nu_{ox}}{\nu_e} \log[ox] \quad (1\text{-}28)$$

Where the standard potential of the reaction can be calculated from the standard Gibbs free energy of formation:

$$U^0 = \frac{\Delta G^0}{\nu_e F} = \frac{\mu^0(products) - \mu^0(reactants)}{\nu_e F} \quad (1\text{-}29)$$

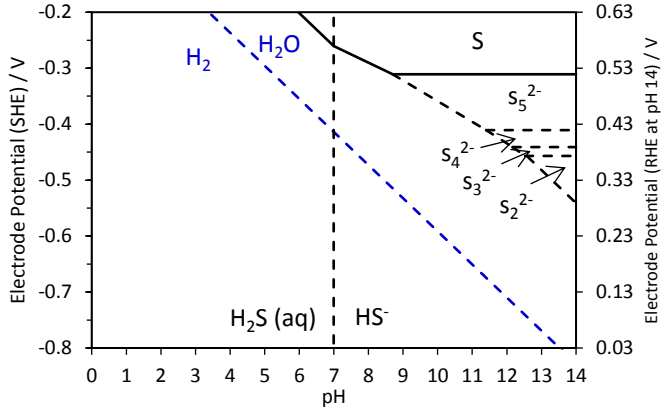


Figure 1-9. E-pH diagram for S-H_2O system, 0.1 MPa, 298 K and total dissolved sulfur activity 0.5 and sulfoxides species excluded.

It can be seen from Figure 1-9, adapted from [73, 74], that in alkaline electrolytes the potential difference between hydrogen sulfide oxidation and the reduction of water is roughly 0.27 V, while

water splitting requires a minimum of 1.23 V. It is also evident that multiple polysulfide species could be generated during the oxidation, depending on the pH and the potential applied to the system.

1.6.3 Photocatalytic

Hydrogen sulfide splitting via photocatalytic decomposition is carried out in a reactor containing suspended particles, made of semiconducting materials, dispersed in solution. Most of the research involving semiconductors for hydrogen sulfide splitting using solar energy is being conducted with this system. The most accepted mechanism for hydrogen sulfide splitting in photocatalytic systems was proposed by Preethi et al. [75]

Dissociation

$$H_2S + OH^- \leftrightarrow HS^- + H_2O \quad (1\text{-}30)$$

$$H_2S + OH^- \leftrightarrow S^{2-} + H_2O \quad (1\text{-}31)$$

Anode

$$\text{Semiconductor} + hv \rightarrow e^-_{CB} + h^+_{VB} \quad (1\text{-}32)$$

$$2HS^- + 2h^+_{VB} \rightarrow S_2^{2-} + 2H^+ \quad (1\text{-}33)$$

$$2S^{2-} + 2h^+_{VB} \rightarrow S_2^{2-} \quad (1\text{-}34)$$

Cathode

$$2H^+ + 2e^-_{CB} \rightarrow H_2 \quad (1\text{-}35)$$

Overall

$$H_2S + h\nu \rightarrow H_2 + S_2^{2-} \text{ (or polysulfide)} \quad (1\text{-}36)$$

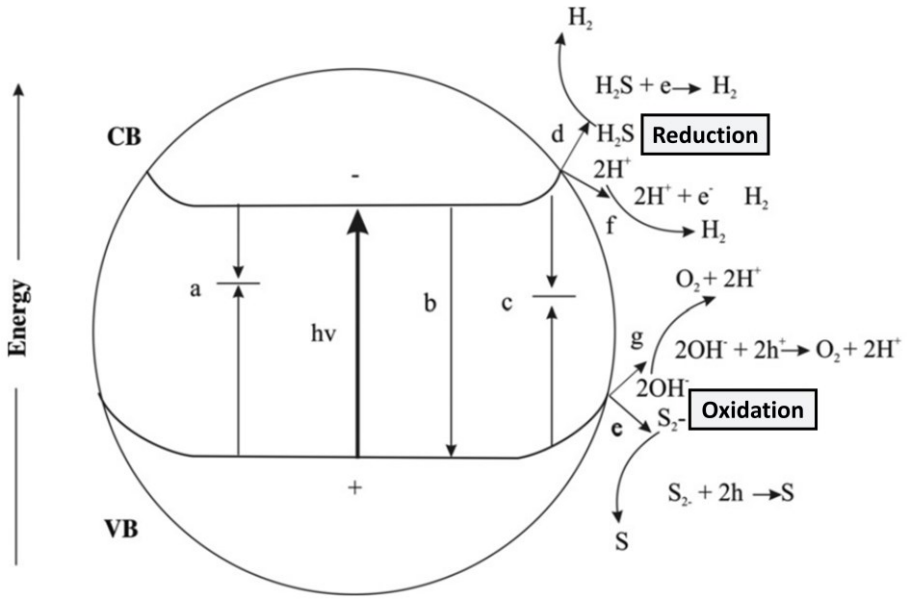


Figure 1-10. Mechanism of liquid-phase photocatalytic hydrogen production from water and H_2S streams [75].

Hydrogen sulfide is a diprotic acid with two dissociation constants of $pK_{H_2S,1} = 7.05$, reaction (1-30) and $pK_{HS^-,2} \cong 19$, reaction (1-31) at 25 °C [76]. At alkaline pH, ca. 14, the predominant active species in solution are HS^- ions. After the generation of an electron-hole pair in the semiconductor, HS^- is oxidised by the holes and a polysulfide is produced, reaction (1-33). The remaining proton is then reduced on the cathodic surface of the particle and then hydrogen is produced, reaction (1-35). A schematic representation of the previously described mechanism is presented in Figure 1-10. The cathode and anode are present in the same particle, then the risk of polysulfide reduction instead of protons is very high, (reaction 1-26). Moreover, and in contrast to electrolysis, the use of a membrane is not an option in these systems.

1.6.4 Photo-electrochemical

There are only a few reports for hydrogen sulfide splitting using photo-electrochemical cells. However, the basic principles of hydrogen sulfide electrolysis are still valid. Hydrogen sulfide splitting by photo-electrochemical methods was first mentioned by Grätzel [77], Licht et al. continued shortly after with an analysis of $CdS|S_n^{2-}$ photo-electrodes in hydrogen sulfide solutions in order to study the instability of such electrodes in photo-electrochemical cells [78]. An early and promising work by Bockris et al, [79] showed the advantages of using a CdSe films as photo-anodes to split hydrogen sulfide to produce hydrogen.

It has been challenging to find stable photo-electrodes for traditional water splitting while keeping high efficiencies and scalability. Hence, the interest of hydrogen sulfide splitting has been renewed in the last decade. Hydrogen sulfide ions have been used as hole scavengers due to their ability to decrease electron-hole recombination at the semiconductor | electrolyte interface, and improve the stability of metal sulfide photo-absorbers, such as Bi_2S_3 [80, 81]. Recently, a novel concept was proposed to split hydrogen sulfide in presence of a redox couple and solar irradiation to produce hydrogen and sulfur in a PEC with anolyte and catholyte separated by a Nafion® membrane [82]. However, this system has some drawbacks: the use of expensive and not commercially scalable electrodes, an additional redox couple in solution and electrical bias makes the system uneconomical an unpractical. Hematite modified with CdS has been used recently [83]. This particular study cited the already published discovery by the author of this thesis, where hematite photo-anodes are a stable and suitable candidate for photo-assisted electrolysis of hydrogen sulfide [74].

1.7 Semiconductor materials for photo-electrochemical processes

Presently, most of the efforts towards the generation of solar hydrogen using photocatalytic or photo-electrochemical systems are focused on material development. A photo-electrode must fulfil the following requirements to be considered a suitable candidate [10, 25, 33]:

- Suitable band gap for light absorption; a large band gap only absorbs high energy wavelengths, but a low band gap restricts the alignment of the band edges. Band gaps of ca. 1.7 eV are often cited as appropriate, as they can deliver enough potential to split water

(1.23 eV + losses) while absorbing ca. 40% of the solar spectrum.

- The band edges should match the redox potential of the reactions of interest.
- A lower flat-band potential, on the electrode potential scale, than the hydrogen reduction potential.
- High efficiency. This can be achieved by minimising electron-hole recombination rates in the semiconductor.
- Long term stability in presence of solar radiation: absence or low kinetics of photocorrosion processes or undesirable reactions in the surface of the electrode (surface poisoning).
- Low cost, abundant material and facile fabrication at large scale.

Also, it is recommended to avoid a semiconductor that requires a bias to yield an acceptable rate of hydrogen production due to disadvantages already mentioned. All materials to date fulfil only some of these requirements. Hence, this material constraint is usually described as the bottleneck for the deployment of photo-electrochemical reactors for water or hydrogen sulfide splitting.

1.7.1 Water splitting

Xu et al, published one of the most complete reviews of semiconductor properties [41]. Both, metal oxides and metal sulfides were considered in this work. However, the majority of the valence and conduction band edges reported in this review were calculated based on the electronegativities, and just a few reported properties are based on experimental work. In this review, it can be seen a general trend where metal oxides generally have a large band gap, but just few of them have a suitable conduction band for hydrogen evolution. Conversely, metal sulfides usually have small band gaps but are better suited for reduction processes.

TiO_2 (anatase phase, $E_g \approx 3.2\,\text{eV}$, $E_{CB} \approx -0.230\,\text{V}\ vs.\,\text{SHE}$) [41] is without a doubt the most studied semiconductor for water splitting processes due to its high stability. Yet, solar hydrogen generation is limited by its ability to absorb photons only in the UV region, $\lambda < 387\,\text{nm}$. $SrTiO_3$ ($E_g \approx 3.4\,\text{eV}$, $E_{CB} \approx -0.830\,\text{V}\ vs.\,\text{SHE}$) has suitable band edges, with a conduction band edge situated below the hydrogen evolution equilibrium potential ($0\,\text{V}\ vs.\,\text{SHE}$ at pH 0, $-0.827\,\text{V}\ vs.\,\text{SHE}$ at pH 14). $SrTiO_3$ is reported to be the only semiconductor capable of spontaneous water splitting in PEC systems (excluding integrated systems) [34], improvements have been made with metal doping while photocurrents are still low due to its large band gap [84].

Metal sulfides such as CdS, RuS_2, and $Zn_{1-x}Cu_xS$ have been studied for water splitting under visible light. However, a sacrificial agent is generally needed to perform the photo-electrolysis [75] and such materials are usually not stable in aqueous solution [10].

Nowadays, the electrochemical properties of a wide range of semiconductors have been reported and improved. However, the requirements for successful water splitting have not been met fully. Current strategies to improve the performance of these materials are described as follows [84]:

- Doping with metallic ions in order to modify the band gap region.

- Surface modification of the semiconductor with luminescent species.
- Mechanical and thermal treatment of the surface.

A list of materials achieving spontaneous water splitting has been summarised by an extensive review by Ager et al. see Figure 1-11 [31]. All the materials reported were used as buried photo-absorbers, meaning that the evolution of hydrogen and oxygen gas does not occurs at the surface of the semiconductor, instead a catalytic material was used. As mentioned before, these are the so-called integrated systems. Most of these materials are rather expensive and complex, and usually unstable. However, remarkable efficiencies have been achieved. 12.4% has been reported for a single junction $GaInP_2$|GaAs monolithic PV integrated to a Pt-catalysts for hydrogen and oxygen evolution [85]; and 18.3% for double junction $Al_{0.15}Ga_{0.85}As$|Si monolithic PV in a similar arrangement [86]. More recently, a triple junction photovoltaic cell (InGaP|GaAs|GaInNAsSb) acting as a photo-absorber in a PV + electrolyser system, i.e. external photo-absorber, achieved STH efficiencies over 30% during 48-hours electrolysis [87]. The materials used in these studies are rather expensive and usually not stable in the long term, this would increase significantly the capital and maintenance costs of the device. Power losses due to the production of electrons outside the electrolyser might also affect the overall performance of the device. Having a single device where the photo-absorbers acts as electrode is preferable. However, only biased systems with low efficiencies has been developed with this approach.

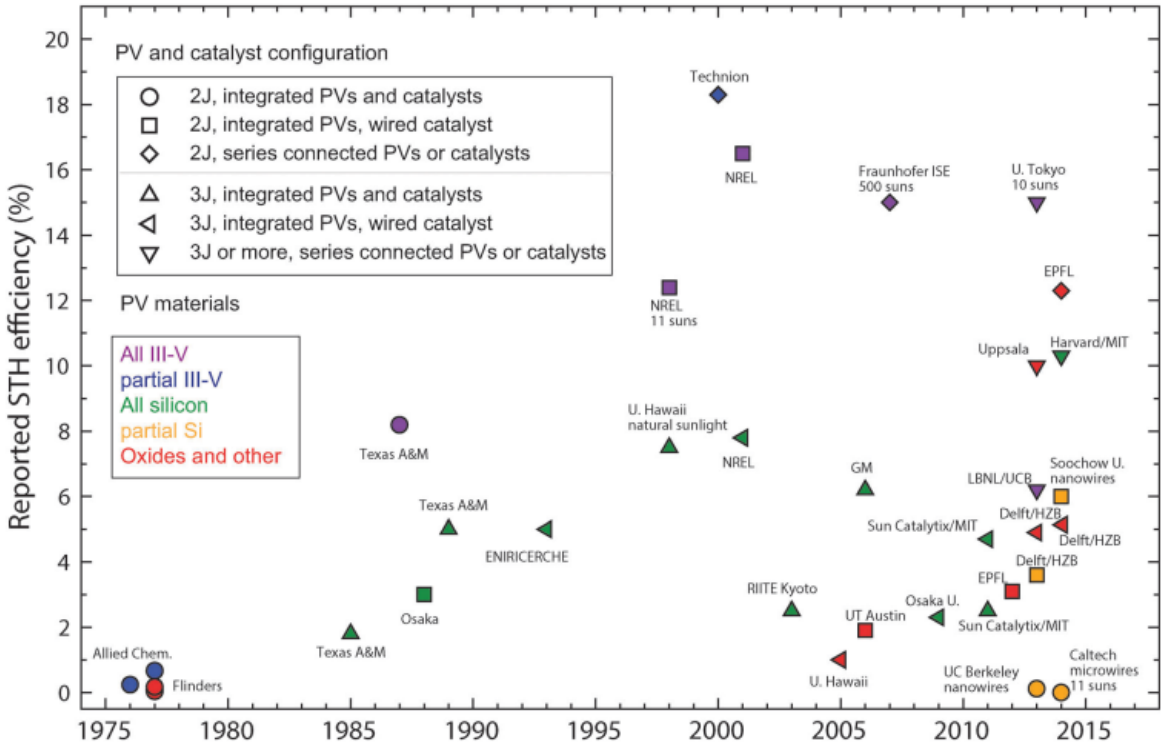


Figure 1-11. Solar-to-hydrogen (STH) conversion efficiencies for integrated systems as a function of year of report [31].

Hematite, Fe_2O_3, has also been studied extensively as a candidate photo-anode material for water splitting [60, 88, 89]. However, very low efficiencies remain an issue due to high electron-hole

recombination rates and high flat band potentials on the electrode potential scale. The main advantage of hematite over other materials, despite the lower efficiencies, is its stability, and diverse and scalable methods for synthesis. Various approaches for improving this material have been suggested [64, 90-94] and will be discussed in detail in Chapter 1.

1.7.2 Hydrogen sulfide splitting

Sulfide minerals are thought to be the best option to consider as photo-absorbers for hydrogen sulfide splitting. These materials usually have a small band gap with low valence band edge on the electrode potential scale, which makes them suitable for hydrogen sulfide splitting. Also, sulfide minerals are the most studied semiconductor for photocatalytic water splitting using colloidal systems [13]. The instability of these semiconductors remains a problem that needs to be resolved. However, as HS^- ions are good hole scavengers, photocorrosion processes at the surface are expected to be minimised [10, 41]. Other authors recommend the deposition of Si on the electrode surface to avoid this problem [95]. Also, noble metals, e.g. Pt, Ru, Rh, or their oxides, are commonly added on the electrode surface to improve catalytic properties for hydrogen evolution [11, 69, 96, 97]. Higher hydrogen yields were achieved using these modified surfaces, but the cost of the materials was also significantly increased.

CdS is one of the most studied semiconductors for photocatalytic hydrogen sulfide splitting. A mixture of this semiconductor with TiO_2 exhibited a good performance in presence and absence of sacrificial agents [12]. On the other hand, mixed crystals of Cd, Fe and S demonstrated inactivity for hydrogen evolution [98]. Despite this, its use is restricted under the REACH Regulation in Europe.

As previously shown by Xu [41], other semiconductors with suitable band edges include ZnS, ZnS_2, MnS, SnS_2, In_2S_3. Except for ZnS and doped In_2S_3 [13], few studies have been published for hydrogen sulfide splitting using these materials. Some efforts have been made with SnS, however its low stability and the need of an extra redox couple as Ce^{4+}/Ce^{3+} [99], in order to prevent photocorrosion, represents a major difficulty; also, the reduction of disulphide ions competes with hydrogen evolution in the cathodic region of the particle [100]. MoS_2 has been reported as an excellent catalytic material for highly efficient electrolysis of water [101, 102], but no reports have been found for hydrogen sulfide oxidation. Bi_2S_3 has been reported as a suitable photo-absorber for hydrogen sulfide splitting in PEC systems [80, 103], and also in photocatalytic systems [81], however very low efficiencies were achieved.

FeS_2 (pyrite) seems a promising semiconductor with a small band gap (0.95 eV). There is no consensus about the position of its band edges; several authors reported different positions for conduction and valence band [41, 104]. At first sight, pyrite seems an excellent candidate due to its high absorption coefficient ($6\times10^5 cm^{-1}$) and natural abundance [105, 106]. However, low photovoltages and photocurrents have been attributed to a Fermi level which is situated far (0.2 eV or higher) from the conduction band when used as photo-electrode [107].

1.7.3 Initial screening of semiconductors for hydrogen sulfide splitting

The materials described above were studied as possible candidates for hydrogen sulfide splitting in this project. However, their synthesis was proved to be difficult by the author of this thesis, and most materials were unstable or photo-inactive. A brief discussion of each one is presented below:

- Pyrite (Fe_2S): Proved to be difficult to synthetize with a correct cubic structure at low temperatures [108]. Electrodeposition on platinum showed very poor stability and photo-inactivity.
- Cobalt sulfide (CoS): Synthesis based on previous study produced unstable films on Pt and FTO [109]. Glassy carbon as a substrate was also explored, but adhesion was poor, though stability was slightly better. There was no indication of photo-activity and very resistant films were achieved with this methodology. A method for CoS synthesis on glassy carbon and Ti was developed using a two-step electrodeposition [110]. This method produced stable CoS films. However, samples were not photo-active.
- Molybdenum disulphide (MoS_2): A reported method suggested an easy and scalable synthetic route to MoS_2|fluorine-doped tin oxide (FTO) on glass [111]. However, films were very unstable and poorly adherent in presence of hydrogen sulfide ions. Different times of electrodeposition were studied in vain. Using the same methodology with titanium as substrate improved the adherence, but stability and lack of photo-activity remained an issue. Alternative routes of synthesis were explored with the same outcome [112].
- Bi_2S_3 was synthesised using a one-step cathodic electrodeposition [113]. It was stable only at low potentials and exhibited very low photo-activity.
- Other semiconductors such as CdS and PbS were avoided due to their toxicity and stringent regulation.
- Hematite (Fe_2O_3), Sn-doped: interestingly, hematite synthesized via spry pyrolysis [89, 114] exhibited uncompromised stability in presence of hydrogen sulfide ions [74]. Under the investigated conditions, hematite was predicted to be thermodynamically unstable; iron sulfides, FeS_2 or FeS, should have been formed as shown in the potential-pH diagram for the system Fe-S-H_2O in Figure 1-12. However, the kinetics of decomposition are so slow that hematite can be considered meta-stable in presence of hydrogen sulfide ions.

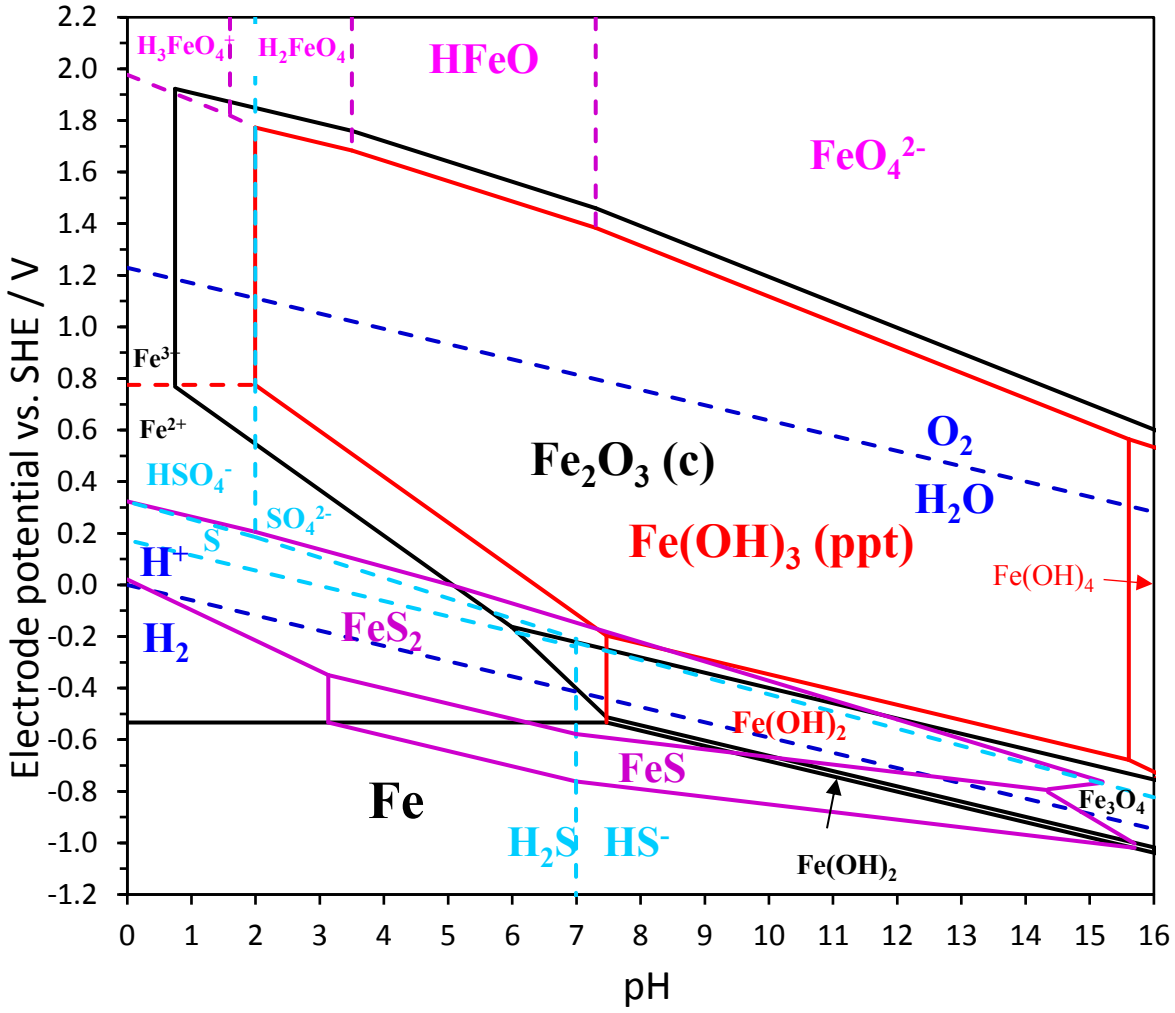


Figure 1-12. E-pH diagram for Fe-S-H_2O system, 0.1 MPa, 298 K and total dissolved iron and sulfur activities 0.01 and 0.1, respectively.

1.8 Standard methods and reporting protocols for material and PEC assessment

As it was mentioned previously, there are plenty of definitions for conversion efficiencies. In order to standardise all of these approaches, a compilation of techniques was published by NREL. The most accepted and popular methods, definitions and reporting protocols were described [44].

Aside from efficiencies, which are more relevant for material development, the properties of the semiconductors and the photo-electrochemical cell arrangement should be assessed accordingly to ensure a proper reactor design. Figure 1-13 shows a suggested flow chart to assess the performance and characterisation of materials to be used in PEC systems. Also, a summary of all techniques, their limitation and the characteristics is summarised in Table 1-3.

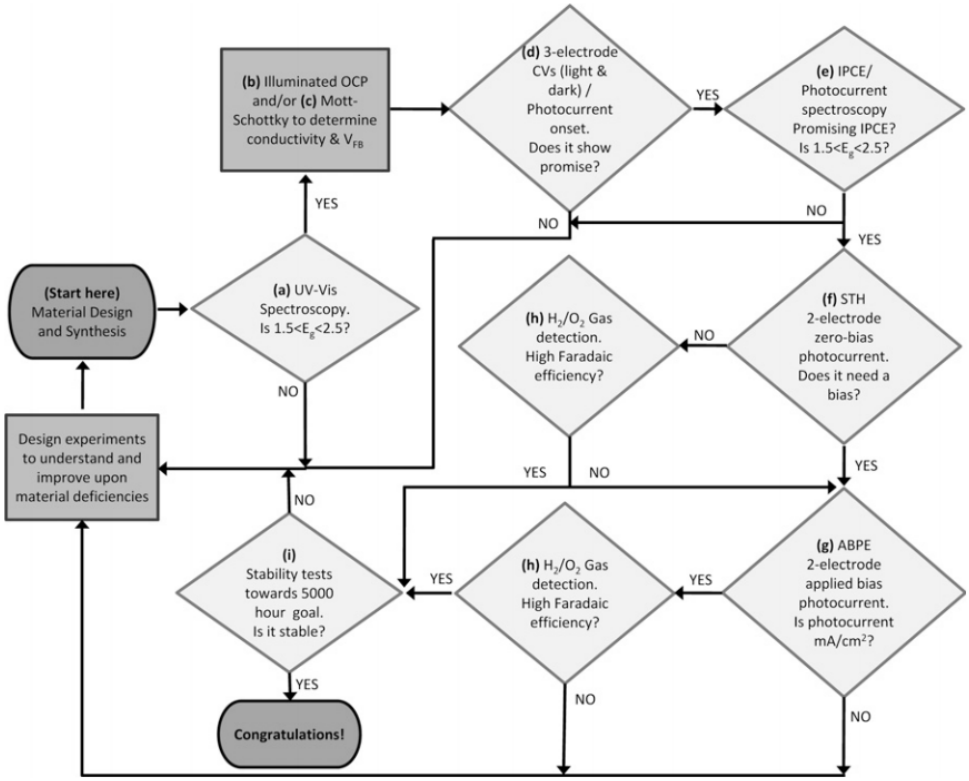


Figure 1-13. PEC characterization flow chart for a single-absorber material for water splitting [44]

Table 1-3. Summary of PEC characterization techniques, properties measured and their limitations.

Technique	Measured properties	Limitations and considerations
UV-vis spectroscopy	Optical bulk band gap Absorption coefficient Direct or indirect semiconductor	Interpretation of data prone to subjective error and is not necessarily conclusive Bulk band gap could not necessarily be the same at surface A good absorber does not mean high efficiency
Illuminated open-circuit potential	Flat band potential	Possible photocorrosion at OCP Materials with high recombination rates can affect the measurement.
Mott-Schottky	Flat band potential Conductivity type (n or p) Doping density Density of charge carriers	Difficult interpretation from impedance spectroscopy.
3-electrode cyclic voltammograms	Saturated photocurrent density Voltage range of photocurrent generation Conductivity type (n or p) Flat band potential	Sample corrosion Catalyst may be needed to minimise overpotential errors in flat-bland potential measurements.
IPCE measurement	IPCE Band gap Absorbed photon-to-current efficiency	Light must be stable and calibrated Possible photocorrosion or side reactions Photoresponse must be a linear function of the light intensity.
2-electrode zero-bias photocurrent	STH efficiency	Possible photocorrosion or side reactions
2-electrode applied bias photocurrent	ABPE efficiency	Possible photocorrosion or side reactions
H_2 or O_2 gas detection	Charge yield	Gas leaking
Stability tests	Lifetime of material	Instability of the light source and non-steady measurements due to external effects, such as heating.
PEIS	Interfacial electron-hole recombination	Difficult interpretation from impedance spectra

1.9 Modelling of photo-electrochemical devices

Modelling of photo-electrochemical devices is essential to understand and predict the behaviour of up-scaled devices and detection of issues that might arise from the engineering point of view. Current density distributions in large electrodes [65], cross-over of species [115-117], the effect of flow [118], membranes [119], and electrode arrangements [47, 114, 120] have been recently investigated. The starting point of modelling of photo-electrochemical devices is the photocurrent prediction [121]. Earlier PEC models were developed as electrolysers operating at low current densities, $2 - 200$ A m^{-2} [122]. However, the photocurrent should be a function of the light intensity and the properties of the photo-absorber. Recently, a modified version of the Gärtner–Butler equation was published for predicting photocurrents in PECs using semiconductor properties determined experimentally [65, 123, 124].

According to Butler [123], the generated electron-hole pairs are a function of incident photons and absorptivity coefficient of the material:

$$G(x) = I_0 \alpha \exp(-\alpha x) \tag{1-37}$$

Where x is the depth from the surface | electrolyte interface and α is the absorption coefficient.

The total photocurrent generated due to the absorption of photons in the semiconductor was derived by Gärtner [124]:

$$j_{ph} = eI_o \left[1 - \frac{\exp(-\alpha d_{sc})}{(1+\alpha L_p)}\right] + \frac{ep_0 D_p}{L_p} \tag{1-38}$$

The first term on the right is associated with the photocurrent due to electron-hole pairs generated in the depletion layer width, d_{sc}. The second term involves the photocurrent generated by diffusion of holes into the bulk of the semiconductor. In this case, the absorptivity coefficient is a function of wavelength, λ; then, the generated photocurrent will be as well a function of λ. The total photocurrent can be obtained after integration of the light source. Gärtner equation (1-38) accounts for recombination losses in the neutral region (outside the depletion layer) and assumed all photons absorbed in the depletion layer are converted to current, i.e. absence of surface recombination.

Later, Butler assumed that for semiconductors with a wide bandgap, e.g. TiO_2 and WO_3, the contribution of the second term due to diffusion can be disregarded. This assumption can also be extended to hematite. Also, if the diffusion length, L_p, is small compared to the absorption depth, α^{-1}, i.e. $\alpha L_p \ll 1$, then the expected photocurrent can be simplified to:

$$j_{ph} = eI_o[1 - \exp(-\alpha d_{sc})] \tag{1-39}$$

This equation is similar to the one proposed initially, equation (1-37). And it can be obtained after integration of equation (1-37) from the electrode | electrolyte interface, $x = 0$, to the depletion layer depth, $x = d_{sc}$.

$$j_{ph} = e \int_0^{d_{SC}} G(x)dx \tag{1-40}$$

$$j_{ph} = -eI_o[\exp(-\alpha d_{sc}) - 1] \tag{1-41}$$

The thickness of depletion region is given by [125]:

$$d_{SC} = 2L_{\mathrm{D,eff}}\left[\frac{e\Delta\phi_{SC}}{k_B T} - 1\right]^{0.5} \tag{1-42}$$

Where $L_{\mathrm{D,eff}}$ is the effective diffusion length:

$$L_{\mathrm{D,eff}} = \left(\frac{\varepsilon_0 \varepsilon_r k_B T}{2n_0 e^2}\right)^{0.5} \tag{1-43}$$

Substituting d_{SC} and $L_{\mathrm{D,eff}}$, and expanding the exponential term in (1-41) under the assumption that the value inside is much lower than one, i.e. $\alpha d_{sc} \ll 1$, the following expression is obtained:

$$j_{ph(GB)} = \left(\frac{2eI_0^2\alpha^2\varepsilon_0\varepsilon_r}{n_0}\right)^{\frac{1}{2}}(\Delta\phi_{\mathrm{SC}})^{\frac{1}{2}} \tag{1-44}$$

Also, assuming that the band bending in the semiconductor can be expressed as the difference between the applied potential and the flat band, and expressing the photon flux and absorptivity as function of the wavelength:

$$\mathrm{j}_{ph(GB)} = \left(\frac{2e\left(\sum_\lambda I_{0,\lambda}\alpha_\lambda\right)^2\varepsilon_0\varepsilon_r}{n_0}\right)^{\frac{1}{2}}\left(U_{\mathrm{applied}} - U_{\mathrm{FB}}\right)^{\frac{1}{2}} \tag{1-45}$$

The photocurrent predicted by the modified Gärtner–Butler equation (1-45) does not account for electron-hole recombination losses in the depletion layer of the semiconductor and in the electrode | electrolyte interface. Hence, the photocurrent obtained by this equation must be corrected further by photon-to-current yields, which can be estimated experimentally.

Dark currents and distribution of overpotential over the electrode surface can be estimated using secondary current distribution approach and the well-known Butler-Volmer equation [35] or any of its simplifications: linearized or Tafel equation, for small or large overpotentials, respectively. Also, it can be assumed there is not mass-transfer control when electroactive species are in excess and the current densities are sufficiently low.

Once the electrochemical aspects of the model are solved, diffusion of generated species at the electrode | electrolyte interface can be modelled by the Faraday's law of electrolysis and Fick's law for the diffusion of diluted species in the electrolyte and membranes. Bubble generation can be estimated from the efficiency of gas evolution, f_G, as a function of the current density [126-128], while desorption can be estimated from the mass transport coefficient [129].

From the geometrical stand point, some models involving perforated electrodes to improve the ionic pathway through the electrolyser while minimising cross-over of species have been developed for integrated systems [130] and photo-electrochemical reactors with contributions of the author

[65]. More recently, there has been an improvement of such models which now includes the effect of temperature and concentrated irradiation [130-132]. However, there is a lack of studies on the effect of bubble generation, diffusion and desorption of gases, and in general, a unified model for the geometrical optimisation of photo-anodes for perforated electrodes.

Figure 1-14 shows typical configurations of PECs. A membrane, not shown in the figure, can be used in any of the configurations to separate anode and cathode to prevent product cross-over. Figure 1-14(a) shows the typical configuration used in this thesis to characterise and assess the performance of photo-anodes in small scale in order to minimise inhomogeneities in current density distributions and significant potential losses in the electrolyte. However, when up-scaled reactors are used, these effects become important, but they can be minimised with perforations in the photo-anode to allow for shorter current paths (dashed lines), as shown in Figure 1-14(c). Figure 1-14(b) shows a configuration where the ionic path is shorter between electrodes; however, photons become scattered by the superposition of the cathode and, if used, the membrane. This arrangement exhibited lower performances compared to configuration (a) with similar electrodes [114]. Finally, the configuration shown in Figure 1-14(d), sometimes named 'wireless' PEC devices, have been studied by Nocera at al. [133] and Newman [120]. In general, 'wireless' configurations perform worse, with efficiencies half of those reported for a 'wired' systems, i.e. configuration (a) to (c) in Figure 1-14 [133]. However, this arrangement can also be optimised with perforations and membranes appropriately placed inside them.

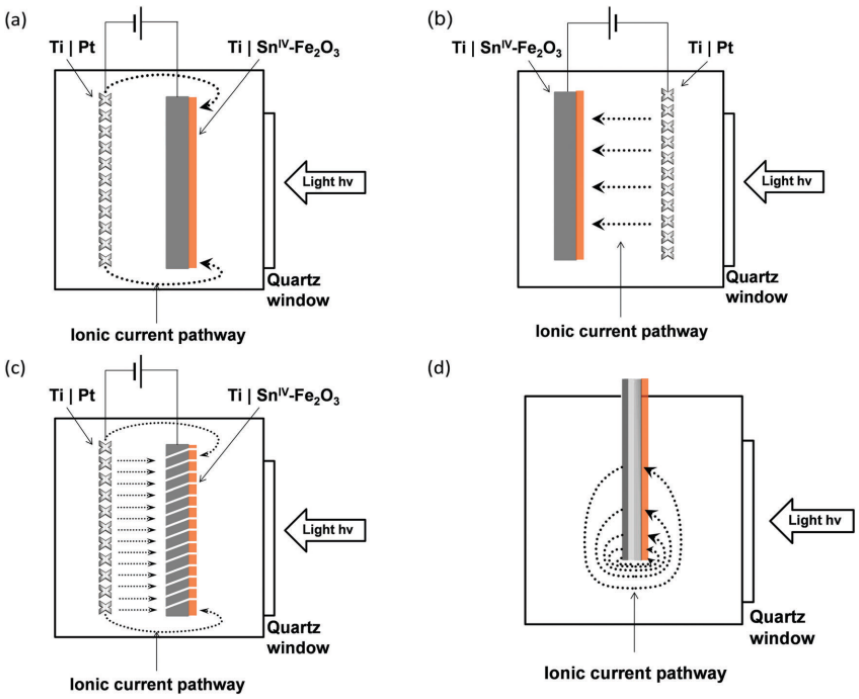


Figure 1-14. Different electrode geometries and configurations of PEC(a) directly illuminated photo-anode surface (hematite film on a Ti foil substrate) facing away from counter electrode; (b) photo-anode surface facing towards the counter electrode mesh, which is interposed between the photo-anode and light source; (c) directly illuminated photo-anode surface (hematite film on a perforated Ti foil substrate) facing away from counter electrode; (d) directly illuminated hematite film, which is a part of a wireless 'photo-bipole' type electrode assembly. The current paths of OH^- anions, corresponding to each scenario, are shown with dotted arrows. The photo-inactive sides of the photo-anodes were covered with insulating varnish, so were not electrochemically active.

1.10 Thesis outline

Subsequent chapters describe results of a study of Sn^{IV}-doped Fe_2O_3 photo-anodes used in photo-electrochemical reactors for hydrogen production via photo-assisted electrolysis of water and hydrogen sulfide in alkaline conditions. Firstly, the photo-anode material was characterised by several electrochemical techniques: photocurrent response in absence and presence of hole scavengers, photo-electrochemical impedance (PEIS) and Mott-Schottky analysis; also, XPS, SEM, Raman, and absorbance were performed on the Sn^{IV}-doped Fe_2O_3 photo-anodes (Chapter 2). This was followed by the use of measured or derived properties from the characterisation to develop a model to predict performances of PECs (Chapter 3) and up-scaled PERs (Chapter 4). Before any comparison between water and hydrogen sulfide splitting, it was necessary to adapt a technique for *in situ* quantification of polysulfide ion concentrations in order to estimate charge yields (Chapter 5), which also served as an introduction to the polysulfide sulfide speciation in alkaline electrolytes. Water and hydrogen sulfide splitting were compared in Chapter 6, accompanied by a proposed mechanism for hydrogen sulfide oxidation to polysulfide ions and elemental sulfur on Sn^{IV}-doped Fe_2O_3 photo-anodes. Predictions were also reported of the performances of PECs and PERs for photo-assisted hydrogen sulfide splitting using the model developed in Chapter 3 and 4. The final chapter summarises the conclusions and proposes future research to address residual problems.

Each chapter was written as a stand-alone section, but connected to the rest of the thesis, as shown in Table 1-4. The introduction of each chapter also serves as a framework, containing relevant and more specific literature followed by theoretical aspects of the results reported and discussed. The experimental details, although shared in some respects, were described separately for each chapter, as each required its own customised experimental methodology(ies).

1.10.1 Project objectives

The project aimed to develop models that could be used to design up-scaled photo-electrochemical reactors for H_2O and H_2S splitting. As an exemplar, Sn^{IV}-doped Fe_2O_3 photo-anodes were used with Ti/Pt cathodes, limiting such reactors to photo-assisted electrolysis. However, the model could be extended in the future to incorporate the behaviour of suitable photocathodes to achieve spontaneous overall photosynthetic reactions. Hence, the projects objectives required:

- Defining the dependences of photo-electrochemical, optical and morphological properties of Sn^{IV}-doped Fe_2O_3 photo-anodes, synthesised under different conditions, on the kinetics of photo-assisted water splitting.
- Developing a model for the prediction of photo-electrochemical cell performances and photocurrent densities as a function of the properties of the photo-anode material, and using electrodes with electro-active areas < 1 cm^2 to avoid effects of current density distributions and to minimise potential losses in electrolyte solutions.

- Validating an up-scaled photo-electrochemical reactor model for water splitting with electroactive areas > 10 cm^2, predicting the optimum geometric structures of modelled up-scaled photo-anodes to maximise hydrogen yields at cathodes.
- Developing a technique for *in situ* concentration determination of (meta-stable) polysulfide ions, the predominant product of (ca. 0.5 mol dm^{-3}) HS^- ion oxidation in alkaline solutions, at concentrations < 0.01 mol dm^{-3} to enable estimation of charge yields.
- Demonstrating that for hydrogen production, the potential requirements for photo-assisted hydrogen sulfide splitting can be decreased by 0.5 V compared to water splitting; also, using Sn^{IV}-doped Fe_2O_3 photo-anodes which should be stable over > 24 hours of continuous photo-electrolysis of HS^- solutions.
- Conceiving a mechanism for hydrogen sulfide oxidation to polysulfide ions in photo-electrochemical reactors using Sn^{IV}-doped Fe_2O_3 photo-anodes.

Table 1-4. Summary of research gaps, tasks and novelties for each chapter.

Chapter	Research gaps	Tasks	Novelties
2: Effects of annealing on the performance of tin-doped hematite photo-anodes	• Few studies on annealing of hematite on metallic substrates and the effect of annealing on them. • There is no consensus about the shift of photocurrent and decrease in current densities with annealing.	• Characterising hematite photo-anodes on titanium and FTO substrates, including photo-electrochemical, morphological, optical and topological properties. • Defining the mechanism affecting the shift in photocurrents in terms of electron-hole recombination rates and dopant redistribution after annealing.	• A mechanism was proposed that explains the shift of photocurrents. • A comprehensive study involving multiple techniques for the confirmation of proposed hypothesis. • Several techniques for flat band potential determination were compared.
3: Model for PEC systems: photocurrent and hydrogen yield predictions	• Bubble generation, diffusion and desorption of gases have not been considered. • Parameters used in models are usually theoretical.	• Predicting photocurrent densities as a function of measurable quantities gathered in **Chapter 2**. • Estimating electron-hole recombination in the bulk and interface from parameters measured in **Chapter 2**. • Selecting a model for bubble formation and gas desorption.	• Proposed methodology for the estimation of electron-hole recombination in the bulk of the semiconductor. • Equation to predict photocurrents in terms of measurable quantities. • Validation of predicted photocurrents in a bench-scale cell.
4: Model for PER systems: up-scaled validation and geometrical optimisation	• Few models are available for geometrical optimisation of photo-anodes in PER. • There is no validation with experimental data in up-scaled reactors. • There are no definitions of targets for optimisation.	• Validating the model developed in **Chapter 3** with experimental data in an up-scaled reactor. • Optimising of perforation geometry to minimise current density distribution and product cross-over. • Measuring hydrogen and oxygen fluxes, and charge yields.	• Model was validated with experimental results in a bench-scale and up-scaled reactor. • Optimisation targets were identified. • Sensitivity analysis was carried out. • Dimensions of optimised photo-anodes were determined.
5: *In situ* determination of polysulfide ions in alkaline hydrogen sulfide solution	• No available technique for *in situ* quantification of polysulfide ions at low concentration.	• Performing calibration curves for polysulfide ion concentration determination. • Identifying possible sources of error. • Validating measurements with polysulfide ion generation in an electrolyser.	• A fast and in situ technique for polysulfide ions concentration quantification was developed. • Low concentrations of polysulfide ions were determined in presence of concentrated hydrogen sulfide ions.
6: Photo-assisted hydrogen sulfide splitting using tin-doped hematite	• A simple and scalable process for hydrogen sulfide splitting is not readily available. • Stability of photo-electrodes is usually not reported. • No mechanism is reported for hydrogen sulfide ion oxidation using a photo-anodes.	• Assessing the photo-response of hematite for hydrogen sulfide splitting *vs.* water splitting, the latter found in **Chapter 2**. • Assessing the stability of photo-anodes. • Quantifying charge yields for hydrogen and polysulfide ion evolution using the technique developed in **Chapter 5**. • Predicting the photocurrent for hydrogen sulfide splitting in a bench-scale and up-scaled reactor using the model developed in **Chapters 3 and 4** respectively.	• A mechanism was proposed for hydrogen sulfide oxidation at different potentials on hematite photo-anodes. • Sn^{IV}-doped α-Fe_2O_3 is a stable photo-anode for hydrogen sulfide splitting. • Lower potentials were required to produce hydrogen while treating hydrogen sulfide waste. • Photocurrents were predicted for the first time for hydrogen sulfide splitting.

Chapter 2

Effects of annealing on the performance of tin-doped hematite photo-anodes[1]

2.1 Introduction

Hematite has been studied extensively as a possible photo-anode material for water splitting [60]. However, it requires an electrical bias to oxidise water effectively as the energy of its conduction band edge is too low and exhibits low energy conversion efficiencies. Numerous approaches for improving this material have been suggested such as doping [64], inclusion of quantum dots [90], improved synthesis pathways such as ALD [91], electrodeposition [92], and high temperature annealing [93] and reductive annealing [94]. In order to enhance the properties of photo-electrodes such as hematite, it is important to understand how the changes produced by different treatments, such as annealing, affect the properties and ultimately their performance. Post-deposition annealing of hematite thin films in air has been suggested as an essential treatment to achieve the adequate crystallinity and decrease concentrations of defects in the structure [134]. Reductive annealing [94] and hydrogen treatment [135] have also been suggested as ways to improve the photo-activity of hematite, creating oxygen deficiencies in its structure and hence improving its conductivity. Other hypotheses have also been proposed to explain the behaviour of hematite after annealing, ranging from catalytic effects to morphological changes [59].

The substrate used as support for the thin films also needs to fulfil several requirements: mechanical and chemical stability, high conductivity that would minimise in-plane ohmic losses and compatibility with photo-electrodes in terms of interfacial properties of electrical junction formed. Behaviour at elevated temperatures should also be considered when the synthesised films require heat treatment. Traditionally, hematite is deposited on conductive films such as fluorine-doped tin oxide (FTO) or indium tin oxide (ITO) on glass. These substrates are readily available and transparent, which is a useful characteristic for back-illumination. Small electrodes fabricated on

[1] This chapter was adapted from: F. Bedoya-Lora, A. Hankin, I. Holmes-Gentle, A. Regoutz, M. Nania, D.J. Payne, J.T. Cabral, G.H. Kelsall, Effects of low temperature annealing on the photo-electrochemical performance of tin-doped hematite photo-anodes, *Electrochim. Acta*, 2017. doi.org/10.1016/j.electacta.2017.08.090

these substrates do not suffer from significant ohmic losses and mechanical fragility. However, scale-up of electrodes to > 0.01 m^2 results in electrical potential losses due to relatively low conductivity [47], 8 Ω per square (FTO, TEC-8 Pilkington) and renders them more easily breakable. Sn^{IV} is also known to interact beneficially with hematite at temperatures > 600 °C [136, 137], demonstrating that FTO and ITO substrates are not entirely inert. Alternatively, hematite has been synthesised on titanium foil due to its chemical stability in alkaline conditions [89] and high conductivity that serves to minimise ohmic losses. However, heat treatment in air causes growth of TiO_2 film of several nanometres [138], which could interact with hematite thin films even at 500 °C [89].

Doping of hematite photo-anodes has been suggested as a strategy to improve their electrical conductivity [139] and decrease electron-hole recombination rates in their bulk [60, 114]. This can also be achieved by back illumination (through the substrate) of undoped hematite, exhibiting up to 3-fold increase of incident photocurrent conversion efficiency [140-142]. This comes with the price of increasing the electrode sheet resistance due to a required transparent substrate. Conversely, back illumination has been proved to be counterproductive for doped-hematite due to the already improved electrical conductivity and reduced electron-hole recombination in the bulk, while the sluggish diffusion of holes through the film was the limiting step [143]. A 90% decrease in photocurrent was reported over front-illumination. Dopants such as Sn^{IV} have been used extensively to enhance photo-activity of hematite photo-electrodes, where Sn^{IV} acts as donor centre after replacing Fe^{III} sites [64]. Sn^{IV}-doped photo-electrodes exhibited higher donor densities of ca. 10^{26} and 10^{27} m^{-3} for doping concentrations between 0.5 and 2% mass [144]. These values are two orders of magnitude greater than for undoped hematite [62, 135]. Donor densities reported here (ca. 1.3% mass Sn^{IV} doping) are as high as 10^{25} to 10^{27} m^{-3}. In this case, these unusually high values could have been affected by the concentration of oxygen vacancies in non-stoichiometric hematite Fe_2O_{3-x}, a higher electro-active area compared to geometrical area, or the presence of chloride ions at the surface [114]. Contrary to the hypothesis that doping with Sn^{IV} affects mainly bulk electron-hole recombination rates, it has been shown recently that it also affects rates of hole transfer and catalysis of the oxygen evolution reaction on hematite photo-anodes [145]. On the other hand, it has been reported that an increase in Sn^{IV} concentrations decreases the absorption of photons substantially in the visible region [64], possibly due to the formation of SnO_2, which has a higher band gap (3.5 eV) [41].

To elucidate further the effects of annealing at 400 – 500 °C of Sn^{IV}-doped hematite on titanium, the performance of spray pyrolysed photo-anodes was assessed as a function of several properties. The understanding of these effects could also clear the path to the improvement of existing models of photocurrent prediction in photo-electrochemical reactors. The quality of such models relies critically on the accuracy of the parameters on which they are based; special attention needs to be paid to parameters such as the flat band potential and donor density as several assumptions, often inappropriate, are made en route to their determination at nanostructured photo-electrodes [43].

2.2 Experimental

2.2.1 Photo-anode fabrication

Sn^{IV}-doped α-Fe_2O_3 photo-anodes were fabricated via spray pyrolysis [89] on TEC-8 fluorine-doped tin oxide (FTO) on glass (Hartford Glass Inc., USA) and titanium foil (0.74 mm, 99.4% Alfa Aesar). Titanium substrates (10 mm × 60 mm) were polished on an automated polishing machine (Buehler) with polishing paper grade 400, 800, 1200 and finally with aqueous dispersion of < 300 nm alumina particles. Then, substrates were degreased with acetone, immersed in 0.5 mol dm^{-3} oxalic acid overnight to minimise the oxide layer thickness, rinsed with acetone and ultra-sonicated in de-ionised water, as for FTO substrates, a few minutes prior to spray pyrolysis. The precursor solution for spray pyrolysis comprised 0.1 mol dm^{-3} $FeCl_3.6H_2O$ (99.99%, Sigma Aldrich, UK) and 6×10^{-4} mol dm^{-3} $SnCl_4$ (99.995% Sigma Aldrich, UK) dissolved in ethanol absolute (AnalaR Normapur, VWR). Sn^{IV} concentration corresponds to 1.3% doping by mass. The precursor was nebulized with a quartz spray nozzle (Meinhard, USA) at a height of 150 mm above the surface of the substrate. The nozzle movement was controlled by WinPC-NC CNC Software (BobCad-CAM, USA). The precursor solution was delivered using a syringe pump at 2 cm^3 min^{-1} and pressurised air was supplied at 345 kPa. Substrates were placed on a hotplate at 480 °C and took approximately 15 min to reach that temperature. Next, 40 passes of the nebuliser over the substrate were programmed to obtain 47 ± 6 nm thick hematite films, which was measured with a profilometer (TencorAlphastep 200 Automatic Step Profiler); each pass took 1 minute with a resting time of 1 minute between passes, and a total time of ca. 90 min. Samples were cooled to 200 °C before being removed from the hotplate to continue cooling at room temperature.

The post-deposition annealing was done in a pre-heated oven (Elite Thermal Systems, Ltd.) at 400 and 500 °C in air at atmospheric pressure over the course of an hour. Ti|Sn^{IV}-Fe_2O_3 samples were extracted at 20, 40 and 60 minutes. All FTO|Sn^{IV}-Fe_2O_3 samples were treated for the full 60 minutes.

In order to minimise dark currents from non-illuminated electrode areas, samples were partially coated using insulating acrylic lacquer (45 kV mm^{-1}, RS component) to obtain an exposed area of 3 mm × 6 mm, corresponding to the dimensions of the incident light beam.

2.2.2 Photo-electrochemical characterization

Photo-electrochemical characterization was carried out using a photo-electrochemical cell (PEC) of 0.06 dm^3 (PVC body with a quartz window). A potentiostat/galvanostat (Autolab PGSTAT 30 + Frequency Response Analysis module, Eco Chemie, Netherlands) was used to control the cell containing Sn^{IV}-Fe_2O_3 samples as working electrodes, a platinised titanium mesh (Expanded Metal Company, UK) as counter electrode and HgO|Hg as reference electrode (0.913 V *vs.* RHE and 0.109 V *vs.* SHE). 1 mol dm^{-3} NaOH was used as electrolyte solution, pH of ca. 13.6 and temperature 25 ± 2 °C. H_2O_2 (30%, AnalaR Normapur, VWR) was added in some cases as sacrificial electron donor at a concentration of 0.5 mol dm^{-3}.

Cyclic voltammograms were run typically from 0.5 to 2.0 V *vs.* RHE at 10 mV s^{-1} scan rate. Incident photon-to-current efficiencies (IPCE) were measured from 300 to 700 nm in 20 nm increments for 100 s at 1.51 and 1.71 V *vs.* RHE. Data for Mott-Schottky (MS) analysis was obtained from potentiostatic electrochemical impedance (EIS) evaluated from 10^5 to 10^{-1} Hz (10 points per decade) at different potentials from 0.6 to 1.8 V *vs.* RHE, and a peak-to-peak amplitude of 10 mV.

Similarly, photo-electrochemical impedance spectra (PEIS) of photo-anodes were measured under high-intensity light, ca. 3 000 W m^{-2}. Following the methodology proposed by Peter et al. [146, 147], resistances corresponding to interfacial charge transfer and recombination processes were extracted after fitting to an equivalent circuit in order to calculate interfacial charge transfer efficiencies.

Flat band potentials were estimated using several methods: Mott-Schottky (MS), Gärtner-Butler and open circuit potential (OCP) under high light intensity in presence and absence of a sacrificial electron donor (H_2O_2) [148]. Donor densities were estimated from Mott-Schottky plots, assuming a relative permittivity of 38.2 ± 0.46 and a thickness of 47 ± 6 nm [65].

A Xe arc lamp (LOT-Oriel) of 300 W with Fresnel lenses was used to obtain a beam of 3 mm × 6 mm and a maximum power intensity of 3 646 W m^{-2}. Intensity was varied with reflective neutral density filters ranging from 15% to 93% transmission (UQG-Optics, UK). The electrodes were irradiated directly (front illumination) in the case of both Ti and FTO substrates. Wavelength was controlled with a monochromator/spectrograph (Omni-λ150, Zolix). The intensity of the light source was corrected by attenuation of electrolyte and quartz window across a wavelength range of 280 – 900 nm. A total transmission of 82% and a maximum effective intensity on the photo-electrode of 3 000 W m^{-2} was estimated for this study. Linearity in photocurrent with light intensity was confirmed experimentally, as reported and discussed in Figure S2-1 in the Appendix. The light source was characterised and calibrated with a UV-Vis spectrophotometer coupled to a CR2 cosine receptor (Black-Comet CXR-25, StellarNet, USA).

2.2.3 Optical and morphological characterization

Raman spectra were obtained from a Dispersive Renishaw 1000 confocal Raman system, 785 nm diode laser with maximum output power of 300 mW and 50x objective (dry), and two-dimensional Peltier cooled charge-coupled device (CCD) camera as detector. These measurements were gathered by Ms. Alessandra Vichi in the Vibrational spectroscopy and chemical imaging group at Imperial College London.

SEM images were captured using a Zeiss Sigma 300 Scanning electron microscope at 5.00 kV. The images were obtained and analysed with the help of Mr. Isaac Holmes-Gentle in the Chemical Engineering Department at Imperial College London. Topographies of samples were determined by AFM using a Bruker Innova microscope in tapping mode at 0.1 Hz with Si tips (MPP-11100-W,

Bruker), and processed with NanoScope software. Ms. Manuela Nania recorded and helped with the analysis of the samples.

Absorption spectra of hematite films samples on FTO substrates were obtained using a Shimadzu UV-2600 UV-Vis spectrophotometer with an integrating sphere and corrected by baseline subtraction assuming reflection and scattering are wavelength independent [46]. It was assumed that the optical properties measured on FTO would be retained for the titanium substrate. These measurements were recorded with the help of Mr. Camilo Mesa in the Chemistry Department at Imperial College London.

The surface of the thin films was characterised using XPS. The spectra were recorded on a Thermo Scientific K-Alpha$^+$ X-ray Photoelectron Spectrometer (XPS) system operating at 2×10^{-9} mbar base pressure. This system incorporates a monochromated, microfocused Al Kα X-ray source ($h\nu = 1\ 486.6$ eV) and a 180 ° double focusing hemispherical analyser with a 2D detector. The X-ray source was operated a 6 mA emission current and 12 kV anodic bias. Data were collected at 200 eV pass energy for survey and 20 eV pass energy for core level spectra using an X-ray spot size of 400 μm^2. A flood gun was used to minimize sample charging. All data were analysed using the Avantage software package. These measurements were gathered and analysed with the help of Dr. Anna Regoutz in the Department of Materials at Imperial College London.

2.3 Theoretical treatment

2.3.1 Mott-Schottky (MS) analysis

MS analysis of the change in semiconductor capacitance as a function of applied potential was used to determine flat band potentials and donor densities. In the absence of surface states, the capacitance of the semiconductor | electrolyte interface, $C_{\text{interface}}$, comprises contributions from the semiconductor capacitance, C_{SC}, and the capacitance of the Helmholtz layer, C_H in series:

$$\frac{1}{C_{\text{interface}}} = \frac{1}{C_{\text{SC}}} + \frac{1}{C_{\text{H}}} \tag{2-1}$$

$C_{\text{interface}}$ was evaluated from electrochemical impedance data; EIS data were fitted to a Randles electrical circuit [$R_s(R_tC_{SC})$] as shown in the inset of Figure 2-7 in the results section. A procedure similar to that suggested by Dias and Durrant [62, 149] was followed. C_{SC} was assumed to be approximately equal to $C_{\text{interface}}$ as typically $C_{\text{H}} \gg C_{\text{SC}}$. Also, it is known that nanostructured hematite does not comply with the assumptions of the MS model [43]. For an improved agreement between experimental data and fittings, a constant phase element (CPE) was used to estimate effective capacitance after correcting for a surface distribution of time constants due to surface roughness [150].

$$C_{\text{SC}} = Q_0^{1/\text{n}} R_{\text{s}}^{(1-\text{n})/\text{n}} \tag{2-2}$$

Where Q_0 and n are the pseudo-capacitance and exponential term of the CPE respectively, and R_s is the electrolyte resistance. Donor density, n_0, and flat band potential, U_{FB}, were computed by linear data fitting of C_{SC}^{-2} against applied potential (U):

$$\frac{1}{C_{SC}^2} = \frac{2}{\varepsilon_0 \varepsilon_r e n_0}\left(U_{applied} - U_{FB} - \frac{k_B T}{e}\right) \quad (2\text{-}3)$$

Where k_B is the Boltzmann constant (1.381×10^{-23} J K^{-1}), e is the electronic charge (1.602×10^{-19} C), ε_0 and ε_r are the vacuum permittivity (8.854×10^{-12} F m^{-1}) and the relative permittivity (38.2 ± 0.46), respectively.

2.3.2 Photo-electrochemical impedance spectroscopy (PEIS)

Surface recombination rate coefficients can be measured using photo-electrochemical impedance spectroscopy (PEIS) [146]. A fraction of the total charge (holes) that reaches the surface recombines with electrons present in the conduction band close to the electrode | electrolyte interface; the remaining charge is then transferred to oxidise species at the interface and only the latter flux is effectively measured as current. These two processes, assuming pseudo-first order, are characterised by rate coefficients assigned to the electron-hole recombination and hole transfer processes, k_r and k_t, respectively. As detailed by Peter at al. [145-147], the interfacial charge transfer efficiency is defined as:

$$\Phi_{surface} = \frac{k_t}{k_t + k_r} \quad (2\text{-}4)$$

This ratio can be estimated indirectly after fitting PEIS spectra to a two-time constant equivalent circuit $R_s(Q_{SC}[R_t(Q_rR_r)])$, as shown in the inset of Figure 2-2 in the results section [151]. This simplified circuit, removes the charge transfer resistance in the bulk, which cannot be easily discriminated from the spectra, and assumes the charge transfer is dominated by surface states [151]. This circuit also explains well the presence of two processes, as shown in Figure 2-9 in the results section: interfacial electron-hole recombination and charge transfer in the photo-anode | electrolyte interface under illuminated conditions. As in the MS analysis, pure capacitances were replaced by CPEs to compensate for surface heterogeneities in order to improve the agreement between fitted and experimental data. The interfacial charge transfer efficiency can be then re-written in terms of fitted resistances:

$$\Phi_{surface} = \frac{R_t}{R_t + R_r} \quad (2\text{-}5)$$

where R_t is the charge transfer resistance and R_r the recombination resistance. Impedance spectra at different applied potentials and under illumination were then analysed as described above to obtain interfacial charge transfer efficiencies, which depend on electron-hole recombination rates. These values were fitted to an exponential equation in order to evaluate the interfacial charge transfer efficiency as a function of applied potential [65].

$$\Phi_{\text{surface}} = \frac{A \exp(B \times \Delta\phi_{SC})}{1 + A \exp(B \times \Delta\phi_{SC})} \quad (2\text{-}6)$$

where A and B are fitted parameters, and $\Delta\phi_{SC}$ is the driving force for photocurrent or 'overpotential' defined here as the difference between the flat band potential and the applied electrode potential, $\Delta\phi_{SC} = U_{\text{applied}} - U_{\text{fb}}$.

2.4 Results and discussion

2.4.1 Effect of doping

In previous in-house studies, the performance of spray pyrolysed undoped hematite was inferior compared with Sn^{IV}-doped samples [114]. Charge transfer efficiencies were analysed by Dr. Anna Hankin for both cases (Figure S2-2 in the Appendix) and showed that the conductivity and photo-activity of the samples were improved drastically after doping, as has been reported in the literature [64, 139, 152]. More importantly, it has been shown that the presence of Sn^{IV} increased hole transfer rates and diminished the interfacial electron-hole recombination rates [145].

2.4.2 Effect of the substrate - FTO *vs.* Titanium

Figure 2-1 compares potential dependences of dark and photo-induced current densities for Sn^{IV}-Fe_2O_3 samples on FTO and Ti substrates. Unannealed samples exhibited essentially the same photocurrent densities for both substrates; however, it was evident that dark current densities for samples on FTO were higher than on titanium. This could have been due to different growth morphologies on the two substrates, giving a larger superficial area for FTO|Sn^{IV}-Fe_2O_3, or a higher electron energy barrier between Ti and Sn^{IV}-Fe_2O_3, caused by the growth of TiO_2 during annealing at 480 °C during the spray process. The latter phenomenon would also explain why after annealing Ti|Sn^{IV}-Fe_2O_3 samples, there is a significant decrease of dark current densities, yet no such change was detected with FTO|Sn^{IV}-Fe_2O_3. A thin layer of TiO_2 can grow during annealing at 400 – 500 °C, as demonstrated by Ong et al [89]. After the comparison of the electron affinities (conduction band energies) of TiO_2, SnO_2 and α-Fe_2O_3: -4.21, -4.55 and -4.78 eV respectively on the physical scale [41], the electrons flowing from hematite to the substrate should tunnel through an energy barrier that is higher when a layer of TiO_2 is present. Tunnelling becomes inhibited with growth of > 1 nm of insulating TiO_2 [89, 153], as will be seen below for different temperatures and times of annealing.

After treatment at 500 °C for 1 hour, there was a known shift of photocurrent onset to lower electrode potentials and a significant decrease in the maximum photocurrent densities [59]. Annealed samples of FTO|Sn^{IV}-Fe_2O_3 exhibited slightly lower photocurrent densities, but the same onset compared to Ti|Sn^{IV}-Fe_2O_3.

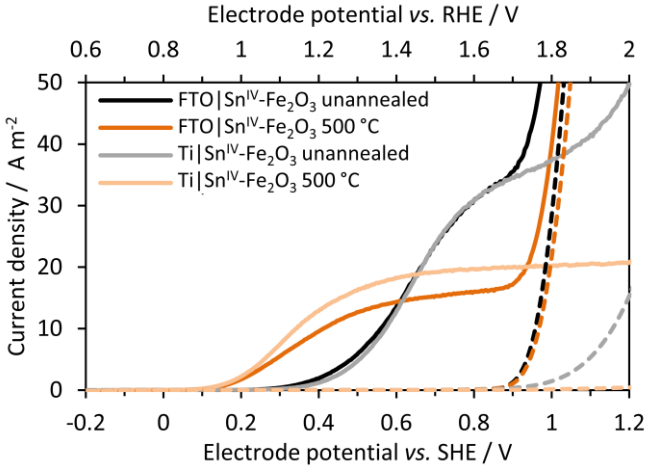


Figure 2-1. Cyclic voltammograms of Sn^{IV}-doped α-Fe_2O_3 films deposited on FTO and Ti, without and with annealing at 500 °C for 60 min. A scan rate of 10 mV s^{-1}, 1 mol dm^{-3} NaOH electrolyte and irradiation of 3 500 W m^{-2} by a Xe arc lamp were used. Dashed lines represent corresponding dark current densities.

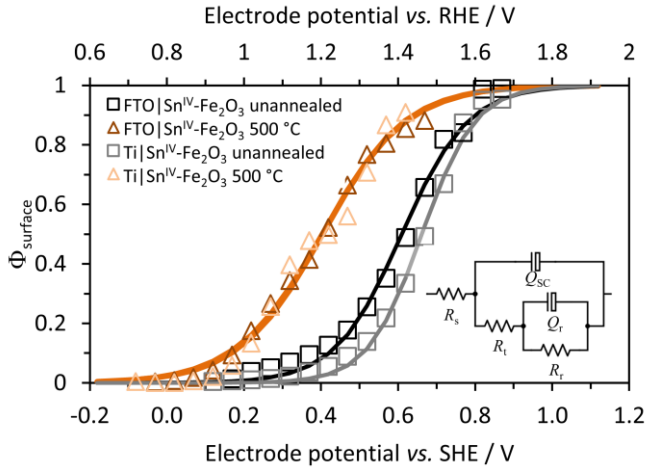


Figure 2-2. Interfacial charge transfer efficiency of Sn^{IV}-doped α-Fe_2O_3 films deposited on FTO and Ti, unannealed and with annealing at 500 °C for 60 min. Calculated from fitting PEIS to the equivalent electrical circuit shown in the inset.

Figure 2-2 shows the interfacial charge transfer efficiencies, $\Phi_{surface}$, obtained from PEIS. Annealed samples showed a shift towards lower electrode potentials, which agrees with voltammograms shown in Figure 2-1. The effect of the substrate was not evident in this case. Annealed samples on FTO and Ti exhibited identical behaviour.

As annealed Ti|Sn^{IV}-Fe_2O_3 samples exhibited greater photocurrent densities compared to FTO-supported samples, and considering that the use of FTO for large scale electrodes is not suitable due to the lower conductivity [47, 89] and fragility, the present research focused mainly on the effect of annealing on photo-electrochemical properties of samples deposited on titanium. However, the use of 'bare' titanium as a substrate for thin films comes with challenges, such as constrained annealing temperatures to minimise rates of oxidation in air. Temperatures higher than 600 °C increase growth rates of TiO_2 significantly [138, 154] and ultimately affect the performance of the photo-anodes due to the properties of TiO_2.

2.4.3 Annealing effect

Ti|Sn^{IV}-Fe_2O_3 samples annealed under different conditions were assessed in the absence and presence of H_2O_2 as a sacrificial electron donor. Figure 2-3 shows that photocurrent densities measured on annealed samples shifted to lower potentials and the maximum photocurrent densities decreased with temperature and annealing time. According to a previous report [59], the shift to lower potentials is attributed to surface chemistry and catalysis effects, while the maximum current is thought to be a function of film morphology. The purpose of this study was to test these hypotheses at annealing temperatures of 400 – 500 °C, considering the following variables: morphology, crystallinity, donor density, absorbance, surface and bulk recombination, oxygen vacancies and dopant distribution inside the hematite semiconductor. Then, the changes of these parameters were measured as a function of annealing temperature and time in order to explain the voltammetric behaviour shown in Figure 2-3.

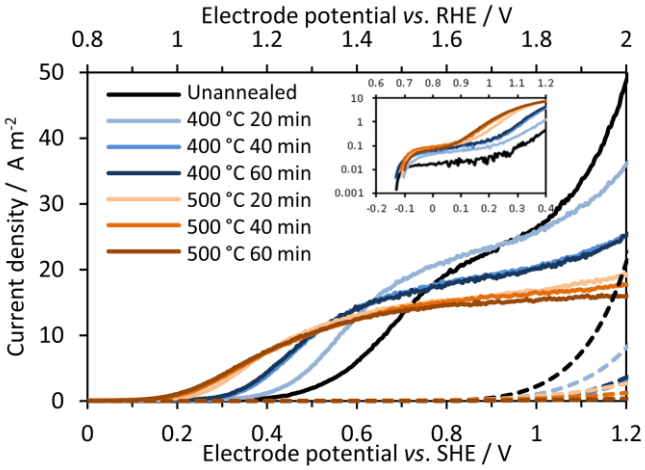


Figure 2-3. Cyclic voltammograms on Ti|Sn^{IV}-doped α-Fe_2O_3 | 1 mol dm^{-3} NaOH at different annealing temperatures and times. A scan rate of 10 mV s^{-1}, and irradiation of 3 000 W m^{-2} by a Xe arc lamp were used. Inset figure shows current densities on log scale. Dashed lines represent dark currents.

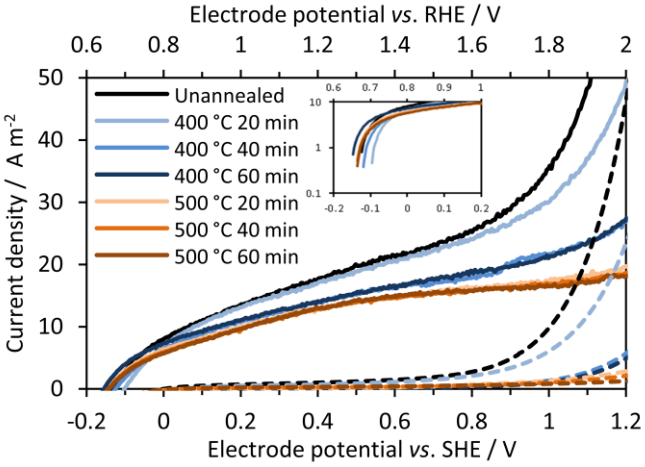


Figure 2-4. Cyclic voltammograms of Ti|Sn^{IV}-doped α-Fe_2O_3 | 1 mol dm^{-3} NaOH + 0.5 mol dm^{-3} H_2O_2 for different annealing temperatures and times. A scan rate of 10 mV s^{-1}, and irradiation of 3 000 W m^{-2} by a Xe arc lamp were used. Inset figure shows current densities on log scale. Dashed lines represent dark currents.

From the inset in Figure 2-3, the onset potentials for all samples were very similar (ca. 0.7 V *vs.* RHE). It is also noteworthy that dark currents were highest for unannealed samples and decreased with annealing temperature and time. This could mean that morphological or catalytic changes happened on the surface of the photo-electrode or that an energy barrier was developed between hematite and titanium, as discussed previously.

Figure 2-4 shows the effects of adding 0.5 mol dm^{-3} H_2O_2 as a hole scavenger to the electrolyte solution on voltammograms of photo-anode samples, thereby minimising electron-hole recombination rates. The onset potentials (also ca. 0.7 V *vs.* RHE) were similar for all samples; only the maximum photocurrent density changed after annealing and followed the same trend found in the absence of H_2O_2. Dark current densities were again greater for the unannealed samples and decreased with increasing temperature and time of annealing. Thus, it can be concluded that the shift of photocurrent densities to lower potentials was due to peroxide ions minimising rates of surface recombination of electrons and holes; maximum photocurrent densities were similar to those in absence of of H_2O_2. This will be discussed further with PEIS measurements.

2.4.4 Incident photocurrent conversion efficiencies (IPCE)

IPCEs were evaluated under steady state conditions at two potentials: 1.51 V (Figure 2-5a) and 1.71 V *vs.* RHE (Figure 2-5b). At lower potentials, unannealed samples produced smaller photocurrent densities than annealed samples; this agrees with voltammograms shown in Figure 2-1 and Figure 2-3. At higher potentials and lower wavelengths, the IPCE values were similar for all samples. Remarkably, a shoulder at 550 nm was observed for unannealed samples and decreased in magnitude with increased temperature and time of annealing. This trend was also observed at 1.51 V *vs.* RHE after normalizing IPCEs with respect to the highest efficiency at 360 nm, shown in the Appendix, Figure S2-3. This feature in IPCEs was also evident in samples deposited on FTO, so was not due to light being reflected from titanium substrates or formation of TiO_2 (see also Figure S2-3).

IPCE values were integrated to estimate total current densities, as shown in detail in the Appendix, Figure S2-4. The IPCE-estimated and measured photocurrent densities from cyclic voltammograms at 10 mV s^{-1} were very similar and supported the hypothesis that the difference in maximum photocurrent densities were related to the shoulder IPCE at 550 nm. This could have been due to a higher absorbance around that particular wavelength, a difference in crystallinity, different material phase or redistribution of dopants in the semiconductor [151]. As the maximum photocurrent was mainly affected by the peak at 550 nm at 1.71 *vs.* RHE, catalytic and morphological changes were disregarded.

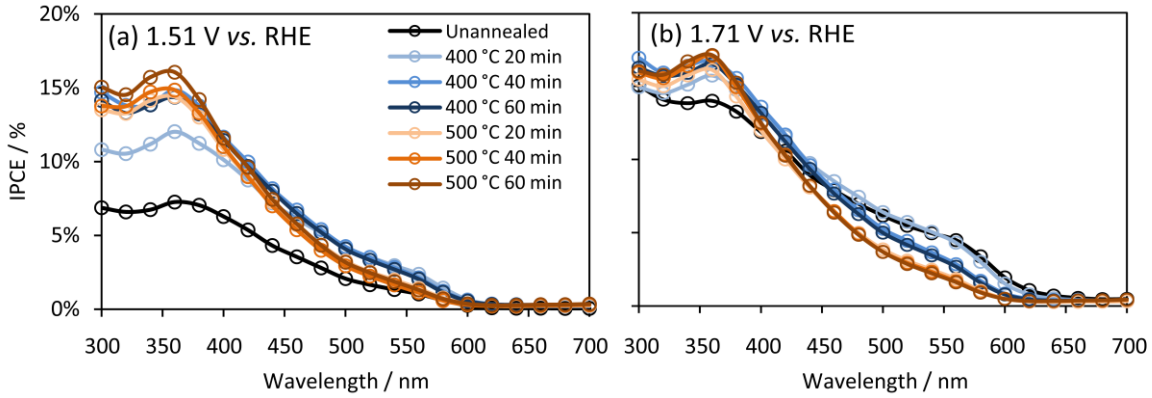


Figure 2-5. IPCE spectra for Ti|Sn^{IV}-doped α-Fe_2O_3 | 1 mol dm^{-3} NaOH at (a) 1.51 and (b) 1.71 V *vs.* RHE.

2.4.5 Interfacial charge transfer efficiencies

Efficiencies of interfacial charge transfer were studied further using the method proposed by Peter et al.[146, 147] together with an equivalent circuit with two time constants to fit the PEIS spectra, as proposed by Klahr et al [151]. Figure 2-6 shows the experimental interfacial charge transfer efficiencies and fitted data for all samples. The shape is very similar to that evident from voltammograms in Figure 2-3. However, such trends do not reflect the performance of the samples in terms of the maximum photocurrent densities, which were determined by other factors as discussed above. Again, the shape and shifting of the photocurrent curve to lower potentials was confirmed by the improvement of interfacial charge transfer efficiency due to lower electron-hole recombination rates at the electrode | electrolyte interface.

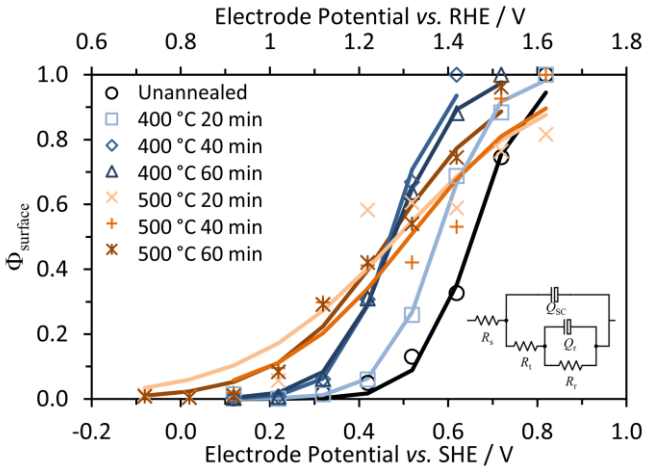


Figure 2-6. Effects of potential and annealing temperature and time on interfacial charge transfer efficiencies for Ti|Sn^{IV}-doped α-Fe_2O_3 | 1 mol dm^{-3} NaOH, together with corresponding fitting to equation (2-6) and resistances were extracted from equivalent electric circuit shown in the inset.

2.4.6 Mott-Schottky analysis

Figure 2-7 shows the Mott-Schottky plots under dark condition, generated using semiconductor capacitance values extracted from impedance data. The MS plots confirmed *n*-type behaviour of all samples and exhibited linear gradients; flat band potentials were estimated from intercepts with

the potential axis. The data also showed a noticeable increase in gradients for annealed samples. Figure 2-8 reports estimated donor densities, calculated using a relative permittivity of 38.2 ± 0.46 and a thickness of 47 ± 6 nm [65]. After annealing, donor density values decreased by two orders of magnitude. Such high values could be explained by adventitious chloride on hematite surfaces residual from $FeCl_3$ used in its spray pyrolysis [114].

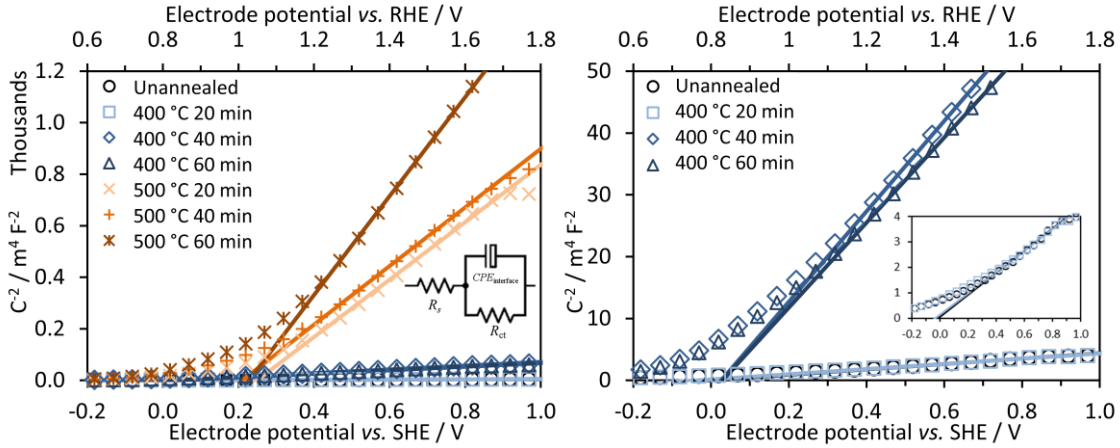


Figure 2-7. Effects of annealing temperature and time on Mott-Schottky plots on Ti|Sn^{IV}-doped α-Fe_2O_3 | 1 mol dm^{-3} NaOH. Capacitances were extracted after fitting to a circuit as shown in the inset.

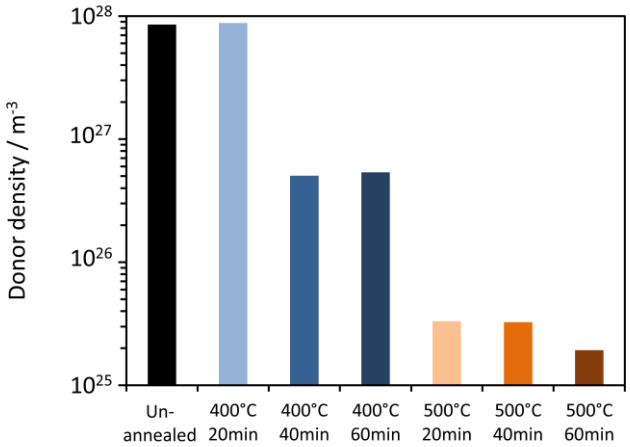


Figure 2-8. Effects of annealing temperature and time on estimated donor densities from Mott-Schottky plots for Ti|Sn^{IV}-doped α-Fe_2O_3 | 1 mol dm^{-3} NaOH.

XPS confirmed the presence of a small amount of around 2 rel. at% of Cl compared to Fe on the film surface and subsequent disappearance after annealing on both FTO and titanium substrates; see Figure S2-5 in the Appendix. The precursors used in the spray pyrolysis ($FeCl_3.6H_2O$ and $SnCl_4$) are the source of Cl contamination. Oxygen vacancies, expressed as Fe^{2+}, could also have contributed to the difference between unannealed and annealed samples, and unusually high donor density (c.f. 1.98×10^{28} molecules Fe_2O_3 m^{-3}). However, XPS shows a Fe 2*p* line shape characteristic of α-Fe_2O_3 and no change in the binding energy at 716 eV, which is associated with the presence of oxygen vacancies close to the surface [155], see Figure 2-13(a) in the XPS analysis section.

Additionally, the activation energy and diffusion coefficients for oxygen and iron self-diffusion were extrapolated from Amami et al. [156] to lower temperatures, in order to assess the possibility of formation or reduction of oxygen vacancies with annealing. Diffusion coefficients accounting for oxygen inclusion and exchange rate at the surface are of the order of 10^{-38} to 10^{-33} m^2 s^{-1} for 400 and 500 °C, respectively, while diffusion coefficients accounting only for bulk diffusion are of the order of 10^{-19} m^2 s^{-1}. Evidently, at such low temperatures, the fastest process is diffusion of oxygen and oxygen vacancies within the semiconductor bulk. Hence, rates of formation and exchange of oxygen vacancies at the surface is very low, so can be disregarded, as supported by XPS analysis.

Other possible reasons for such high donor densities and their decrease after annealing could be the existence of pinholes or changes in the Sn^{IV}-doped α-Fe_2O_3 | 1 mol dm^{-3} NaOH interfacial area; e.g. a change in the morphology could decrease the exposure of the substrate as a result of sintering. However, the morphology and topography of the samples on Ti and FTO, as shown later by SEM and AFM measurements, showed no substantial change with annealing at 400 and 500 °C.

It is worth mentioning that decoupling the relative permittivity and donor density ($\varepsilon_r n_0$) from Mott-Schottky relationship, equation (2-3), is experimentally challenging. Hence, there is a wide range of relative permittivity (25 - 120) [152, 157-159] and donor density [43] values reported for hematite. Estimated donor densities of annealed and chloride-free Sn^{IV}-doped α-Fe_2O_3 samples were between 3.3×10^{25} and 1.9×10^{25} m^{-3}. These values were in agreement with previous studies for Sn-doped hematite [137, 144, 152, 158].

2.4.7 Flat band potential

The flat band potential of all samples was estimated using several methods, including MS analysis. Although the linear trends in C_{SC}^{-2}, shown in Figure 2-7, appear reliable for the determination of flat band potential, the resulting values should be treated cautiously. Assumptions involved in MS analysis such as perfect smoothness of electrode surfaces (roughness factor of ≈ 1) were invalid [43], as evident from the AFM reported below in Figure 2-12. Flat band potential values found using MS analysis for unannealed and 400 °C annealing (~0.8 V *vs.* RHE) were similar to the values reported by Klahr, (-0.22 V *vs.* AgCl|Ag or 0.78 V *vs.* RHE at pH 13.6) [151]. However, flat band potentials after annealing at 500 °C where much higher (~1 V *vs.* RHE). Values found with the Gärtner-Butler method (extrapolation of the linear portion of squared-photocurrent as a function of potential) and open circuit potential with high-intensity light [148], reported in Table 2-1, are very consistent and match with flat band potential constraints presented by Hankin et al. [43], and values reported by Butler et al. (0.725 V *vs.* RHE) [160]. There was no clear trend for the reported values with temperature using the latter techniques, so it can be assumed that low temperature annealing did not affect the flat band potential of Sn^{IV}-doped α-Fe_2O_3 significantly. The effect of changes in the flat band potential has also been discussed previously [43, 148]. However, difficulties of measuring and constraints when using MS analysis make its estimation difficult. For hematite samples, squared-photocurrent in the presence of a hole scavenger (0.5 mol dm^{-3} H_2O_2) and under

illumination with high light intensity appears to be a more practical and accurate method for quantifying this property as seen in Figure S2-6 in the Appendix.

Table 2-1. Effects of annealing temperature and time on flat band potential *vs.* RHE (V) for Ti|Sn^{IV}-doped α-Fe_2O_3 | 1 mol dm^{-3} NaOH estimated by different methods.

Sample	MS / V	OCP(photo) / V 1 mol dm^{-3} NaOH	OCP(photo) / V 1 mol dm^{-3} NaOH + 0.5 mol dm^{-3} H_2O_2	j_{ph}^2
Unannealed	0.77	0.71	0.68	0.71
400 °C 20min	0.75	0.71	0.71	0.70
400 °C 40min	0.80	0.67	0.69	0.70
400 °C 60min	0.81	0.67	0.65	0.66
500 °C 20min	1.03	0.71	0.67	0.69
500 °C 40min	0.99	0.71	0.67	0.71
500 °C 60min	1.01	0.73	0.67	0.72

2.4.8 Photo-electrochemical impedance spectroscopy

The impedance under high-intensity light (3 000 W m^{-2}) was measured at different potentials. Figure 2-9 shows two different scenarios under biased conditions. When the electrode was operating at 1.21 V *vs.* RHE, a process at 1 Hz can be seen, which is completely absent at 1.71 V *vs.* RHE. This process could be related to surface electron-hole recombination. A second process at high frequencies was always present and was shifted to higher frequencies with time and temperature of annealing. This shift could be associated with the decrease of interfacial capacitance, $C_{\text{interface}}$, which is actually the same as seen in MS analysis. The disappearance of the low frequency process agrees with the cyclic voltammograms, where at low potentials the surface recombination was predominant for unannealed samples. It is also evident from the bode plot at 1.21 *vs.* RHE that annealed samples exhibited lower overall resistance, i.e. low frequency modulus, which is also in agreement with the reported cyclic voltammograms. This means that at that particular potential, surface recombination contributes significantly to the total impedance. On the other hand, at higher potentials (e.g. 1.71 V *vs.* RHE), the surface recombination process was suppressed in all cases, but the low frequency modulus behaves in the opposite way. Unannealed samples exhibit lower resistance, which agrees again with previous voltammograms for unannealed samples (see Figure 2-3 and Figure 2-4).

In order to elucidate this point further, the phase from the impedance spectra was plotted in a heat map against potential and frequency for three samples: unannealed and annealed samples at 400 and 500 °C for 60 min, as shown in Figure 2-10. The process at 1 Hz related to surface recombination became weaker with annealing at higher potentials, while the charge transfer process became predominant and slightly shifted to higher frequencies with heat treatment. The phase shift of the impedance spectra is closely related to the characteristic frequency ($f_c = 1/(2\pi RC)$ and time constant ($\tau = RC$) of an RC process, but it is not numerically equal. The characteristic frequency of a process is the frequency at which the imaginary component of the impedance is at its maximum, but is usually around the same order of magnitude than the frequency at the maximum phase shift,

which also depends on the associated resistances and arrangement of the electrical equivalent circuit. Hence, values reported in a phase shift plot should only be considered qualitatively to visualise the appearance and disappearance of processes in impedance spectra.

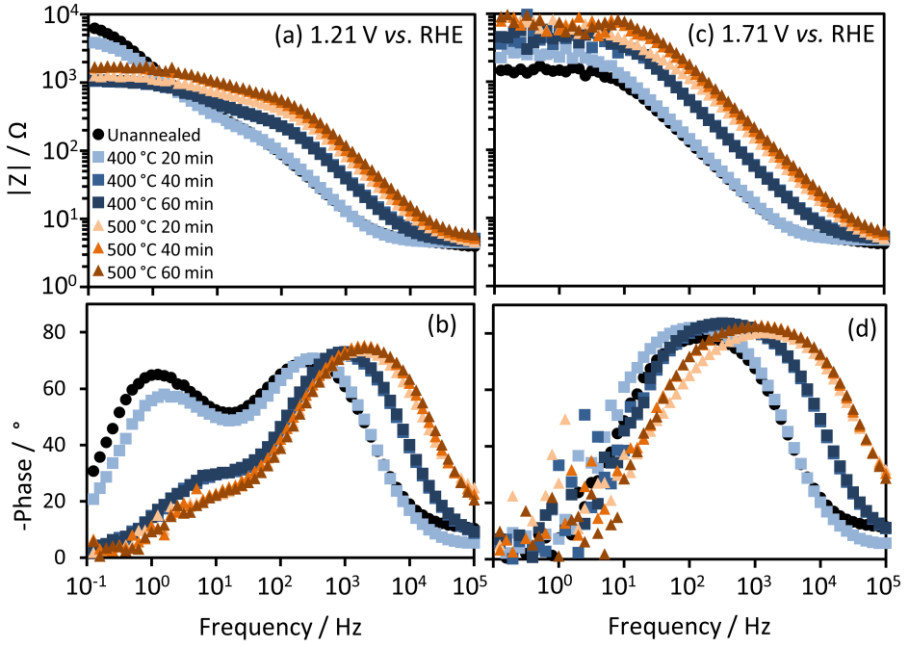


Figure 2-9. Effect of annealing temperature and time on impedance spectra: 1.21 V *vs.* RHE (a) Bode and (b) phase plot, and 1.71 V *vs.* RHE (c) Bode and (d) of Ti|Sn^{IV}-doped α-Fe_2O_3 | 1 mol dm^{-3} NaOH at and 3 000 W m^{-2} Xe arc lamp.

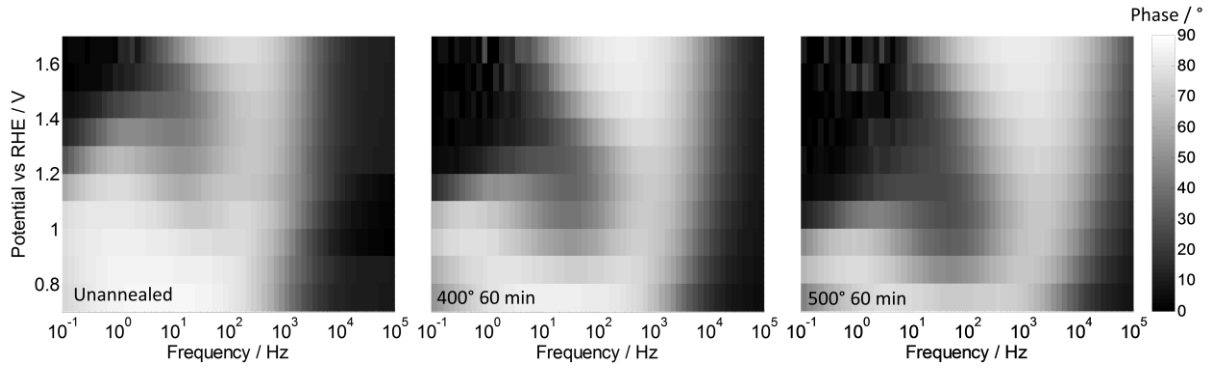


Figure 2-10. Effects of potential and frequency on phase (colour, y2 scale) of PEIS behaviour of illuminated Ti|Sn^{IV}-doped α-Fe_2O_3 unannealed, and annealed at 400 °C and 500 °C for 60 minutes.

2.4.9 Morphology and optical properties

The crystallinity of the samples was evaluated for the two extremes investigated in this study: unannealed samples and those annealed at 500 °C for 60 min. Raman spectra, presented in the Appendix, Figure S2-7, confirmed that the crystallinity of the samples did not change with annealing at temperatures up to 500 °C, and no other phases were present in the film according to the expected peaks of hematite and TiO_2 phases, anatase and rutile, Table S2-1 [161-163]. A weak peak at 654 cm^{-1} could be associated with high density of defects in doped samples [164]. SEM images of Sn^{IV}-doped Fe_2O_3 deposited on FTO and Ti, Figure 2-11, confirmed the nano-structured

nature of the samples and also the independence of the morphology from annealing temperature (< 500 °C), which is also in agreement with previous findings of annealing at low temperatures [155, 164]. Morphological changes with thermal treatment have been reported previously, but only for temperatures higher than 600 °C and longer exposures times [165].

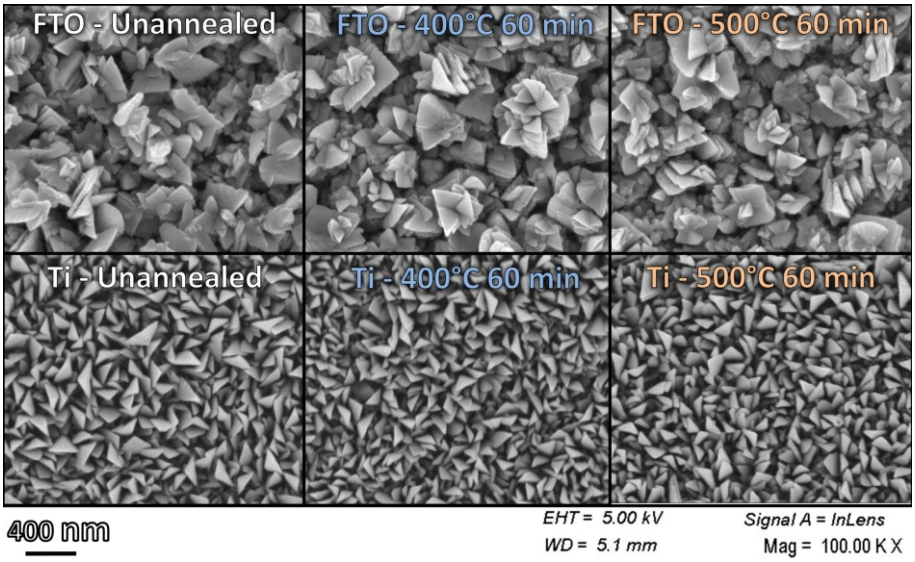


Figure 2-11. SEM images (100k ×) of Sn^{IV}-doped α-Fe_2O_3 deposited on FTO and Ti, unannealed and annealed at 400 °C and 500 °C for 60 min. Images recorded with the help of Mr. Isaac Holmes-Gentle.

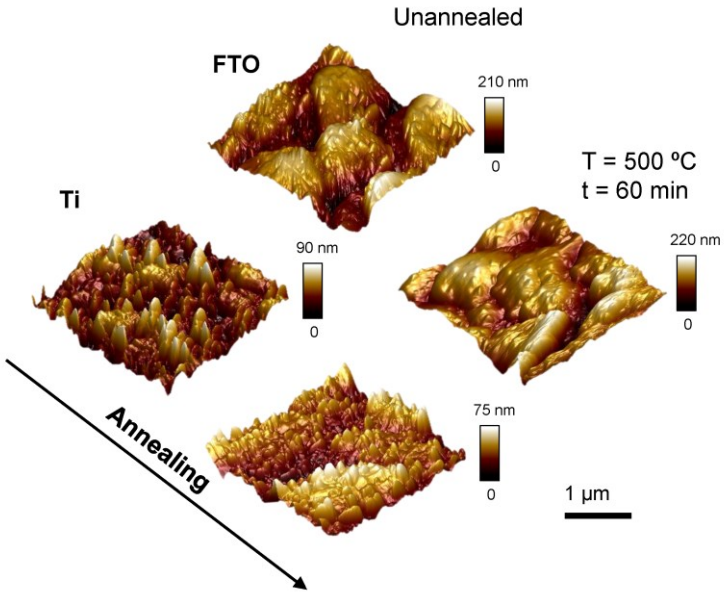


Figure 2-12. AFM images of Sn^{IV}-doped α-Fe_2O_3 deposited on FTO and Ti, unannealed, 400 °C and 500 °C annealing for 60 minutes. AFM images were recorded by Ms. Manuela Nania.

Figure 2-12 shows AFM images of the surface topography of Sn^{IV}-doped α-Fe_2O_3 on FTO and Ti substrates. Only a slight decrease in active area (< 11.6 % for FTO and < 7.6% for Ti samples) and roughness was evident after annealing, as reported in Table S2-2 in the Appendix. The increase of total active area with respect to the projected area was ca. 15% for samples deposited on FTO

and 10% on Ti, in agreement with the SEM images. The AFM images also support the hypothesis that the unusually high values of donor density, via equation (2-3), and their substantial decrease (several orders of magnitude) with annealing were not associated with drastic changes in electro-active area, so were likely to be related to chloride contamination.

The absorbances of the various photo-anodes were measured to determine if the increase in IPCEs at 550 nm and 1.71 V *vs.* RHE was related to differences in absorbance at this wavelength. Samples treated at 500 °C showed higher absorbances in the UV region, consistent with a higher IPCE at 360 nm after annealing. However, there was no significant change in absorbance at 550 nm, as shown in Figure S2-8 in the Appendix. Annealing at higher temperatures has been reported to affect the absorbance of samples significantly [165], but this was not evident for the 400 – 500 °C temperature range used in this work. No differences in band gaps were found from Tauc plots, shown in Figure S2-9. Thus again, it can be concluded that the decrease of maximum photocurrent density with annealing at low temperatures was not related to changes in absorbance, crystallinity or morphology of the samples.

2.4.10 XPS Analysis

As the remaining hypothesis, the change in the maximum photocurrent and arrest at 550 nm in the IPCE could be related to a redistribution of the dopant. This is supported by a slight increase in the intensity of Sn 3*d* relative to Fe 2*p* core lines in the XPS spectra after annealing, see Figure 2-13(b). From the comparison of the peak areas of the Sn $3d_{5/2}$ and Fe $2p_{3/2}$ lines, the Fe:Sn surface ratios are 98.4:1.6 and 98.2:1.8 for the unannealed films on FTO and Ti, respectively, and 97.9:2.1 and 97.8:2.2 for films annealed at 500 °C for 60 minutes on FTO and Ti, respectively. Thermal treatment is known to redistribute defects in semiconductors at the surface, where defects are at their lowest energy [166]. This would explain the diffusion of Sn^{IV} from the bulk to the surface after annealing.

Uchiyama et al. found a strong dependence of the optical absorption of hematite in the presence of Sn^{IV}. A molar ratio of 0.9:0.1 Fe^{III} : Sn^{IV} exhibited lower absorbance in the visible region compared to samples in the absence of Sn^{IV}. A molar ratio 0.75:0.25 decreased the absorbance substantially, especially between 500 and 600 nm. It has also been reported that increasing Sn^{IV} doping levels from 0.75 to 2% can increase the band gap from 2.12 to 2.2 eV [144], i.e. decrease the absorption to lower wavelengths.

Frydrych et al. reported a correlation of the concentration of Sn^{IV} and the height of the Sn 3*d* XPS peak for hematite samples [139]. Assuming that after annealing, Sn^{IV} was concentrated within the depletion layer of the semiconductor, as well as the effective electron-hole separation happened in this region [140, 142], the decrease of the IPCE peak at 550 nm could be explained by a corresponding decrease of photon absorption. However, this was not evident in the absorption spectra (Figure S2-8), because photons between 500 and 600 nm would still be absorbed in the bulk of the photo-anode, but would not be converted effectively to charge due to electron-hole recombination in the bulk hematite. Depletion of Sn^{IV} in the bulk of the semiconductor due to its

diffusion to the surface could also have caused the decrease in maximum photocurrent on annealing. Sn^{IV} depletion in the bulk could increase the electron-hole recombination rates there and also alter the electrical conductivity [64]. Also, a decrease in the semiconductor Debye length due to higher concentrations of donors (Sn^{IV}) near the surface could result in a decrease in the number of absorbed photons in the depletion layer [144].

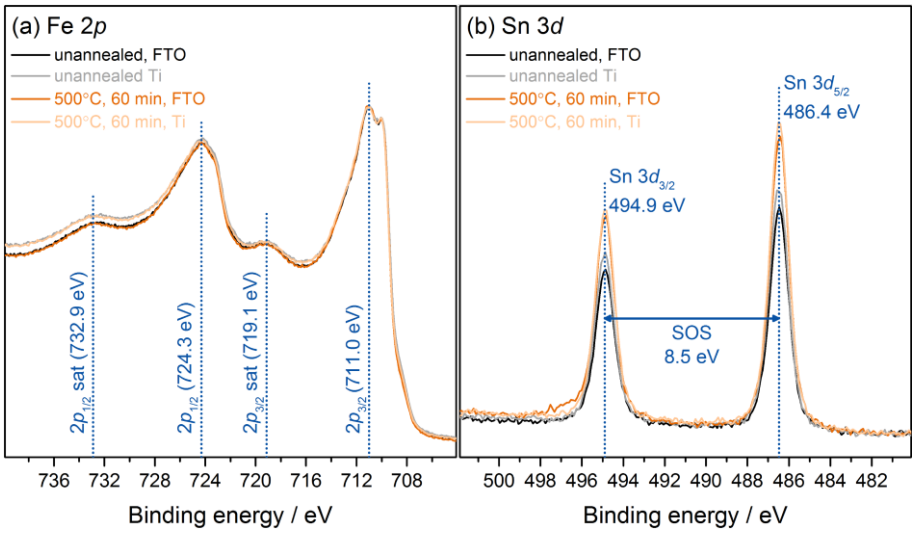


Figure 2-13. XPS core level spectra of Sn^{IV}-doped α-Fe_2O_3 on FTO and titanium unannealed and after annealing at 500 °C for 60 minutes, including (a) Fe 2p and (b) Sn 3d. Spectra was recorded and analysed by Dr. Anna Regoutz.

Sn^{IV}-doped α-Fe_2O_3 exhibited higher efficiencies of interfacial charge transfer compared to undoped samples [145]. The presence of higher Sn^{IV} concentrations close to the Sn^{IV}-doped α-Fe_2O_3 | 1 mol dm^{-3} NaOH interface increased photocurrent densities which were shifted to lower potentials, due to decreased surface electron-hole recombination rates and / or improved catalysis of the oxygen evolution reaction.

Profiling of dopant concentration inside Sn^{IV}-doped α-Fe_2O_3 is necessary to elucidate further the effects of annealing on the photo-electrochemical properties of hematite. This can be done via ion beam sputtering. However, Sn and Fe might sputter at different rates and also be reduced to elemental form, changing the stoichiometry and concentration of the sample [167, 168]. Intensity modulated photo-electrochemical impedance spectroscopy (IMPS) and transient absorption spectroscopy (TAS) with 550 nm monochromatic light may also prove useful in elucidating the origin of this phenomenon.

2.5 Conclusions

Sn^{IV}-doped α-Fe_2O_3 photo-anodes were fabricated via spray pyrolysis on titanium and FTO substrates and the effects studied of subsequent annealing at 400 and 500 °C, at which spatial redistributions of Sn^{IV} was suggested to occur. The shift of photocurrent densities with annealing temperature in absence of hole scavenger was associated with a decrease of electron-hole recombination rates caused by an increase of dopant concentration near the Sn^{IV}-doped α-Fe_2O_3 | 1 mol dm^{-3} NaOH interface. No evidence was found for annealing causing significant changes in

morphology, crystallinity or topography. The decrease in maximum photocurrent densities with annealing appeared to be associated with a decrease in photon absorption within the depletion layer where Sn^{IV} dopant was believed to have accumulated, with supporting evidence from IPCE spectra and XPS measurements. After excluding effects due to changes in morphology [59], which occurs only at higher temperatures, changes in photo-electrochemical behaviour after annealing were explained in terms of Sn^{IV} dopant concentration profiles, leading to decreased fluxes of holes [169].

A complete summary of all the phenomena and hypotheses investigated are listed in Table 2-2. The results and a clearer understanding of the effects of various parameters on photo-anode performance could serve as a framework to improve models to predict photocurrent densities in up-scaled photo-electrochemical reactors for hydrogen production.

Table 2-2. Summary of phenomena detected. Hypotheses listed first (in bold) for each phenomenon are the proposed explanation with techniques listed for its validation. Subsequent hypotheses are disregarded or assumed to have minimum effect, with techniques listed for validation.

Phenomena	Hypothesis	Technique
Shift in photocurrent density to lower potentials with annealing	**Decrease of surface electron-hole recombination / improved hole transfer rates**	PEIS Photo-voltammetry with hole scavenger
Decrease in maximum photocurrent density with annealing	**Redistribution of dopant / concentration at the surface and depletion in the bulk hematite**	IPCE XPS Photo-voltammetry with hole scavenger
	Change in morphology and active area	SEM AFM
	Catalytic properties / change in iron oxide phase	ICPE Raman
	Change in absorptivity	Absorbance spectra
High values of donor densities and decrease with annealing	**Chloride at hematite surface**	XPS
	Oxygen vacancies at hematite surface	XPS
	Pin holes	SEM AFM Photo-voltammetry for Ti and FTO substrates
Decrease in dark current densities with annealing for samples on titanium substrates	**TiO_2|Fe_2O_3 junction energy barrier**	Comparison of conduction band energies
	Decrease in active area	SEM AFM
	Different phase / catalytic properties	Raman XPS

Chapter 3

Model of PEC systems: photocurrent and hydrogen yield predictions[2]

3.1 Introduction

Recent advances in technologies such as water splitting via PV + electrolyser,[87] integrated photo-electrochemical [170], photo-electrochemical [171] and particulate photocatalysts [172] are approaching a level of readiness for up-scaling. However, commercial deployment is still constrained by the degradation of the systems with time and the cost of the produced hydrogen, which must be competitive with current technologies, e.g. steam reforming. Recently, most of the efforts have been directed towards the development and prediction of performance of photo-anodes [173] and in a lesser extent towards photo-cathode development [174, 175]. Hence, techno-economic modelling and engineering optimisation need to be started in parallel with addressing scientific and engineering challenges. The seminal review of Gerisher [121] mapped the path towards a fundamental understanding and modelling of semiconductors coupled with electrochemical devices. Carver et al. [47] and Haussener [122] started proper electrochemical modelling of such devices, often operating as an electrolyser at relatively low current densities of $2 - 200$ A m^{-2}, c.f. $1000 - 3000$ A m^{-2} for conventional water electrolysers [176]. Berger et al.[119, 177] expanded this work for membrane based systems. The effects of conductivity and geometrical parameters, such as electrode and membrane thicknesses, on the reactor performance were analysed. However, most of the parameters that defined material performances were from the literature. The effects of bubbles and desorption of gas were not quantified and there was a limited comparison of predictions with experimental data. A more complete integrated solar driven water-splitting device operating at neutral pH was modelled by Jin et al.[115] This model considered pH gradients and cross-over losses in presence and absence of a membrane. Low yields were found with a membrane-based system due to the slow proton transfer at neutral pH and model predictions were compared successfully to experimental

[2] This chapter was adapted from: F. Bedoya-Lora, A. Hankin, G.H. Kelsall, *En route* to a unified model for photo-electrochemical reactor optimisation. I - Photocurrent and H_2 yield predictions, *J. Mater. Chem. A*, 2017. doi.org/10.1039/C7TA05125E.

data. Little attention was paid to the effects of bubble generation, causing light reflection/scattering, decreasing conductivities of electrolyte solutions and spatial distribution of current densities of larger electrodes. However, it showed clearly the issues related to current density distribution even at small size electrodes (16 mm). More recently, this model was expanded to study the effect of electrolyte flow on membrane based systems [117]. Recent works by Haussener et al. [130-132] extended their model for temperature dependence under concentrated irradiation, statistical analysis validated against experimental data and the effect of perforations on the performance of integrated solar devices. However, hitherto a model had yet to be developed for photo-electrochemical reactors, in which the photo-absorber and electrode are the same material, coupled with bubble generation at the electrode and bulk of electrolyte. Incorporating bubble formation at the photo-electrode | electrolyte interface is important as: (*i*) it enables quantification of the amount of gas produced near the surface and the actual dissolved gas flux diffused into the bulk of the electrolyte that could take part in cross-over losses [127]; (*ii*) rates of generation of bubbles in photo-electrochemical reactors should be minimised by judicious design, to minimise resistive losses [36, 178] and the reflection and scattering of incoming light [179] that otherwise would decrease photo-electro-active areas.

Validation against experimental results obtained with different photo-electrodes materials is often bypassed. In this chapter, the prediction of the performance and model validation using an photo-electrochemical cell based on easily measurable characteristics of components of the system at small scale is reported. Sn^{IV}-doped α-Fe_2O_3 photo-anodes treated at different annealing times were used to obtain parameter values as inputs to a 1D model and validate it against experimental data measured in small scale cells. Next, a hypothetical and enhanced photo-anode was studied in an analogous 2D model. This will be followed in the next chapter by 3D geometrical optimisation and additional validation against hydrogen yields obtained in an up-scaled reactor.

3.2 Theoretical treatment

3.2.1 Definition of bulk and surface electron-hole recombination

Definitions of bulk and surface electron-hole recombination rates in semiconductors are widely spread and vary depending on the framework in which they are discussed. For clarity, herein the bulk recombination is defined as the annihilation of generated holes and electrons in the bulk of the semiconductor, outside the depletion region or space charge layer. This recombination accounts for low conductivity or sluggish charge transfer into the substrate, as well as for absorbed photons in the bulk that ultimately do not generate charge. Surface recombination is closely related to the rate of charge carrier extraction at the surface of the semiconductor and the rate at which the charge is migrating and diffusing from the depletion region to and across the semiconductor | electrolyte interface. Generally, surface electron-hole recombination depends on the chemistry of the surface and is a function of the applied potential. A schematic view of these definitions is shown in Figure 3-1.

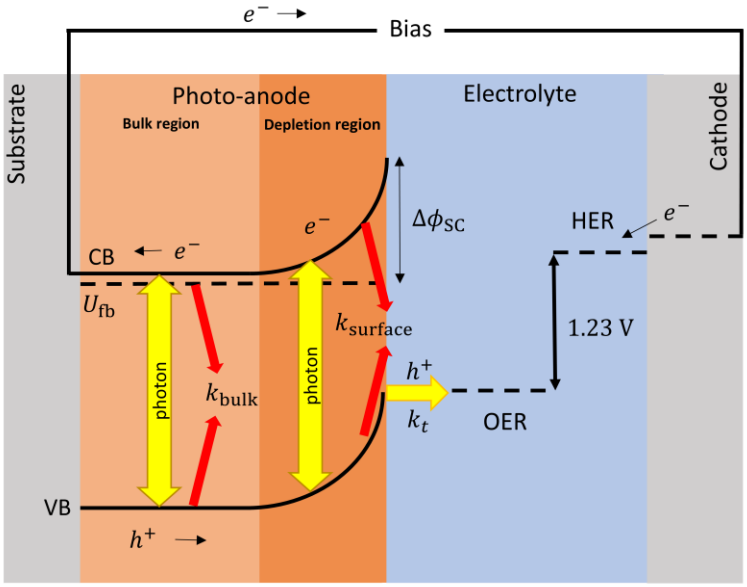


Figure 3-1. Scheme of recombination processes (in red) happening in the bulk and surface of a photo-anode after charge separation (yellow).

3.2.2 Photocurrent density prediction

The photocurrent density produced in the anode was predicted using a modified version of the Gärtner–Butler equation [65, 123, 124], see Chapter 1 page 53, which does not account for charge migration and diffusion rates into the semiconductor bulk, where electron-hole recombination may occur.

$$j_{\mathrm{ph(GB1)}} = \left(\frac{2e\left(\sum_\lambda I_{0,\lambda}\alpha_\lambda\right)^2 \varepsilon_0 \varepsilon_\mathrm{r}}{n_0}\right)^{\frac{1}{2}} (\Delta\phi_{\mathrm{SC}})^{\frac{1}{2}} \tag{3-1}$$

After correction for photon absorption:

$$j_{\mathrm{ph(GB2)}} = \left(\frac{2e\left(\sum_\lambda (I_0 - I_x)_\lambda \alpha_\lambda\right)^2 \varepsilon_0 \varepsilon_\mathrm{r}}{n_0}\right)^{\frac{1}{2}} (\Delta\phi_{\mathrm{SC}})^{\frac{1}{2}} \tag{3-2}$$

where $(I_0 - I_x)_\lambda$ is the actual absorbed light after attenuation e.g. by electrolyte solutions, window quartz etc. and correction for the semiconductor's thickness and absorptivity. I_x is the transmitted photon intensity given by equation (3-3) or obtained from absorbance/transmittance measurements.

$$I_{x,\lambda} = I_{0,\lambda} \exp(-\alpha_\lambda x) \tag{3-3}$$

The photocurrent density should also be limited by the photon flux $(I_0 - I_x)_\lambda$ as:

$$j_{\mathrm{ph(GB3)}} = j_{\mathrm{ph(GB2)}} \Big/ \left[1 + \frac{j_{\mathrm{ph(GB2)}}}{e \times \sum_\lambda (I_0 - I_x)_\lambda}\right] \tag{3-4}$$

According to Dotan et al. [180], photocurrent densities should also be corrected for surface and bulk recombination rates as:

$$j_{\mathrm{ph}} = j_{\mathrm{absorbed}} \times \Phi_{\mathrm{surface}} \times \Phi_{\mathrm{bulk}} \tag{3-5}$$

j_{absorbed} is a value that does not depend on the potential and is the maximum achievable current density that corresponds to $e \times \sum_{\lambda}(I_0 - I_x)_{\lambda}$. Hence, bulk efficiencies are a function of potential. Herein, a modified version of this equation is proposed in order to decouple the dependence of Φ_{bulk} from the potential and, instead, account for this dependence in the absorbed photocurrent as predicted by the Gärtner–Butler equation:

$$j_{\mathrm{ph}} = j_{\mathrm{ph(GB3)}} \times \Phi_{\mathrm{surface}} \times \Phi_{\mathrm{bulk}} \tag{3-6}$$

In which only $j_{\mathrm{ph(GB3)}}$ and Φ_{surface} are a function of the band bending $\Delta\phi_{\mathrm{SC}}$, whereas Φ_{bulk} is independent of potential, as will be described below.

Surface recombination

The interfacial charge transfer efficiency, Φ_{surface}, can be estimated from photo-electrochemical impedance spectroscopy (PEIS) as a function of potential [145-147] as described in Chapter 1, page 64.

Bulk recombination

As defined here, the recombination in the bulk should not be a function of applied potential. If surface recombination is avoided, that means $\Phi_{\mathrm{surface}} = 1$ when using a fast hole scavenger such as H_2O_2, see reaction (3-7), Φ_{bulk} can be determined as the ratio between the experimental photocurrent j_{ph,H_2O_2} and the expected photo-current from the modified Gärtner–Butler equation, $j_{\mathrm{ph(GB3)}}$.

$$HO_2^- + OH^- + 2h^+ \longrightarrow O_2 + H_2O \tag{3-7}$$

$$\Phi_{\mathrm{bulk}} = \left| \frac{j_{\mathrm{ph},H_2O_2}}{j_{\mathrm{ph(GB3)}}} \right|_{\Phi_{\mathrm{surface}}=1} \tag{3-8}$$

Then, the rate of bulk recombination should be determined by the Shockley-Read-Hall effect, which does not depend on the applied potential, but on the charge carrier concentration in the bulk of the semiconductor. As shown in Figure 3-1, photons absorbed deeper into the semiconductor than the depletion layer tend to recombine, due to the absence of an electric field, so produce no net charge. This can be tested by comparing the absorbed photons in the depletion layer and total number of photons absorbed by the whole depth of the semiconductor, $(I_0 - I_x)_{\lambda}$. The former photon flux can be estimated using the semiconductor Debye length as an approximation for the depletion layer width in a nanostructured electrode, L_D, equation (3-9) [181]. Then, the absorbed photons inside the

region of the Debye length can be estimated by a modified Gartner relationship, equation (3-10) [124].

$$L_D = \left(\frac{\varepsilon_0 \varepsilon_r k_B T}{2e^2 n_0}\right)^{0.5} \tag{3-9}$$

$$I_0 - I_{L_D} = I_0\left(1 - \frac{\exp(-\alpha_\lambda L_D)}{1+\alpha_\lambda L_p}\right) = I_0(1 - \exp(-\alpha_\lambda L_D)) \tag{3-10}$$

Using values for charge carrier concentration and absorptivity of annealed Sn^{IV}-doped α-Fe_2O_3 reported in Chapter 1, the number of absorbed photons inside the Debye length is only 7.3% of the total absorbed photons. This value is comparable to the values measured here for Φ_{bulk} of annealed samples, ca. 7%.

3.2.3 Dark (anodic and cathodic) current

Dark anodic current densities were approximated by the Tafel equation, as dark overpotentials are usually high for oxygen evolution on hematite electrodes (>100 mV), so the rate of the reverse reaction could be neglected:

$$j_{a,\mathrm{dark}} = j_{0,a} 10^{\eta_a / A_a} \tag{3-11}$$

The overpotential for oxygen evolution reaction (OER) was computed against its equilibrium potential:

$$U_{O_2|H_2O}(\mathrm{SHE})/\,\mathrm{V} = 1.229 - 0.0592\mathrm{pH} + 0.0148\log(p_{O_2}) \tag{3-12}$$

Assuming small changes of local pH in the electrolyte and insignificant change in the partial pressure of oxygen, it can be assumed that $U_{O_2|H_2O}(\mathrm{RHE}) = 1.229\ \mathrm{V}$. Likewise, cathodic currents were computed with the Butler-Volmer equation for hydrogen evolution on platinized titanium.

$$j_{c,\mathrm{dark}} = j_{0,c}\left[\exp\left(\frac{\alpha_{\mathrm{ox},c} F\eta}{RT}\right) - \exp\left(\frac{\alpha_{\mathrm{red},c} F\eta}{RT}\right)\right] \tag{3-13}$$

The hydrogen overpotential was calculated from the equilibrium potential for the hydrogen evolution reaction (HER):

$$U_{H_2O|H_2}(\mathrm{SHE})/\,\mathrm{V} = -0.0592\mathrm{pH} + 0.0296\log p_{H_2} \tag{3-14}$$

Again, assuming small changes of local pH and negligible change in partial pressure of hydrogen, it was assumed that $U_{H_2O|H_2}(\mathrm{RHE}) = 0\ \mathrm{V}$.

3.2.4 Ionic current

The ionic current in the electrolyte for (infinitely dilute) charged electro-active species was modelled after substituting Faraday's law into the Nernst–Planck equation:

$$j_{\text{ionic}} = -F^2\nabla\phi\sum_i \frac{z_i D_i c_i}{RT} - F\sum_i z_i D_i c_i + F\mathbf{v}\sum_i z_i c_i \tag{3-15}$$

Assuming electroneutrality conditions:

$$\sum_i z_i c_i = 0 \tag{3-16}$$

and in the absence of concentration gradients, the distribution of potential satisfies Laplace's equation:

$$\nabla^2\phi = 0 \tag{3-17}$$

The mass transport limited current density for a quiescent 1 mol dm^{-3} NaOH electrolyte is $j_{\text{L,OH}^-} = 10^4\ \text{A m}^{-2}$ [65]. All experiments and predicted current densities in this chapter were < 50 A m^{-2}. Hence, the OH$^-$ gradients and ion depletion at the photo-anode | electrolyte interface were such that $\nabla c_i = 0$ was a suitable assumption.

Assuming negligible resistance for the electric contacts and wiring in the cell, a potential balance gives [47]:

$$\Delta U = \phi_c - \phi_a = \left(U_{\text{O}_2|\text{H}_2\text{O}} - U_{\text{H}_2\text{O}|\text{H}_2}\right) + \eta_a + |\eta_{\text{c}}| + \sum_i \frac{I d_i}{\sigma_i A_i} \tag{3-18}$$

Where $U_{\text{O}_2|\text{H}_2\text{O}} - U_{\text{H}_2\text{O}|\text{H}_2}$ is the required thermodynamic potential difference; $\eta_a + |\eta_{\text{c}}|$ the overpotentials at the anode and cathode respectively; and the last term is the sum of the ohmic potential losses in the phases i with conductivity σ_i, path length d_i and cross section area A_i.

3.2.5 Bubble formation and gas desorption

The evolution of gas at the surface of anode and cathode was modelled in terms of efficiency of gas evolution, f_G [127].

$$f_G = \frac{N_G}{N_D} \tag{3-19}$$

where N_D is the flux of hydrogen or oxygen produced by the faradic current at the surface of the electrode. N_G is the fraction of N_D converted into bubbles at the electrode surface, $N_{\text{desorption}}$ is the gas evolving from natural desorption under supersaturated conditions and N_{bulk} is the diffusive flux. A schematic representation of these processes is present in Figure 3-2, following definitions proposed by Vogt [127].

The effect of bubble generation on scattering of light has yet to be implemented. Also, the present model does not consider the effect of flow, which can decrease gas evolution efficiencies substantially [127] and modify the micro and macro convectional effects due to the removal of bubbles at the electrode surface.

Efficiency of gas evolution

Several models have been proposed to estimate f_G in terms of measurable quantities such as current density and fractional surface coverage. Vogt recently updated [128, 182] his own model for oxygen and hydrogen bubble evolution [127, 183]. However, these models are difficult to implement when coupled to other physics, such as electrochemical reaction and transport of dissolved species. Root squared and exponential expressions often result in complex values when evaluated under certain conditions. Furthermore, these models are normally discontinuous and require several constrains at low current densities (<10 A m^{-2}). Vogt was wary to use simplified and ad hoc models, but also was aware of difficulties found when using fundamental models [182]. A phenomenological model for gas evolution proposed by Kwie et al. [126] relates closely to the system studied here. Hydrogen and oxygen bubble efficiencies at nickel and platinum-wire electrodes in alkaline solutions over current densities of 10 to 10^4 A m^{-2} were predicted by a power function:

$$\frac{f_{G,i}}{1+f_{G,i}} = a_{G,i} j^{n_{G,i}} \tag{3-20}$$

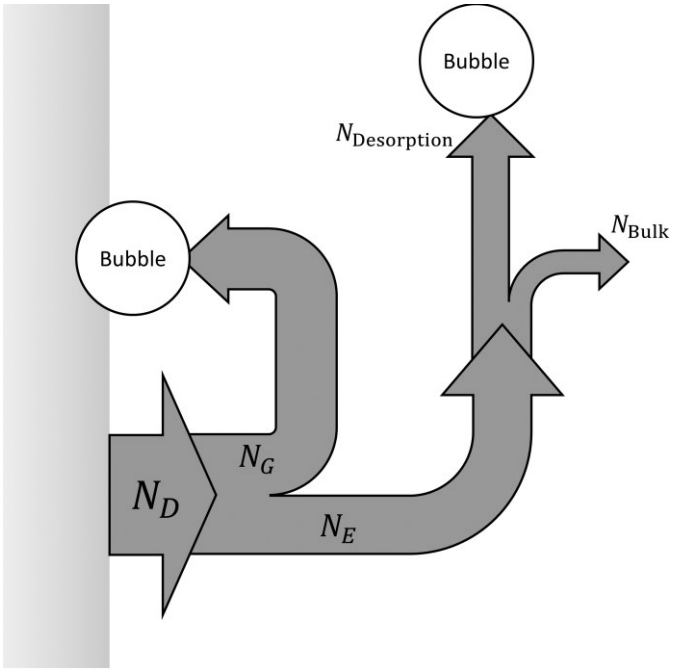


Figure 3-2. Scheme of gas evolution on an electrode and in the electrolyte, modified version from Vogt [127].

where $a_{G,i}$ and $n_{G,i}$ are fitted parameters from experimental data for a given system. The measurements by Kwie et al. differ mainly in two aspects: the electrode material was a nickel wire and the fluid was not quiescent, but flowing at 0.12 m s^{-1} (Re ≈ 67). However, it is still a reasonable approximation that enables estimation of gas evolution efficiencies as a function of local current density. A more detailed comparison between Vogt and Kwie models can be

found in the Appendix, Figure S3-2. The semi-empirical equation developed by Kwie, equation (3-20), for the estimation of f_G was used in the model described in here.

Volumetric mass transfer coefficient

Gas desorption was modelled by a simple mechanism of volumetric desorption when the species are above the saturated concentration.

$$N_{\text{desorption}} = k_L a(c_{\text{sat},i} - c_i) \tag{3-21}$$

where, k_L is the mass transport coefficient and a the area of transfer per unit volume. Usually, these values are reported as $k_L a$, the volumetric mass transfer coefficient. The seminal work by Frossling [184] has been used widely [129] in order to estimate k_L as a function of Re and Sc numbers for bubbles of small diameter (0.1 to 2 mm).

$$k_L = \frac{D_i}{d_B}(2 + 0.6\text{Re}^{0.5}\text{Sc}^{0.5}) \tag{3-22}$$

The minimum average bubble diameter for mass transport in quasi-static conditions in a variety of electrolytes, including 1 mol dm^{-3} KOH, was found to be $d_B = 4.5 \times 10^{-5}$ m [185]. This value can be used to estimate the bubble slip velocity (relative to the liquid) using the Wüest relationship [186, 187].

$$v_B = 4474\left(\frac{d_B}{2}\right)^{1.357} \tag{3-23}$$

Then, Re and Sc are calculated as usual for a spherical geometry:

$$\text{Re} = \frac{v_B d_B}{\upsilon} \tag{3-24}$$

$$\text{Sc} = \frac{\upsilon}{D_i} \tag{3-25}$$

Where υ is the kinematic viscosity of the fluid and D_i the diffusion coefficient of the oxygen or hydrogen in the liquid, see a detailed list of used parameters in the Appendix, Table S3-2. The area of transfer per unit volume, a, can be estimated using the correlation by Deckwer [129, 188]:

$$a = 34.4 v_B^{0.25} \varepsilon_G \tag{3-26}$$

where ε_G is the gas holdup, which can be estimated graphically as a function of v_B [189] or using the correlation by Joshi and Sharma [129, 190]:

$$\varepsilon_G = \frac{v_B}{0.3 + 2v_B} \tag{3-27}$$

For a detailed numerical calculation of $k_L a$ see Table S3-2 in the Appendix. It was found that $k_L a$ is 1.94×10^{-4} s^{-1} for oxygen and 3.02×10^{-4} s^{-1} for hydrogen at 298 K and quiescent state. These values are similar to the predictions by Wüest (2.76×10^{-4} s^{-1}) [187], but are

significantly lower than those predicted by Deckwer [189] for oxygen absorption and desorption in tap water for a well stirred reactor (3.58×10^{-2} and 9.96×10^{-2} s^{-1}, respectively). The differences with the latter values were due to the absence of electrolyte flow and convectional effects in the cells.

3.2.6 Diffusion of dissolved species

Dissolved gases, oxygen and hydrogen, were modelled by the Nernst-Planck equations assuming infinite dilution of species.

$$\frac{\partial c_i}{\partial t} + \nabla \cdot N_i = R_i \tag{3-28}$$

$$N_i = -D_i \nabla c_i - z_i u_{m,i} F c_i \nabla \phi_l + \mathbf{v} c_i \tag{3-29}$$

where c_i is the concentration of species i, D_i is the diffusion coefficient, z is the charge, u_m is the mobility, F is the Faraday constant (96485.3 C mol^{-1}), ϕ is the medium potential, $\mathbf{v}$ is the velocity of the fluid, and R is the reaction rate or in this case the rate of desorption. Assuming there is no migration in static electromagnetic conditions for neutral species, and absence of homogeneous reactions and convectional effects, the equation is simplified to:

$$\frac{\partial c_i}{\partial t} = D_i \nabla^2 c_i + N_{\text{desorption}} \tag{3-30}$$

The flux of species at the surface of the electrode was modelled according to Faraday's law of electrolysis and reaction stoichiometry for water splitting in alkaline conditions, hydrogen (HER) by reaction (3-33) and oxygen evolution (OER) by reaction (3-34) which can also be expressed in terms of photo-generated oxidising species, h^+, by reallocating the charge on the right-hand side of the reaction.

$$N_i = R_i = \frac{\nu_i j}{\nu_{e,i} F} \tag{3-31}$$

$$\sum_{\text{ox}} |\nu_{\text{ox}}| S_{\text{ox}} + \nu_e e^- \leftrightarrow \sum_{\text{red}} \nu_{\text{red}} S_{\text{red}} \tag{3-32}$$

$$2H_2O + 2e^- \Leftrightarrow H_2 + 2OH^- \tag{3-33}$$

$$O_2 + 2H_2O + 4e^- \Leftrightarrow 4OH^- \tag{3-34}$$

In the case of electrolyte | membrane interface, the concentrations of oxygen and hydrogen at the interface were modelled using a partition coefficient.

$$c_{i,\text{surface}} = \left.\frac{c_{i,m}}{K_{i,m}}\right|_{\text{surface}} \tag{3-35}$$

The partition coefficient was estimated from the saturated concentrations in the membrane and electrolyte, as follows:

$$K_{i,m} = \frac{c_{\mathrm{sat},i,m}}{c_{\mathrm{sat},i}} \tag{3-36}$$

In some cases, OH^- ions were included with an initial concentration of 1 mol dm^{-3}. However, the depletion and increase in concentration at the anode and cathode, respectively, prevented the model converging to a steady state solution, specifically when a cation-permeable membrane was used to separate the catholyte and anolyte. Then, quasi-stable state, i.e. depletion of OH- in the bulk of electrolyte is very slow compared to other processes in the model, was considered.

Lastly, the flux of hydrogen and oxygen, N_i, is defined as the total amount of the gas coming from bubble formation at the surface of the electrode and desorption in the electrolyte, or catholyte and anolyte when a membrane is used, according to equation (3-37). Fluxes were normalized by the area of the electrodes, defined as hydrogen flux density and reported in units mol m^{-2} s^{-1}. The charge yield, Φ_i^e, for hydrogen and oxygen evolution is defined as usual: the ratio between the charge transferred for hydrogen evolution (HER) or oxygen evolution reaction (OER), and the total charge transferred at the electrode, according to equation (3-38). The collection efficiency, $\Phi_{\mathrm{collection},i}$, is defined here as the ratio between the flux density and the maximum achievable gas evolution given by the total current at the electrode and Faraday's law, according to equation (3-39). The collection efficiency is intrinsically related to the cross-over of products between anolyte and catholyte, via the membrane if present.

$$N_i = N_{G,i} + N_{\mathrm{desorption},i} \tag{3-37}$$

$$\Phi_i^e = \frac{j_i}{j_{\mathrm{total}}} \tag{3-38}$$

$$\Phi_{\mathrm{collection},i} = \frac{N_i}{j_{\mathrm{total}}/\nu_{e,i}F} \tag{3-39}$$

An overall efficiency for a photo-electrochemical device was estimated following the definition proposed previously [65] for photo-electrodes operating under an electrical bias: assisted solar to hydrogen efficiency (ASTH). This efficiency is defined as the energy rate associated to the rate of hydrogen evolution (hydrogen flux density) divided by the amount of energy rate applied to the system (photons and electrical bias in this case):

$$\mathrm{ASTH} = \frac{E_{\mathrm{H_2}} N_{\mathrm{H_2}}}{P^0 + j_{\mathrm{total}} \Delta U_{\mathrm{bias}}} \tag{3-40}$$

3.2.7 Boundary conditions

Boundary conditions are described in Figure 3-3 for the 1D model. Photo- and dark current densities were calculated at the boundary electrode | electrolyte. The potential applied through the system was set by the potential at the anode *vs.* the reference potential (RHE at the cathode). The spatial distribution of electric potential is then solved between the

electrodes in such a way that the cell potential difference is resolved for $\Delta U_{\text{bias}} = \phi_a - \phi_c$. Similarly, the flux of species, associated with currents by the Faraday's law, was coupled to transport of species at the interface electrode | electrolyte. Bubble evolution and gas desorption rates were estimated after volumetric integration along the electrolyte to compute the rate of oxygen and hydrogen collection in the anolyte and catholyte, respectively. The oxidation of hydrogen and reduction of oxygen at the anode and cathode, respectively, were assumed to be controlled by mass transport, i.e. assuming concentrations of these species at the electrode is zero. The concentration in the membrane was limited by the solubility of gas in the membrane (saturated concentration).

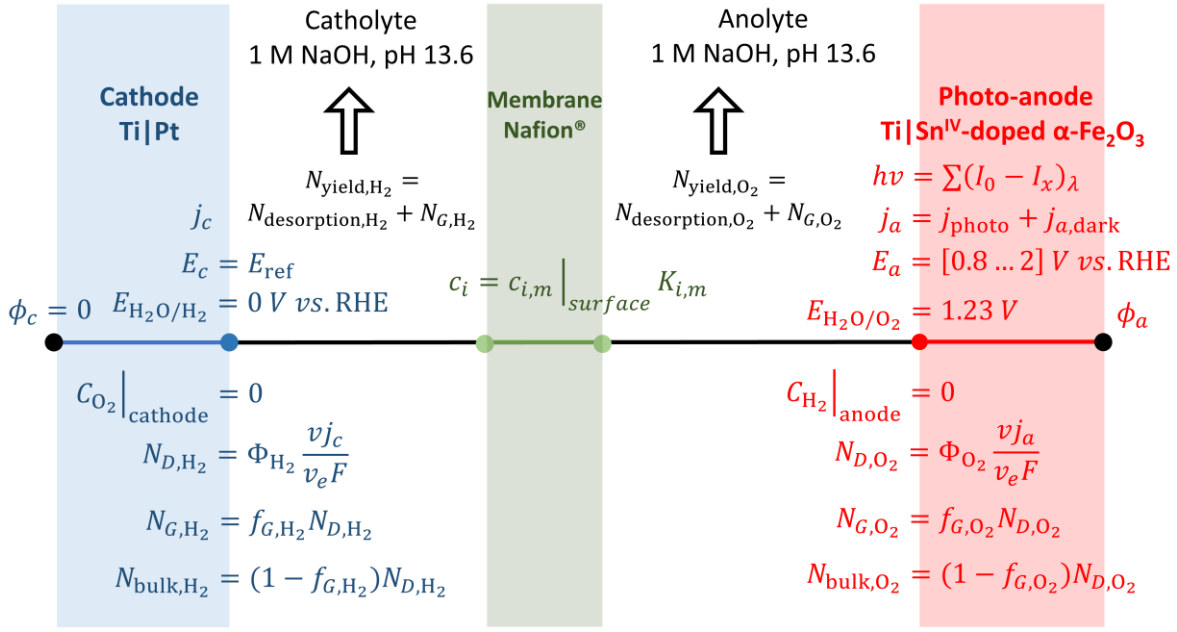


Figure 3-3. Scheme of boundary conditions for 1D model photo-electrochemical reactor cathode | catholyte | membrane | anolyte | photo-anode and electrodes facing each other.

The same boundary conditions can be applied for 2D and 3D geometries, with different distances between electrodes, membrane and perforations and different electrode arrangements. For a simplified 1D model, the electrode surfaces were facing each other and 0.02 m apart, the membrane was 330 µm thick and positioned equidistant from the 740 µm thick electrodes.

A summary of all parameters from the literature [126, 191-196] and input to the model, is presented in the Appendix, Table S3-5.

3.3 Experimental

3.3.1 Photo-anode fabrication and characterization in a PEC

Sn^{IV}-doped α-Fe_2O_3 photo-anodes deposited on titanium and FTO were fabricated by spray pyrolysis and post-annealed as described in Chapter 1, page 61 [89]. The Photo-

electrochemical characterisation has been also described in Chapter 1, page 61. For the photo-electrochemical cell described here, i.e. small beam size to volume ratio, there was not a significant increase in temperature after long term exposition to illumination.

3.3.2 Numerical considerations

Comsol Multyphysics 5.2a with a Batteries and Fuel Cells module was used to solve the system using the finite element method. Secondary current distribution (siec) and transport of diluted species (tds) physics were coupled; gas desorption was treated as a homogeneous reaction in the electrolyte. A stationary non-linear solver with a relative tolerance of 0.001 and a maximum of 100 iterations was typically used. The mesh was geometry dependent with a minimum element size of 4×10^{-7} m and maximum size of 2×10^{-2} m; the mesh was optimized for higher resolutions in narrow regions. The model converged typically in less than 20 seconds (1D) or one minute (2D) for a given set of conditions. A parametric sweep was used to evaluate a wide range of settings and geometries. The suitability of the mesh size and tolerance is demonstrated in Table S3-10 to S3-13 in the Appendix.

3.4 Results and discussion

3.4.1 Photo-anode characterization

The photo-anode characterisation discussed below was based on the results presented in Chapter 1, 65.

Photocurrent response

Figure 3-4 shows linear sweep voltammograms of Ti|Sn^{IV}-doped α-Fe_2O_3 samples. Samples were characterised in alkaline conditions in presence and absence of a hole scavenger, 0.5 mol dm^{-3} H_2O_2. In the absence of H_2O_2, the effect of annealing on the surface electron-hole recombination was evident in the shift of photocurrent to lower potentials. This effect disappeared once photo-anodes were immersed in electrolyte containing hydrogen peroxide. Maximum photocurrents were also affected by the annealing process and were comparable in the presence and absence of the hole scavenger. The decrease in the maximum photocurrent with annealing could be associated with an increase of electron-hole recombination rates in the bulk of the semiconductor. The migration of the dopant to the surface after heat treatment seemed to have been responsible for this behaviour, as discussed in more detail in Chapter 1.

Mott-Schottky analysis was used to estimate the charge carrier concentration of the semiconductor, as shown in Figure S3-3 in the Appendix and using the results of Chapter 1, page 69. However, due to the presence of adventitious chloride after deposition of the photo-anode on the Ti and FTO substrate, unannealed samples exhibited unusually high values (ca. 10^{27} m^{-3}). The removal of chloride by annealing was confirmed by XPS measurements.

Hence, apparent donor densities of annealed samples decreased to 1.9×10^{25} m^{-3}, in agreement with previous reports for Sn^{IV}-doped hematite [144]. This charge carrier concentration was used for all samples in the model calculations.

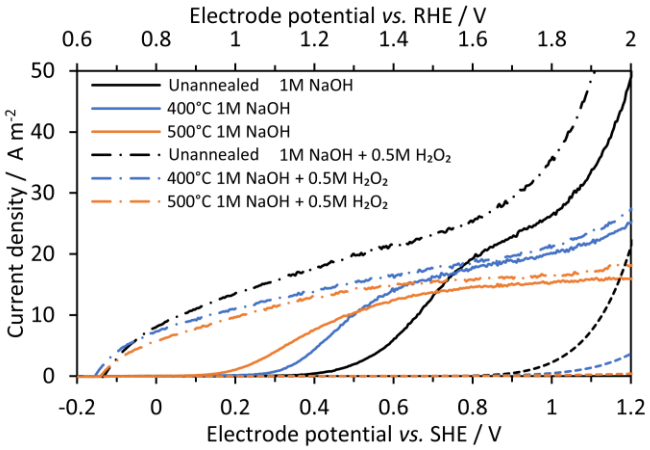


Figure 3-4. Linear sweep voltammograms on Ti|Sn^{IV}-doped α-Fe_2O_3 annealed previously at different temperatures for 1 hour. 1 mol dm^{-3} NaOH electrolyte solution with and without 0.5 mol dm^{-3} H_2O_2 as hole scavenger; 3 000 W m^{-2} irradiation from Xe arc lamp; 10 mV s^{-1} potential scan rate. Dashed lines represent dark current densities.

The flat band potential was estimated using several methods. As shown in Figure S3-4 and Table S3-6 in the Appendix, good estimations can be obtained from open circuit potential (OCP) measurements at high intensity or from the linear portion of the squared photocurrent in presence of a hole scavenger. As spray-pyrolysed hematite samples were nano-structured, they violated one of the assumptions of Mott-Schottky analysis: the interface electrode | electrolyte should be perfectly planar [43, 197]. Therefore, Mott-Schottky analysis should not be used for determination of flat band potentials of such materials.

The absorbance and absorptivity were calculated using a film thickness of 47 ± 6 nm and were very similar for all samples. The photon flux from the light source was integrated between wavelengths of 280 and 800 nm to obtain I_0. Next, the absorbed photon flux $I_0 - I_x$ and the product between this and the absorptivity $(I_0 - I_x)\alpha$ were also integrated to be used in the Gärtner–Butler equation. A typical band gap of 2.11 eV was found for all hematite samples and determined from absorbance measurements using Tauc plot analysis [46]. All the spectra were reported in Figure S3-5 and S3-6 in the Appendix.

Electron-hole recombination rates

Electron-hole recombination rates at Ti|Sn^{IV}-doped α-Fe_2O_3 | 1 mol dm^{-3} NaOH interfaces were extracted and analysed from photo-electrochemical impedance spectroscopy (PEIS) measurements, following the methodology proposed by Peter et al. [145-147], similarly as described in Chapter 1, page 69. Figure 3-5 shows typical impedance spectra, in which the charge transfer and recombination processes are evident at ca. 1 kHz and 1 Hz, respectively. After extracting the resistances corresponding to charge transfer, R_t, and recombination

processes, R_r, $\Phi_{surface}$ was fitted to equation (2-6) as a function of the potential and fitting parameters A and B, see Figure 3-6.

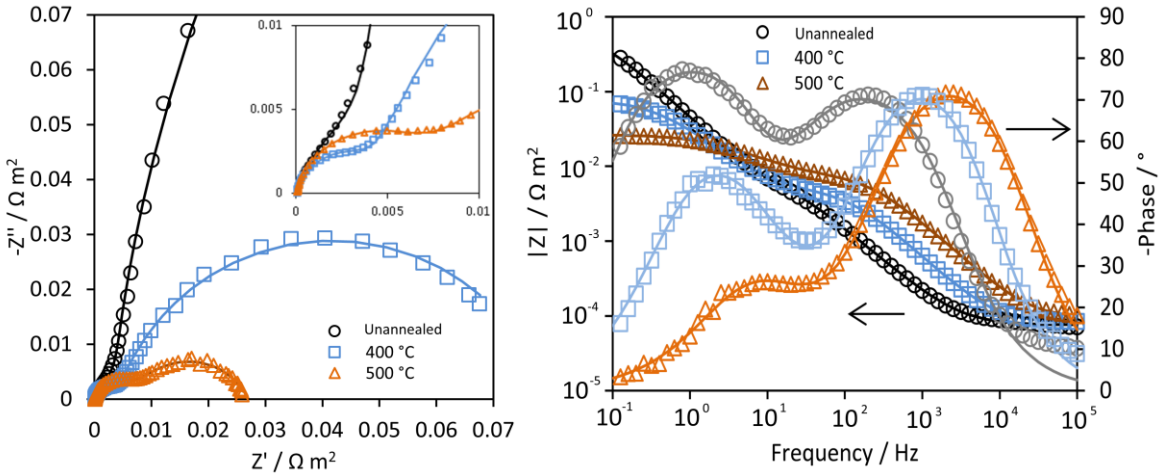


Figure 3-5. Nyquist and Bode-phase plots of Ti|Sn^{IV}-doped α-Fe_2O_3 | 1 mol dm^{-3} NaOH at 1.1 V *vs.* RHE obtained by PEIS under irradiation of 3 000 W m^{-2} by a Xe arc lamp. Continuous lines represent fitting to an electrical equivalent circuit R(C[R(RC)]).

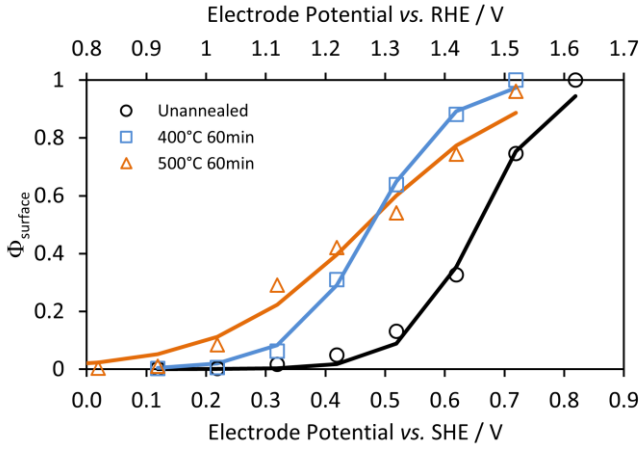


Figure 3-6. Effects of electrode potential and annealing temperature on interfacial charge transfer efficiencies (symbols) and fitted exponential functions (lines, equation (2-6)) for Ti|Sn^{IV}-doped α-Fe_2O_3 | 1 mol dm^{-3} NaOH.

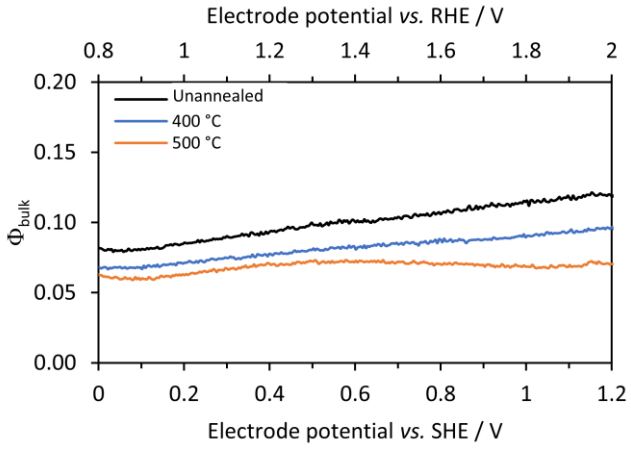


Figure 3-7. Calculated bulk recombination for Ti|Sn^{IV}-doped α-Fe_2O_3 samples annealed at different temperatures. 1 mol dm^{-3} NaOH + 0.5 mol dm^{-3} H_2O_2 electrolyte and irradiation of 3 000 W m^{-2} by a Xe arc lamp were used.

Electron-hole recombination rates in bulk Sn^{IV}-doped α-Fe_2O_3 were derived using equation (3-8) and the charge transfer efficiency (Φ_{bulk}) plotted in Figure 3-7 as a function of the applied potential. As expected, Φ_{bulk} was not as dependent on the potential as $\Phi_{surface}$. The slight increase could have been due to a residual surface recombination at lower potentials. In order to estimate a constant and potential independent $\Phi_{surface}$ for each sample, an average value was calculated in the range between 1.4 and 2 V *vs.* RHE. Φ_{bulk} can also be estimated from the photo-response in the absence of a hole scavenger (1 mol dm^{-3} NaOH), but after correction for surface recombination, i.e. dividing by $\Phi_{surface}$. Similar values were found with this approach; data from the two methods are compared in the Appendix (Figure S3-7 and Table S3-7).

3.4.2 1D Model

A summary of all measured parameters input into the model and the techniques used for their determination is presented in the Appendix, Table S3-3 and S3-4.

Photocurrent prediction.

Figure 3-8 shows the effect of electrode potential on predicted photocurrent densities for different versions of the Gärtner–Butler equation: (3-2), (3-4) and (3-6). The maximum achievable photocurrent densities are limited significantly by absorbed photon fluxes, as expected. After correction for surface and bulk electron-hole recombination rates, *j-E* data exhibited behaviour typical of hematite photo-anodes. Predicted dark current densities were very low for potentials < 1.6 V *vs.* RHE, in agreement with experimental data shown in Figure 3-4.

Figure 3-9 shows good agreement between predicted and experimental current densities (photo + dark), with regression analysis giving R^2 values of 0.987, 0.994 and 0.935 for Ti|Sn^{IV}-doped α-Fe_2O_3 samples unannealed and annealed at 400 and 500 °C, respectively. All properties values input to the model were obtained from independent experimental measurements. Surface recombination [146], absorbed photon flux [46] and flat band potential [148] were obtained using well documented methodologies. However, charge carrier concentration values estimated from Mott-Schottky analysis can vary by several orders of magnitude from sample to sample, especially when the semiconductor surface is contaminated and nanostructured. The estimation of bulk recombination rates from measurements in the presence of a hole scavenger, supressing surface recombination, has a known origin as discussed previously in the theoretical treatment section, but still lacks a complete fundamental explanation. For modelling purposes and assuming these properties do not change drastically with the size of the electrode, predicted photocurrent densities can be used to predict the behaviour of up-scaled reactors using photo-electrochemical results obtained at small scale. In practice, larger solar simulators may produce photon flux inhomogeneities.

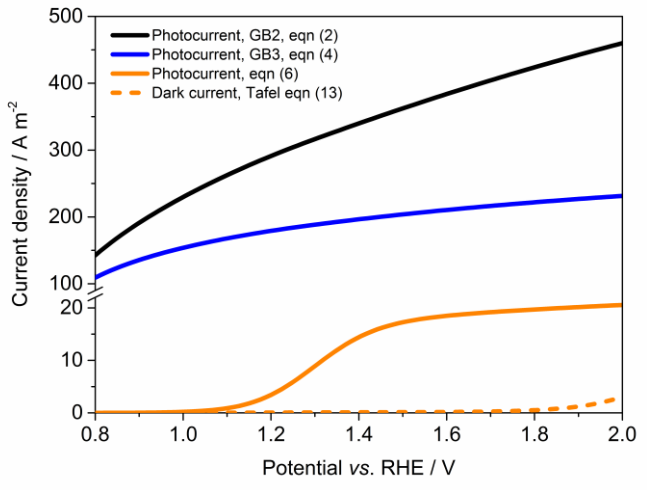


Figure 3-8. Predicted photocurrent densities according to the Gärtner–Butler equation, after correction for photon absorption, equation (3-2); photon flux limitation, equation (3-4); and surface and bulk recombination, equation (3-6). Ti|Sn^{IV}-doped α-Fe_2O_3 annealed at 400 °C, 1 mol dm^{-3} NaOH electrolyte and 3 000 W m^{-2} irradiation by Xe arc lamp.

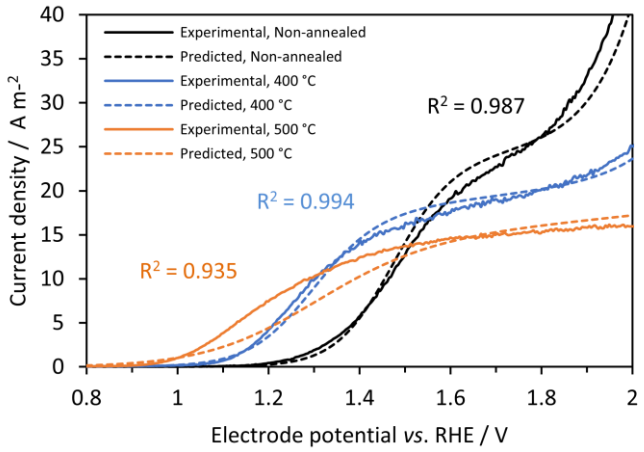


Figure 3-9. Effect of electrode potential and annealing temperature on predicted (dashed) and experimental (continuous) current densities (photo + dark currents) for Ti|Sn^{IV}-doped α-Fe_2O_3 | 1 mol dm^{-3} NaOH electrolyte solution. 3 000 W m^{-2} irradiation by Xe arc lamp.

The difference between predicted photocurrent densities and experimental results can be associated to several causes: (*i*) uncertainties in the measurement of photo-anode properties. Difficulties in the fitting of the impedance spectra might alter the estimated interfacial electron-hole recombination; this seems to be the main reason of disagreement between predicted and experimental values for the sample annealed at 500 °C. The higher the recombination rate, the easier to discriminate it from the charge transfer rate. This would also explain why the predictions for the other samples were more accurate. (*ii*) Irradiated photo flux can be affected by small changes in the position of the cell, and decrease of intensity with time due to degradation of the lamp. (*iii*) Dark current densities, predominant only at higher current densities, were dependent on the electro-active area of the electrode, which could also vary from sample to sample

Hydrogen yield predictions in membrane-less configurations

Hydrogen yields, charge yields and collection efficiencies were predicted for all samples in a 1D membrane-less model. Experimental data for comparison with these predictions are not available, since anode and cathode were immersed in the same electrolyte with no gas separation and the bench-scale cell for photo-electrochemical characterisation was not gas tight. Figure 3-10 shows that there was a potential for each sample at which efficiencies started to increase towards unity. These potentials correspond to the current density ($j_{\text{total}} \approx 0.04\ \text{A m}^{-2}$ for conditions used) at which bubble generation rates became significant at the surface ($f_G > 0.01$) and desorption of gas due to the saturation near the electrode started to contribute to the hydrogen flux density, as shown in Figure S3-8 in the Appendix. With increasing photo-anode potential, all efficiency values approached unity asymptotically. Hence, the contribution of bubble generation and desorption rates should be considered when operating at low current densities. However, once a certain photocurrent density threshold is reached, depending on the geometry and photo-electrode properties, the effects of potential on the charge yields and collection efficiencies are minimal. Also, it is noteworthy that the collection efficiency estimated for a membrane-less reactor was estimated assuming that oxygen and hydrogen are separated effectively in a subsequent process and that the explosion limit of > 4 vol% O_2 in H_2 is not exceeded [115].

Hydrogen fluxes followed a similar pattern, as shown in Figure 3-11, which plots fluxes against both current densities (bottom *x*-axis) and electrode potential (upper *x*-axis). As expected, the dependence of hydrogen fluxes on current density were independent of the photo-anode, the properties of which determined its current density-potential relationship, so hydrogen fluxes were ultimately highly dependent on the potential. At current densities < 0.04 A m^{-2}, bubble generation and desorption rates were predicted not to contribute to hydrogen fluxes, as most of the hydrogen was notionally oxidised at the anode, resulting in hydrogen fluxes close to zero.

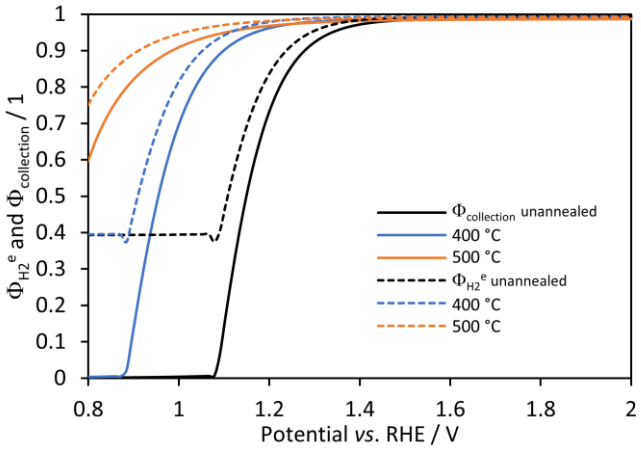


Figure 3-10. Effect of (Ti|Sn^{IV}-doped α-Fe_2O_3 | 1 mol dm^{-3} NaOH) photo-anode potential on predicted charge yields (dashed) and collection efficiencies (continuous) for hydrogen evolution on Ti|Pt.

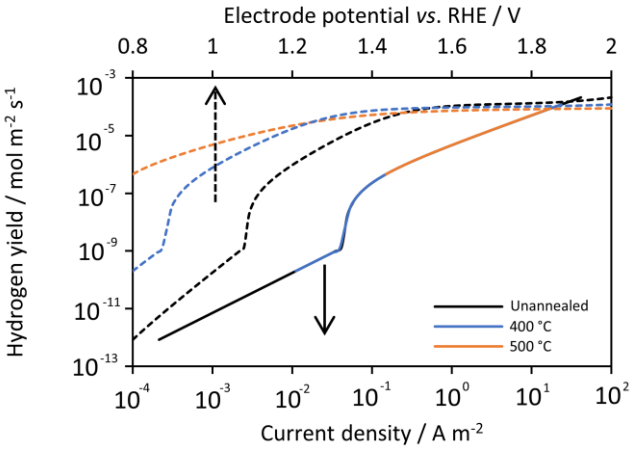


Figure 3-11. Predicted effects on hydrogen fluxes of cathode current density (continuous), photo-anode potentials (dashed) and annealing temperature for Ti|Sn^{IV}-doped α-Fe_2O_3 | 1 mol dm^{-3} NaOH.

Hydrogen yield predictions using a membrane.

Charge yields and collection efficiencies for hydrogen evolution were estimated modelling a Nafion® membrane (330 μm) positioned between the electrodes. As shown in Figure 3-12, charge yields were higher and almost unity at any given potential for all samples. This demonstrates the utility of using a membrane or micro-porous separator to separate gases when operating at low current densities.

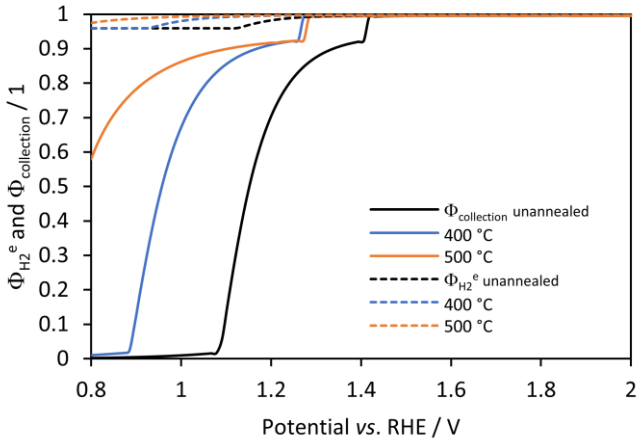


Figure 3-12. Predicted effects of electrode potential charge yields (dashed) and collection efficiencies (continuous) as a function of potential for hydrogen evolution on Ti|Pt when using a photo-anode Ti|Sn^{IV}-doped α-Fe_2O_3 | 1 mol dm^{-3} NaOH and separated by Nafion® membrane.

On the other hand, collection efficiencies were predicted to be lower when compared to the membrane-less model, because predicted hydrogen fluxes came only from the catholyte, which was then only half of the electrolyte volume. However, the use of a membrane or micro-porous separator is more practical, as it obviates the need of further gas separation and circumvents safety issues related to hydrogen and oxygen gas mixtures [115]. The discontinuities in collection efficiencies at ca. 1.3 and 1.4 V was due to gas saturation of the membrane, in which transport of hydrogen and oxygen occurs by diffusion only. Hydrogen

fluxes were predicted to be slightly greater for a membrane reactor, i.e. shifted to lower current densities, but followed a similar behaviour to that shown in Figure 3-11 for a membrane-less model. In this case, the tipping point of current density for gas evolution at the cathode and desorption rate was 0.025 A m^{-2}. Hydrogen fluxes at greater current densities were the same as predicted in a membrane-less model. This means that once the current setup is operating at current densities at which gas is evolving via bubbles or desorption for saturated electrolytes, then a membrane or microporous separator is needed only to separate the products and prevent H_2-O_2 explosions, but otherwise is predicted not to affect the reactor performance significantly. As proposed by others [119, 122], instead of using membranes, a material with pores smaller than the Sauter diameter of bubbles, usually between 50 [198, 199] and 450 μm [185], may be sufficient to separate H_2 and O_2 gases. However, this will depend heavily on the (*i*) thickness of the microporous separator; (*ii*) the superficial and morphological properties of the electrodes and its effect on the size and life time of the adhered bubbles; (*iii*) the flow rate of the electrolyte, which affects the flow regime and physical separation of the products, which in turn is also affected by the distance and characteristic length of the electrodes.

3.4.3 2D Model

A simple monolithic photo-electrode was modelled in order to confirm the importance of geometrical optimisation. A membrane was absent for this case. The current density distribution and hydrogen fluxes of a hypothetical enhanced photo-anode material and a platinized cathode were predicted. The properties of this hypothetical photo-anode are described in the Appendix, Table S3-8. Surface and bulk recombination were minimized; its band gap was deceased to 1.7 eV, so that the wavelength corresponding to the photon absorption edge was increased to 729 nm. Photon fluxes were taken from the solar AM1.5D spectrum. A membrane was not included in the model, but hydrogen fluxes were integrated only over the 1 mol dm^{-3} NaOH catholyte. The electrolyte volume (projected as 2D) was proportional to the electrode length on both dimensions.

Figure 3-13 shows the resulting current density distribution for 1 V *vs.* RHE electrical bias as a function of the relative distance to the edge of the electrode. A significant decrease of local current densities (mostly photocurrent densities at this potential) was predicted along the photo-electrode, especially for electrodes with characteristic lengths > 0.02 m. These results are not as severe as the reported current distributions for neutral pH [115]. After integration of current densities on the anode and hydrogen fluxes in the catholyte, collection efficiencies and charge yields were also predicted, as shown in Figure 3-14. Total current densities (normalized by the length of the electrode) were greater for shorter electrodes, as implied by the current density distributions shown in Figure 3-13. However, hydrogen fluxes were smaller for shorter electrodes and reached a maximum at ca. 0.01 m, with a subsequent decrease for longer electrodes. A similar behaviour was predicted in ASTH

efficiencies as a function of length. This means that due to H_2-O_2 cross-over losses and current density distributions, there is an optimized length at which photo-electrodes should be fabricated. Charge yields and collection efficiencies are also reported in Figure 3-14.

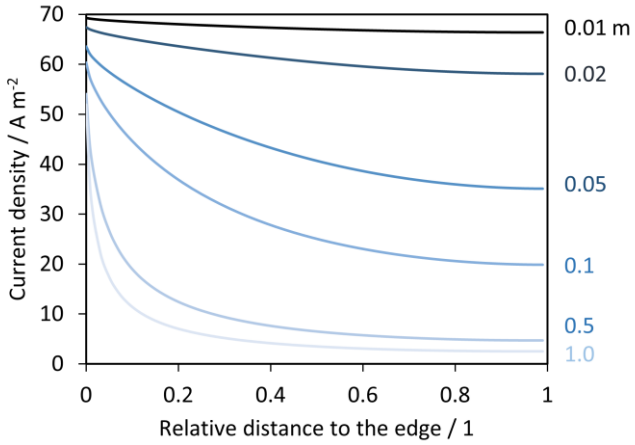


Figure 3-13. Current density distributions over the length of a hypothetical enhanced photo-anode operating at 1 V *vs.* RHE in 1 mol dm^{-3} NaOH and without a membrane. Distances are relative to the total length of the electrode varied between 0.01 and 1 m, and the edge at relative distance 0.

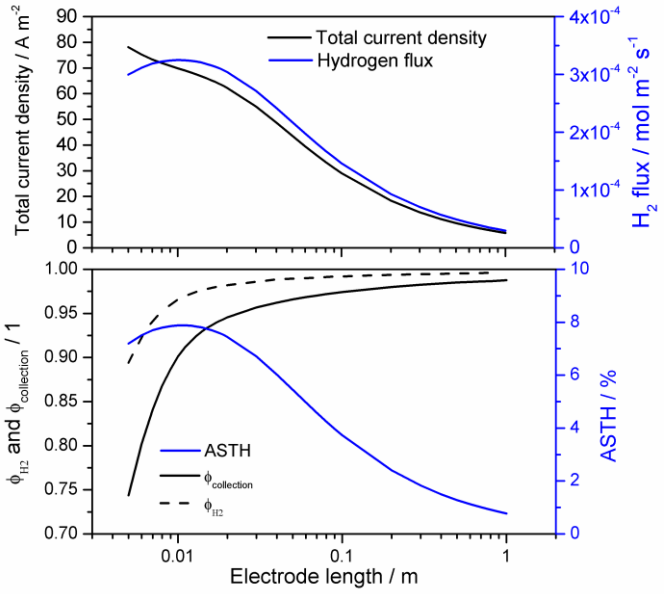


Figure 3-14. Current density and hydrogen flux (top); charge yields, collection and ASTH efficiencies (bottom) as a function of the electrode length for 'enhanced' photo-anode operating at 1 V *vs.* RHE in 1 mol dm^{-3} NaOH and without a membrane.

As expected for electrodes shorter than 0.03 m, the cross-over losses and reduction of oxygen at the cathode, causing loss of charge yields, were significant. For longer electrodes, both efficiency values approached unity asymptotically. Electrochemical reduction of oxygen at the cathode occurred close to the cathode edge, at which overpotentials were highest, decreasing towards the centre. Hence, longer cathodes will have less area at which oxygen reduction occurs, so increasing average charge yields and gas collection efficiencies. The

consequences of current density distributions and cross-over losses for ASTH efficiencies and hydrogen flux data in Figure 3-14 emphasise the importance of geometrical optimisation.

Given a set of electrode arrangements and having characterised materials with a set of methodologies proposed here, it is possible to use this model to define optimized conditions to achieve the highest ASTH and hydrogen fluxes. More detailed results and comparisons with other efficiency definitions (ABPE and AB-STH) can be found in the Appendix, Figure S3-10.

For the case presented above, product-gas cross-over, i.e. H_2 flux in the anolyte and O_2 in the catholyte, was not as severe as reported by Jin [115]. For small electrodes (< 0.01 m), product-gas cross-overs were ca. 2% to 10% molar for oxygen and hydrogen in the catholyte and anolyte, respectively. This still represents a safety issue and increased risk associated with ignition of stored products [115, 122]. For electrodes longer than 0.1 m, the predicted product-gas cross-over was $< 2\%$ in both cases. If a membrane is used, the amount of hydrogen collected in the anolyte reached zero values, as predicted by the 1D model, due to the low fluxes of hydrogen and oxygen crossing between anolyte and catholyte are effectively anodically oxidised and cathodically reduced, respectively.

3.5 Conclusions

A model for photo-electrochemical reactors was developed to describe the behaviour of Sn^{IV}-doped α-Fe_2O_3 photo-anodes deposited on titanium and annealed in air at different temperatures. Photo-anodes were characterised in terms of photon absorption, electron-hole recombination rates in the bulk semiconductor and at the semiconductor | electrolyte interface, and other electrochemical parameters obtained experimentally. Charge carrier concentration and bulk recombination rates were found to require special care and theoretical treatment for their estimations. Predicted values showed good agreement with experimental data. For the first time, bubble formation rates at the electrodes and in the bulk of electrolyte solution for supersaturated conditions, were predicted as a function of current density; hence, reactor performance did not increase drastically by including a membrane or microporous separator when operating at current densities $> 0.04\,\mathrm{A\,m^{-2}}$. This critical current density depended mainly on the geometry and properties of the photo-anode. Charge yields for hydrogen formation reached unity when the photo-anode was operating at a sufficiently high potential and when the reactor incorporated a membrane separator. In addition, product collection efficiencies and current density distributions were predicted successfully for a hypothetical photo-anode with 'enhanced' behaviour and are decisive parameters for further geometrical optimisation of the electrodes. The electrolyte flow, light scattering and reflection due to bubbles and other optical phenomena, pH and temperature changes were not included in the present model, which will be extended to include them, based on the works of Singh [117], Haussener [131] and Holmes-Gentle [118].

Chapter 4

Model of PER systems: up-scaled validation and geometrical optimisation[3]

4.1 Introduction

Research on photo-electrochemical reactors for hydrogen production has been focused mainly on material property developments [44, 200]. Engineering challenges have not been addressed widely, due to the lack of suitable up-scaled reactors for material assessment. For these reasons, testing of highly efficient materials [85, 201, 202] and modelling of photo-electrochemical cells [30, 115] are done usually with electrodes of active area ≤ 1 cm^2. Only recently, there has been interest in modelling and experimental characterisation of up-scaled devices [47, 170, 203]. However, there is still an on-going discussion about which internal arrangements should be implemented for up-scaled photo-electrochemical reactors. It has been suggested that large-scale monolithic photo-absorbers are not practical and electrode dimensions should be fabricated at a scale of $10^{-3} - 10^{-2}$ m [204]. A summary of existing models was discussed in Chapter 3. Recent developments in modelling photo-electrochemical reactors have been reported by Haussener [36, 130, 131], Lewis [115-117], Newman [119, 120, 177] and Kelsall [47, 65, 143]. However, each team has focused on different aspects and configurations. For example, Haussener et al., has reported mainly on integrated systems using photo-absorbers and the effects of temperature and concentrated light. Lewis's publications have been focused on devices operating with neutral solutions and product cross-over issues, while Newman's models have been implemented in 1D and 2D geometries. Kelsall et al. have predicted current density distributions and geometrical optimisation with experimental validation using an up-scaled reactor. Following the description of the model in 1D and 2D geometries reported in Chapter 3, an experimental validation in 3D using 0.1×0.1 m^2 hematite photo-anodes is reported below. Subsequently, simulation-based geometrical optimisation of different configurations in the absence and presence of a membrane was carried out. The model can be used to design composite

[3] This chapter was adapted from: F. Bedoya-Lora, A. Hankin, G.H. Kelsall, *En route* to a unified model for photo-electrochemical reactor optimisation. II - Up-scaled validation and geometrical optimisation, submitted.

photo-electrodes, fabricated at μm scale and optimised geometrically for a given set of conditions and photo-electrode properties.

4.2 Theoretical description of reactor in 3D

4.2.1 Geometrical definitions

All fluxes and current densities were normalized by the geometrical area of the photo-anode. A 3D model was developed using the dimensions of an up-scaled reactor to predict photocurrent densities and hydrogen fluxes, enabling comparison with values determined experimentally. A planar photo-anode with dimensions 0.1×0.1 m^2 was exposed to illumination with (photo-electro-) active surface facing away from the cathode, as shown in Figure 4-1. Hydrogen and oxygen gases were collected in two chambers separated by a cation-permeable Nafion® membrane.

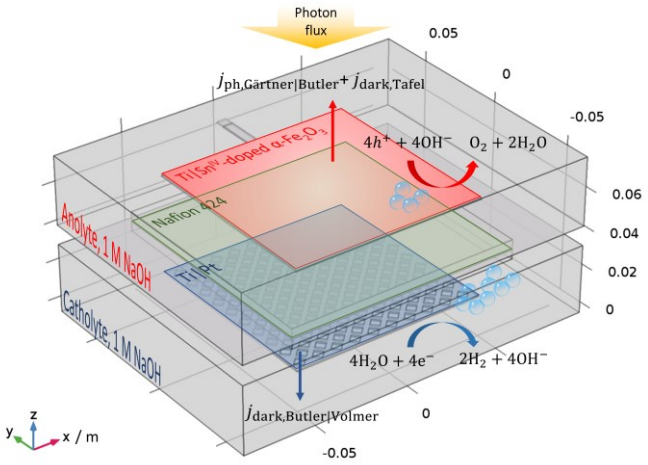


Figure 4-1. Schematic view of the up-scaled photo-electrochemical reactor for model validation.

A symmetrical 3D model was developed to perform the geometrical optimisation with the aim of reducing losses due to ohmic potential drops and cross-over of O_2 and H_2 products. Perforations were introduced in the planar photo-anode structure; square and hexagonal perforation distribution were considered as shown in Figure 3-1. The ratio between the separation and size of the perforation, l_d/l_p, was optimised for several perforation sizes, l_p, and electrode thicknesses, l_e. As mentioned previously, to enable fair comparison between the performance of different configurations, all the fluxes and currents densities were referred to the geometrical area (including perforated area) and not only the electro-active area, as shown in Figure 3-1(a). Furthermore, two electrodes arrangements were studied as shown in Figure 3-1(b) and (c): spatially separated electrodes ('wired') with the photo-anode facing away from the cathode and a monolithic photo-bipole ('wireless') [120]. The distance between electrodes for the wired configuration, l_{a-c}, was kept constant at 0.01 m.

4.2.2 Target definitions

As defined in Chapter 3, systems were assessed in terms of four parameters: current densities (j), hydrogen fluxes (N_i), charge yields (Φ_i^e) and collection efficiencies ($\Phi_{\text{collection},i}$).

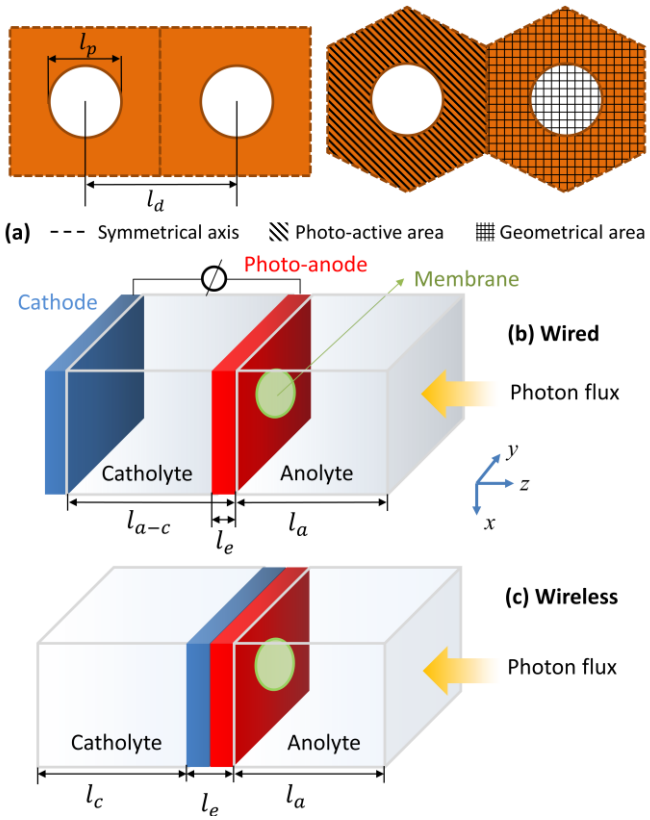


Figure 4-2. (a) Square and hexagonal distribution of perforations in the photo-anode, and definitions of lengths and areas of interest. Arrangement of electrodes for geometrical optimisation; (b) photo-anode facing away from cathode ('wired') and (c) monolithic photo-bipole with a single photo-anode ('wireless').

$$N_i = N_{G,i} + N_{\text{desorption},i} \tag{4-1}$$

$$\Phi_i^e = \frac{j_i}{j_{\text{total}}} \tag{4-2}$$

$$\Phi_{\text{collection},i} = \frac{N_i}{j_{\text{total}}/\nu_{e.i}F} \tag{4-3}$$

4.3 Experimental

4.3.1 Photo-anode fabrication

0.1×0.1 m^2 Sn^{IV}-doped α-Fe_2O_3 photo-anodes were deposited on titanium via spray pyrolysis following the procedure reported previously and described in Chapter 1, page 59 [89]. The electrodes were produced on planar and perforated Ti sheets with perforations of

ca. 3 mm × 1.5 mm, spaced 5.8 mm horizontally and 2 mm vertically apart. In this study, photo-anodes were not annealed after the deposition of hematite films.

4.3.2 Photo-electrochemical reactor

Photo-electrochemical measurements were carried out in a photo-electrochemical reactor designed for operation with 0.1 × 0.1 m^2 electrodes. The reactor comprised two chambers, each with a volume of ca. 1 dm^3 and separated by a cation-permeable membrane (PTFE-reinforced Nafion® 424, DuPont Inc.), selected for its chemical stability, durability and superior mechanical properties over an anion-permeable counterpart, which otherwise would have been more appropriate for alkaline water splitting. Both compartments were filled with 1 mol dm^{-3} NaOH (pH 13.6). A potentiostat/galvanostat (Autolab PGSTAT 30) was used to control the reactor with a three-electrode configuration for voltammetry on the photo-anode at 50 mV s^{-1}, and two-electrode configuration for chronoamperometry at an applied cell potential difference of 1.6 V (resulting in a photo-anode potential of ca. 1.51 V *vs.* RHE) for 24 hours. Hematite photo-anodes acted as working electrodes, platinised titanium mesh (Expanded Metal Company, UK) as counter electrode and saturated AgCl|Ag as reference electrode (1.001 V *vs.* RHE and 0.197 V *vs.* SHE). The reactor was operated in batch mode without recirculation of electrolyte solution, the hydrodynamic effects of which have yet to be implemented in the model.

A solar simulator (Sun 2000, Abet technologies, USA) with a 550 W Xe arc lamp was used to irradiate the photo-anode. The light source was calibrated and mapped at the reactor working distance using a UV-Vis spectrophotometer coupled to a CR2 cosine receptor (Black-Comet CXR-25, StellarNet, USA). An average power intensity of 433 ± 82 W m^{-2} was achieved over an area of 0.12 × 0.12 m^2 and an estimated 497±12 W m^{-2} over 0.1 × 0.1 m^2, which corresponds to the photo-anode area, as shown in Figure S4-1 and S4-2 in the Appendix. A degree of non-uniformity in the spatial distribution of the irradiance was evident. The intensity of incoming light was corrected for attenuation by electrolyte and quartz to give an effective power intensity of 461 W m^{-2} over the photo-anode surface.

Photo-electrochemical properties of unannealed Ti|Sn^{IV}-doped α-Fe_2O_3 were measured previously using a photo-electrochemical cell (0.06 dm^3) and an exposed area of 3 × 6 mm^2, as described in Chapter 1, page 61. Results were reported in Chapter 1, page 65 and Chapter 3, page 90, these parameters evaluated experimentally were also employed in this study and corrected for any changes in the power density delivered by the light source and temperature increase, this will be expanded in the next section.

Voltammograms in the present study were performed within a period that was sufficiently short for electrolyte temperatures to remain constant at 25 °C. Prolonged illumination caused electrolyte temperatures to rise to ca. 40 °C within the first 6 hours, after which thermal equilibrium with surroundings was achieved, as shown in Figure S4-4 in the Appendix. Hence, chronoamperometry results are not shown for this initial 6-hour

period. Gas flow rates for cathode (hydrogen) and anode (oxygen) compartments were recorded during long term (24 hours) chronoamperometry with gas flow meters (MilliGascounter MGC-1, Ritter, Germany); molar fluxes were corrected by the steady state temperature assuming ideal gas behaviour.

4.3.3 Numerical considerations

Comsol Multiphysics 5.2a with a Batteries and Fuel Cells module was used to solve the system using the finite element method as described in Chapter 3, page 90.

For this study, the mesh of the 3D up-scaled reactor was geometry-dependent with a minimum element size of 3.33×10^{-3} m and maximum size of 0.02 m. The mesh was optimised for higher resolutions in narrow regions. The model converged typically in under 3 minutes for a given set of conditions. In the case of symmetrical models for geometrical optimisation, a minimum element size of 8×10^{-7} m and maximum size of 8×10^{-4} m was used. The model converged usually in under 10 seconds. A parametric sweep was used to evaluate a wide range of settings and geometries.

4.4 Preliminary considerations

4.4.1 Effects of temperature on the performance of the cell

Efficiency of bubble formation for hydrogen, f_{G,H_2}, does not depend significantly on the temperature, whereas oxygen bubble formation increase rapidly with temperature [126]. However, those results did not include a proper correlation for higher temperatures, but the data reported for 1000 A m^{-2} and 40 °C showed that f_{G,O_2} was double the efficiency measured at 25 °C. Given the lack of specific data for oxygen bubble evolution at higher temperature, it was assumed that during chronoamperometric operation at thermal equilibrium (at ca. 40 °C), f_{G,O_2} is approximately double that calculated at 25 °C in Chapter 3. Coefficients for hydrogen gas evolution remained unchanged. Diffusion coefficients were corrected for higher temperatures using the Stokes-Einstein equation:

$$\frac{D_1}{D_2} = \frac{T_1}{T_2}\frac{\mu_2}{\mu_1} \tag{4-4}$$

Concentrations of dissolved oxygen and hydrogen at saturation were interpolated from published experimental data for KOH solutions at different temperatures and concentrations [205]. Values estimated at 25 °C using these experimental data were remarkably similar to more recent values determined for this temperature [126, 206, 207], so it was assumed that interpolations at 40 °C and 1 mol dm^{-3} KOH were sufficiently reliable to be used in the model. In contrast with oxygen, it was found that hydrogen solubility decreased only slightly with temperature, offering an explanation of why f_{G,H_2} did not increase significantly with temperature, while f_{G,O_2} was double at 40 °C [126]. Furthermore, this is in agreement with Vogt's model, in which the saturation concentration plays an important role in the efficiency

of gas evolution [127]. Due to changes in diffusion coefficients and kinematic viscosity of water with temperature, volumetric mass transfer coefficients, $k_L a$, were recalculated as a function of these parameters. A numerical description of these corrections can be found in the Appendix, Table S4-1 to S4-3 [129, 184-188, 190].

The effects of the change in temperature, from 25 to 40 °C, on the properties of the semiconductor (Sn^{IV}-doped hematite) were considered too small to merit consideration, as it was confirmed experimentally in an independent study by Ms. Faye Alhersh in the Department of Chemical Engineering at Imperial College London (unpublished work) for the same Sn^{IV}-doped α-Fe_2O_3 photo-anodes used in this thesis. This is opposite to the findings by Dias et al. for Si-doped α-Fe_2O_3 photo-anodes [58], which reported 33% and 83% higher photocurrent densities when the photo-anode temperature was increased from 25 to 45 and 65 °C, respectively. However, the latter study associated the increase in photocurrent densities with a decrease of the semiconductor's bandgap, which would result in a highly unlikely band gap of hematite of 2.0 and 1.75 eV at 45 and 65 °C, respectively. The effect of temperature on membrane properties were disregarded due to the lack of data available for 40 °C under the conditions and materials assessed in this work.

4.4.2 Photon flux distribution of solar simulator

As discussed and demonstrated earlier, the photon flux delivered by the solar simulator was not radially uniform across the photo-anode surface. This non-uniformity was a potential concern as it can cause a significant distribution in overpotentials and photocurrents across a 0.1 × 0.1 m^2 electrode. The photon flux was evaluated as a function of position on the photo-anode surface, $I_0 = f(x, y)$, Figure S4-5 in the Appendix. Measurements were corrected for attenuation by electrolyte and the quartz window, and were fitted by regression analysis into a spatially rotated exponential function that was subsequently fed into the Comsol Multiphysics model:

$$I_0 = D_1 + D_2 \exp\left[-\left(x\cos\frac{\pi}{4} - y\sin\frac{\pi}{4}\right)^2\right] + D_3 \exp\left[-\left(x\sin\frac{\pi}{4} + y\cos\frac{\pi}{4}\right)^2\right] \quad (4\text{-}5)$$

I_0, $I_0 - I_x$ and $(I_0 - I_x)\alpha$ functions were fed into the model and used to estimate the spatial distribution of photons absorbed locally by the photo-anode. A more detailed numerical description of these functions can be found in the Appendix, Table S4-4 and Figure S4-5.

4.5 Results and discussion

4.5.1 3D reactor model validation

Figure 4-3 shows that voltammograms of a planar 0.1 × 0.1 m^2 Ti|Sn^{IV}-doped α-Fe_2O_3 | 1 mol dm^{-3} NaOH photo-anode at 25 °C in the reactor exhibited acceptable agreement with predicted photo-responses. Note that the small 3 × 6 mm^2 electrodes used for

characterisation in Chapter 3 were synthesized separately from the scaled 0.1 × 0.1 m^2 electrodes. Hence, the quality of the agreement between model predictions and experimental data in Figure 4-3 also includes potential effects of human and instrumental errors in the preparation of precursor solution and control during deposition.

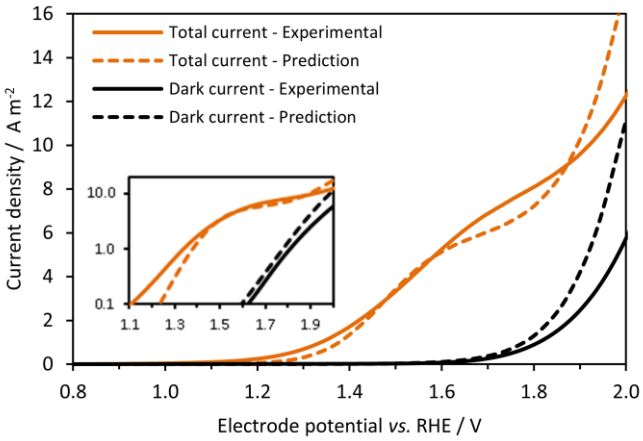


Figure 4-3. Photo-response of planar unannealed Ti|Sn^{IV}-doped α-Fe_2O_3 | 1 mol dm^{-3} NaOH and predicted behaviour using a solar simulator, 497 W m^{-2}. Inset with logarithmic *y*-axis.

The predictions were within the error of measurement as confirmed in an earlier version of the model [65]. The discrepancy of photocurrent at higher potentials (1.6 – 1.8 V *vs.* RHE) could have been associated with non-uniform deposition and temperature during the spray pyrolysis of hematite on the substrate. This might affect the catalytic properties at the surface, thickness and morphology of the samples. As shown in the inset of Figure 4-3, the divergence of predicted and measured dark currents at photo-anode potentials > 1.8 *vs.* RHE was probably due to deviation from Tafel-type behaviour caused by the onset of bubble formation. Coverage of photo-anodes by bubbles was expected to decrease current densities by ca. 0.2 (1 – 10 A m^{-2}) [208], exacerbated by decreased electrolyte solution conductivities due to bubble accumulation close to the photo-anode, especially with increasing electrode height.

Hydrogen and oxygen fluxes were measured and estimated after operating the reactor at 1.6 V cell potential difference, which corresponds to ca. 1.51 V *vs.* RHE at the anode. During the first 6 hours, oxygen and hydrogen fluxes were not stable and produced non-stoichiometric yields due to a combination of heating of the system and gradual saturation of catholyte and anolyte with gases. Reactor performance was relatively stable after 10 hours of operation. As shown in Figure 4-4, predicted current densities and flux of hydrogen and oxygen agreed with experimental data after 10 hours of photo-electrolysis. Figure 4-5 shows the molar ratio between evolving gases, H_2:O_2. It oscillated between 2.3 and 2.0, suggesting the generation of hydrogen and oxygen took place; values of H_2:O_2 above and below 2.0 may have been caused by oxygen leaking from the anolyte, due to imperfect sealing around the membrane and quartz window, and lower precision of the gas flow meters in measuring slower rates of oxygen evolution compared to hydrogen evolution. Charge yields for the

planar electrode were ca. 0.9 and 0.8 for hydrogen and oxygen evolution, respectively. In the case of the perforated photo-anode, charge yields oscillated between 0.9 and 1.0 for both oxygen and hydrogen. However, the expected charge yields values according to the model should have been close to unity (0.99). Again, the deviation of experimental data from model predictions was probably associated with non-steady state operation and leaking of gases during prolonged experiments. However, the agreement of the model with experimental results was still remarkable.

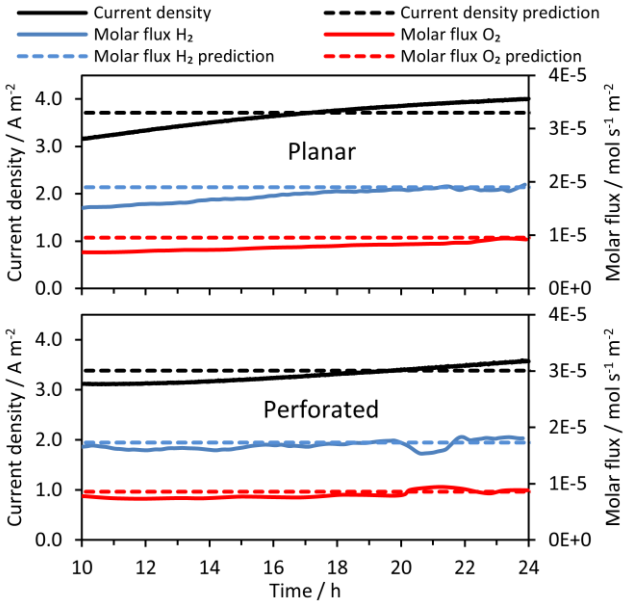


Figure 4-4. Average photocurrent density, hydrogen and oxygen molar fluxes evaluated during chronoamperometric operation at a cell potential difference of 1.6 V for 0.1 × 0.1 m² Ti|Sn^{IV}-doped α-Fe_2O_3 (planar and perforated) | 1 mol dm^{-3} NaOH irradiated with 497 W m^{-2} from a solar simulator. Dashed lines are model predicted values.

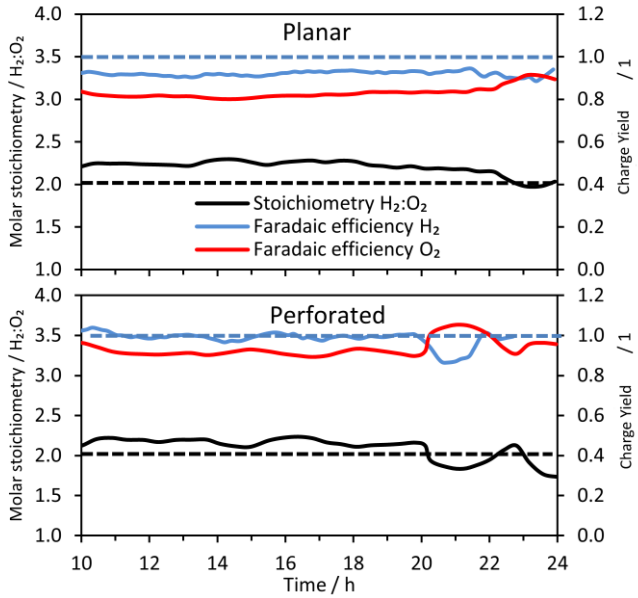


Figure 4-5. Molar stoichiometry for H_2:O_2 and (y2) estimated charge yields for hydrogen and oxygen fluxes evaluated during chronoamperometric operation at a cell potential difference of 1.6 V for 0.1 × 0.1 m² Ti|Sn^{IV}-doped α-Fe_2O_3 (planar and perforated) | 1 mol dm^{-3} NaOH using a solar simulator and a power density of 497 W m^{-2}. Dashed lines represent predicted values.

Figure 4-6 shows the distribution of current densities at the planar photo-anode and cathode surface. Current densities at the centre of the photo-anode were higher than at the edges due to the non-uniform illumination. However, the overpotential follows the opposite trend and is higher at the edges of the electrode. Distributions of current densities were not as pronounced due to the low photocurrent densities reported for hematite. More heterogeneous distributions are expected for enhanced photo-electrodes as discussed in Chapter 3.

According to the model, steady state oxygen concentrations reached supersaturation in the anolyte chamber in the vicinity of the photo-anode surface. Analogous behaviour was predicted for hydrogen in the catholyte. Consequently, the diffusive flux of dissolved gases through the compartments was small and was minimised effectively when a membrane was present, as shown in Figure S4-6 and Figure S4-7 in the Appendix). This also means that significant desorption rates were present only near the surface of the electrodes (< 10 mm). Although small fluxes of dissolved gas were established through the membrane, their magnitude even in absence of membrane was not sufficient to affect model predictions, which computed an O_2 and H_2 collection efficiency of ca. 0.99. In contrast, experimentally determined values of 0.8 suggested potential leakage of gases through the membrane reactor seals.

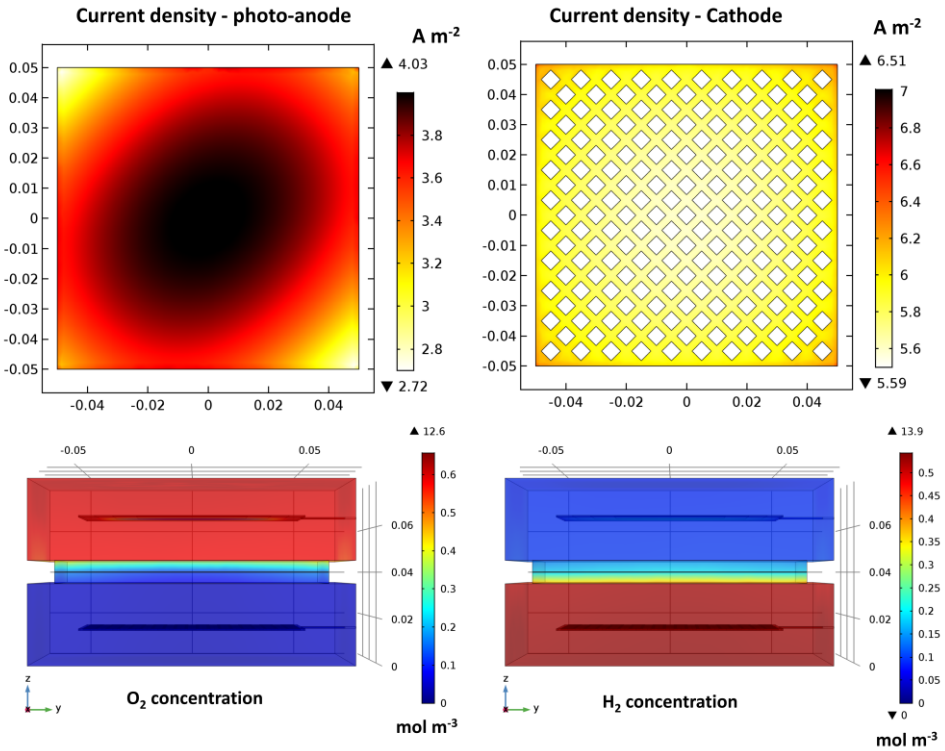


Figure 4-6. Current density distribution at Ti|Sn^{IV}-doped α-Fe_2O_3 | 1 mol dm^{-3} NaOH photo-anode at 1.51 V *vs.* RHE with cathode (Ti | Pt | 1 mol dm^{-3} NaOH), and steady state spatial distributions of oxygen and hydrogen concentrations for up-scaled reactor operating at 40 °C.

4.5.2 3D (symmetrical) model optimisation

An unannealed Ti|Sn^{IV}-doped α-Fe_2O_3 photo-anode in 1 mol dm^{-3} NaOH at 25 °C and a potential of 1.51 V *vs.* RHE was modelled under illumination by 1.5AM light; see properties in the Appendix, Table S4-5, S4-7 and S4-8 [126, 129, 184, 185, 191-196, 209]. A planar Ti|Pt cathode was used in 1 mol dm^{-3} NaOH electrolyte solution. Nafion® was used in some cases as membrane and for filling the perforations in the photo-anode to its thickness, which was assumed initially as 500 μm. This model was used to determine an optimum value for the ratio between perforation size/distance, l_d/l_p, in terms of current density and hydrogen flux. Similar to the results reported in Chapter 3, the optimum for hydrogen flux was affected by the collection efficiency, which was lower for shorter photo-anodes and reached almost unity when the distance (l_d) was increased between perforations. On the other hand, inhomogeneous current density distributions were exacerbated for higher values of l_d/l_p. Furthermore, the net current density was also affected by the inactive area due to perforations, so for very low values of l_d/l_p, low current densities and hence low rates of hydrogen evolution were achieved.

Hexagonal *vs.* square perforation distributions

The effects of spatial distributions of perforations on current densities and hydrogen fluxes for a 'wired' reactor configuration without membrane filling the perforations are presented in the Appendix, Figure S4-8. There was no difference between squared and hexagonal distributions, when current densities and hydrogen fluxes were plotted as functions of the ratio between the active and geometrical area. When plotted as a function of l_d/l_p, there was a noticeable shift towards higher values of current densities and hydrogen fluxes for the hexagonal geometry. However, the optimum value was very similar for both geometries, with small changes in a range of $l_d/l_p = 5.0 \pm 1$ for maximum current density and $l_d/l_p = 6.5 \pm 2$ for maximum hydrogen fluxes. Evidently, using current densities as target for optimisation is incorrect, since higher current densities do not translate into higher collection efficiencies, particularly in the absence of a membrane.

For $l_p < 50$ μm, there was no significant increase in the resulting current densities and hydrogen fluxes, as shown in Figure 4-7. Hence, 50 μm was selected as an appropriate perforation size in a hexagonal geometry for the simulations reported below.

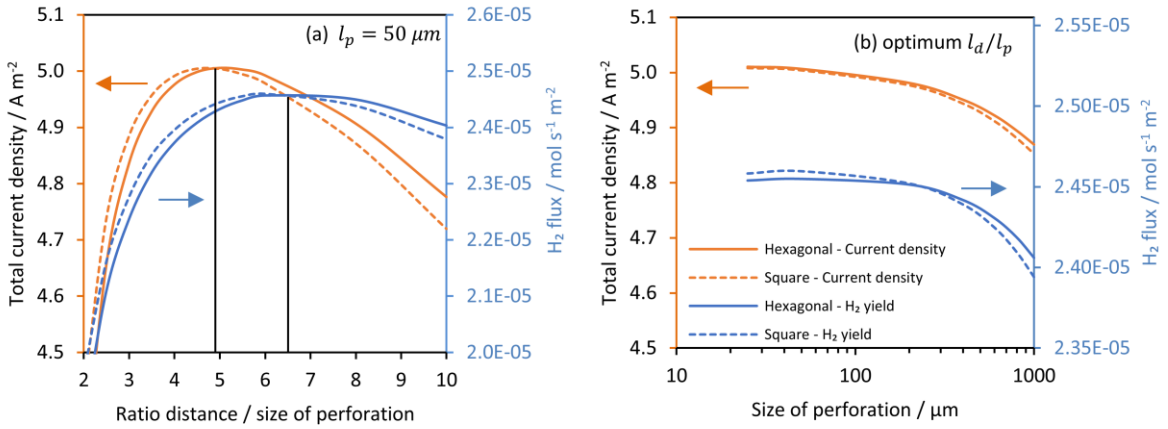


Figure 4-7. Total current densities and (y2) hydrogen fluxes as a function of (a) l_d/l_p for $l_p = 50\ \mu m$ and (b) l_p for an optimum l_d/l_p, in a wired symmetrical 3D model with perforations in a square and hexagonal distribution. Wired cell without membrane in 1 mol dm^{-3} NaOH and 1.51 V *vs.* RHE.

Optimised l_d/l_p for a 'wired' reactor configuration

Figure 4-8(a) compares the model reactor's performance with and without a membrane. As shown in Figure 4-8(b), when a membrane was used, the collection efficiency was almost unity for all geometries, so that the optimum point for current density and hydrogen fluxes occurred at the same $l_d/l_p = 4.5 \pm 0.5$. Figure 4-8(c) shows the maximum current densities and hydrogen fluxes for different perforation sizes with electrodes separated by a membrane; both outputs were lower for larger perforations. This figure also confirms that perforations in the range of 200 to 50 µm did not affect the photo-anode's performance significantly at optimised conditions. When a membrane was used to separate the hydrogen and oxygen, the optimum geometries for hydrogen evolution rates and current densities were essentially the same, due to the collection efficiencies having been maximised. However, current densities were higher in the absence of a membrane, due to decreased ohmic potential losses across the perforation.

In contrast, Figure 4-8(a) also shows that optimum hydrogen fluxes reached similar values of ca. 2.45×10^{-5} mol m^{-2} s^{-1} with or without a membrane at different l_d/l_p ratios. Hence, the decision whether or not to incorporate a membrane rests on the amount of H_2-O_2 cross-over, which is significant in the absence of a membrane: 3 mol % of oxygen in the collected H_2 gas in the catholyte for $l_d/l_p = 6.5$, as shown in Figure 4-8(b). This value can be as high as 14% for $l_d/l_p = 2$. For safety purposes, this concentration of oxygen in the hydrogen collected is undesirable and considered a safety hazard.

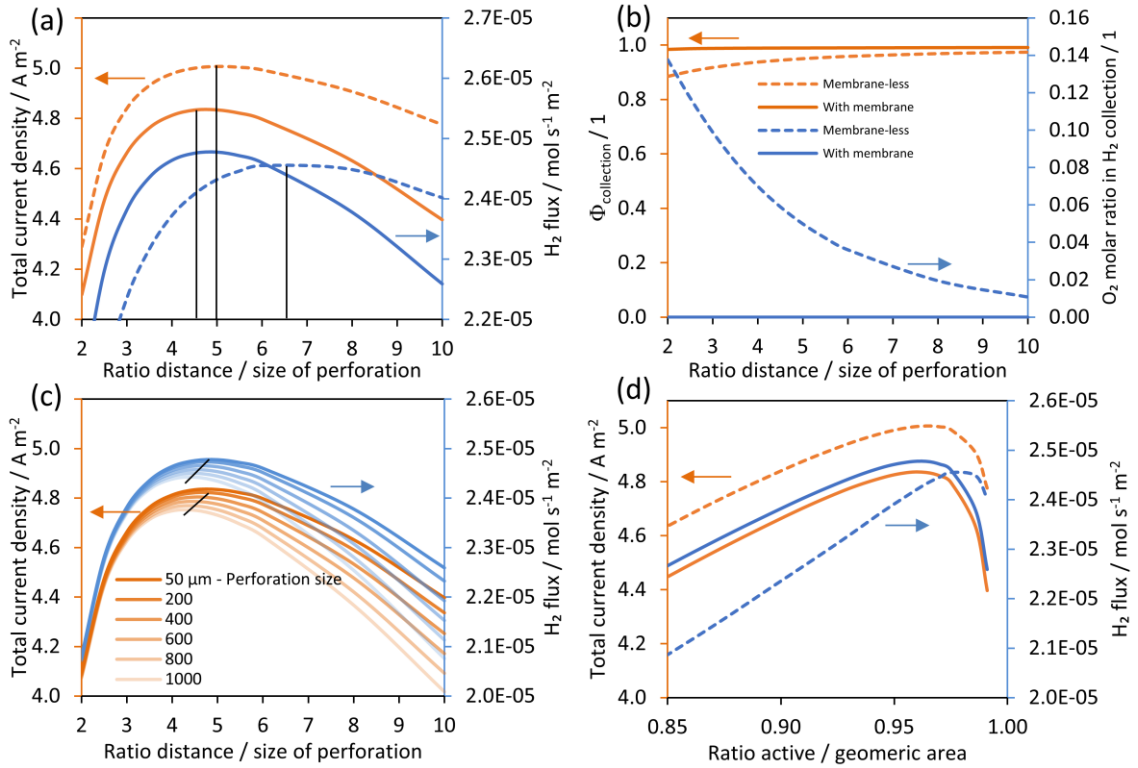


Figure 4-8. Optimisation of l_d/l_p for 'wired' reactor with Ti|Sn^{IV}-doped α-Fe_2O_3 | 1 mol dm^{-3} NaOH photo-anode at 1.51 V *vs.* RHE without a membrane (dashed) and with a membrane (solid). (a) Current densities and hydrogen fluxes for $l_p = 50\ \mu m$. (b) Collection efficiencies and amount of O_2 collected in the catholyte. (c) Current densities and hydrogen fluxes for different perforation sizes, and (d) current densities and hydrogen fluxes as a function of the ratio of active and geometric areas.

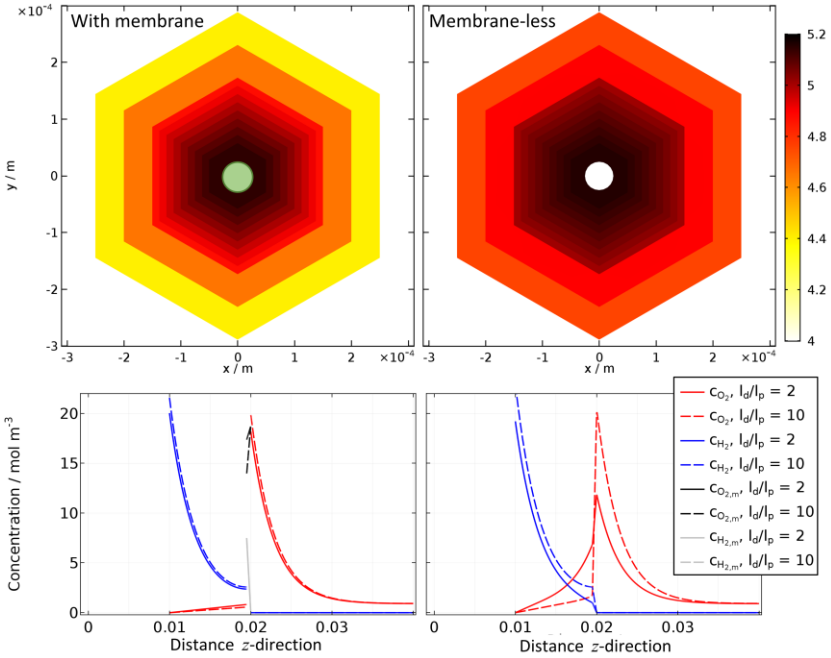


Figure 4-9. (top) Effect of inter-perforation distance (l_d) on current densities for 'wired' reactor with and without a membrane, with Ti|Sn^{IV}-doped α-Fe_2O_3 | 1 mol dm^{-3} NaOH photo-anode at 1.51 V *vs.* RHE with a perforation size of $l_p = 50\ \mu m, l_d/l_p = 2\ or\ 10$, and (bottom) concentration profiles of oxygen and hydrogen in the z-direction in the centre of the perforation ($x = 0$, $y = 0$).

Figure 4-9 shows that higher current densities can be achieved without using a membrane, but a higher concentration of oxygen (above saturation concentration) was found in the catholyte. The use of a membrane effectively separated hydrogen and oxygen gases, and concentrations were almost identical for low and higher values of l_d/l_p. However, current densities for $l_d/l_p = 10$ decreased by almost 10% compared to the optimum l_d/l_p.

Optimised l_d/l_p for a 'wireless' (monolithic photo-bipole) configuration

Predicted current densities and hydrogen fluxes were greatly different in the presence and absence of a membrane filling the perforations in a 'wireless' system. In absence of a membrane, current densities and hydrogen fluxes were at their maximum when $l_d/l_p = 2.5$ and 8.5, respectively, as shown in Figure 4-10(a). Again, this was explained by the increase of H_2-O_2 cross-over rates in the absence of a membrane. However, the amount of oxygen collected in the catholyte was 2 orders of magnitude lower ($< 0.18\%$ molar) when compared to a 'wired' configuration ($< 14\%$ molar). In a monolithic photo-bipole, oxygen reached the cathode surface faster and most of it was reduced near the perforation, while in a 'wired' reactor, oxygen had to diffuse through the membrane, into the catholyte then transported by diffusion to the cathode surface, at which it was reduced under transport control.

This was confirmed by predictions shown in Figure 4-11, in which concentrations of oxygen and hydrogen in the catholyte and anolyte, respectively, were near zero. Despite the lack of oxygen found in the collected hydrogen in the catholyte, collection efficiencies of a membrane-less photo-bipole decreased greatly for low values of l_d/l_p, as shown in Figure 4-10(b). Consequently, hydrogen fluxes were 7% lower when compared with perforations filled with ion-permeable membrane material. In the latter case, current densities and hydrogen fluxes were again found to be optimal at $l_d/l_p = 4.5$. Hydrogen fluxes were greater than for 'wired' reactors, but comparable current densities were predicted for 'wired' and 'wireless' reactors. Newman et al.[120] predicted up-scaled 'wired' reactors produced superior performance, but effects of perforations were not considered and hydrogen fluxes were not reported.

The optimum geometry does not change significantly after increasing the perforation size. However, larger perforations still affect negatively the total current density and net hydrogen fluxes, Figure 4-10 (c), and perforations smaller than 50 μm are preferred.

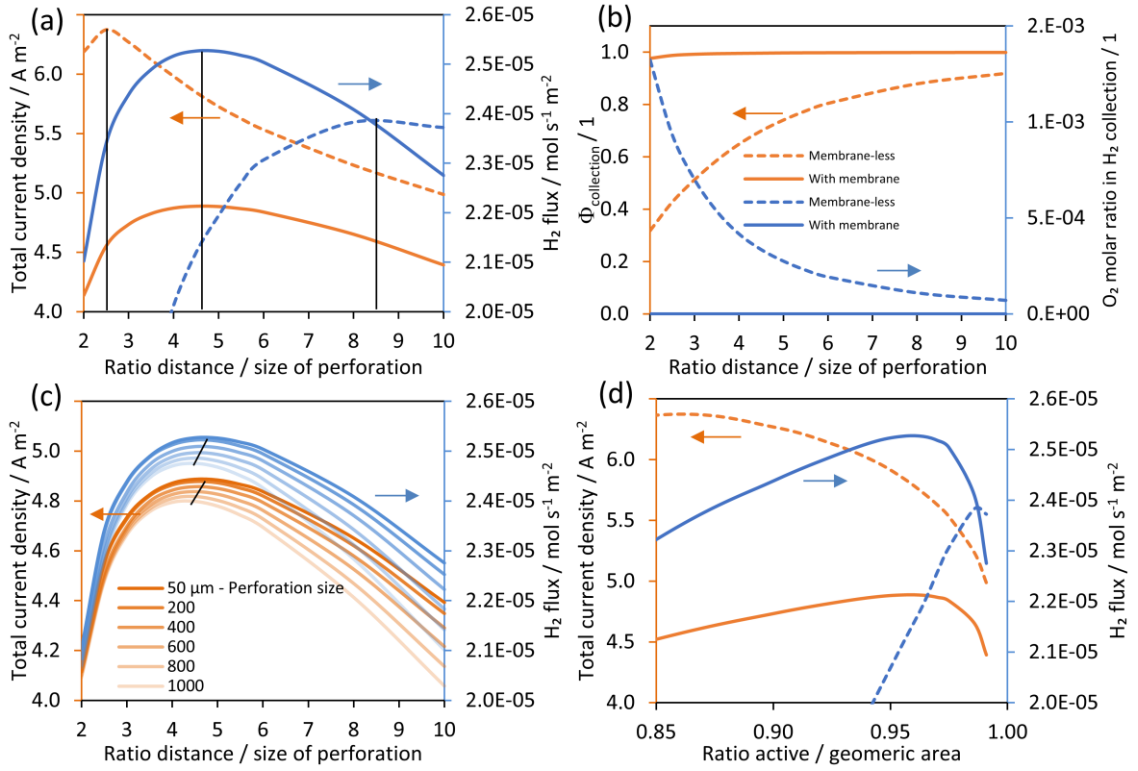


Figure 4-10. Effect of l_d/l_p on current densities for 'wireless' reactor, 1 mol dm^{-3} NaOH | Pt | Ti | Ti | Sn^{IV}-doped α-Fe_2O_3 | 1 mol dm^{-3} NaOH with (solid lines) and without (dashed lines) a membrane, photo-anode at 1.51 V *vs.* RHE. (a) Current densities and hydrogen fluxes for perforation size $l_p = 50\ \mu m$. (b) Collection efficiencies and amounts of O_2 collected in the catholyte. (c) Current densities and hydrogen fluxes for different perforation sizes, and (d) current densities and hydrogen fluxes as a function of the ratio of active and geometric areas.

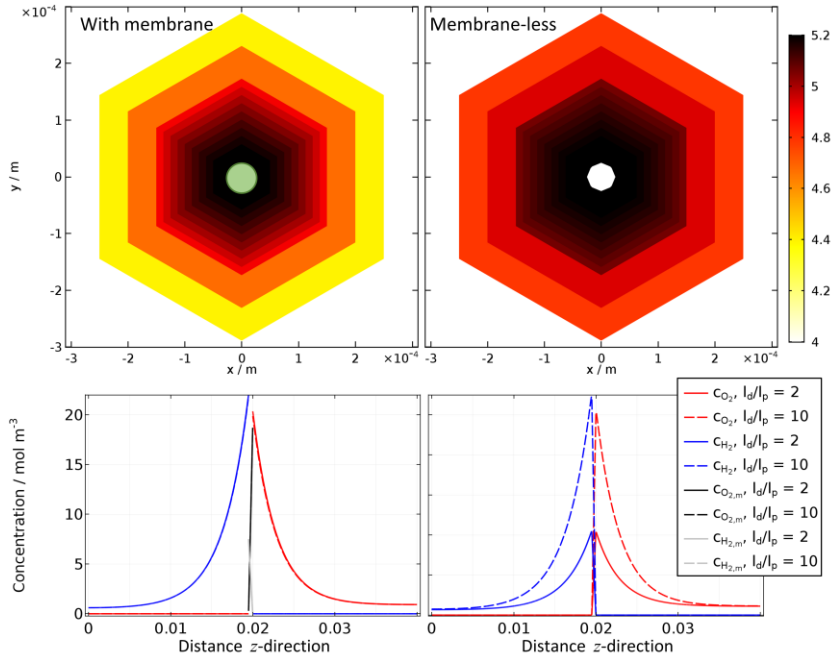


Figure 4-11. (top) Current densities for different perforation distances using a perforation size of $l_p = 50\ \mu m$ and (bottom) concentration profiles of oxygen and hydrogen in the z-direction in the centre of the perforation ($x = 0$, $y = 0$) for a 'wireless' reactor, 1 mol dm^{-3} NaOH | Pt | Ti | Ti | Sn^{IV}-doped α-Fe_2O_3 | 1 mol dm^{-3} NaOH with and without a membrane, photo-anode at 1.51 V *vs.* RHE.

In terms of hydrogen and oxygen concentrations in the presence of a membrane, there is no difference between the concentration profiles at low and high l_d/l_p values, as shown in Figure 4-11. In the absence of a membrane, concentration profiles were higher for $l_d/l_p = 10$ due to an increased diffusion resistance through the perforation. Nevertheless, concentration of oxygen and hydrogen on the catholyte and anolyte, respectively, were significantly lower than for a 'wired' system without a membrane, meaning that cross-over of products are minimised but charge yields are negatively affected. Current densities for different l_d and a perforation size of $l_p = 50$ μm are also presented in Figure 4-11. All values are only slightly higher than the ones found for a 'wired' system, with small difference at the optimum $l_d/l_p = 4.5$. The difference between the use and absence of a membrane was the same as discussed in the section above for a 'wired' system.

4.5.3 Sensitivity analysis

The effects on hydrogen fluxes were predicted by varying: donor density ($10^{24} - 10^{27}$ m^{-3}), irradiance ($10^{-1} - 10^{2}$ suns), electrode thickness (0.1 – 3 mm) and electrolyte conductivity ($10^{-1} - 10^{2}$ S m^{-1}). The relative optimum hydrogen fluxes were found for each condition as a function of l_d/l_p. Figure 4-12 and Figure 4-13 illustrate these predictions for 'wired' and 'wireless' reactors, respectively, with perforations filled with ion-permeable membrane material. Dashed lines represent the typical values used into the model (see Table S4-7 and S4-8 in the Appendix); under these conditions an optimum hydrogen flux was reached at ca. $l_d/l_p = 4.5$. From these figures, it can also be seen how the electrode thickness and irradiance have a significant influence on the optimum configuration.

The effect of electrode thickness, increasing ohmic potential losses, was as expected and comparable to results reported previously [130]. When the perforation diameter / area was smaller while maintaining the same electrode thickness, the local cell constant, $K_{cell} = l_e/A_{perforation}$, increased as did ohmic resistances. Hence, for thicker electrodes, higher perforation areas should be used (lower l_d/l_p). More importantly, when solar concentrators are to be used, the need to define an optimum l_d/l_p was clear; hydrogen fluxes were more highly dependent on photon fluxes reaching the photo-anode compared to the effects of the other three parameters.

On the other hand, the optimum for donor density and electrolyte conductivity were near the same $l_d/l_p \approx 5 \pm 1$ in a wide range of values for these properties. However, values presented in these figures are relative to hydrogen fluxes at the local maximum; current densities and hydrogen fluxes were affected greatly by changes in donor densities and, to a limited extent, by electrolyte conductivities, as shown in Figure S4-9 and S4-10 in the Appendix.

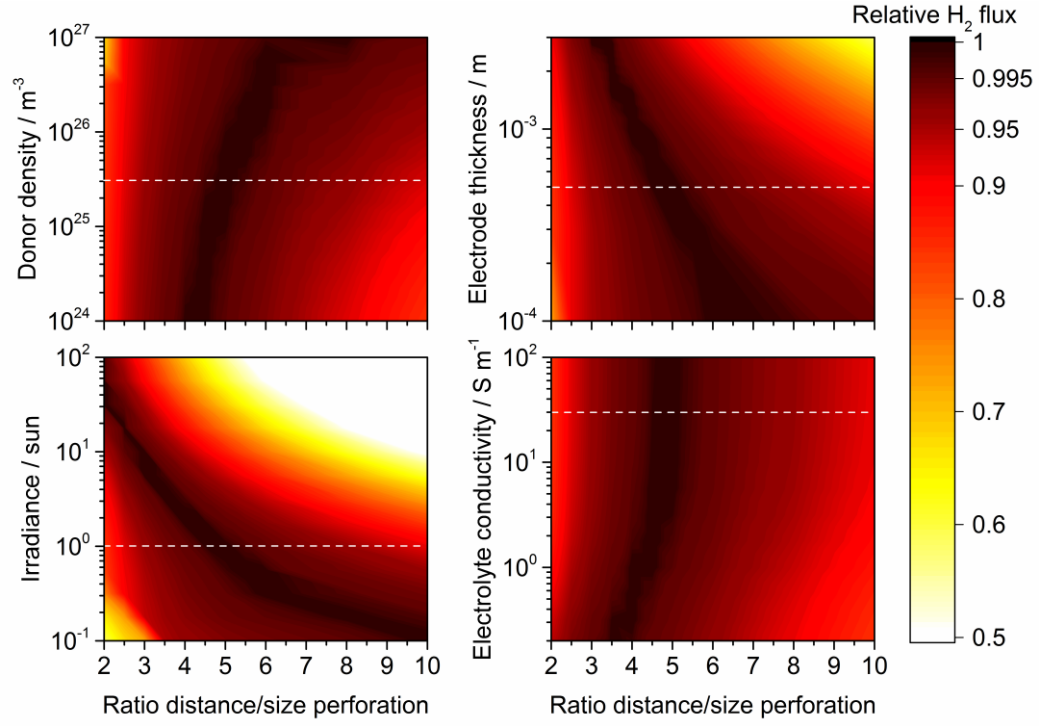


Figure 4-12. Hydrogen fluxes relative to maxima achieved as a function of l_d/l_p for different ranges of donor densities, electrode thicknesses, irradiance and electrolyte conductivity while keeping other parameters unchanged. 'Wired' Ti | Pt | 1 mol dm^{-3} NaOH | Sn^{IV}-doped α-Fe_2O_3 | Ti with and without a membrane, photo-anode at 1.51 V *vs.* RHE. Dashed lines represent the values used typically in the model.

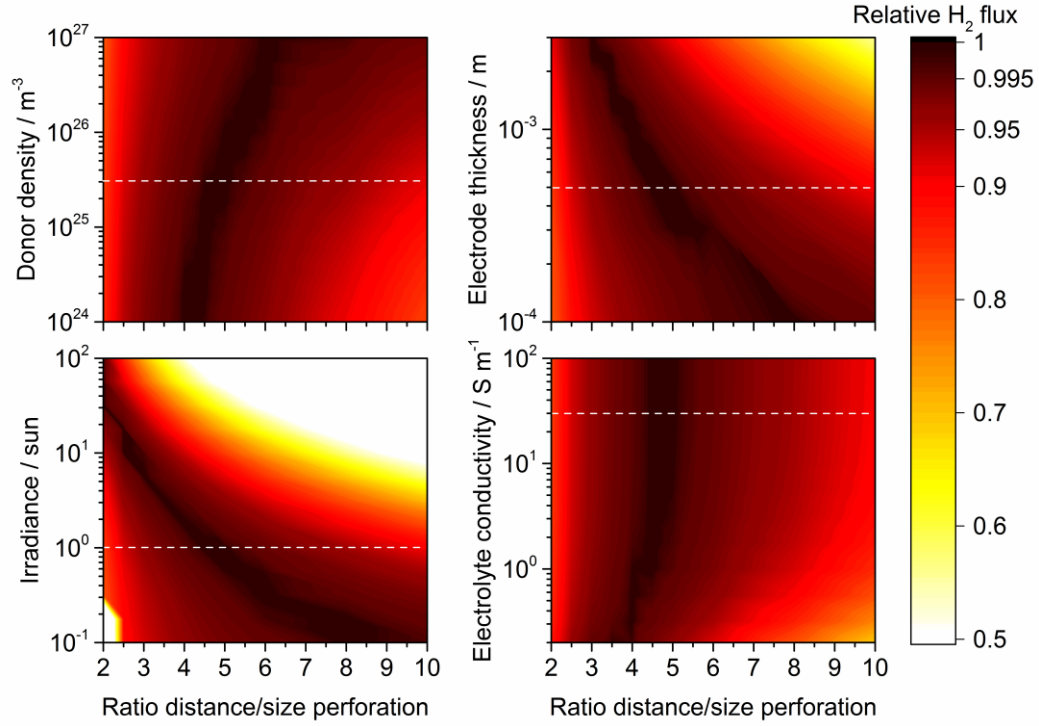


Figure 4-13. Hydrogen fluxes relative to maxima achieved as a function of l_d/l_p for different ranges of donor densities, electrode thicknesses, irradiance and electrolyte conductivity while keeping the other parameters unchanged. 'Wireless' reactor, 1 mol dm^{-3} NaOH | Pt | Ti | Ti | Sn^{IV}-doped α-Fe_2O_3 | 1 mol dm^{-3} NaOH with photo-anode at 1.51 V *vs.* RHE and a hexagonal array of perforations. Dashed lines represent the values typically used in the model.

4.6 Conclusions

A model was developed in terms of measurable properties of the photo-electrode (donor density, photon absorption, bulk and interfacial electron-hole efficiencies, flat band, thickness, exchange current density and Tafel slope), spectrally resolved photon flux of the light source, volumetric mass transfer for gas desorption, bubble formation of hydrogen and oxygen at the electrode surface, and the presence or absence of a membrane between electrodes. The model was validated successfully against experimental data obtained from an up-scaled reactor using a 0.1×0.1 m^2 photo-anode, Sn^{IV}-doped α-Fe_2O_3 spray pyrolysed on titanium. Different scenarios and geometries were studied and optimised as a function of current densities, hydrogen fluxes and collection efficiencies, accounting for H_2-O_2 cross-over, ohmic potential losses and current density distributions. Optimal ratios of separation to size of perforations were found for a wide range of geometrical configurations and photo-anode properties. The effects of temperature were considered to a limited extent, but a deeper understanding of its effects on the photo-anode properties should be addressed, as well as the inclusion of convectional effects (or flow) on the gas evolution and H_2-O_2 cross-over.

The model predictions emphasised the importance of using a membrane for quiescent electrolytes, especially when a monolithic photo-bipole is used. Hydrogen fluxes for 'wired' and 'wireless' (monolithic photo-bipole) configurations were comparable when using a membrane. By contrast, in the absence of a membrane, the model predicted significant cross-over of H_2 and O_2 products for a 'wired' system, while 'wireless' systems exhibited low charge yields for the conditions evaluated in the photo-electrochemical model.

Chapter 5

In situ determination of polysulfide ions in alkaline hydrogen sulfide solution[4]

5.1 Introduction

Attempts to determine concentrations of polysulfide ions, S_n^{2-}, and the speciation of sulfur compounds in aqueous solutions was first reported in 1822 [210]. Polysulfides are involved in a wide range of applications and energy-related systems in which fast kinetics, reversibility and low thermodynamic energy barriers are required, such as aqueous lithium-sulfur batteries [211] and, more recently, hydrogen production combined with aqueous hydrogen sulfide waste treatment driven by solar energy [74, 82]. Polysulfides are known to be intermediate and meta-stable species in the oxidation mechanism of hydrogen sulfide ions, HS^-, to elemental sulfur and sulfoxy species, such as sulfate (SO_4^{2-}), sulfite (SO_3^{2-}) and thiosulfate ($S_2O_3^{2-}$) ions [212]. Numerous *ex situ* techniques have been developed aiming to quantify individual polysulfide ions, including polarography, potentiometric titration, UV and infrared spectrophotometry [70], iodometric and acidimetric methods [213]. These techniques require high concentrations of zero-valent sulfur with respect to dissolved sulfur ($Na_2S:S^0 > 1:0.1$), when tetra- and penta-sulfides are the predominant and most (meta-)stable species. Cyclic voltammetry can also be used to quantify organic polysulfides (R-S_n-R) at concentrations as low as 5 to 6 × 10^{-3} mol dm^{-3} [214]. A novel method involving several stages of enrichment coupled with HPLC-UV analysis is the most recent development for analysing polysulfide ions at low concentrations (10^{-9} mol dm^{-3}) [215]. UV spectrophotometry has been used extensively to study polysulfide solutions [70, 210, 216, 217] in alkaline aqueous solutions, but usually for relatively high ratios of zero-valent sulfur to dissolved sulfur. A thorough literature review of the available techniques for polysulfide determinations and a summary of equilibrium properties has been reported [218]. Herein, a methodology is developed and described for measuring low concentrations of polysulfide ions (ca. 10^{-3} mol dm^{-3}), expressed as zero-valent sulfur, in alkaline aqueous solution using an immersion probe coupled to a UV spectrophotometer. *In situ* and real-

[4] This chapter was adapted from: F. Bedoya-Lora, A. Hankin, G.H. Kelsall, In situ determination of polysulfides in alkaline hydrogen sulfide solution, in preparation.

time quantification of polysulfides ions is critical for the assessment of (photo-) electrochemical reactors for hydrogen production by means of aqueous hydrogen sulfide splitting. The methodology was implemented and validated using four cases of (photo-) electrochemical reactors at bench and up-scaled size, operating at relatively low current densities.

5.2 Polysulfide disproportionation

5.2.1 Polysulfide concentrations at equilibrium

Equilibrium polysulfide speciation was predicted as a function of dissolved zero-valent sulfur, 'S', following a mass balance based on reports by Licht [78, 216] and Giggenbach [72, 210]. Full details of these calculations can be found in the Appendix, Figure S5-10. However, the numerical model was not able to converge for small concentrations of zero-valent sulfur (<0.001 mol dm^{-3}) due to the complexity and non-linear behaviour of the equilibria. Thus, a simplified model was required, assuming a constant concentration of OH^- and HS^-. The validity of this assumption was confirmed with the full mass balance, in which the pH (14.158 − 14.160), ionic strength (2.003 − 2.005) and HS^- concentration (0.4987 − 0.4943 mol dm^{-3}) remained relatively constant for zero-valent sulfur concentrations between 0.001 and 0.01 mol dm^{-3}. This behaviour was also noticed experimentally after measuring the pH of polysulfide ion solutions with different concentrations. Furthermore, the concentrations of penta-sulfide ions were found to be several orders of magnitude lower at equilibrium in presence of high concentrations of HS^- and OH^-, as predicted by reaction (5-1), where $[HS^-]\times[OH^-]$ displace the equilibrium to lower polysulfide activities / concentrations.

$$(n-2)S_n^{2-} + HS^- + OH^- \overset{K}{\Leftrightarrow} (n-1)S_{(n-1)}^{2-} + H_2O \qquad (5\text{-}1)$$

Figure 5-1 shows the predicted concentrations assuming a constant product of $[HS^-]\times[OH^-]$. S_3^{2-} ions were the predominant species for ['S'] > 0.0005 mol dm^{-3}, whereas S_2^{2-} ions predominated for even lower ['S']; S_4^{2-} ions became the main species only at concentrations > 0.1 mol dm^{-3} (not shown in figure). These predictions were supported by experimental data, in which S_4^{2-} ions accounted for up to 90% of the zero-valent sulfur at 1 mol dm^{-3} of added elemental sulfur [219]. Polysulfides of order n > 5 have been proposed theoretically [220] and more recently, experimental proof was reported of such species in natural ground water [215]. However, there is a consensus that polysulfides with n > 5 are not stable due to the limited aqueous solubility of zero-valent sulfur [70, 71]. For this reason, the study of their disproportionation has focused on polysulfides with $2 \leq n \leq 5$. More importantly, Figure 5-1 also shows how S_4^{2-} ion concentrations are predicted not to increase linearly as a function of zero-valent sulfur concentrations. This behaviour was reported first by Pringle for higher concentration [70], but implies that absorbance peaks related to S_4^{2-} ions would not be expected to increase linearly with concentration. S_2^{2-} ions disproportionate rapidly with increasing sulfur at very low concentrations, also causing deviations from linear behaviour.

Table 5-1 summarises the molar attenuation coefficients, ε_λ, of polysulfides with characteristic peak absorbances at ca. 300, 360 and 420 nm [78, 210], whereas solutions of 1 mol dm^{-3} NaOH

absorb only at wavelengths < 200 nm and 260 nm, when Na_2S is added [217, 221], typical of sulfide compounds (< 280 nm). However, S_2^{2-} ions are known to have an additional absorbance peak at 360 nm, to which S_4^{2-} and S_5^{2-} ions also contribute with their higher attenuation coefficients, in contrast to S_3^{2-} ions which absorb at ca. 420 nm. Hence, it was expected that any absorbance at ca. 420 nm was due exclusively to S_3^{2-} ions, while S_4^{2-} ions had a higher absorbance at 300 nm, assuming that the concentration of S_5^{2-} ions was negligible. Consequently, any deviation from linearity at 300 nm could be associated with the disproportionation of S_4^{2-} ions, specifically for concentration between 0.001 and 0.006 mol dm^{-3}, as evident in Figure 5-1.

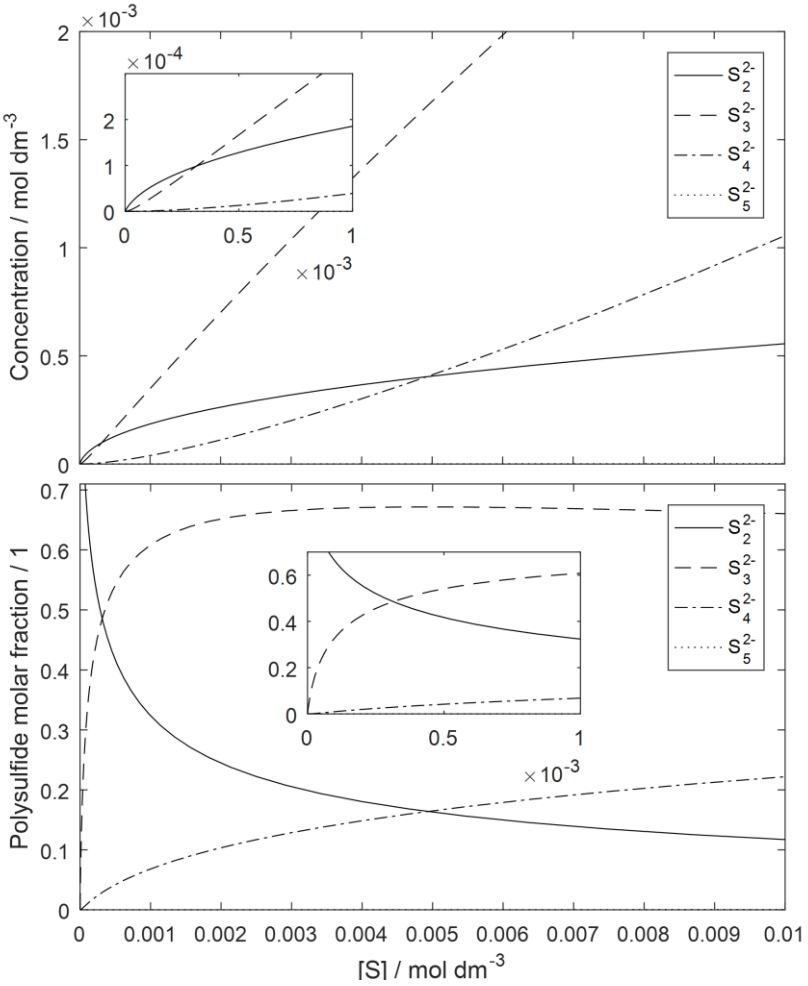


Figure 5-1. Predicted (top) concentration and (bottom) molar fraction of S_n^{2-} as a function of zero-valent sulfur in 1 mol dm^{-3} NaOH and 0.5 mol dm^{-3} Na_2S, pH 14, 298 K.

5.2.2 Effect of electrode potential on polysulfide concentration

In an electrochemical reactor, an electrode potential applied across an electrode | solution interface causes anodic oxidation or cathodic reduction of solute species such as the polysulfide - hydrogen sulfide ion redox couple:

$$S_n^{2-} + nH_2O + 2(n-1)e^- \Leftrightarrow nHS^- + nOH^- \qquad (5\text{-}2)$$

The next oxidation to zero-valent sulfur requires 2 electrons and can be expressed as:

$$'S' + H_2O + 2e^- \Leftrightarrow HS^- + OH^- \quad (5\text{-}3)$$

Reduction and oxidation of water in alkaline aqueous solution, with hydrogen and oxygen as products respectively, can also take place at the electrode surface:

$$2H_2O + 2e^- \Leftrightarrow H_2 + 2OH^- \quad (5\text{-}4)$$

$$O_2 + 2H_2O + 4e^- \Leftrightarrow 4OH^- \quad (5\text{-}5)$$

Table 5-1. Estimated molar attenuation coefficients of polysulfides ions in aqueous solution.

	Giggenbach [210]		Licht [78]	
	Wavelength / nm	ε_λ / dm³ mol⁻¹ cm⁻¹	Wavelength / nm	ε_λ / dm³ mol⁻¹ cm⁻¹
S_2^{2-}	358	850	358	990
S_3^{2-}	303	2280	302	2600
	417	190	429	206
S_4^{2-}	303	3420	302	3690
	368	960	372	1140
S_5^{2-}	299	8000	296	6800
	375	2560	377	1800

Using critically reviewed thermodynamic data [73], the E-pH diagram in Figure 5-2 was computed recently for a (meta-stable) $S - H_2O$ system from which sulfoxide species had been excluded; though more thermodynamically stable than polysulfide ions, rates of oxidative formation of sulfoxides are limited by relatively large activation energies. Elemental sulfur 'S' is predicted to be the stable form of sulfur at pH 14 and potentials > 0.53 *vs.* RHE. Based on previous reports [73, 222], Figure 5-3 shows the effect of electrode potential on activities of polysulfide ions for pH 14, 298 K and dissolved sulfur activity of 0.5. These results were computed after solving numerically the equilibrium equations for the electrochemical reactions, represented by Nernst equations, and homogeneous dissolution of hydrogen sulfide ions in alkaline conditions, as shown in the Appendix 5.2. Figure 5-3 predicts that S_5^{2-} ions become the predominant polysulfide ions for electrode potentials > 0.45 V *vs.* RHE. These species formed by reaction (5-2) were expected to diffuse in the photo-anode diffusion / reaction layer towards the bulk of the solution, then being reduced by the fast homogeneous reaction (5-1) by HS^- ions to lower polysulfides, and eventually equilibrating with species in the bulk solution.

$$n'S' + HS^- + OH^- \Leftrightarrow S_{n+1}^{2-} + H_2O \quad (5\text{-}6)$$

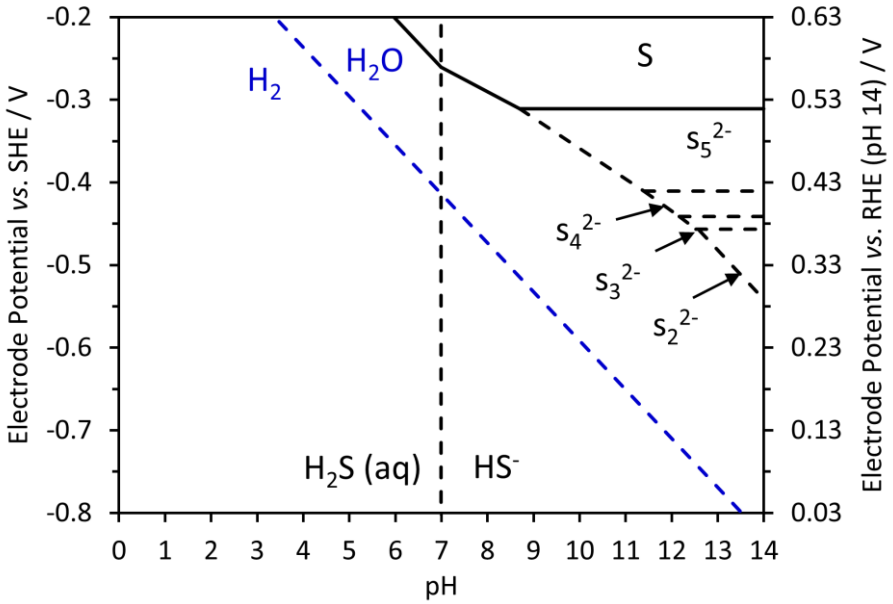


Figure 5-2. Potential-pH diagram for a meta-stable S-H_2O system with sulfoxides excluded; total dissolved sulfur activity 0.5, 298 K and 0.1 MPa [74].

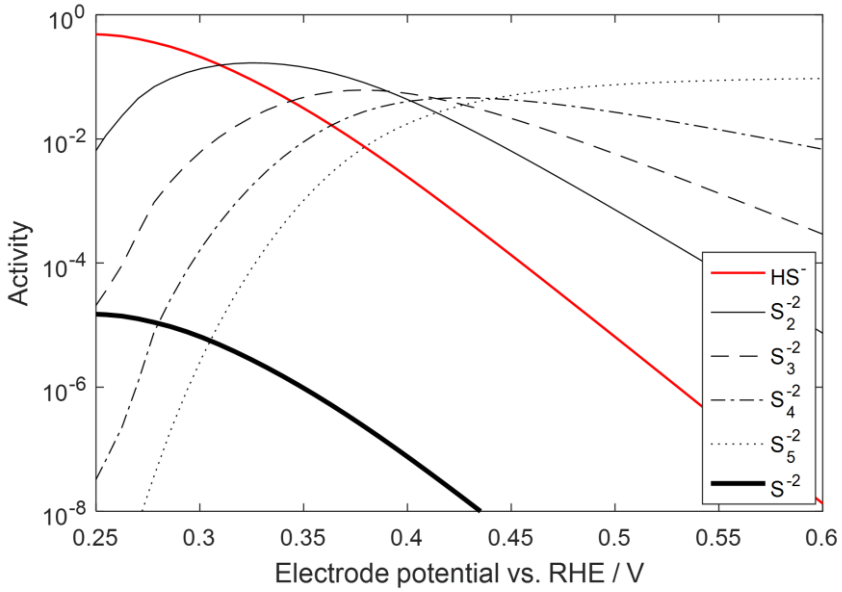


Figure 5-3. Effect of electrode potential on polysulfide distribution; dissolved sulfur activity 0.5, pH 14, 298 K and 0.1 MPa.

Depending on the electrode potential, Figure 5-3, initial oxidation of HS^- ions would have produced high concentrations of S_5^{2-} ions near the anode, so given the high molar attenuation coefficient of these species, increasing absorption at 300 nm was expected. Elemental sulfur was also expected to be deposited on the anode at applied potentials > 0.53 V *vs.* RHE, reaction (5-3), followed by reduction to S_n^{2-} ions by HS^- present in the bulk solution, reaction (5-6). The mechanism of oxidation of HS^- ions will be discussed in the next chapter.

5.2.3 Decomposition of polysulfide ions to sulfoxides

Oxygen ingress into the electrolyte solution potentially can result in the oxidation of the added zero-valent sulfur and hydrogen sulfide ions to form sulfate, sulfite and thiosulfate according to reactions (5-7) to (5-11), as predicted thermodynamically [212]:

$$2HS^- + O_2 \Leftrightarrow 2S + 2OH^- \tag{5-7}$$

$$2HS^- + 2O_2 \Leftrightarrow S_2O_3^{2-} + H_2O \tag{5-8}$$

$$2HS^- + 3O_2 + 2OH^- \Leftrightarrow 2SO_3^{2-} + 2H_2O \tag{5-9}$$

$$HS^- + 2O_2 + OH^- \Leftrightarrow SO_4^{2-} + H_2O \tag{5-10}$$

Polysulfide ions are intermediates in the above reactions and can be oxidised faster than hydrogen sulfide in presence of oxygen, by reactions such as [223]:

$$2S_n^{2-} + 3O_2 \Leftrightarrow S_2O_3^{2-} + (n-2)S \tag{5-11}$$

Polysulfide solutions, which are yellow in colour, usually become fully decolourised in the presence of oxygen over 1 to 9 days [223]. However, this is sufficiently fast to affect concentrations of polysulfide ions due to their decomposition during experiments and calibrations, which are usually run over the course of a day. Early studies on polysulfide ions found that elemental sulfur can also react directly with hydroxide species in absence of oxygen and at room temperature to form thiosulfate and polysulfides [224]:

$$(2n+2)S + 6OH^- \Leftrightarrow 2S_n^{2-} + S_2O_3^{2-} + 3H_2O \tag{5-12}$$

Likewise, decolouration of polysulfide solutions has also been proposed to be promoted by temperature, accelerating their conversion to thiosulfate ions in alkaline conditions [216, 225].

$$S_4^{2-} + 8OH^- + H_2O \Leftrightarrow S_2O_3^{2-} + 10HS^- \tag{5-13}$$

$$S_5^{2-} + 3OH^- \Leftrightarrow S_2O_3^{2-} + 3HS^- \tag{5-14}$$

Figure 5-4 shows an E-pH diagram for which, unlike Figure 5-2, sulfoxy species other than sulfate(VI) were included in the calculation. This predicts that under alkaline conditions and relatively low electrode potentials, SO_3^{2-} and $S_2O_3^{2-}$ ions may form as metastable species, sulfate ions being the thermodynamically stable species under those conditions. However, activation energies of such reactions are higher than of those for polysulfide formation, so hydrogen sulfide oxidation to polysulfide ions is faster than to sulfoxy species.

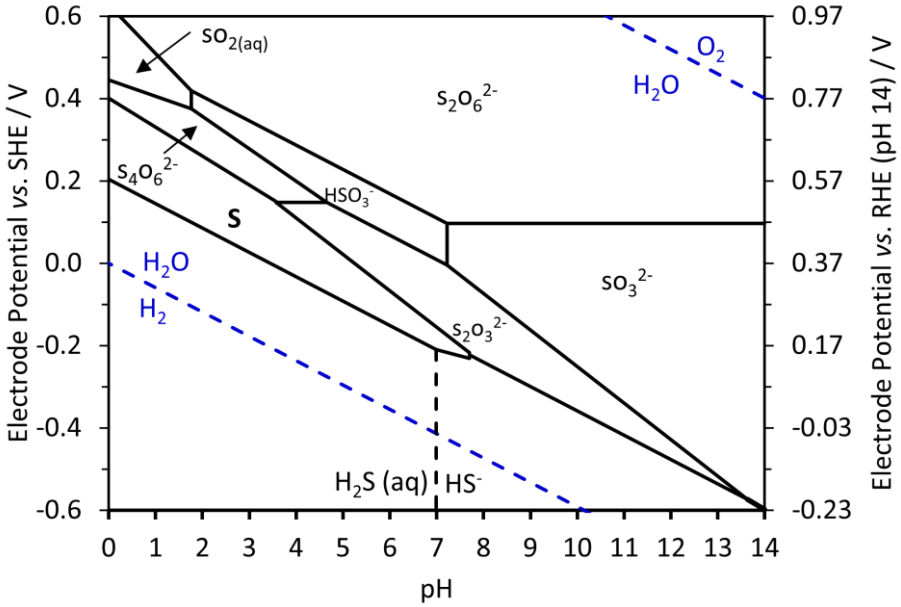


Figure 5-4. Potential-pH diagram for a S-H_2O system excluding sulfate(VI) species 0.01, 298 K and 0.1 MPa.

The consequences of the decomposition of polysulfides was observed experimentally, when deaerated solutions were sonicated without temperature control reaching ca. 60 °C, they turned completely transparent, and in some cases typical absorbance peaks disappeared completely. The lower the concentration of zero-valent sulfur and higher that of hydroxide ions, the faster the decomposition to thiosulfate and the lower the temperature required to drive the reaction. For example, it took 1 hour to decompose half of the amount of zero-valent sulfur in an equimolar solution of S_4^{2-}-S_3^{2-} ions at 100 °C and pH 14 [225], 31 days at 60 °C and 5400 days at 20 °C [78]. A recent extensive study of polysulfide disproportionation found that at 25 °C and in absence of oxygen, there was minimal decomposition after 50 days [216]. Hence, even at lower concentrations, it is reasonable to believe that at room temperature and in absence of dissolved oxygen, the polysulfide decomposition can be disregarded.

It is essential to minimise the ingress of oxygen to minimise rates of decomposition reactions (5-7) to (5-14) driven by oxygen and temperature at high pH, as well as ensuring a fresh source of sulfur. This is contrary what was recommended in a recent report [217]; solutions prepared in a typical laboratory atmosphere showed no difference compare to another solution prepared with deaerated water in a controlled nitrogen environment. However, no details were given for the purity of nitrogen, which, as it will be shown in the results section, can influence the polysulfide decomposition even with only traces of oxygen.

5.3 Experimental

5.3.1 Polysulfide ions alkaline solutions

All solutions were prepared in distilled water purged for more than one hour with zero grade nitrogen (99.998% and oxygen impurity removed) to remove residual dissolved oxygen. Once

solutions were prepared, contact with air was minimised by purging with nitrogen at times when the container had to be opened. 1 mol dm^{-3} NaOH (97%, Sigma-Aldrich) and 0.5 mol dm^{-3} Na_2S ($Na_2S{\cdot}9H_2O \geq 99.99\%$, Sigma-Aldrich) were prepared as the blank solution; typically, 1 dm^3 of solution was needed for a single calibration curve.

Polysulfide solutions were prepared by adding elemental sulfur (99.998%, Sigma-Aldrich, UK), which was weighted (A&D Weighing GH-252 Delta Range) rapidly in atmospheric conditions and added to prepared stock solutions of 0.1 dm^3: 0.015 mol dm^{-3} (48.09 ± 0.03 mg) for low concentration and 0.03 mol dm^{-3} (96.18 ± 0.03 mg) for medium and high concentrations. The formation of polysulfide ions from elemental sulfur in alkaline aqueous solutions follows reaction (5-6) [72].

Stock solutions were closed and sonicated for 1 h until sulfur was dissolved completely. Heating of the solution was prevented by changing the sonicator (SW 6H, Sonno Swiss) bath every 15 min or by using ice to keep the bath cooled. The effect of sonication on hydrogen sulfide solution was tested and found not to be significant if solutions were kept at room temperature, as shown in Figure S5-1 in the Appendix. Solutions at different concentration (0.3 – 0.001 mol dm^{-3}) were prepared by diluting stock solution in 0.05 dm^3 of blank solution, and left closed for more than 15 h until polysulfide species reached equilibrium, as shown in Figure S5-2 and S5-3 in the Appendix.

5.3.2 Absorbance measurements

Absorbance spectra were measured using a reflective immersion probe (AIFDP-7UV200-2VAR-PK8, Anglia Instruments) made of PEEK with an aperture of 5 mm (10 mm optical path) and a suitable wavelength range of 200 – 1100 nm. The probe was connected to a deuterium arc lamp (8453 UV-Vis SP, Agilent). Absorbance spectra were recorded with a UV-vis spectrometer (Black-Comet CXR-25, StellarNet) using an integration time of 0.8 s between 270 and 900 nm. Three measurements were recorded and averaged for each data point. A scheme of the set-up for the determination of polysulfide ions concentration is shown in Figure 5-5.

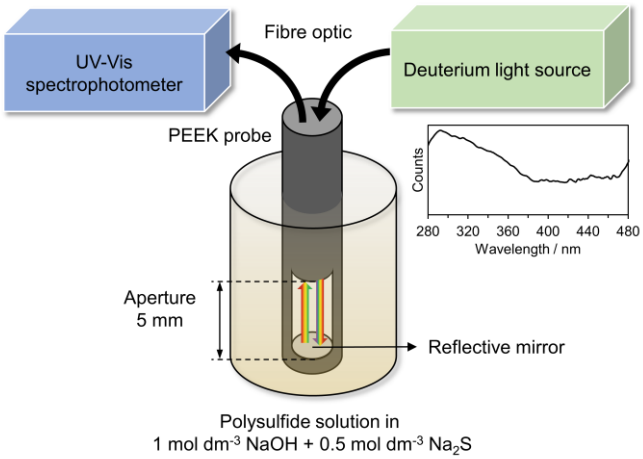


Figure 5-5. Equipment for polysulfide determination as zero-valent sulfur in alkaline solution using an immersion probe and UV-vis spectrophotometer.

5.3.3 Generation of polysulfides ions in PERs

Synthetic polysulfide solutions were produced by HS^- oxidation, reaction (5-2), in two photo-electrochemical reactors, each with anolyte and catholyte were separated by a cation-permeable membrane (PTFE reinforced Nafion® 424, DuPont Inc.). The smaller, bench-scale reactor comprised of an anolyte and catholyte compartment of 0.1 dm^3 (PVC body) each with an Sn^{IV}-doped hematite photo-anode supported on a titanium sheet and electro-active area of 1.8×10^{-5} m^2; constant potential electrolyses over 23 h and 50 h resulted in current density – time data to correlate with polysulfide formation rates. An up-scaled and gas-tight reactor, as described in Chapter 1, page 104, utilising electrodes with geometrical areas of 0.01 m^2 had a greater area:volume ratio, so greater rates of polysulfide formation could be achieved. Planar and perforated Sn^{IV}-doped hematite anodes were used and compared in this study. In both reactors, bench and up-scaled, platinised titanium mesh (Expanded Metal Company) acted as a counter electrode and a homemade 0.5 mol dm^{-3} Na_2S | Ag_2S | Ag as pseudo-reference electrode (0.145 V *vs.* RHE at pH = 14). Blank solution (1 mol dm^{-3} NaOH and 0.5 mol dm^{-3} Na_2S) was used as anolyte and 1 mol dm^{-3} NaOH as catholyte. Sn-doped hematite photo-anodes, described in previous the chapters, were used as working electrodes for hydrogen sulfide oxidation to polysulfide ions.

Rates of cross-over of S_n^{2-} and HS^- ions between compartments was decreased effectively by the membrane, so no absorbance difference was found in the catholyte after extended periods. A potentiostat/galvanostat (Autolab PGSTAT 30) was used to record current-time data at an applied potential of 1.15 V *vs.* RHE at the anode, over 25 h for the bench-scale reactor and at a fixed cell potential difference of 1.226 V for 15 h for the up-scaled reactor.

Spectra were recorded typically every 1 or 5 minutes in the anolyte, and current densities recorded every 10 seconds. Zero grade nitrogen was bubbled at all times, which prevented the ingress of oxygen and maintained a well-stirred electrolyte. Hydrogen flux densities generated at the cathode were measured with a gas flow meter (MilliGascounter MGC-1, Ritter). The time to reach steady state was typically 3 to 8 hours.

Charge yields, Φ_i^e, were computed as the fraction of the flux density of the products in the reaction of interest and the total current density (j) passed:

$$\Phi_i^e = \frac{j_i}{j_{\text{total}}} = \frac{N_i \nu_{e,i} F}{j_{\text{total}}} \tag{5-15}$$

Where N_i is the flux density of the species i, $\nu_{e,i}$ is the charge number for reaction i, j_{total} is the total current density at the electrode and F is the Faraday constant, 96 485.33 C mol^{-1}.

5.4 Results and discussion

5.4.1 Calibrations curves

The characteristic three absorption peaks at 295 nm, 360 nm and 420 nm were observed in polysulfide solutions prepared as reported above. Figure 5-6 shows typical spectra of polysulfide

solutions at different concentrations of zero-valent sulfur. The peak at 295 nm had a characteristic higher absorbance, followed by a less-defined peak at 360 nm. The shoulder at 420 nm exhibited a lower absorbance as expected, and was possibly associated to S_3^{2-} ions according to the values presented in Table 5-1. However, this peak appeared peculiarly only for ['S'] > 4×10^{-3} mol dm^{-3}. This could be explained by the appearance of polysulfide ions which became predominant at about this concentration. However, according to the predictions of disproportionation shown in Figure 5-1, S_3^{2-} ions predominated at concentrations > 0.5×10^{-3} mol dm^{-3}. This is an indication that predictions at such low ['S'] could be misleading and a revision of the equilibrium constants is recommended, as also was suggested recently by Safyan [217]. No features were evident at wavelengths > 520 nm.

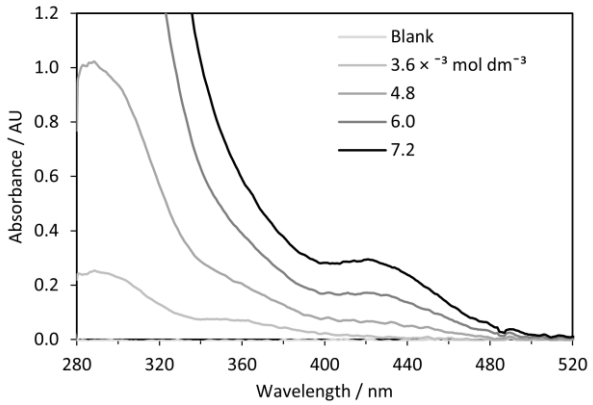


Figure 5-6. Typical absorbance spectra of different polysulfide solutions expressed as zero-valent sulfur content in 1 mol dm^{-3} NaOH and 0.5 mol dm^{-3} Na_2S.

Figure 5-7 shows the calibration at three different ranges: low, medium and high. The first two calibration curves used the absorbance peak at 295 nm and the latter at 420 nm. Due to the low signal in the low range, the determination coefficient, R^2, was relatively low for a calibration curve not forced through zero. Nevertheless, a linear behaviour was evident, associated with S_3^{2-} ions. S_2^{2-} ions did not absorb at this wavelength and S_4^{2-} and S_5^{2-} ions were predicted to be present at low concentrations, as shown in Figure 5-1. The calibration at medium range showed a clear non-linear behaviour, which could be associated with the non-linear increase in concentrations of the highly absorbing S_4^{2-} ions. The calibration curve was fitted to an exponential function. Lastly, the calibration curve for the high concentration range was again linear at 420 nm, but with a distinct offset towards higher concentrations. As described previously, this might have been due to a wrongly assigned absorptivity peak, predicted to be S_3^{2-} ions, instead of possibly higher polysulfide ions with n > 3. However, for calibration purposes, the curve was still useful to determine the concentration of zero-valent sulfur in the solution.

Calibrations were also performed using an inferior grade of nitrogen, the small traces of impurities in which can affect calibrations significantly. Oxygen, even in small amounts, would partially oxidise the elemental sulfur and polysulfides to sulfoxy species; thus, lower absorbances were observed in all peaks, as shown comparatively in Appendix Figure S5-4 for different calibration curves and Appendix Figure S5-6 for solutions with added sulfoxy species. Following an opposite

trend and after prolonged and excessive exposure to oxygen (i.e. bubbling air), elemental sulfur and intermediated polysulfides were formed directly from the aerial oxidation of hydrogen sulfide ion present in blank solution, and higher absorbances were observed over time, as shown in Figure S5-5 in the Appendix.

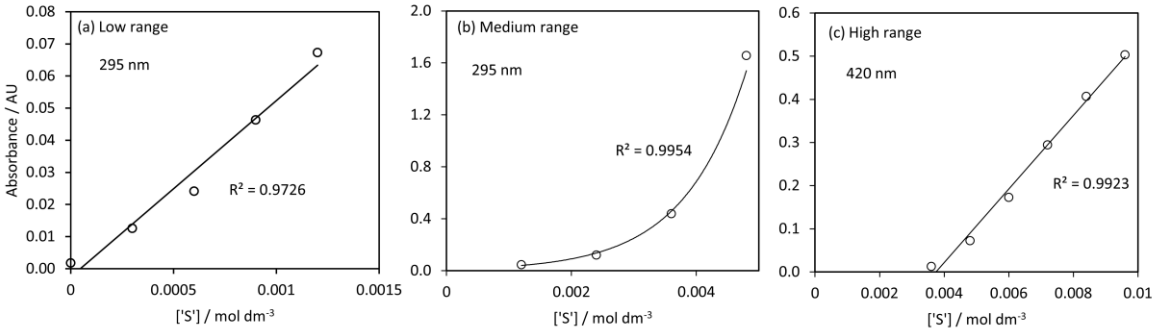


Figure 5-7. Calibration curves of polysulfide solutions expressed as 'S' for different ranges of concentrations in 1 mol dm^{-3} NaOH and 0.5 mol dm^{-3} Na_2S. (a) Linear regression for low range at 295 nm (b) exponential regression for medium range at 295 nm, affected by polysulfide disproportionation, and (c) linear regression for high range at 420 nm.

Table 5-2 shows the calibration functions used for the estimation of 'S' rate evolution after oxidation of HS^- at the anode.

Table 5-2. Calibration curve parameters for different ranges of polysulfide concentration expressed as zero-valent sulfur in 1 mol dm^{-3} NaOH and 0.5 mol dm^{-3} Na_2S.

Range / × 10^{-3} mol dm^{-3}	Wavelength / nm	Calibration curve $y[\text{mol dm}^{-3}] = f(x(\text{absorbance}))$	R^2
0 – 1.2	295	$1.646 \times 10^{-3}x + 1.683 \times 10^{-3}$	0.973
1.2 - 5	295	$1.061 \times 10^{-3} \ln(x) + 4.398 \times 10^{-3}$	0.995
3.6 - 10	420	$1.165 \times 10^{-2}x + 3.761 \times 10^{-3}$	0.992

5.4.2 Estimation of molar attenuation coefficient

In order to confirm the molar attenuation coefficients, ε_λ, reported by other authors, an estimation of these parameters was attempted using the spectra and predictions of polysulfide disproportionation. The absorbance at 420 nm was used exclusively for the quantification of ε_λ for S_3^{2-} ions, which were predicted to be the only species absorbing at that wavelength. After assuming a negligible presence of S_5^{2-} and that S_2^{2-} did not absorb at 295 nm, ε_λ was estimated for S_3^{2-} and S_4^{2-} ions for this wavelength. Table 5-3 summarises and compares these estimations with the values reported by Licht [78] and Giggenbach [210]. Attenuation coefficients at 295 nm for S_4^{2-} ions and at 420 nm for S_3^{2-} ions were similar to the values found in the literature. However, the absorbance of S_3^{2-} ions was significantly lower at 295 nm. As shown in the inset of Figure 5-8, this might be due to an over-estimation of the concentration of S_4^{2-} ions in the disproportionation models. The non-linear behaviour should be more pronounced in order to fit the experimental data. This might be the case only if at low ['S'] the disproportionation of S_4^{2-} ions, or even higher polysulfides, had a more abrupt increase in concentration compared to lower polysulfides.

The incongruities found between the data presented here and the reports from the literature are an indication that the equilibrium constants and molar attenuation coefficients of polysulfides, especially at low ['S'], should be revised. Deconvolution of spectra for a wider range of concentrations, including OH^- and HS^- species, could be useful for this purpose. This requires more meticulous studies, as described previously [70, 78, 210], but was beyond the scope of this investigation. Although the indication of unsuitability and uncertainty of these parameters, calibration curves are fitted as a function of zero-valent sulfur and still valid for estimating its content in polysulfide solutions, as it will be shown in the next section.

Table 5-3. Molar attenuation coefficient of S_3^{2-} and S_4^{2-} ions in aqueous solution derived from experimental data reported here compared to values reported in the literature.

Polysulfide	Wavelength / nm	ε_λ / dm³ mol⁻¹ cm⁻¹		
		This work	Giggenbach[210]	Licht[78]
S_3^{2-}	295	157	2280	2600
	420	289	190	206
S_4^{2-}	295	3609	3420	3690

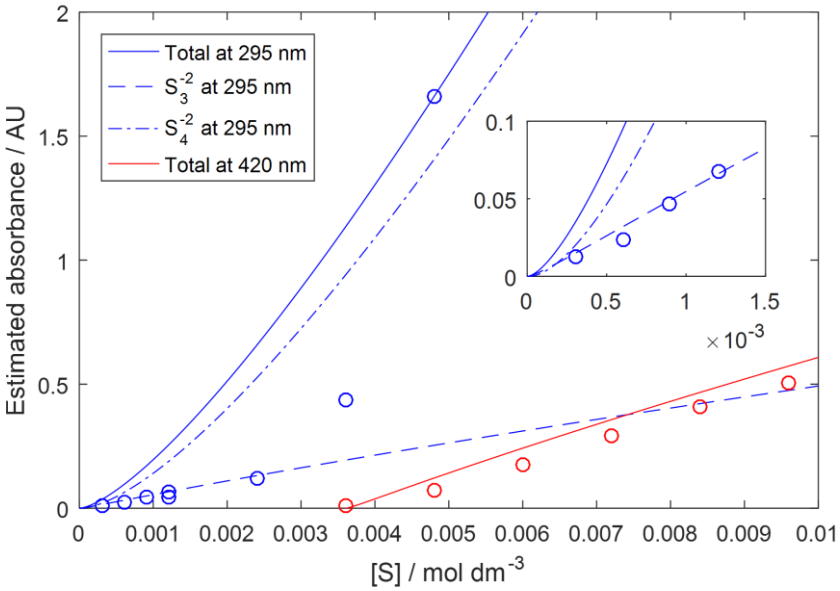


Figure 5-8. Estimated absorbance of polysulfide ions in 1 mol dm⁻³ NaOH and 0.5 mol dm⁻³ Na_2S and contributions of S_3^{2-} and S_4^{2-} in absorbance at 295 nm, compared to (○) experimental data.

5.4.3 Validation via electrochemical generation of polysulfides

Figure 5-9 and Figure 5-10 show the time dependences of current densities and zero-valent sulfur concentrations, for the bench-scale and up-scaled reactors, respectively. In the bench-scale reactor, current densities were constant after stability was achieved, usually after 5 or more hours. The initial transient state arises for two inter-related reasons: (*i*) newly oxidised polysulfides near the surface of the electrode are usually of high order (n = 5), as predicted in Figure 5-3. The reduction of these species by HS^- via reaction (5-1) in the bulk of the electrolyte, did not happen instantaneously, so equilibration time was required. (*ii*) Elemental sulfur was deposited on the

electrode surface by electrochemical reaction (5-3) or indirectly by oxygen evolution by reaction (5-5), followed by its consumption by reaction (5-7). The area covered by elemental sulfur increased with time, until these reactions occurred at similar rates to sulfur and higher polysulfide reduction by HS^- ions via reactions (5-6) and (5-1), respectively.

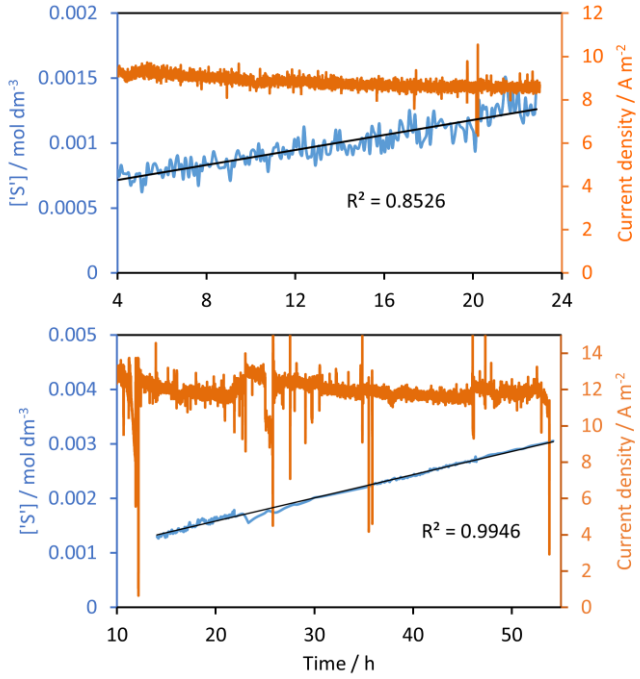


Figure 5-9. Time dependences of polysulfide concentrations expressed as zero-valent sulfur in 1 mol dm^{-3} NaOH and 0.5 mol dm^{-3} Na_2S after HS^- oxidation in an 0.1 dm^{-3} electrochemical reactor, (top) short and (bottom) long term current densities for two different anode samples. Electrode potential of 1.15 *vs.* RHE.

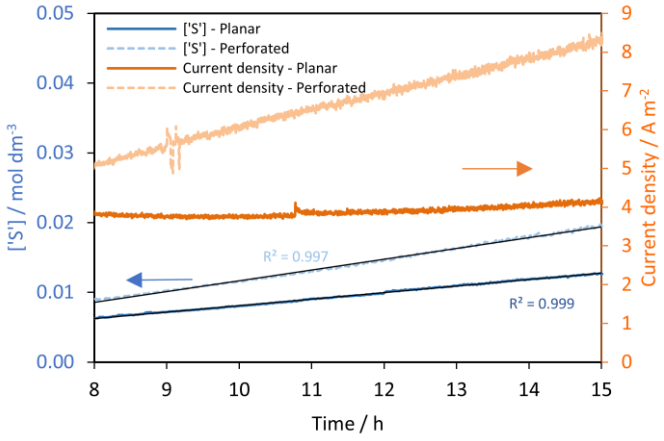


Figure 5-10. Time dependences of polysulfide concentrations expressed as zero-valent sulfur in 1 mol dm^{-3} NaOH and 0.5 mol dm^{-3} Na_2S after HS^- oxidation in an 0.8 dm^{-3} electrochemical reactor for two different electrodes (planar and perforated) and applied cell potential difference of 1.226 V.

In the bench-scale reactor, there was a clear and steady increase of polysulfide concentrations, expressed here as zero-valent sulfur. The rate of polysulfide generation was then extracted from the slope as $d['S']/dt$ and used to estimate the charge yield, equation (5-15), i.e. the fraction of charge effectively transferred in the polysulfide (5-2) and hydrogen evolution (5-4) reactions. For these estimations, the transfer of 2 electrons was assumed to produce zero-valent sulfur from HS^- ions by

reaction (5-3). In fact, the ratio of electron to HS^- ion reactant stoichiometries, 2(n-1):n, is always < 2 when polysulfides are formed directly at anodes, according to reaction (5-2). However, given that the reported concentrations and calibrations are expressed as zero-valent sulfur, the speciation issue can be circumvented while still being consistent.

In the case of the up-scaled reactor, the perforated electrode did not show a stable current density even after 8 hours. This was due to an autocatalytic process being carried out in the presence of polysulfide ions, which can be oxidised faster than hydrogen sulfide ions [223]. Then, charge yields were alternatively calculated with charge integration between two given times. In the case of the bench-scale reactor, polysulfides were produced with a steady rate after 8 hours of operation. The absorbance spectra for the four cases is presented in the Appendix, Figure S5-7 to S5-9. Hydrogen fluxes were also measured and charge yields for hydrogen evolution were estimated, assuming the measured gas was pure hydrogen and that the cation-permeable membrane precluded cross-over of S_n^{2-} or HS^- ions to the catholyte.

Figure 5-11 shows the temporal trends in charge yields for polysulfide formation at the anode by reaction (5-2) and hydrogen evolution at the cathode by reaction (5-4). Charge yields for hydrogen evolution were less than unity, sometimes decreasing to values < 0.8, probably due to expected gas leaks in the reactor over the course of longer term experiments. On the other hand, charge yields for polysulfide formation were very close to unity and their deviation could be explained by the uncertainty of the measurements and calibrations. This uncertainty ought to be computed in future studies with a larger number of samples and different rates of polysulfide oxidation by reaction (5-2).

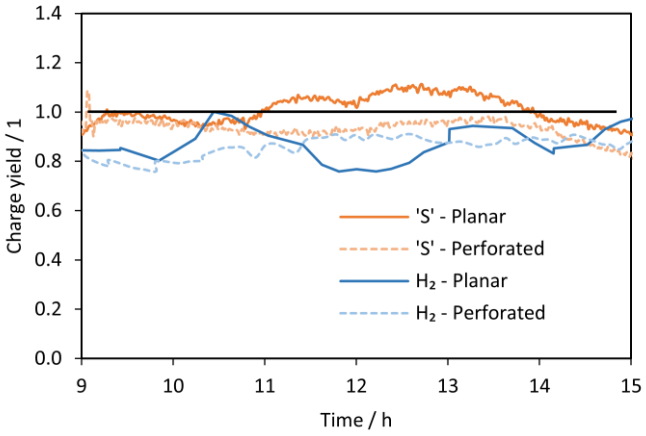


Figure 5-11. Time dependences of charge yields of polysulfide formation expressed as zero-valent sulfur in 1 mol dm^{-3} NaOH and 0.5 mol dm^{-3} Na_2S after HS^- oxidation and hydrogen in an 0.8 dm^3 electrochemical reactor for two different electrodes (planar and perforated) and applied cell potential difference of 1.226 V.

Table 5-4 summarises averaged charge yields for polysulfide formation in the electrochemical reactor. All estimations were very close to unity, reflecting the quality of the calibration, from which to determine, in situ and uninterruptedly, the rate of polysulfide evolution in electrochemical reactors for hydrogen sulfide oxidation.

Table 5-4. Summary of charge yields obtained by (top) charge integration of current densities and (bottom) averaged currents.

Reactor / dm^3	Calibration range / $\times 10^{-3}$ mol dm^{-3}	Time range / h	Integrated charge / C	Moles 'S' / $\times 10^{-3}$ mol	Charge yield
0.1	0 – 1.2	2 – 23	12.09	0.06518	1.040
0.1	1.2 – 5.0	14 – 54	30.65	0.1718	1.082
0.8	3.6 – 10	8 – 15	978.5	5.130	1.012
0.8	3.6 – 10	8 – 15	1685	8.323	0.953

Reactor / dm^3	Calibration range / $\times 10^{-3}$ mol dm^{-3}	Time range / h	Average current / mA	Molar rate 'S' / $\times 10^{-9}$ mol s^{-1}	Charge yield
0.1	0 – 1.2	2 - 23	0.1599 ± 0.012	0.8078	0.975 ± 0.071
0.1	1.2 – 5.0	14 - 54	0.2138 ± 0.019	1.180	1.065 ± 0.087
0.8	3.6 – 10	8 - 15	38.82 ± 2.39	207.2	1.030 ± 0.113
0.8	3.6 – 10	8 - 15	67.33 ± 18.28	344.2	0.986 ± 0.346

5.5 Conclusions

A methodology was developed for the quantification of polysulfide concentrations, expressed as zero-valent sulfur, via UV-vis spectrophotometry, and with the advantage of being able to measure in situ and uninterruptedly low concentrations of polysulfides. Charge yields close to unity confirmed the effectiveness of the developed technique.

Absorptions at 295 and 420 nm were used to build calibration curves at polysulfide concentrations between 0 and 0.01 mol dm^{-3} zero-valent sulfur. Three ranges of concentrations were necessary due to the non-linear behaviour of polysulfide speciation. This was confirmed by predicted polysulfide concentrations using equilibrium constants and molar absorption coefficients. Nevertheless, these parameters should be revised, as the only available data can be traced to dated studies. The effect of oxygen depletion and the purity of nitrogen (or any inert gas) used to deaerate the solutions was critical to avoid adventitious formation of sulfoxy species by homogeneous oxidation of HS^- and S_n^{2-} ions, reactions (5-7) to (5-11).

Chapter 6

Photo-assisted hydrogen sulfide splitting using tin-doped hematite[5]

6.1 Introduction

Hydrogen is produced conventionally via steam reforming of natural gas, partial oxidation of fossil fuels and electrolysis of water, with 96% of global hydrogen produced by the first two processes and 4 % by the third [24]. Clean hydrogen can be produced by a range of technologies, including biomass (combustion and gasification) and renewable energy source (solar, wind and hydro) + electrolyser [27]. The former technologies, although mature, require an initial conversion of energy to electrons which incurs power losses and increases capital costs. Photovoltaics + electrolyser have been reported to have the lowest exergy efficiency, while hydro + electrolyser has the highest [27].

6.1.1 Water splitting in photo-electrochemical cells

An emerging technology and the focus of this work, consists of the production of solar hydrogen directly at the electrode | electrolyte interface in a photo-electrochemical cell (PEC) [44]. Water electrolysis, often called water splitting, can be achieved using oxidising holes or reducing electrons produced at photo-electrode | electrolyte interfaces as a result of photon absorption in the semiconductor(s). In alkaline electrolytes, this process follows two half reactions for hydrogen and oxygen production at the (photo-) cathode and (photo-)anode, respectively.

$$2H_2O + 2e^-_{CB} \Leftrightarrow H_2 + 2OH^- \quad (6\text{-}1)$$

$$O_2 + 2H_2O \Leftrightarrow 4OH^- + 4h^+_{VB} \quad (6\text{-}2)$$

[5] This chapter was adapted from:
F. Bedoya-Lora, A. Hankin, G.H. Kelsall, Photo-electrochemical hydrogen sulfide splitting using Sn^{IV}-doped hematite photo-anodes, Electrochem. Commun., 68 (2016) 19-22.
F. Bedoya-Lora, A. Hankin, G.H. Kelsall, Solar-driven hydrogen sulfide splitting using Sn^{IV}-doped hematite photo-anodes, in preparation.

The potential difference between these two reactions plus the potential required to achieve thermo-neutral conditions, due to phase change (liquid to gas), represents the minimum potential difference requirement to drive the electrolysis at 298 K:

$$U_{\mathrm{H_2O|H_2}}(\mathrm{SHE})/\,\mathrm{V} = -0.0592\mathrm{pH} + 0.0296\log(p_{H_2}) \tag{6-3}$$

$$U_{\mathrm{O_2|H_2O}}(\mathrm{SHE})/\,\mathrm{V} = 1.229 - 0.0592\mathrm{pH} + 0.0148\log(p_{O_2}) \tag{6-4}$$

Hence, at a given pH, water splitting requires a standard equilibrium potential difference of 1.23 V, whereas the thermo-neutral potential is 1.48 V.

6.1.2 Hydrogen sulfide treatment

Most hydrogen is used as reactant for ammonia production (50%) and methanol (8%), and ironically, 37% is used back in petroleum processing [226], specifically in hydrodesulfurisation processes (HDS) to remove sulfur from gas and petroleum products, which in the generic case of methanethiol treatment follows the reaction [227]:

$$\mathrm{CH_3SH + H_2 \rightarrow CH_4 + H_2S_{(g)}} \tag{6-5}$$

The resulting highly toxic and corrosive hydrogen sulfide gas is then treated as waste using a Claus process to obtain elemental sulfur by the overall reaction:

$$\mathrm{6H_2S + O_2 \rightarrow 3S + 3H_2O} \tag{6-6}$$

This involves an initial thermal oxidation 950-1250 °C, followed by a catalytic oxidation stage at 170-350 °C, the conversion of which is limited by equilibria, so that tail gas from Claus plants requires further treatment to achieve adequate removal [10].

H_2S emissions also can be treated via thermal decomposition [68, 69, 228], photocatalysis [75, 229], and more attractively, by electrolysis of dissolved hydrogen sulfide ions in alkaline aqueous solutions between 25 and 80 °C and relatively low potentials (cell potential difference < 0.9 V) [73, 230, 231], due to lower energy requirements compared to water splitting:

$$\mathrm{'S' + H_2O + 2e^- \Leftrightarrow HS^- + OH^-} \tag{6-7}$$

$$\mathrm{2H_2O + 2e^- \Leftrightarrow H_2 + 2OH^-} \tag{6-1}$$

However, the oxidation of hydrogen sulfide ions to elemental sulfur by reaction (6-7) is not direct, but occurs via meta-stable polysulfide ions, S_n^{2-}, intermediate species [212]. That anode reaction can be coupled to cathodic hydrogen evolution by reaction (6-1) with a predicted equilibrium potential difference of ca. 0.3 V *vs.* RHE at pH 14 and a dissolved sulfur activity of 0.5 [74].

$$U_{\mathrm{S_2^{2-}|HS^-}}(\mathrm{RHE})/\,\mathrm{V} = 0.278 + 0.0296\log(\mathrm{S_2^{2-}}) - 0.0592\log(\mathrm{HS^-}) \tag{6-8}$$

6.1.3 Hydrogen sulfide splitting

In principle, solar energy may be used to drive water reduction reaction (6-1) with photogenerated electrons, coupled to oxidation of hydrogen sulfide ions by photogenerated holes:

$$S_n^{2-} + nH_2O \Leftrightarrow nHS^- + nOH^- + 2(n-1)h_{VB}^+ \quad (6\text{-}9)$$

Then elemental sulfur could be produced in an external reactor by aerial oxidation of dissolved polysulfides in alkaline aqueous solutions, thereby minimising passivation of photo-anodes by elemental sulfur:

$$S_n^{2-} + 0.5O_2 + H_2O \rightarrow n'S' + 2OH^- \quad (6\text{-}10)$$

The main issue with the electrolysis of hydrogen sulfide (photo-assisted or not) is to find suitable materials for highly corrosive environments and the passivation of the electrodes by sulfur deposition [69]. Both issues can be minimised by using alkaline solutions, reaction (6-9), and operating at optimised potentials in order to produce polysulfides directly at the anode by reaction (6-9) instead of elemental sulfur.

$$n'S' + HS^- + OH^- \Leftrightarrow S_{n+1}^{2-} + H_2O \quad (6\text{-}11)$$

The process of photo-assisted hydrogen sulfide splitting is summarised in Table 6-1.

Table 6-1. Steps for photo-assisted electrolysis of hydrogen sulfide ions in alkaline aqueous solution.

Process	Reaction	
Gas absorption	$H_2S + OH^- \rightarrow HS^- + H_2O$	(6-12)
Photo-activation	$\text{Semiconductor} + h\nu \Leftrightarrow \text{Semiconductor}(h_{VB}^+, e_{CB}^-)$	(6-13)
Oxidation	$nHS^- + nOH^- + 2(n-1)h_{VB}^+ \Leftrightarrow S_n^{2-} + nH_2O$	(6-9)
Reduction	$2H_2O + 2e_{CB}^- \Leftrightarrow H_2 + 2OH^-$	(6-1)
Aerial oxidation	$S_n^{2-} + 0.5O_2 + H_2O \rightarrow n'S' + 2OH^-$	(6-10)
Overall	$\mathbf{nH_2S + 0.5O_2 + 2(n-1)h\nu \rightarrow nS + H_2O + (n-1)H_2}$	(6-14)

Photo-assisted electrolysis of hydrogen sulfide has been known for several decades. Following its first mention by Grätzel [77], Licht et al. analysed the behaviour of $CdS|S_n^{2-}$ photo-electrodes in hydrogen sulfide solutions as a means of studying the instability of such electrodes in photo-electrochemical cells [78]. Bockris et al. found direct evidence of the feasibility of H_2S photo-electrolysis using CdSe photo-anodes, reporting conversion efficiencies of 1.5% for unbiased devices and 1.8% at a cell potential difference of 0.3 V [79]. The interest in this process was renewed recently as the delay in the deployment of devices for the less toxic water splitting is caused by difficulties in finding stable, efficient and scalable photo-electrodes. Also, hydrogen sulfide ions are often used as hole scavengers, due to faster kinetics and lower potential requirements with photo-absorbers such as Bi_2S_3 in small scale photo-electrochemical cells [80, 81]. Overall, hydrogen sulfide splitting to produce elemental sulfur without the need of further aerial oxidation was achieved for the first

time using an integrated PEC-chemical loop [82]; additional developments showed the possibility of unbiased and simultaneous production of hydrogen peroxide, achieving 1.1% conversion efficiencies [232]. However, a I_3^- / I^- redox couple and anthrahydroquinone is required in the anolyte and catholyte, respectively.

In order to avoid complexities and the use of intermediate chemical loops, the direct oxidation of hydrogen sulfide was studied on stable and easily fabricated Sn^{IV}-doped α-Fe_2O_3 photo-anodes. However, conversion efficiencies remained low due to the high electron-hole recombination losses of these photo-anodes.

Results are reported below for hydrogen sulfide oxidation and hydrogen production via photo-assisted electrolysis using Sn^{IV}-doped α-Fe_2O_3 photo-anodes, a well-characterised semiconductor for photo-electrochemical water splitting, see Chapter 1. This included an extended experiment of the stability of such photo-anodes for hydrogen sulfide splitting [74], the improved energy requirements versus water splitting, a possible mechanism of hydrogen sulfide ion oxidation in alkaline solutions, and photocurrent predictions using a modified model for up-scaled photo-electrochemical reactors, as the one described in Chapter 3. The modified model accounts for improved kinetics due to the presence of hydrogen sulfide ions in the anolyte.

6.2 Experimental

6.2.1 Photo-anode fabrication

Sn^{IV}-doped α-Fe_2O_3 photo-anodes were fabricated by spray pyrolysis and post-annealed as described in Chapter 1, page 61. Additionally, to the typical spray with 40 passes of precursor solution, films with 20, 60, 80 and 100 passes (precursor layers) were also produced, photographs of samples can be found in the Appendix, Figures S6-11. The effect of post-deposition annealing on the properties of the films were as discussed in Chapter 2, page 67. Briefly, electron-hole recombination rates decrease with annealing, while the maximum achievable photo-current decreases due to redistribution of Sn^{IV} dopant in the depletion layer of the photo-anode. Most of the Sn^{IV}-doped α-Fe_2O_3 samples used in here were not annealed after deposition in order to maximise photocurrent densities, albeit at the expense of higher applied potential; however, the effects of annealing Sn^{IV}-doped α-Fe_2O_3 on hydrogen sulfide splitting are discussed.

Before and after hydrogen sulfide splitting, photo-anodes were imaged and analysed by scanning electron microscopy (SEM) and energy-dispersive X-ray spectroscopy (EDX) in a Hitachi TM3030 SEM at 15 kV accelerating voltage. However, Sn^{IV}-doped α-Fe_2O_3 film thicknesses are much thinner, 47 ± 6 nm, than the EDX spatial resolution, ca. 1 μm^3. Then, the substrate, Ti, was expected to have a significant signal relative to the hematite films.

Sample replicates were synthesised in different batches of samples over 2 years using the same methodology. The confidence intervals of experimental averages are reported as ± 2σ, where σ is the standard deviation.

6.2.2 Photo-electrochemical cell (PEC) and reactor (PER)

A 0.06 dm^3 photo-electrochemical cell (PEC) with PVC body and a quartz window was used, typically with an aqueous electrolyte solution of 1 mol dm^{-3} NaOH (97%, Sigma-Aldrich) and 0.5 mol dm^{-3} Na_2S ($Na_2S{\cdot}9H_2O$ ≥99.99%, Sigma-Aldrich); in some experiments, the concentration of Na_2S was varied between 1 and 0.032 mol dm^{-3} at pH 14. 1 mol dm^{-3} NaOH solution, pH 13.6, was used for regular water splitting. A similar cell, bench-scale PER, but with two compartments (0.1 dm^3 each) separated by a cation-permeable membrane (PTFE reinforced Nafion® 424, DuPont Inc.) in order to minimise cross-over of HS^- and S_n^{2-} ions, was used for determination of polysulfide concentration to enable estimation of charge yields. In this case, the anolyte consisted of 1 mol dm^{-3} NaOH and 0.5 mol dm^{-3} Na_2S, while the catholyte was 1 mol dm^{-3} NaOH alone. Ti|Sn^{IV}-doped α-Fe_2O_3 electrodes with an active area of 1.8×10^{-5} m^2 were used as photo-anodes and a platinised titanium mesh (Expanded Metal Company) as counter electrode. All measurements in the PEC were carried out at 25 ± 2 °C.

An up-scaled photo-electrochemical reactor (PER) with PVDF body and quartz window, as described in Chapter 1, page 104, was used for estimation of hydrogen fluxes and charge yields. The planar and perforated Ti|Sn^{IV}-doped α-Fe_2O_3 photo-anodes used had geometric areas of 0.1 × 0.1 m^2. Planar photo-anodes were produced on 0.74 mm thick titanium foil (99.4% Alfa Aesar). Perforated (partially expanded) 1 mm thick titanium sheets (3 mm × 1.5 mm perforation size, spaced 5.8 mm horizontally and 2 mm vertically apart; The Expanded Metal Company) enabled less inhomogeneous spatial distributions of reaction rates / current densities in the reactor. The back and edges of the planar electrodes were covered with insulating acrylic lacquer, so exposing an effective electro-active and geometric area of 0.1 × 0.1 m^2. The back of perforated electrodes was fully covered; however, the walls inside the perforation were only partially covered due to their small size. Then, the electrode-active areas were expected to be higher than those in 0.1 × 0.1 m^2 electrodes. A thinner film of hematite was also expected to be present in some portions of the perforations, as the precursor could reach the walls during the spray pyrolysis. Photocurrent densities and fluxes of species were defined by the geometric area, which is the same for both, planar and perforated electrodes, 0.1 × 0.1 m^2. Anolyte, catholyte and cathode were as described for the PEC. Prolonged illumination during longer term experiments caused electrolyte temperatures to rise to ca. 40 °C within the first 6 hours.

Zero-grade nitrogen (99.998% and oxygen impurity removed, BOC) was bubbled into the anolyte for 1 hour before and continuously during experiments involving the quantification of polysulfide ion concentrations, in order to remove oxygen from the electrolyte and enforce a degree of convection/mixing. When nitrogen purging was not required, a magnetic stirrer was used to homogenise electrolyte solutions.

6.2.3 Electrochemical measurements

A potentiostat/galvanostat (Autolab PGSTAT 30 + Frequency Response Analysis module, Eco Chemie, Netherlands) was used to control both PEC and PER. A homemade 0.5 mol dm^{-3} Na_2S |

Ag_2S | Ag was used as pseudo-reference electrode with a theoretical equilibrium potential of 0.145 V *vs.* RHE at pH = 14. The Ag_2S|Ag pseudo-reference electrode was made by anodising a silver wire in 1.0 mol dm^{-3} Na_2S for 30 seconds at 1.5 V *vs.* RHE [233]. It was found to have fast kinetics and be very stable over extended periods. It was also checked regularly against a saturated calomel reference electrode (SCE) in alkaline sulfide solution (pH 14), with a measured equilibrium potential between 0.16 – 0.17 V *vs.* RHE. The Ag_2S|Ag equilibrium potential was corrected when using different concentrations of dissolved sulfur. For regular water splitting in 1 mol dm^{-3} NaOH (pH 13.6), a home-made HgO|Hg acted as reference electrode (0.913 V *vs.* RHE) for the PEC and a standard saturated AgCl|Ag (1.001 V *vs.* RHE) for measurements in the PER.

Frequencies of 10^5 to 10^{-1} Hz (10 points per decade) were used typically in electrochemical impedance spectroscopy measurements under dark (EIS) and illuminated (PEIS) [146, 147] conditions at different potentials (0.15 – 2.1 V *vs.* RHE) or at different times during long term (2 – 12 hours) electrolysis at fixed potentials. PEIS spectra were analysed following procedures reported elsewhere in order to estimate interfacial charge transfer efficiencies of photo-anodes [145-147]. A more detailed description of this analysis for Ti|Sn^{IV}-doped α-Fe_2O_3 photo-anodes was described in Chapter 1, pages 64 and 72, using an electrical equivalent circuit $R_s(Q_{SC}[R_t(Q_rR_r)])$, where constant phase elements (CPE), *Q*, were used instead of pure capacitances, *C*. Similarly, Mott-Schottky (MS) analysis was made after fitting the spectra gathered under dark conditions to an electrical equivalent circuit $R_s(Q_{SC}R_t)$. Flat band potentials and donor densities were estimated. However, as presented in Chapter 2, pages 63 and 69, these values are to be used cautiously when nano-structured electrodes are used [43], due to the violation of some key underlying premises in the derivation of the Mott-Schottky equation (e.g. perfect homogeneity of the electrode surface).

Incident photon-to-current conversion efficiencies (ICPE) were evaluated under steady state conditions at different applied potentials (0.51 – 1.71 *vs.* RHE) from 300 to 700 nm in 20 nm increments for 100 s. Cyclic voltammograms were run from 0.1 and 1.7 V *vs.* RHE for hydrogen sulfide splitting and 0.5 and 2.0 V *vs.* RHE for water splitting at scan rates of 500, 100, 50, 10 and 1 mV s^{-1} under unstirred, stirred, illuminated and dark conditions.

6.2.4 Quantification of polysulfide concentrations and hydrogen fluxes

Polysulfide ions were determined as zero-valent sulfur, 'S', in the anolyte using in-situ UV spectrophotometry, and hydrogen fluxes using a gas flow meter as described in Chapter 5, page 125. The time to reach steady state was typically 3 to 8 hours for experiments with the PER. All fluxes and current densities were normalized by the geometrical area of the photo-anodes. Charge yields were estimated as described in Chapter 5, page 127.

6.2.5 Light sources

The PEC was illuminated with a 300 W Xe arc lamp (LOT-Oriel) with a beam size of 1.8×10^{-5} m^2, as described in Chapter 1, page 61. Power densities between 3 600 – 3 000 W m^{-2} were recorded and reported accordingly for each experiment in the results section. Greater light intensities

(> 1 000 W m^{-2}) allowed a better resolution of the processes in the impedance spectra and increased the magnitude of photocurrent with respect to dark currents, especially for hydrogen sulfide splitting. Also, concentrated solar has been studied recently as a possible solution to reduce the cost of PEC devices [131, 234]. The linearity of the photo-response of hematite as a function of the light intensity was confirmed in Chapter 2, Figure S6-1, for power densities between 400 and 2 500 W m^{-2} and also supported by independent studies using a wider range of photon fluxes, 570 to 27 200 W m^{-2} [234]. In the case of the PER, a solar simulator (Sun 2000, Abet technologies, USA) with a 550 W Xe arc lamp was used to irradiate the photo-anode as described in detail in Chapter 4, page 104.

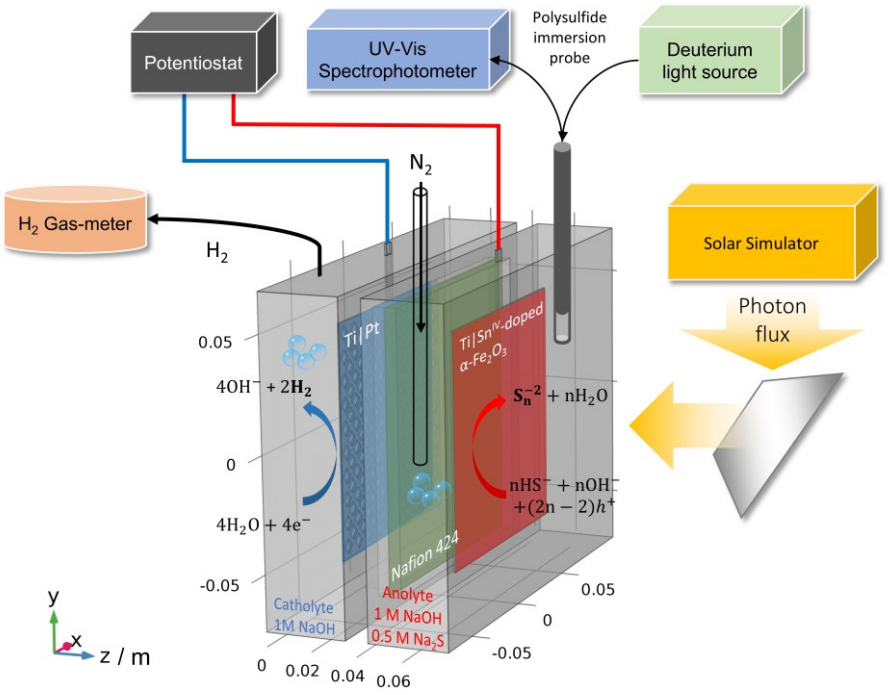


Figure 6-1. Equipment for photo-assisted electrolysis of hydrogen sulfide ions in alkaline solution.

The intensity of light was corrected for attenuation by electrolyte and quartz window using an average transmittance of 0.92 and 0.87 for alkaline (1 mol dm^{-3} NaOH) and hydrogen sulfide (1 mol dm^{-3} NaOH and 0.5 mol dm^{-3} Na_2S) solution, respectively.

Figure 6-1 shows a schematic of the equipment arrangement used for hydrogen sulfide splitting studies in a PER.

6.2.6 Numerical considerations

Comsol Multiphysics 5.2a with a Batteries and Fuel Cells module was used to solve the system using the finite element method. A detailed description of the model, mesh and processing times can be found in Chapter 3, page 90.

6.3 Results and discussion

6.3.1 Hydrogen sulfide splitting *vs.* water splitting

Na_2S dissolves in alkaline solutions ($pH \approx 14$) to form mainly HS^- ions ($pK_{HS^-} = 7$), see Figure 5-4 [73]. The presence of S^{2-} ions can be disregarded as $pK_{S^{-2}} = 17 - 19$ [73, 216]. The predicted thermodynamic potential for oxidation of hydrogen sulfide ions is 0.9 V lower than that required for water splitting. This was confirmed in the inset of Figure 6-2 for dark currents, the onset of polysulfide ion evolution was ca. 0.4 V *vs.* RHE, while for oxygen evolution was ca. 1.3 V. Accordingly, photocurrent densities were shifted (ca. 0.5 V) towards lower potentials due to the increased rates of interfacial charge transfer. Figure 6-2 shows the photo-response of three different samples synthesised at different periods over 2 years using the same methodology. It shows clearly the reproducibility of unannealed Ti|Sn^{IV}-doped α-Fe_2O_3 samples. The improved interfacial charge transfer was confirmed by IPCE measurements and interfacial charge transfer efficiencies, as shown in Figure 6-3. Water splitting reached similar IPCE values to hydrogen sulfide splitting only for photo-anode potentials > 1.7 V *vs.* RHE (Figure 6-3(a)), c.f. 1.24 V *vs.* RHE in Figure 6-3(b).

Interfacial charge transfer efficiency associated with a decreased electron-hole recombination at the surface of the photo-anode is shown in Figure 6-3(c). Similarly, there was a shift towards lower electrode potentials of ca. 0.5 V when hydrogen sulfide ions were present in the electrolyte. When a better hole scavenger is used, e.g. H_2O_2, interfacial charge transfer efficiency could reach unity at any potential starting from the flat band of hematite samples (0.7 V *vs.* RHE), as shown in Figure 2-3 and Figure 2-4. However, this was not observed entirely for hydrogen sulfide solutions. As seen in Figure 6-3(c), interfacial electron-hole recombination was still predominant for hematite samples between 0.7 and 0.9 V vs. RHE. In the presence of hydrogen sulfide recombination was greatly minimised compared with methanol as hole scavenger [235].

Compared with those for water splitting (Figure 6-3(a)), smaller IPCEs were recorded for hydrogen sulfide splitting at wavelengths < 350 nm (Figure 6-3(b)), due to photon absorbance by hydrogen sulfide and polysulfide ions in the UV region as light passes through the electrolyte. However, this accounts for only 1.4% of the total irradiance and ca. 4% of the absorbed light by hematite photo-anodes after integration of the solar spectrum. The atypical IPCE tail at longer wavelengths in the presence of hydrogen sulfide ions ($\lambda < 600$ nm in Figure 6-3(b)), might be due to the formation of iron sulfides (lower band gaps) on the photo-anode surface.

The estimation of flat band potentials of Ti|Sn^{IV}-doped α-Fe_2O_3 samples was attempted using Mott-Schottky analysis, as shown in Figures S6-1 and Table S6-1 in the Appendix. However, flat band potentials were not very reproducible and not consistent with previous estimations for the same material using different techniques as presented in Chapter 2, page 71. Then, flat band potentials were estimated using open circuit potential (OCP) measurements using high intensity illumination (> 2 600 W m^{-2}), resulting in values between 0.72 and 0.76 V *vs.* RHE, which are similar to the values reported in Chapter 2, page 71 (ca. 0.71 V *vs.* RHE).

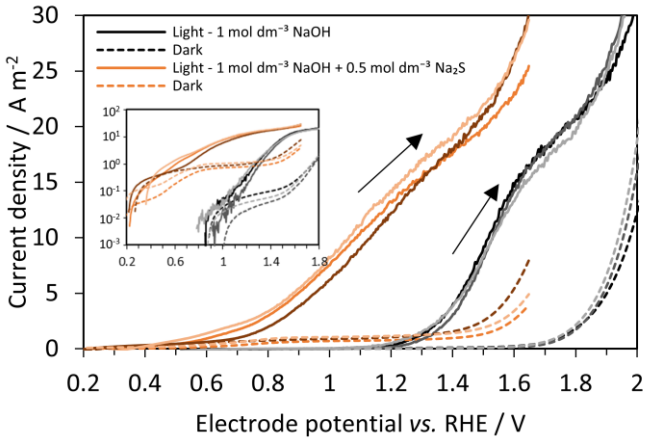


Figure 6-2. Linear sweep voltammograms for 3 replicates of Ti | Sn^{IV}-doped α-Fe_2O_3 | 1 mol dm^{-3} NaOH ± 0.5 mol dm^{-3} Na_2S (pH = 14) | Pt | Ti under dark and illuminated conditions in a PEC; 10 mV s^{-1} scan rate. Xe arc lamp irradiance 2 670 W m^{-2}. Inset: semi-log plot.

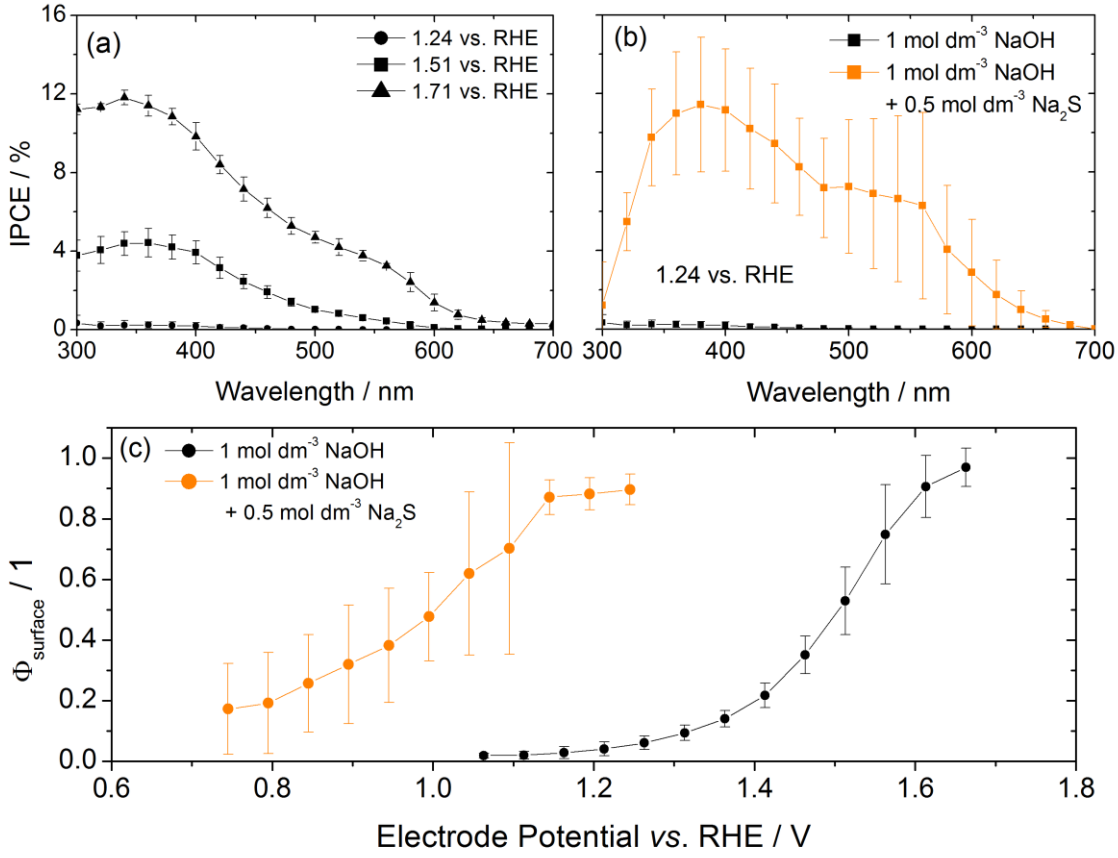


Figure 6-3. (a) Effects of irradiation wavelength and photo-anode potentials on IPCE of Ti | Sn^{IV}-doped α-Fe_2O_3 | 1 mol dm^{-3} NaOH | Pt | Ti (water splitting). (b) IPCE of water splitting and hydrogen sulfide splitting for Ti | Sn^{IV}-doped α-Fe_2O_3 | 1 mol dm^{-3} NaOH + 0.5 mol dm^{-3} Na_2S | Pt | Ti at 1.24 V *vs.* RHE. (c) interfacial charge transfer efficiencies of Ti|Sn^{IV}-doped α-Fe_2O_3 in presence and absence of hydrogen sulfide ions.

As shown in Figure S6-2 in the Appendix, the effect of the number (20 to 100) of passes of the nebuliser head spraying Fe^{III} precursor during the synthesis of Ti|Sn^{IV}-doped α-Fe_2O_3 was not significant on photocurrent densities for water splitting. There was a small shift towards lower

electrode potentials that could have been associated with the effect of longer exposure to heat while the substrate was kept at 480 °C during the nebulisation of the precursor. This could have had an annealing effect on the photo-anode that, as discussed in Chapter 2, could have decreased electron-hole recombination rates due to the diffusion of dopant Sn^{IV} towards photo-anode surfaces. Although electron-hole recombination rates were not affected significantly, IPCE values at 1.51 V *vs.* RHE increased from 6% to 8% from 20 to 100 layers, but no significant trend was detected at 1.71 V *vs.* RHE. The absorption length, α^{-1}, of hematite at $\lambda = 400\,\text{nm}$ and $550\,\text{nm}$ are $\alpha^{-1} = 44\,\text{nm}$ [236] and $118\,\text{nm}$ [60], respectively. However, the charge separation due to photon absorption occurs only in the depletion layer of the semiconductor, which is ca. 10 nm for hematite [91]. Thus, film thicknesses greater than 10 nm, i.e. 40 or more layers, should not have affected maximum photocurrent densities significantly. On the other hand, rates of hydrogen sulfide oxidation increased greatly from 20 to 60 layers. This may have been due an increased electro-active area or morphological changes in the nano-structured samples, but also decreased electron-hole recombination rates due to annealing during the spray pyrolysis. The absorbance of the samples with 20 and 40 layers confirmed a band gap of ca. 2.1 eV; however, samples with $>$ 40 layers were very opaque, making it difficult to study the effect of photon absorption on thicker samples with significant light scattering. A more detailed study of the effect of film thickness on hydrogen sulfide splitting will be carried out in the future.

As presented previously for regular water splitting in Chapter 2, the effects were studied of time and temperature of annealing after spray pyrolysis. Figure 6-4 shows the photo-response of Ti | Sn^{IV}-doped α-Fe_2O_3 annealed at different conditions. For regular water splitting in 1 mol dm^{-3} NaOH (dashed lines in Figure 6-4), annealing decreased electron-hole recombination rates in HS^- solutions. The effect was evident from the shift of photocurrent densities toward lower electrode potentials, while the maximum photocurrent densities decreased with annealing time and temperature. IPCE and PEIS spectra showing the effect of annealing were also reported in Figure S6-3 and S6-4 in the Appendix. Hydrogen sulfide splitting rates increased after annealing for between 20 and 40 min at 400 °C. PEIS spectra showed a decreased of recombination process, shifting photocurrents towards lower electrode potentials with annealing. This is also evident in Figure 6-4, in which the maximum photocurrent densities (at a. 1.4 V vs. RHE) for hydrogen sulfide splitting decreased only slightly for samples annealed at 400 °C between 20 and 40 min, while the shift towards lower electrode potentials was significant. In spite of this, unannealed Ti|Sn^{IV}-doped α-Fe_2O_3 samples and those annealed at 400 °C exhibited similar photocurrent densities ca. 1.4 V vs. RHE.

The results shown above confirmed that the photo-response of Ti|Sn^{IV}-doped α-Fe_2O_3 can be improved to some extent with annealing treatment and increasing the hematite thickness. However, these improvements are needed to be proved worthy considering the extra energy used for the synthesis. From this point forward, the samples studied were not treated with heat (unannealed) and deposited with 40 passes of precursor during spray pyrolysis to achieve a film thickness of 47 ± 6 nm.

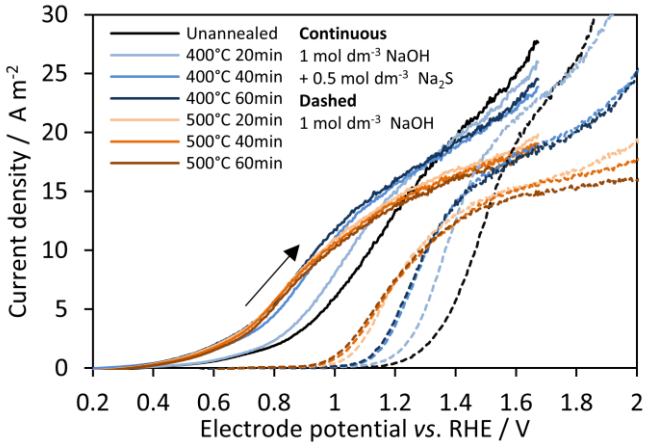


Figure 6-4. Linear sweep voltammograms for Ti|Sn^{IV}-doped α-Fe_2O_3 samples, annealed at different temperatures and times, under illumination in 1 mol dm^{-3} NaOH (dashed) and 1 mol dm^{-3} NaOH + 0.5 mol dm^{-3} Na_2S (continuous); 10 mV s^{-1} scan rate. Xenon arc lamp irradiance 3 000 W m^{-2}.

6.3.2 Stability of Sn^{IV}-doped α-Fe_2O_3 photo-anodes

Potentiostatically controlled Sn^{IV}-doped α-Fe_2O_3 photo-anodes exhibited stable photocurrent densities for hydrogen sulfide splitting for up to 75 hours [74]. Figure 6-5 shows the temporal dependence of current densities at 1.15 V *vs.* RHE of Ti|Sn^{IV}-doped α-Fe_2O_3 in solutions with different hydrogen sulfide concentrations. The same figure also shows time dependence of the low frequency admittance (inverse of impedance at 1 Hz, measured every 10 min). The results confirmed that higher hydrogen sulfide ion concentrations allowed the elemental sulfur deposited on the electrode to be chemically reduced in the diffusion layer by reaction (6-11), but only once it detached from the electrode due to its weak adhesion to the photo-anode by Van der Waals forces [237].

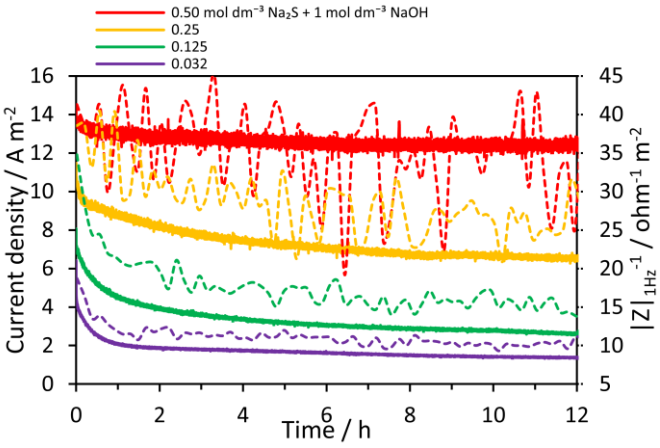


Figure 6-5. Time dependences of current densities (continuous, left axis) and admittances at 1 Hz (dashed, right) for Ti | Sn^{IV}-doped α-Fe_2O_3 | 1 mol dm^{-3} NaOH + X mol dm^{-3} Na_2S | Pt | Ti at an applied photo-anode potential of 1.15 V *vs.* RHE and in the presence of different concentrations of hydrogen sulfide ions. Xenon Arc lamp irradiance 2670 W m^{-2}.

The decrease in admittance can be associated with a partial deactivation of electro-active area due to sulfur deposition, as will be discussed in detail later. This was confirmed by visual inspection after electrolysis with concentrations < 0.125 mol dm^{-3} Na_2S: photo-anodes were covered partially with a yellow layer, which disappeared subsequently after immersion in concentrated hydrogen

sulfide ions solutions (> 0.5 mol dm^{-3} Na_2S). The phase shift extracted from the PEIS spectra is shown Figure 6-6. The process between 10^3 and 10^4 Hz, which was associated with the hindrance to charge transfer by coverage by sulfur of electro-active area, appeared to become more predominant as concentrations of hydrogen sulfide were decreased. It was also evident for 0.125 mol dm^{-3} Na_2S electrolyte solutions that this process was not predominant in the first hour, but developed fully with increasing time. The complete PEIS spectra were reported in Figure S6-5 in the Appendix.

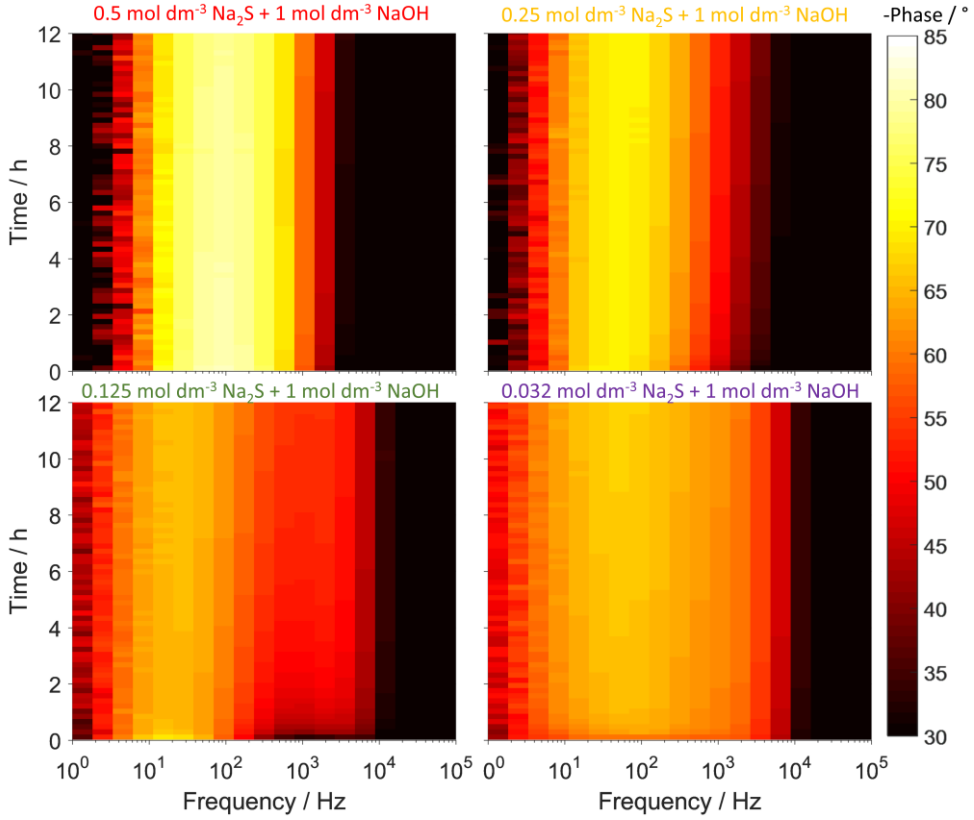


Figure 6-6. Phase shift of PEIS spectra as a function of time for Ti | Sn^{IV}-doped α-Fe_2O_3 | 1 mol dm^{-3} NaOH + X mol dm^{-3} Na_2S | Pt | Ti at an applied photo-anode potential of 1.15 V *vs.* RHE and in the presence of different concentrations of hydrogen sulfide ions. Xenon arc lamp irradiance 2 670 W m^{-2}.

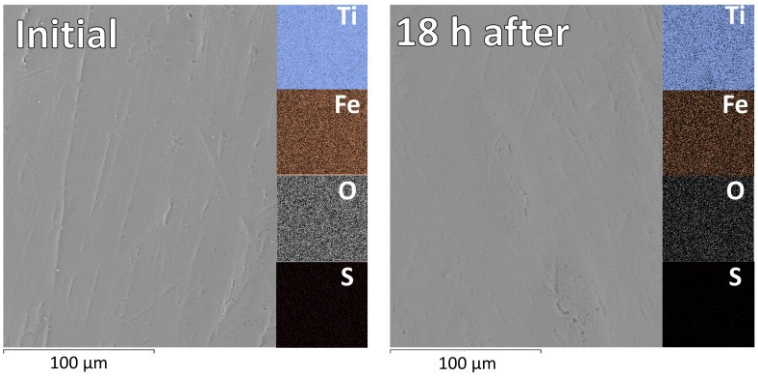


Figure 6-7. SEM images and EDX analysis of Ti|Sn^{IV}-doped α-Fe_2O_3 photo-anodes before and after continuous hydrogen sulfide splitting at 1.15 V *vs.* RHE.

Ti|Sn^{IV}-doped α-Fe_2O_3 photo-anodes were stable for 18 hours of photo-assisted hydrogen sulfide electrolysis, as confirmed by SEM images and EDX analysis, shown in Figure 6-7 and Table 6-2, respectively. The electrodes were washed carefully after the electrolysis to remove any residual sulfur deposited on the surface. Elemental analysis showed almost no change in the atomic concentration of the main elements. The presence of sulfur was not significant after 18 hours of photo-assisted electrolysis. This could be due to the oxidation of possible iron sulfide species formed during photo-electrolysis back to the hematite when the electrode is exposed to air. The presence of Ti in the EDX analysis both before and after exposure to HS^- was due to the substrate as the Sn^{IV}-doped α-Fe_2O_3 film was ca. 50 nm thick.

Table 6-2. EDX elemental analysis of Ti|Sn^{IV}-doped α-Fe_2O_3 photo-anodes before and after 18 h of continuous hydrogen sulfide splitting at 1.15 V *vs.* RHE.

Element	Atomic %	
	Before	After 18 h of HS^- exposure
S	0.00 ± 0.03	0.01 ± 0.07
Ti	30.22 ± 0.07	31.64 ± 0.41
Fe	4.57 ± 0.06	4.67 ± 0.04
Sn	0.06 ± 0.02	0.01 ± 0.04
O	65.14 ± 0.11	63.68 ± 0.24

6.3.3 Mechanism of hydrogen sulfide splitting

The possible reactions occurring at the surface of the cathode and photo-anode for hydrogen sulfide electrolysis are described below, followed by chemical reactions happening in the diffusion layer and bulk in the electrolyte. For dark conditions, the photo-generated holes on the right-hand side of the electrochemical reaction in the photo-anode can be replaced by an equal number of electrons on the left-hand side.

Electrochemical reactions:

On the cathode:

E_1: $$2H_2O + 2e^-_{CB} \Rightarrow H_2 + 2OH^- \quad (6\text{-}1)$$

On the photo-anode:

E_2: $$O_2 + 2H_2O \Leftrightarrow 4OH^- + 4h^+_{VB} \quad (6\text{-}2)$$

E_3: $$'S' + H_2O \Leftrightarrow HS^- + OH^- + 2h^+_{VB} \quad (6\text{-}15)$$

E_4: $$S_n^{2-} + nH_2O \Leftrightarrow nHS^- + nOH^- + 2(n-1)h^+_{VB} \quad (6\text{-}9)$$

E_5: $$n'S' \Leftrightarrow S_n^{2-} + 2h^+_{VB} \quad (6\text{-}16)$$

E_6: $$S_{n+1}^{2-} + H_2O \Leftrightarrow S_n^{2-} + HS^- + OH^- + 2h^+_{VB} \quad (6\text{-}17)$$

Chemical reactions in the anolyte:

C_1: $$HS^- + 0.5O_2 \Leftrightarrow 'S' + OH^- \quad (6\text{-}18)$$

C_2: $$S_n^{2-} + 0.5O_2 + H_2O \Leftrightarrow n'S' + 2OH^- \quad (6\text{-}10)$$

C_3: $$n'S' + HS^- + OH^- \Leftrightarrow S_{n+1}^{2-} + H_2O \quad (6\text{-}11)$$

C_4: $$(n-2)S_n^{2-} + HS^- + OH^- \Leftrightarrow (n-1)S_{(n-1)}^{2-} + H_2O \quad (6\text{-}19)$$

The limiting current density for a process controlled by diffusion can be estimated as follows [35]:

$$j_L = \nu_{e,i} F D_i \frac{c_{i,\text{bulk}}}{\delta} \quad (6\text{-}20)$$

Where δ is the mean thickness of the diffusion layer, $c_{i,\text{bulk}}$ the concentration in the bulk and $\nu_{e,i}$ the reaction charge number. The diffusion coefficient of sulfide species were reported to be $D_i = 1.73 \times 10^{-9}\ m^2\ s^{-1}$, at 298 K, the mean thickness of the diffusion layer can be estimated as $\delta = 1 \times 10^{-4}$ [238] and assuming conversion of hydrogen sulfide ions to zero-valent sulfur, i.e. $\nu_{e,i} = 2$, the estimated limiting current for 0.5 and 0.032 mol dm^{-3} Na_2S were $j_L = 1.7 \times 10^3\ A\ m^{-2}$ and $1.1 \times 10^2\ A\ m^{-2}$, respectively. Comparing these values with current densities reported in Figure 6-5, showed that photo-assisted oxidation of hydrogen sulfide ions to polysulfide ions or elemental sulfur was several orders of magnitude lower than the solution phase transport limited current densities. Hence, processes reported here were controlled by the charge transfer rate, except for oxidation of polysulfide ions in the diffusion layer near the photo-anode | electrolyte interface, which were at lower concentrations. Also, depletion of hydrogen sulfide ions during long term electrolysis ($>$ 2 hours), assuming unity charge yields, was $<$ 0.1% mol in the bench-scale reactors and $<$ 3.5 % mol for electrolysis in the up-scaled reactor. Thus, the effects on the current densities of hydrogen sulfide ion depletion can be disregarded.

The homogeneous chemical reaction of elemental sulfur to polysulfide ions, C_3, usually requires long periods ($>$ 6 hours) to reach equilibrium, as reported in the previous chapter. On the other hand, polysulfide speciation [210], C_4, is fast and can be achieved inside the diffusion layer of polysulfide ions.

Cyclic voltammograms under dark and illuminated conditions were carried out in presence of hydrogen sulfide ions for stirred and quiescent electrolytes in the PEC. Figure 6-8(a) shows the current densities at different ranges of electrode potential without illumination of Ti|Sn^{IV}-doped α-Fe_2O_3 in 1 mol dm^{-3} NaOH + 0.5 mol dm^{-3} Na_2S solution without stirring. Under these conditions, the increase in current densities with every cycle after 1.6 V *vs.* RHE was due to the accumulation near the photo-anode | electrolyte interface surface of polysulfide ions, which have more facile oxidation kinetics than their HS^- ion precursors. Current densities increased with every cycle but stabilised after the rate of deposition of elemental sulfur, due to direct oxidation (reaction (6-7) and

(6-16)) or indirect oxidation in presence of oxygen (reaction (6-2) followed by (6-10)), at equilibrium with the reduction of detached sulfur to polysulfides by reaction (6-11) in the diffusion layer. The photo-response was also affected by the accumulation of polysulfides near the photo-anode surface, which means that the dark current contribution increased the total current density at potentials 0.8 > V *vs.* RHE, as shown in Figure 6-8(b). Figure 6-8(c) shows a linear polarisation at 1 mV s^{-1} scan rate for negative-going and positive-going potentials, with experimentally measured equilibrium potentials for polysulfide production from HS^- oxidation by reaction (6-9), $E^0 = 0.29$ to 0.41 V *vs.* RHE depending on the order of the polysulfide generated; and the sulfur reduction on the negative-going scan due to sulfur deposited on the electrode by reaction (6-16), $E^0 = 0.517$ V *vs.* RHE, as shown in the previous chapter in Figure 5-2. Experimentally measured equilibrium potentials were close to the theoretical values, the small shifts to positive potentials can be due to the presence of adventitious oxygen in solution or inaccuracy of the reference electrode.

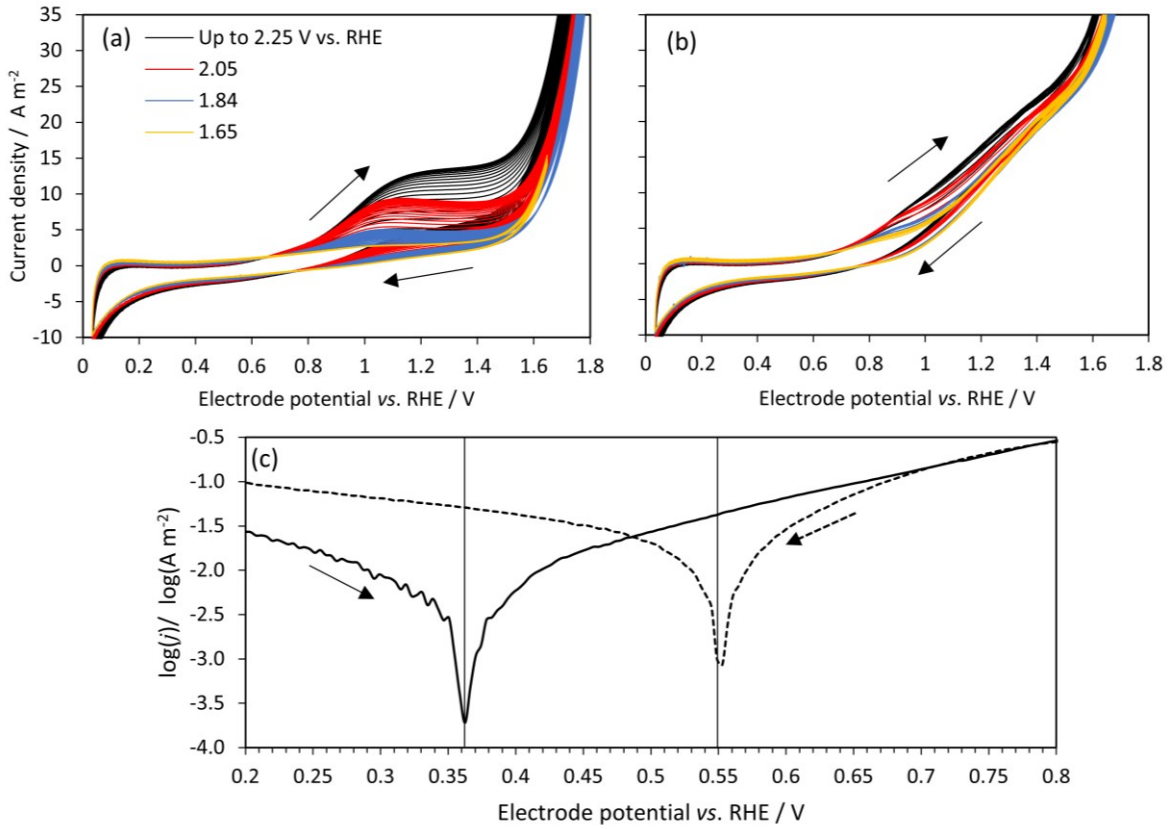


Figure 6-8. Cyclic voltammograms (20 cycles) under (a) dark and (b) illuminated conditions and quiescent electrolyte for Ti | Sn^{IV}-doped α-Fe_2O_3 | 1 mol dm^{-3} NaOH + 0.5 mol dm^{-3} Na_2S | Pt | Ti with different upper limits of photo-anode potential and 500 mV s^{-1} scan rate. (c) Linear polarizations for positive-going and negative-going potentials under dark conditions and 1 mV s^{-1} scan rate. Xenon arc lamp irradiance 2 900 W m^{-2}.

Figure 6-9 shows cyclic voltammograms for narrower electrode potential ranges and higher concentrations of hydrogen sulfide ions (1 mol dm^{-3} Na_2S), with and without stirring. As in Figure 6-8, current densities increased with every scan for quiescent solutions when the upper potential limit was increased from 0.89 to 1.19 V *vs.* RHE, as shown in Figure 6-9(a). Polysulfide ions were produced at the electrode and to some degree elemental sulfur was also deposited at the surface

until a stable current density was achieved after several cycles, as discussed for Figure 6-8. There was not a significant increase of current densities with further increase of electrode potential from 1.19 to 1.39 V *vs.* RHE, implying that direct oxidation to sulfur by reactions (6-7) and (6-16), and polysulfide formation by reaction (6-9), were still the only predominant reactions. Further increase of electrode potential to 1.64 V *vs.* RHE again resulted in current densities increasing with each cycle. This can be due to indirect oxidation, due to oxygen generation, of polysulfide and hydrogen sulfide ions to elemental sulfur which is then reduced back to polysulfide ions in solution. Polysulfide ions then accumulated near the photo-anode surface and were easier to oxidise than hydrogen sulfide ions. The effect of polysulfide ion accumulation near the surface and the increase of current densities with every cycle disappeared completely on stirring of the electrolyte, as shown in Figure 6-9(b). Current densities were then due only to reactions involving hydrogen sulfide ions (< 1.2 V vs. RHE) and oxygen evolution (> 1.4 V vs. RHE) because of the dispersion of polysulfide ions into the bulk of the electrolyte.

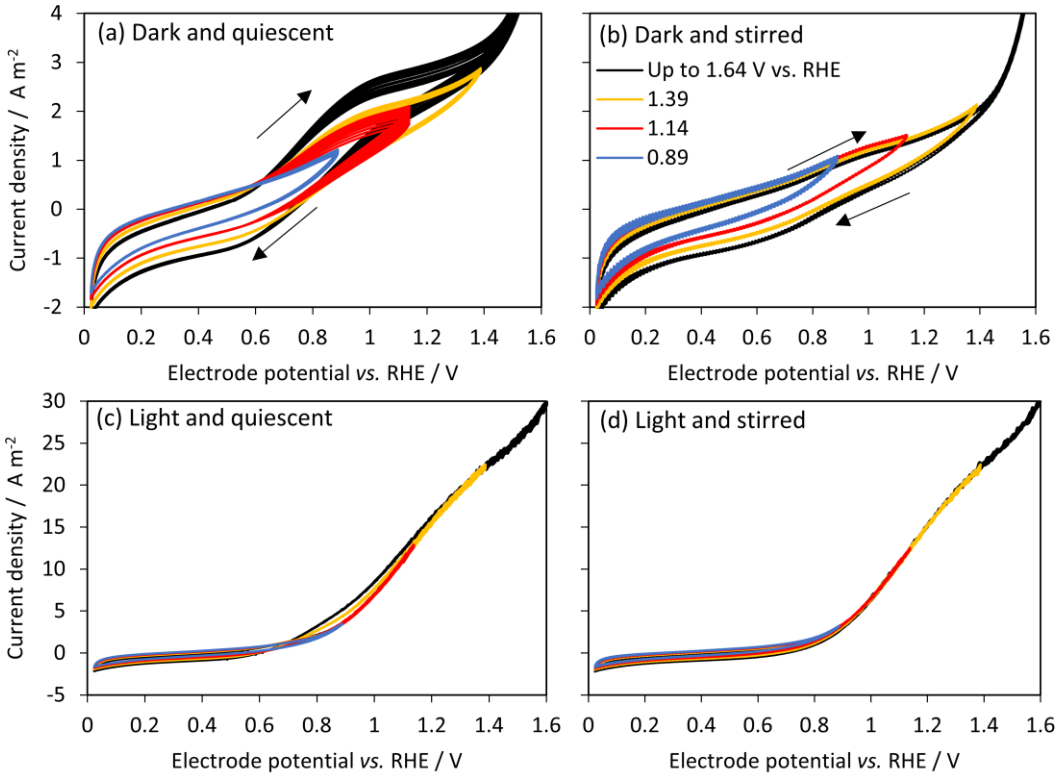


Figure 6-9. Cyclic voltammograms (20 cycles) under (a) dark and quiescent electrolyte, (b) dark and stirred electrolyte, (c) illuminated and quiescent and (d) illuminated and stirred conditions for Ti | Sn^{IV}-doped α-Fe_2O_3 | 1 mol dm^{-3} NaOH + 1.0 mol dm^{-3} Na_2S | Pt | Ti with different photo-anode potential upper limits and 50 mV s^{-1} scan rate. Xenon arc lamp irradiance 2 900 W m^{-2}.

The effect of polysulfide ion accumulation on the photocurrent densities was less evident for higher concentrations of HS^- ions, as photocurrent densities were typically an order of magnitude greater than dark current densities. Figure 6-9(c) shows a slight increase in the photocurrent densities between 0.7 and 1.1 V *vs.* RHE for quiescent electrolytes and illuminated photo-anodes after increasing the upper-limit electrode potential. As shown in Figure 6-9(d), this effect was even

less evident for stirred electrolytes. A comparison of current densities for hydrogen sulfide splitting under stirred and quiescent electrolytes and different concentrations of hydrogen sulfide ions is presented in Figure S6-7 in the Appendix.

These results confirm how the accumulation of polysulfide ions near the surface of the photo-anode for quiescent conditions affected the current densities at every cycle. At the same time, current densities were stabilised after several cycles by the deposition of elemental sulfur on the surface of the electrode at lower concentrations of hydrogen sulfide ions, which hindered the reduction of sulfur back to soluble polysulfides. It also showed that photocurrent densities for stirred electrolytes were slightly lower than quiescent electrolytes. This again can be explained by the accumulation of easily oxidise polysulfides ions in quiescent electrolytes near the photo-anode that were not present otherwise.

Figure 6-10(a) and Table 6-3 summarise a possible mechanism for hydrogen sulfide splitting in alkaline conditions, with sulfoxide species excluded from consideration. At electrode potentials < 1.4 V *vs.* RHE, the evolution of oxygen was minimised and the oxidation of HS^- to S_n^{2-} and 'S' would be the predominant reactions. Also, it is expected that operating at potentials close to 1 V *vs.* RHE and at hydrogen sulfide concentrations > 0.5 mol dm^{-3}, the amount of deposited sulfur on the surface is also minimised, as concluded from Figure 6-5 and Figure 6-6. The rates of the different reactions involved in hydrogen sulfide splitting on Sn^{IV}-doped α-Fe_2O_3 and confirmation of the equilibrium potentials require a more comprehensive future study. However, it can be concluded that when operating at potentials < 0.6 V *vs.* RHE, elemental sulfur was almost absent. On the other hand, the amount of sulfur electrodeposited increased at lower concentrations of hydrogen sulfide ions and potentials > 1 V *vs.* RHE; additionally, it was exacerbated after oxygen began to be evolved at the photo-anode, resulting in a decreased electro-active area by reactions involving the generation of elemental sulfur, E_3, E_5, C_1 and C_2 in Table 6-3. If the electrolyte was stirred, reactions involving polysulfide ions (dissolved species) were minimised, reactions E_5, E_6 and C_2. While the only reaction 'dissolving' the elemental sulfur back to polysulfide ions, corresponding to C_3 in Table 6-3, depended on the hydrogen sulfide ion concentration and was overtaken by electrochemical reactions (6-16) and (6-15) at potentials > 0.6 V vs. RHE.

A scheme of the expected concentration profiles of sulfide species is shown in Figure 6-10(b), accompanied by electrochemical and homogeneous chemical reactions associated with their formation. Several assumptions were considered: intermediate electrode potentials, i.e. ca. 1 V *vs.* RHE; fast kinetics for homogeneous chemical reactions, C_3 and C_4; charge transfer controlled process at lower current densities for hydrogen sulfide ion oxidation, E_3 and E_4; while reactions associated with $S_{n<5}^{2-}$ oxidation, E_5 and E_6, were mass transport controlled due to their relatively low concentrations. Elemental sulfur and S_5^{2-} ions were formed at surface of the electrode (E_3 to E_6), while being reduced by HS^- ions in the diffusion layer. A bell-shaped concentration profile of $S_{n<5}^{2-}$ ions was caused by the oxidation of these species back to S_5^{2-} and elemental sulfur at the electrode | electrolyte interface. Conversely, $S_{n<5}^{2-}$ ions diffused towards the bulk to be chemically reduced by HS^- ions, producing polysulfide ions of lower order. Elemental sulfur can be electrodeposited on the

surface of the electrode at potentials between 1 and 1.6 V *vs.* RHE; but lower concentrations of hydrogen sulfide ions, ca. 0.005 mol dm^{-3} Na_2S, are necessary for total passivation of the electrode under mass transport control electrolysis [238]. Elemental sulfur adheres to the surface of the electrode by weak Van der Waals forces [237], as it is not expected to react with hematite and could be washed off with sulfide aqueous solution or distilled water relatively easy. The reduction of elemental sulfur, by reaction C_3, is not expected to happen at the electrode | electrolyte interface, which is maintained at potentials at which this reaction should not be possible. Instead, particles of sulfur were expected to be detached from the electrode and move towards the bulk through the diffusion layer, in which it was reduced by HS^- ions, forming polysulfide ions. The higher the concentration of HS^- ions, the higher rate of the homogeneous chemical reduction of elemental sulfur to highly soluble polysulfide ions. The proposed mechanism is supported by the temporal behaviour of the low frequency admittance ($|Z|_{1Hz}^{-1}$) at different hydrogen sulfide ion concentrations and high electrode potentials, as shown in Figure 6-11. The admittance decreased with time for all conditions as the electrode became covered by elemental sulfur over time. However, this decay was faster for quiescent electrolytes as there were two additional reactions promoting the formation of elemental sulfur from dissolved species. In contrast, this decay was slower for low concentrations of hydrogen sulfide as the area was rapidly covered from the beginning of the test and elemental sulfur was not reduced fast enough back to polysulfide ions. Stirred electrolytes showed lower admittance than in quiescent solution as hydrogen sulfide ions were the only species being oxidised directly at the anode. The impedance spectra of the data in Figure 6-11 is presented in the Appendix, Figure S6-8.

Figure 6-12 shows the effect of increasing hydrogen sulfide ion concentrations increasing Ti|Sn^{IV}-doped α-Fe_2O_3 photo-current densities, by decreasing electron-hole recombination rates, resulting in the expected shift towards lower electrode potentials. However, even at 1 mol dm^{-3} Na_2S, the S-shape in the photocurrent density is typical for processes affected by interfacial electron-hole recombination rates. As shown in Figure 6-12(b), there was no significant increase in the photocurrent densities for hydrogen sulfide concentrations > 0.5 mol dm^{-3} and operating at electrode potentials of 1.15 V *vs.* RHE; however, the total current density increased as a result of polysulfide accumulation near the surface of the electrode, as discussed above. It can be concluded that 0.5 mol dm^{-3} Na_2S would be an optimum concentration for hydrogen sulfide splitting in the initial stages of electrolysis, avoiding sulfur coverage of the electrode, and also accumulation of polysulfide ions near the surface electrode due to chemical reduction of sulfur by hydrogen sulfide ions. Ideally, this concentration can be maintained as the reaction progress by bubbling hydrogen sulfide gas in a separate reservoir.

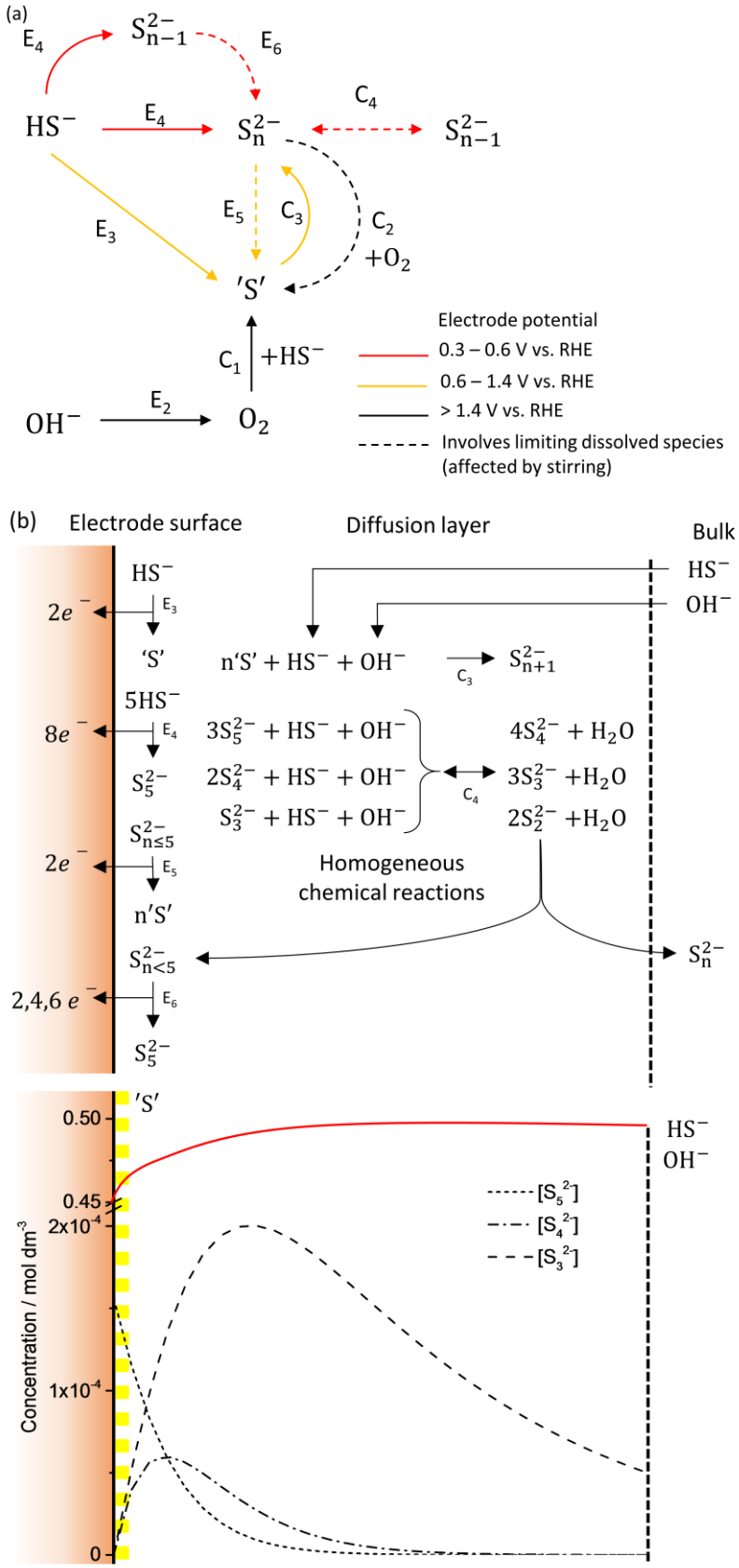


Figure 6-10. (a) Mechanism of hydrogen sulfide oxidation on Ti|Sn^{IV}-doped α-Fe_2O_3 without illumination at different potentials; sulfoxides excluded from consideration, (b) schematic concentration profile of sulfide and polysulfide ions in the diffusion layer assuming fast kinetics for chemical reactions, low current densities (charge transfer controlled process) and quiescent electrolyte.

Table 6-3. List of electrochemical-chemical reactions for hydrogen sulfide splitting at different potentials in absence of sulfoxide species.

Electrode potential vs. RHE / V	0.3 – 0.6	0.6 – 1.4	> 1.4
Electrochemical	E_4	E_3, E_4,	E_2, E_3, E_4,
Electrochemical intermediates	E_6	E_5, E_6	E_5, E_6
Chemical surface		C_3	C_1, C_2, C_3
Chemical bulk	C_4	C_4	C_4

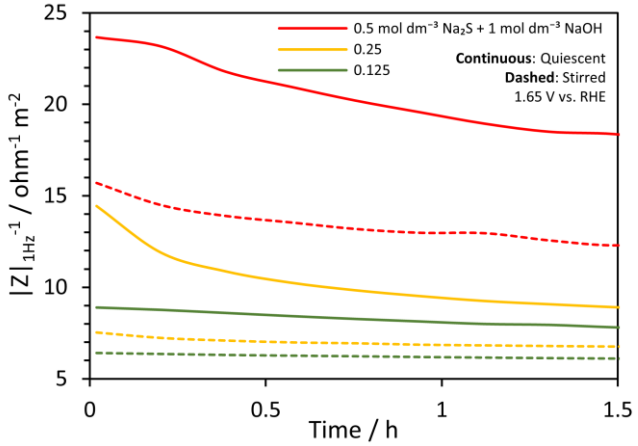


Figure 6-11. Time dependence of low frequency admittance (EIS spectra) for Ti | Sn^{IV}-doped α-Fe_2O_3 | X mol dm^{-3} NaOH + 1.0 mol dm^{-3} Na_2S | Pt | Ti operating at a photo-anode potential of 1.65 V *vs.* RHE with different hydrogen sulfide concentrations and with quiescent and stirred electrolytes.

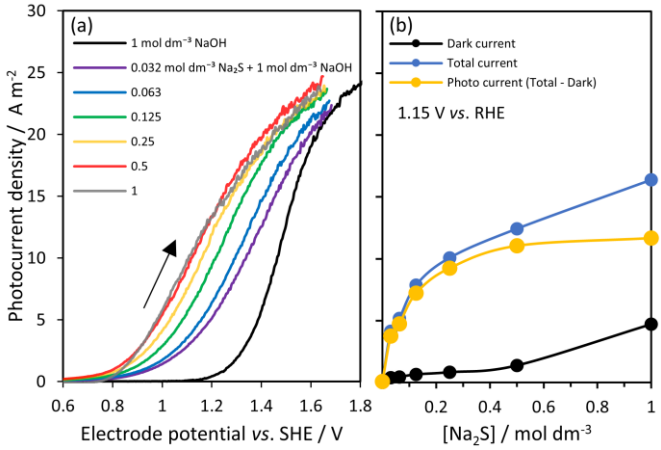


Figure 6-12. Photocurrent densities as a function of potential of Ti | Sn^{IV}-doped α-Fe_2O_3 | 1 mol dm^{-3} NaOH ± X mol dm^{-3} Na_2S (pH = 14) | Pt | Ti at different concentrations of hydrogen sulfide ions in quiescent electrolyte solutions. 10 mV s^{-1} scan rate. Xenon arc lamp irradiance 2 670 W m^{-2}.

PEIS spectra was fitted to an electrical equivalent circuit $R_s(Q_{SC}[R_t(Q_rR_r)])$. Capacitances were replaced by constant phase elements and corrected by a surface distribution of time constant as discussed in Chapter 2, pages 64 and 72. The processes at low frequencies (R_rQ_r, ca. 1 Hz) were associated with electron-hole recombination and at high frequencies (R_tQ_{SC}, ca. 10^2 Hz) with the charge transfer at the semiconductor | electrolyte interface. As shown in Figure 6-13(a), R_t showed little dependence on electrode potential; it was lower in the absence of hydrogen sulfide ions, but there was no clear trend as a function of hydrogen sulfide concentration. In contrast, R_r was higher

in the absence of hydrogen sulfide ions and it decreased significantly in their presence, as shown in Figure 6-13(c). R_r decreased with electrode potential as electron-hole recombination rates decreased due to increased band bending; hence, higher interfacial charge transfer efficiencies were achieved at less positive electrode potentials, mirroring the photocurrent behaviour shown in Figure 6-12. The capacitances of the semiconductor, C_{SC}, were not affected significantly by hydrogen sulfide ion concentration, as shown in Figure 6-13(b).

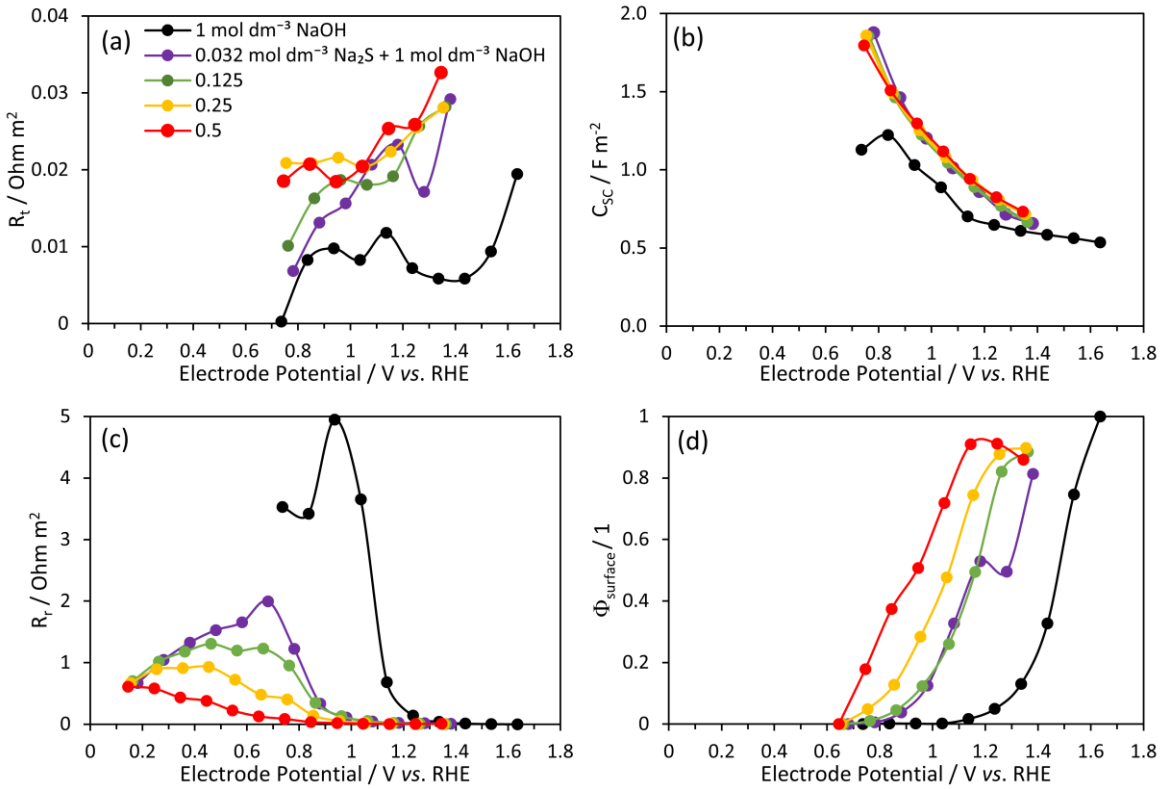


Figure 6-13. Fitted parameters from PEIS spectra, (a) Charge transfer resistance, (b) semiconductor capacitance, (c) electron-hole recombination resistance and (d) interfacial charge transfer efficiency for Ti | Sn-doped α-Fe_2O_3 | 1 mol dm^{-3} NaOH ± X mol dm^{-3} Na_2S (pH = 14) | Pt | Ti at different concentrations of hydrogen sulfide ions. Xenon arc lamp irradiance 2 670 W m^{-2}.

A better way to visualise this behaviour is presented in Figure 6-14, in which the phase shift extracted from PEIS spectra is displayed as a function of potential and frequency, as discussed in Chapter 2, page 72. The recombination process around low frequencies (left) was less predominant at concentrations of 1 mol dm^{-3} Na_2S, while at 0.032 mol dm^{-3} Na_2S, the process was predominant even at higher potentials. Charge transfer processes at high frequencies showed little dependence on potential and appeared only when interfacial electron-hole recombination rates were minimised.

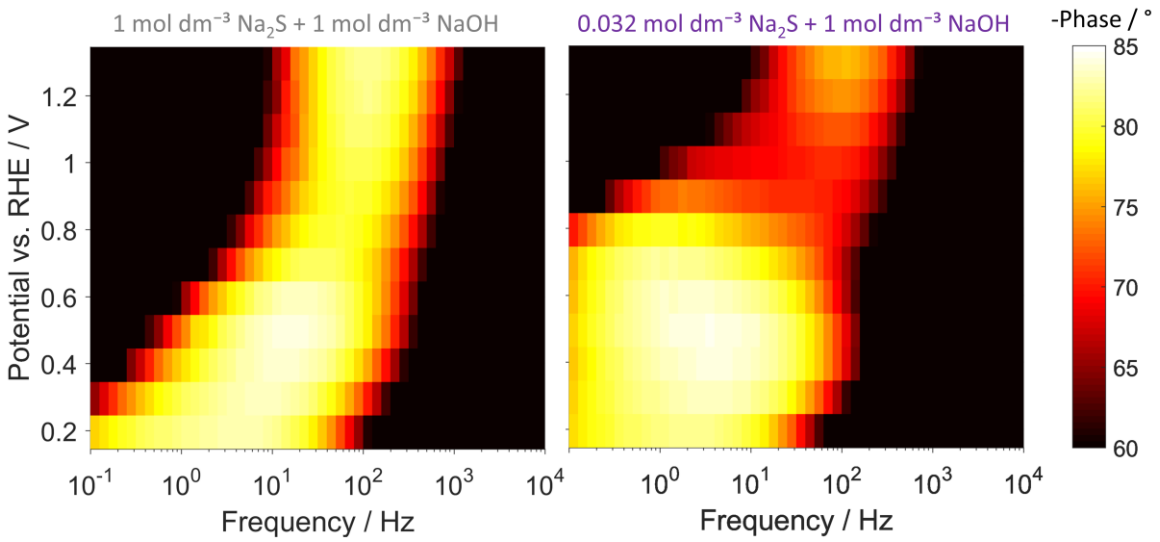


Figure 6-14. Phase shift of PEIS spectra as a function of photo-anode potential for Ti | Sn^{IV}-doped α-Fe_2O_3 | 1 mol dm^{-3} NaOH + X mol dm^{-3} Na_2S | Pt | Ti at different concentrations of hydrogen sulfide ions. Xenon arc lamp irradiance 2 670 W m^{-2}.

Figure 6-15 summarises the temporal photo-response and PEIS spectra for hydrogen sulfide oxidation under stirred conditions at Ti|Sn^{IV}-doped α-Fe_2O_3 photo-anodes for three electrode potentials. As expected, current densities were increased with increasing concentrations, but the decreased rapidly at higher potentials due to the electrodeposition of sulfur. The high frequency admittance, the inverse of the electrolyte resistance, other resistive components being negligible, did not change with time and was higher for higher hydrogen sulfide concentrations, due to an increase in the electrolyte conductivity. On the other hand, the low frequency admittance mirrored the behaviour of the current densities. At electrode potentials of 1.15 V *vs.* RHE and concentrations higher than 0.5 mol dm^{-3} Na_2S, the coverage by sulfur was minimised and did not increase with time, resulting in a stable impedance compared to the other reported conditions. The photo-impedance spectra at electrode potentials of 1.15 V *vs.* RHE were also fitted to an electrical equivalent circuit $R_s(Q_{SC}[R_t(Q_aR_a)])$, and presented as a function of time in Figure 6-16. R_tQ_{SC} (10^1 – 10^2 Hz) was still associated with the charge transfer as interfacial electron-hole recombination rates were minimised; as presented in Figure 6-6, R_aQ_a (10^3 to 10^4 Hz) represented the process associated with area coverage by elemental sulfur. The phase shift of the PEIS spectra as a function of time and frequency can be found in the Appendix, Figure S6-9. The admittance, R_t^{-1}, decreased substantially with decreasing hydrogen sulfide concentrations, ultimately due to their restricted transport rates due to the start of mass transport control. This trend was not clearly evident in Figure 6-13, probably due to the absence of stirring in those measurements and accumulation of polysulfide ions near the photo-anode. The coverage of electro-active area with sulfur was then well represented by the evolution of R_a with time, which followed a similar trend as the current densities shown in Figure 6-15 for 1.15 V *vs.* RHE. These data can be used to study the kinetics of sulfur coverage with time for hydrogen sulfide splitting on photo-anodes; however, this would require additional elemental analysis of the surface *in situ*, as dissolved hydrogen sulfide ions can be oxidised to elemental sulfur in contact with air when the sample is taken out of the PEC.

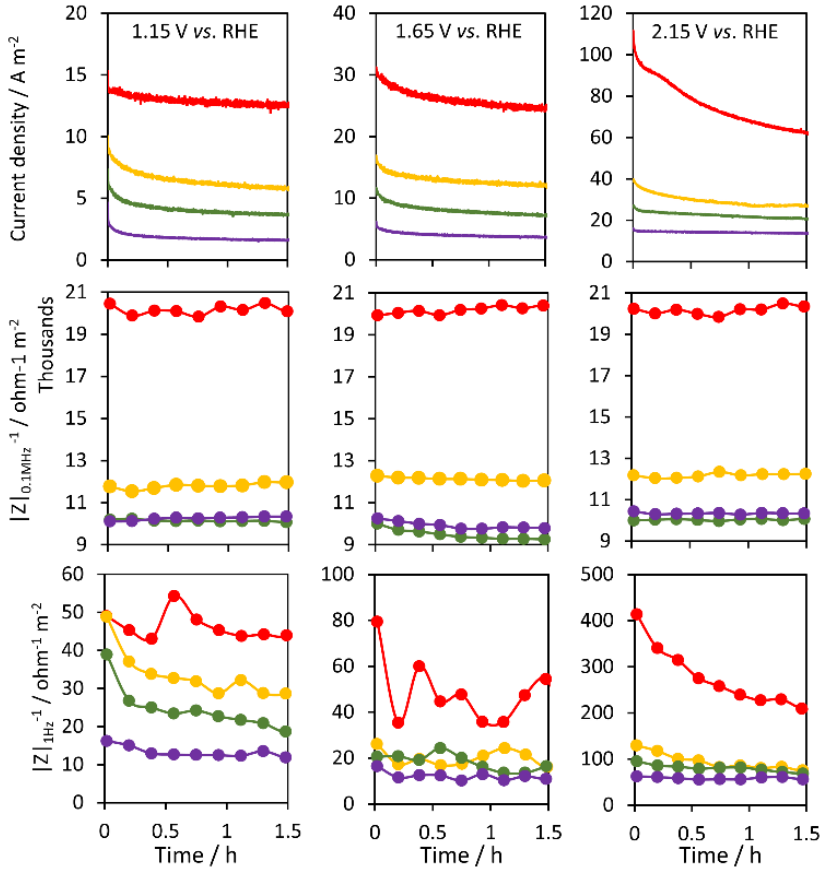


Figure 6-15. Time dependence of current density for Ti | Sn^{IV}-doped α-Fe_2O_3 | 1 mol dm^{-3} NaOH + X mol dm^{-3} Na_2S (pH = 14) | Pt | Ti at different concentrations of hydrogen sulfide and high and low admittance for photo-assisted electrolysis during 1.5 hours at different photo-anode potentials and stirred electrolyte. Xenon arc lamp irradiance 2 670 W m^{-2}. Legends are the same as Figure 6-13.

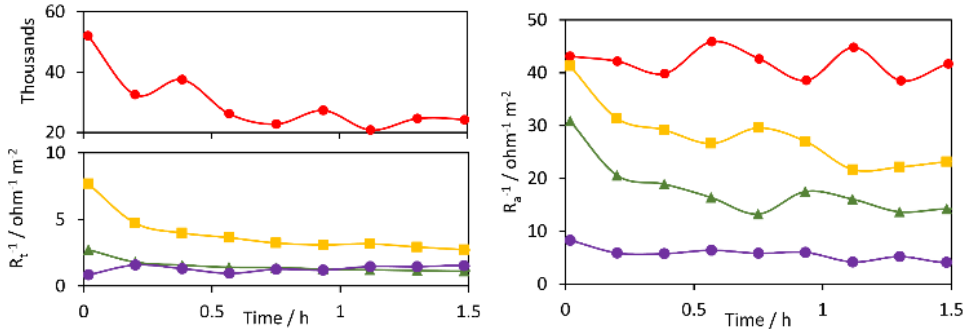


Figure 6-16. Fitted parameters from PEIS spectra of Ti | Sn^{IV}-doped α-Fe_2O_3 | 1 mol dm^{-3} NaOH + X mol dm^{-3} Na_2S (pH = 14) | Pt | Ti at different concentrations of hydrogen sulfide ions for photo-assisted electrolysis during 1.5 hours at 1.15 V *vs.* RHE and stirred electrolyte. Xenon arc lamp irradiance 2 670 W m^{-2}. Legends the same as for Figure 6-13.

6.3.4 Long term electrolysis and charge yields

Current densities of hydrogen sulfide splitting were measured over 16 hours at a fixed potential in the bench-scale PER (0.1 dm^3) and up-scaled PER (0.8 dm^3). Polysulfide ion concentrations were analysed as described in Chapter 5 for both bench-scale and up-scaled reactors, while hydrogen fluxes at the cathode were measured only in the up-scaled reactor using gas flow meters as described in Chapter 4, page 104.

Current densities obtained in the bench-scale reactor were stable after 4 hours until the end of the experiments. The signal noise was a result of the stirring by nitrogen bubbles and occasional scattering of light. Integration of current densities with time and estimation of polysulfide concentrations enabled charge yields to be estimated as ca. 1.04 and 1.08 in replicated experiments in the bench-scale reactor, with values greater than unity reflecting uncertainties in determining concentrations of polysulfide ions as discussed in Chapter 5, page 130. As demonstrated previously, at 1.15 V vs. RHE hydrogen sulfide oxidation at the photo-anode produced only polysulfide ions and elemental sulfur. Evolution of oxygen on illuminated unannealed Ti|Sn^{IV}-doped α-Fe_2O_3 can be disregarded at these potentials, as evident from Figure 6-2 and Figure 6-4. However, even at higher electrode potentials when oxygen evolves and oxidises hydrogen sulfide ions in solution indirectly to polysulfide by reaction (6-2) followed by (6-18), the same number of electrons ($2e^-$ per HS^- ion) are needed to produce elemental sulfur, assuming oxygen does not desorb as gas or diffuses towards the cathode.

Similar behaviour was found in the up-scaled reactor with larger Ti|Sn^{IV}-doped α-Fe_2O_3 photo-anodes operating at a cell potential difference of 1.23 V, which corresponded to photo-anode potentials of ca. 1.15 V vs. RHE. Hydrogen and polysulfide molar fluxes are reported in Figure 6-17(a). In the case of planar electrodes, molar fluxes for both species were stable after 8 hours of photo-assisted electrolysis; the initial transient behaviour can be assigned to the heating of the system, polysulfide accumulation near the surface and electrodeposition of elemental sulfur. In the case of perforated electrodes, molar fluxes of polysulfide ions were never stable and increased indefinitely with time after 7 hours. This can be associated with the accumulation of sulfur and polysulfides in the walls of the perforations which were only partially covered with lacquer due to their small size (3 mm × 1.5 mm perforation size). This was confirmed by the existence of significantly greater dark current densities (> 6 A m^{-2}) after 10 hours of photo-assisted electrolysis and the high concentration of polysulfides in solution, which was then dark yellow. Despite current densities being expected to decrease with increasing depth into perforations of (monopolar) photo-anodes, the geometrically constrained convective diffusion of polysulfide ions out of perforations may have enabling higher local concentrations of polysulfide ions to accumulate. Hence, the more facile oxidation of lower to higher polysulfides compared with HS^- oxidation, may have produced greater current densities than the external surfaces of photo-anodes, depending on the polysulfide concentration in the bulk solution and mass transport rate coefficients.

Hydrogen and oxygen fluxes were also reported in Figure 6-17(b) for comparison with regular water splitting. Same reactor and samples were used in 1 mol dm^{-3} NaOH electrolyte and operating at 1.60 V *vs.* RHE. Slightly lower molar fluxes were achieved as evident from the temporal behaviour of current densities, as shown in Figure 6-17(d). It can be concluded then that reactors for hydrogen sulfide splitting using Ti|Sn^{IV}-doped α-Fe_2O_3 require lower bias potential differences, while achieving greater photocurrent densities compared to water splitting at any given electrode potential. In the case of the up-scaled reactor, charge yields were also close to unity, 1.01 and 0.95 for planar and perforated electrodes, respectively, after integration of current densities between 8 and 15 hours of

photo-electrolysis. The temporal dependence of charge yields for polysulfide and hydrogen evolution for photo-assisted hydrogen sulfide splitting is also shown in Figure 6-17(c). Charge yields and molar fluxes followed a similar trend while the system was reaching steady state during the first 8 hours. Hydrogen yields were found to be lower than unity due to gas leaks in the reactor and were similar to the yields obtained for water splitting in Chapter 4. Polysulfide ion cross-over from the anolyte to catholyte was disregarded, due to the presence of the cation-permeable membrane and absence of colour change in the catholyte.

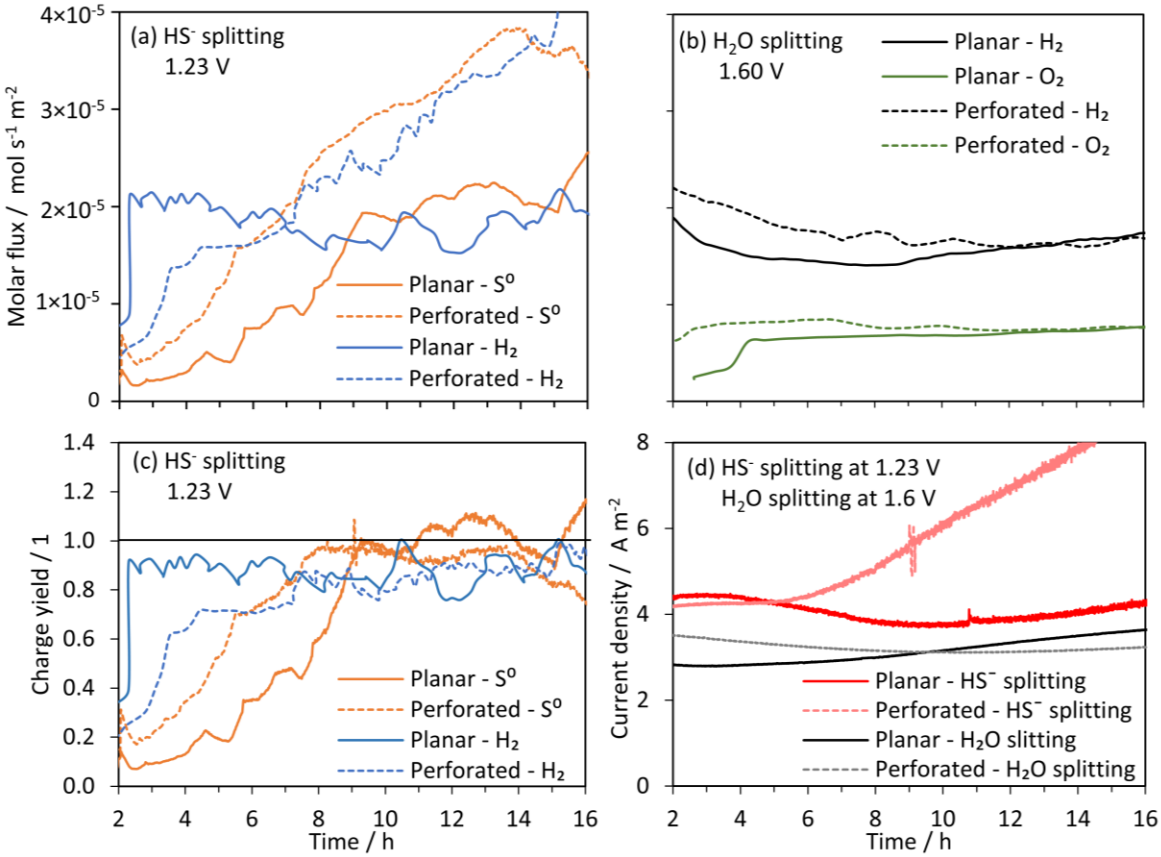


Figure 6-17. Time dependence of (a) hydrogen and elemental sulfur molar flux in the PER for hydrogen sulfide splitting (1 mol dm^{-3} NaOH + 0.5 mol dm^{-3} Na_2S) operating at cell potential difference of 1.23 V, (b) Hydrogen and oxygen molar flux for water splitting (1 mol dm^{-3} NaOH) at 1.60 V. (c) Charge yield for hydrogen sulfide splitting and (d) current density for both hydrogen sulfide and water splitting, in a planar and perforated 0.1×0.1 m^2 photo-anode Ti|Sn^{IV}-doped α-Fe_2O_3. Xenon arc lamp irradiance 457 W m^{-2}.

6.3.5 Model predictions for hydrogen sulfide splitting

The photocurrent responses (total – dark current densities) of the bench-scale and up-scaled experiments were predicted using a modified model for water splitting. The function of interfacial charge transfer efficiencies of unannealed Ti|Sn^{IV}-doped α-Fe_2O_3 photo-anodes in presence of hydrogen sulfide ions were obtained from the experimental data presented in Figure 6-3(c) after fitting to an exponential function as described in Chapter 1, page 64 and 69 and equation (2-6). Values of other photo-electrochemical properties such as flat band potential and electron-hole recombination rate in the bulk of the semiconductor were retained as reported previously. The spectra of light reaching the photo-anode surface were corrected for the absorption of UV light by

hydrogen sulfide ions in electrolyte + quartz windows, ca. 0.87 transmission. Then, the photocurrent was predicted in a 1D model, as that described in Chapter 3, page 81, equation (3-4) and (3-6), using a modified version of the Gärtner–Butler equation and compared to the photocurrent (total - dark) densities obtained from linear potential sweeps of three different Ti|Sn^{IV}-doped α-Fe_2O_3 samples in the PEC, Figure 6-2. As shown in Figure 6-18, the agreement was remarkable and only an expected deviation at high potentials was observed due to possible oxygen and polysulfide ions near the surface of the photo-anode, as discussed above.

In the case of photo-assisted hydrogen sulfide splitting in an up-scaled reactor during the first few hours (avoiding the effects of coverage by sulfur and polysulfide accumulation near the electrode) at a cell potential difference of 1.23 V, corresponding to a photo-anode potential of ca. 1.15 V *vs.* RHE, the predicted photocurrent densities in a 3D model, as described in Chapter 1, were lower and outside the experimental range of uncertainty, but only 8% lower than the experimental values. The predicted photocurrent density was 3.74 A m^{-2} (experimental: 4.04 ± 0.20 A m^{-2}) for the planar photo-anode and 3.29 A m^{-2} (experimental: 3.57 ± 0.10 A m^{-2}) for the perforated photo-anode at an irradiance of 457 W m^{-2}.

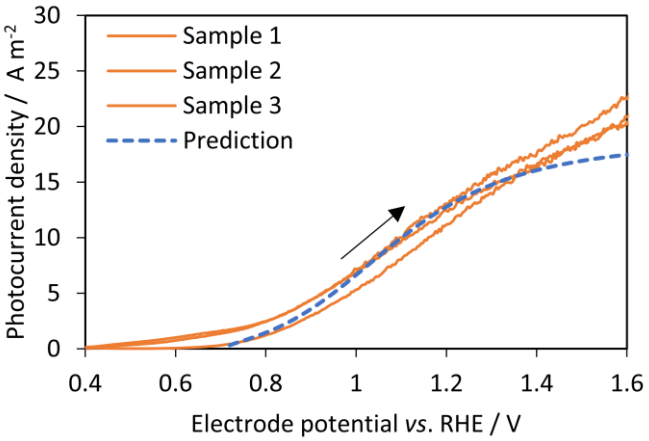


Figure 6-18. Experimental and predicted effects of photo-anode potential on photocurrent densities (total - dark) of Ti | Sn^{IV}-doped α-Fe_2O_3 | 1 mol dm^{-3} NaOH + 0.5 mol dm^{-3} Na_2S (pH = 14) | Pt | Ti in a PEC with Xe arc lamp irradiance 2 670 W m^{-2}.

6.4 Conclusions

Photo-assisted oxidation of hydrogen sulfide ions to polysulfide ions in alkaline aqueous solution was achieved using Ti|Sn^{IV}-doped α-Fe_2O_3 photo-anodes with lower electrode potentials than for water splitting and at greater photocurrent densities, which were quite stable over 50 hours, with no morphological changes up to 18 hours. The effect of annealing and thickness of Sn^{IV}-doped α-Fe_2O_3 films opened possible ways to optimise the properties of the photo-anode for improved hydrogen sulfide splitting. A mechanism for hydrogen sulfide ion oxidation is proposed and validated using a wide range of electrochemical techniques and under different hydrogen sulfide concentrations and electrode potentials. 1 mol dm^{-3} NaOH + 0.5 mol dm^{-3} Na_2S was found to be a suitable electrolyte for this process, when operating at relatively low potentials (1.15 V *vs.* RHE) to avoid sulfur deposition and evolution of oxygen under illuminated and dark conditions. Stirring

was required in order to disperse polysulfide ions near the surface of the anode to the bulk solution, as well as bubbling of zero grade nitrogen to avoid oxidation of polysulfides due to adventitious oxygen dissolved in the electrolyte. Increased photocurrent densities compared to water splitting were achieved due to decreased electron-hole recombination rates, resulting from the fast kinetics of hole-driven hydrogen sulfide oxidation. Stable photocurrents of ca. 12.5 A m^{-2} were recorded in a bench-scale reactor under an irradiance of 2 670 W m^{-2} and 4.3 A m^{-2} in an up-scaled reactor with an effective irradiance of 457 W m^{-2} operating at 1.15 V *vs.* RHE electrode potential. Similar photocurrent densities were achieved for regular water splitting at electrode potentials of 1.6 V *vs.* RHE, then the potential requirements were decreased by ca. 0.5 V. obtained in the Interfacial charge transfer efficiencies were measured as a function of potential and inputted to 1D and 3D photo-electrochemical reactor models. A good agreement was achieved for the bench-scale cell, while a refinement for an up-scaled reactor is required due to different chemistry (kinetics and concentration profiles of species) related to the presence of hydrogen sulfide / polysulfide species in solution compared to water splitting.

Chapter 7

Conclusions and future work

The photo-electrochemical, optical and morphological properties of Sn^{IV}-doped α-Fe_2O_3 photo-anodes fabricated via spray pyrolysis for water splitting and the effects of annealing at 400 and 500 °C on the photocurrent were reported. Spatial redistributions of Sn^{IV} dopant was suggested to occur. The shift of photocurrent densities towards lower electrode potentials with annealing temperature was associated with a decrease of electron-hole recombination rates caused by an increase of dopant concentration near the Sn^{IV}-doped α-Fe_2O_3 | 1 mol dm^{-3} NaOH interface. No evidence was found for annealing causing significant changes in morphology, crystallinity or topography at these temperatures. On the other hand, the decrease in maximum photocurrent densities with annealing appeared to be associated with a decrease in photon absorption within the depletion layer where Sn^{IV} dopant was accumulated.

Based on the previous characterisation of Sn^{IV}-doped α-Fe_2O_3, a model for photo-electrochemical reactors was developed to describe the behaviour of such photo-anodes during photo-assisted water splitting. Firstly, the photocurrent was predicted as a function of the properties of the photo-anode and light source using a modified Gärtner-Butler equation. Charge carrier concentration and bulk electron-hole recombination rates were found to require special care and theoretical treatment for their estimations. Predicted values showed good agreement with experimental data gathered in a bench-scale PEC (3×6 mm^2 photo-anode). For the first time, bubble formation rates at the electrodes and in the bulk of electrolyte solution for supersaturated conditions, were predicted as a function of current density; the reactor performance did not increase drastically by including a membrane or microporous separator. The model was validated in an up-scaled reactor (0.1×0.1 m^2 photo-anode). Different scenarios and geometries were studied and optimised as functions of current densities, hydrogen fluxes and collection efficiencies, accounting for H_2-O_2 cross-over, ohmic potential losses and current density distributions. Optimal ratios of separation to size of perforations were found for a wide range of geometrical configurations and photo-anode properties. Hydrogen fluxes for 'wired' (two monopolar electrodes) and 'wireless' (monolithic photo-bipole) configurations were comparable when using a membrane. By contrast, in the

absence of a membrane, the model predicted significant cross-over of H_2 and O_2 products for a 'wired' system, while 'wireless' systems exhibited low charge yields for the conditions evaluated in the photo-electrochemical model. Nevertheless, from a safety perspective, a membrane is still necessary to avoid the risk of H_2-O_2 cross-over and explosive conditions developing in the reactor. There was no significant increase in the resulting photocurrent densities and hydrogen fluxes for perforation sizes $l_p < 50$ μm. 'Wired' and 'wireless' reactors with a membrane performed at optimum conditions with photo-anodes perforated using ratios of separation to size of perforations of $l_d/l_p = 4.5 \pm 0.5$.

A methodology was developed for the quantification of polysulfide ions at low concentrations, expressed as zero-valent sulfur, via UV-visible spectrophotometry in concentrated hydrogen sulfide solution (0.5 mol dm^{-3}). Absorptions at 295 and 420 nm were used to build calibration curves at polysulfide ion concentrations between 0 and 0.01 mol dm^{-3} as zero-valent sulfur. Three ranges of concentrations were necessary due to the non-linear behaviour of polysulfide speciation. The effect of oxygen depletion and the purity of nitrogen (or any inert gas) used to deaerate the solutions was critical to avoid adventitious decomposition of polysulfide ions.

Photo-assisted oxidation of hydrogen sulfide ions to polysulfide ions in alkaline aqueous solution was achieved using Ti|Sn^{IV}-doped α-Fe_2O_3 photo-anodes with lower electrode potentials than for water splitting and at greater photocurrent densities, which were quite stable over 50 hours, with no morphological changes up to 18 hours. A study of the effect of post-deposition annealing and film thickness showed possible routes to improve the performance of the photo-anodes for hydrogen sulfide splitting. A mechanism for hydrogen sulfide ion oxidation is proposed and validated using a wide range of electrochemical techniques and under different hydrogen sulfide concentrations and electrode potentials. 1 mol dm^{-3} NaOH + 0.5 mol dm^{-3} Na_2S was found to be a suitable electrolyte for this process, when operating at relatively low potentials (1.15 V *vs.* RHE) to avoid sulfur deposition and evolution of oxygen under illuminated and dark conditions. Stable photocurrents of ca. 12.5 A m^{-2} were recorded in a bench-scale reactor under an irradiance of 2 670 W m^{-2}, and 4.3 A m^{-2} in an up-scaled reactor with an effective irradiance of 457 W m^{-2} operating at 1.15 V *vs.* RHE electrode potential. In contrast, similar photocurrent densities were achieved only for regular water splitting at electrode potentials of 1.6 V *vs.* RHE for the same Ti|Sn^{IV}-doped α-Fe_2O_3 photo-anodes. Charge yields for the production of polysulfide ions were estimated using the methodology developed previously. Unity charge yields of polysulfide ions were determined for electrode potentials of 1.15 V *vs.* RHE. Lastly, photocurrents for photo-assisted hydrogen sulfide splitting were predicted using a modified model accounting for the improved kinetics at the photo-anode | electrolyte interface. Good agreement between experimental and model-predicted data was achieved for the bench-scale reactor while a refinement of the model for an up-scaled reactor is required for hydrogen sulfide splitting predictions.

Future work

Spontaneous water and hydrogen sulfide splitting still constitute a challenge to be solved. The incorporation of suitable photocathodes (to complement the photo-anodes) should be addressed as a possible answer to this issue. Sulfide and selenide materials (CIGS, CIGSS, CZTS), provided they are stable in aqueous sulfide solution, could be used as photo-cathodes to provide the missing electrical bias for spontaneous hydrogen sulfide splitting.

The present model of PEC for water splitting does not account for electrolyte flow, light scattering and reflection due to bubbles and other optical phenomena in the semiconductor. The model could be extended to include these effects using the results of Singh [117], Haussener [131] and Holmes-Gentle [118]. The study of light scattering and reflection of bubbles is being carried out independently in the Department of Chemical Engineering by Mr. Isaac Holmes-Gentle. The light transmission through a layer of bubbles generated by electrolysis on a conductive and transparent electrode, e.g. FTO, can be used to estimate the effective light on its surface. The attenuation by bubbles can then be expressed as a function of the electrode material, current density and electrolyte. This can be implemented easily in the model by multiplying the photon flux by a correction factor. Bubble generation can also be diminished by increasing the flow of the electrolyte. This will require the inclusion of fluid dynamics and convection effects in the diffusion of species in the electrolyte, several models accounting for this have been already published [117, 118].

The effects of the temperature on the performance of PECs were considered to a limited extent in the model. However, a deeper understanding of its effects on the photo-anode properties should be addressed, as well as the inclusion of convection effects on gas evolution and H_2-O_2 cross-over. The former effect is being researched by Ms. Faye Alhersh in the Department. Preliminary results showed that photocurrent densities for water splitting using spray pyrolysed hematite photo-anodes do not change significantly at electrolyte temperatures between 25 and 65 °C. However, this contradicts previous findings [58]; a more detailed investigation about the possible reasons for this behaviour must be conducted.

Profiling of dopant concentration inside Sn^{IV}-doped α-Fe_2O_3 is necessary to elucidate further the effects of annealing on the photo-electrochemical properties of hematite on titanium substrates. This can be done via ion beam sputtering and XPS. However, Sn and Fe might sputter at different rates and also be reduced to elemental form, changing the stoichiometry and concentration of the sample [167, 168]. Intensity modulated photo-electrochemical impedance spectroscopy (IMPS) and transient absorption spectroscopy (TAS) with 550 nm monochromatic light may also prove useful in elucidating further the effect of annealing on hematite performance.

The molar absorption coefficients of polysulfide ions should be revised, as the only available data can be traced to dated studies. Some of these values were measured and were consistent with published data. However, there is indication that at such low polysulfide ion concentrations, the speciation is not as expected from these studies and lower polysulfides (S_3^{2-} and

S_2^{2-}) may be present in higher concentrations. This can be achieved by deconvolution of absorbance spectra for a wider range of polysulfide ion concentrations, while keeping high concentrations of OH^- and HS^-.

A mechanism for hydrogen sulfide oxidation on Ti|Sn^{IV}-doped α-Fe_2O_3 photo-anodes was proposed. The speciation of polysulfides and oxidation of sulfide on the photo-anode are reported to have fast kinetics compared to water oxidation; however, little is known about the kinetics of such processes when operating at low current densities in a PEC. Meticulous studies of the kinetics are required, considering electrolyte flow and mass transport controlled oxidation of polysulfide ions in a wider range of sulfide and polysulfide ion (HS^- and S_n^{2-}) concentrations.

References

[1] A. Salvo, F.M. Geiger, Reduction in local ozone levels in urban Sao Paulo due to a shift from ethanol to gasoline use, *Nature Geoscience*, pp. 450-458, 2014.

[2] Z. Xing, X. Zong, J. Pan, L. Wang, On the engineering part of solar hydrogen production from water splitting: Photoreactor design, *Chemical Engineering Science*, 104, pp. 125-146, 2013.

[3] Key world energy statistics, International Energy Agency, France, 2016.

[4] P. Gadonneix, World Energy Resources 2013 Survey, World Energy Council, United Kingdom, 2013.

[5] M.A. Green, K. Emery, Y. Hishikawa, W. Warta, E.D. Dunlop, D.H. Levi, A.W.Y. Ho-Baillie, Solar cell efficiency tables (version 49), *Progress in Photovoltaics: Research and Applications*, 25, pp. 3-13, 2017.

[6] N.S. Lewis, Toward Cost-Effective Solar Energy Use, *Science*, 315, pp. 798-801, 2007.

[7] H. Ibrahim, A. Ilinca, J. Perron, Energy storage systems—Characteristics and comparisons, *Renewable and Sustainable Energy Reviews*, 12, pp. 1221-1250, 2008.

[8] S. Ould Amrouche, D. Rekioua, T. Rekioua, S. Bacha, Overview of energy storage in renewable energy systems, *International Journal of Hydrogen Energy*, 41, pp. 20914-20927, 2016.

[9] R. van de Krol, M. Grätzel, Photoelectrochemical Hydrogen Production, Springer Science+Business Media, 2012.

[10] S.V. Tambwekar, M. Subrahmanyam, Photocatalytic generation of hydrogen from hydrogen sulfide: An energy bargain, *International Journal of Hydrogen Energy*, 22, pp. 959-965, 1997.

[11] G. Lu, S. Li, Hydrogen production by H_2S photodecomposition on $ZnFe_2O_4$ catalyst, *International Journal of Hydrogen Energy*, 17, pp. 767-770, 1992.

[12] J.S. Jang, H. Gyu Kim, P.H. Borse, J.S. Lee, Simultaneous hydrogen production and decomposition of H_2S dissolved in alkaline water over $CdS.TiO_2$ composite photocatalysts under visible light irradiation, *International Journal of Hydrogen Energy*, 32, pp. 4786-4791, 2007.

[13] L.M. Corredor-Rojas, Review of Photocatalytic Materials for Hydrogen Production from H_2S, *Ingenieria y Universidad*, 15, pp. 171-195, 2011.

[14] R.O. Shamim, I. Dincer, G. Naterer, Thermodynamic analysis of solar-based photocatalytic hydrogen sulphide dissociation for hydrogen production, *International Journal of Hydrogen Energy*, 39, pp. 15342-15351, 2014.

[15] Mineral commodity summaries 2015, U.S. Geological Survey, U.S. Department of the Interior and U.S. Geological Survey, 2015.

[16] K. Rajeshwar, R. McConnell, K. Harrison, S. Licht, Renewable Energy and the Hydrogen Economy, in: K. Rajeshwar, R. McConnell, S. Licht (Eds.) Solar Hydrogen Generation, Springer New York, pp. 1-18, 2008.

[17] Energy transition: Measurement needs within the hydrogen industry, National Physical Laboratory, NPL, London, UK, 2017.

[18] Hydrogen Energy Storage: Grid and Transportation Services, National Renewable Energy Laboratory, NREL, USA, 2015.

[19] Technology Roadmap: Hydrogen and Fuel Cells, International Energy Agency, IEA, Paris, France, 2015.

[20] T. Bak, J. Nowotny, M. Rekas, C.C. Sorrell, Photo-electrochemical hydrogen generation from water using solar energy. Materials-related aspects, *International Journal of Hydrogen Energy*, 27, pp. 991-1022, 2002.

[21] M.S.D. George W. Crabtree, and Michelle V. Buchanan The Hydrogen Economy, *Physics Today*, 57, pp. 39-45, 2004.

[22] G.C.a.F. Wheeler, Hydrogen Production via Steam Reforming with CO_2 Capture, *Chemical Engineering Transactions*, 17, pp. 37, 2010.

[23] International Energy: Outlook 2016, U.S. Energy Information Administration, Washington, US, 2016.

[24] S. Koumi Ngoh, D. Njomo, An overview of hydrogen gas production from solar energy, *Renewable and Sustainable Energy Reviews*, 16, pp. 6782-6792, 2012.

[25] B.A. Pinaud, J.D. Benck, L.C. Seitz, A.J. Forman, Z. Chen, T.G. Deutsch, B.D. James, K.N. Baum, G.N. Baum, S. Ardo, H. Wang, E. Miller, T.F. Jaramillo, Technical and economic feasibility of centralized facilities for solar hydrogen production via photocatalysis and photoelectrochemistry, *Energy & Environmental Science*, 6, pp. 1983-2002, 2013.

[26] A.S. Joshi, I. Dincer, B.V. Reddy, Exergetic assessment of solar hydrogen production methods, *International Journal of Hydrogen Energy*, 35, pp. 4901-4908, 2010.

[27] K. Christopher, R. Dimitrios, A review on exergy comparison of hydrogen production methods from renewable energy sources, *Energy & Environmental Science*, 5, pp. 6640-6651, 2012.

[28] P.C. Hallenbeck, J.R. Benemann, Biological hydrogen production; fundamentals and limiting processes, *International Journal of Hydrogen Energy*, 27, pp. 1185-1193, 2002.

[29] J.R. Bolton, Solar photoproduction of hydrogen: IEA Agreement on the production and utilisation of hydrogen, IEA Technical ReportLondon, Canada, 1996.

[30] T. Lopes, L. Andrade, H.A. Ribeiro, A. Mendes, Characterization of photoelectrochemical cells for water splitting by electrochemical impedance spectroscopy, *International Journal of Hydrogen Energy*, 35, pp. 11601-11608, 2010.

[31] J.W. Ager, M.R. Shaner, K.A. Walczak, I.D. Sharp, S. Ardo, Experimental demonstrations of spontaneous, solar-driven photoelectrochemical water splitting, *Energy & Environmental Science*, 8, pp. 2811-2824, 2015.

[32] A.J. Bard, R. Parsons, J. Jordan, Standard Potentials in Aqueous Solution, Taylor & Francis, 1985.

[33] L.J. Minggu, W.R. Wan Daud, M.B. Kassim, An overview of photocells and photoreactors for photoelectrochemical water splitting, *International Journal of Hydrogen Energy*, 35, pp. 5233-5244, 2010.

[34] M.S. Wrighton, A.B. Ellis, P.T. Wolczanski, D.L. Morse, H.B. Abrahamson, D.S. Ginley, Strontium titanate photoelectrodes. Efficient photoassisted electrolysis of water at zero applied potential, *Journal of the American Chemical Society*, 98, pp. 2774-2779, 1976.

[35] A.J. Bard, L.R. Faulkner, Electrochemical Methods: Fundamentals and Applications, 2nd Edition, John Wiley & Sons, 2001.

[36] M.A. Modestino, S. Haussener, An Integrated Device View on Photo-Electrochemical Solar-Hydrogen Generation, *Annual Review of Chemical and Biomolecular Engineering*, 6, pp. 13-34, 2015.

[37] S. Takabayashi, R. Nakamura, Y. Nakato, A nano-modified Si/TiO_2 composite electrode for efficient solar water splitting, *Journal of Photochemistry and Photobiology A: Chemistry*, 166, pp. 107-113, 2004.

[38] S. Licht, O. Khaselev, T. Soga, M. Umeno, Multiple Bandgap Photoelectrochemistry: Energetic Configurations for Solar Energy Conversion, *Electrochemical and Solid-State Letters*, 1, pp. 20-23, 1998.

[39] E.L. Miller, R.E. Rocheleau, X.M. Deng, Design considerations for a hybrid amorphous silicon/photoelectrochemical multijunction cell for hydrogen production, *International Journal of Hydrogen Energy*, 28, pp. 615-623, 2003.

[40] N. Sato, Electrochemistry at metal and semiconductor electrodes, Elsevier, Amsterdan, The Neterlands, 2003.

[41] Y. Xu, M.A.A. Schoonen, The absolute energy positions of conduction and valence bands of selected semiconducting minerals, *American Mineralogist*, 85, pp. 543-556, 2000.

[42] J.R. Bolton, A.F. Haught, R.T. Ross, Photochemical energy storage: an analysis of limits, in: J.S. Connolly (Ed.) Photochemical Conversion and Storage of Solar Energy, Academic Press, pp. 297-339, 1981.

[43] A. Hankin, J.C. Alexander, G.H. Kelsall, Constraints to the flat band potential of hematite photo-electrodes, *Physical Chemistry Chemical Physics*, 16, pp. 16176-16186, 2014.

[44] Z. Chen, T.F. Jaramillo, T.G. Deutsch, A. Kleiman-Shwarsctein, A.J. Forman, N. Gaillard, R. Garland, K. Takanabe, C. Heske, M. Sunkara, E.W. McFarland, K. Domen, E.L. Miller, J.A. Turner, H.N. Dinh, Accelerating materials development for photoelectrochemical hydrogen production: Standards for methods, definitions, and reporting protocols, *Journal of Materials Research*, 25, pp. 3-16, 2010.

[45] T. Hisatomi, J. Kubota, K. Domen, Recent advances in semiconductors for photocatalytic and photoelectrochemical water splitting, *Chemical Society Reviews*, 43, pp. 7520-7535, 2014.

[46] H.N.D. Zhebo Chen, Eric Miller, Photoelectrochemical Water Splitting Standards, Experimental Methods, and Protocols, Springer, 2013.

[47] C. Carver, Z. Ulissi, C.K. Ong, S. Dennison, G.H. Kelsall, K. Hellgardt, Modelling and development of photoelectrochemical reactor for H_2 production, *International Journal of Hydrogen Energy*, 37, pp. 2911-2923, 2012.

[48] E.L. Tsege, T.S. Atabaev, M.A. Hossain, D. Lee, H.-K. Kim, Y.-H. Hwang, Cu-doped flower-like hematite nanostructures for efficient water splitting applications, *Journal of Physics and Chemistry of Solids*, 98, pp. 283-289, 2016.

[49] H.X. Dang, N.T. Hahn, H.S. Park, A.J. Bard, C.B. Mullins, Nanostructured Ta_3N_5 Films as Visible-Light Active Photoanodes for Water Oxidation, *The Journal of Physical Chemistry C*, 116, pp. 19225-19232, 2012.

[50] T.W. Kim, Y. Ping, G.A. Galli, K.-S. Choi, Simultaneous enhancements in photon absorption and charge transport of bismuth vanadate photoanodes for solar water splitting, *Nature Communications*, 6, pp. 8769, 2015.

[51] Y. Yuan, J. Gu, K.-H. Ye, Z. Chai, X. Yu, X. Chen, C. Zhao, Y. Zhang, W. Mai, Combining Bulk/Surface Engineering of Hematite To Synergistically Improve Its Photoelectrochemical Water Splitting Performance, *ACS Applied Materials & Interfaces*, 8, pp. 16071-16077, 2016.

[52] A.G. Tamirat, W.-N. Su, A.A. Dubale, C.-J. Pan, H.-M. Chen, D.W. Ayele, J.-F. Lee, B.-J. Hwang, Efficient photoelectrochemical water splitting using three dimensional urchin-like hematite nanostructure modified with reduced graphene oxide, *Journal of Power Sources*, 287, pp. 119-128, 2015.

[53] Y. Qiu, W. Liu, W. Chen, W. Chen, G. Zhou, P.-C. Hsu, R. Zhang, Z. Liang, S. Fan, Y. Zhang, Y. Cui, Efficient solar-driven water splitting by nanocone $BiVO_4$-perovskite tandem cells, *Science Advances*, 2, pp., 2016.

[54] A.G. Tamirat, W.-N. Su, A.A. Dubale, H.-M. Chen, B.-J. Hwang, Photoelectrochemical water splitting at low applied potential using a NiOOH coated codoped (Sn, Zr) α-Fe_2O_3 photoanode, *Journal of Materials Chemistry A*, 3, pp. 5949-5961, 2015.

[55] Z. Wang, G. Liu, C. Ding, Z. Chen, F. Zhang, J. Shi, C. Li, Synergetic Effect of Conjugated $Ni(OH)_2/IrO_2$ Cocatalyst on Titanium-Doped Hematite Photoanode for Solar Water Splitting, *The Journal of Physical Chemistry C*, 119, pp. 19607-19612, 2015.

[56] S.U. Dipika Sharma, Surbhi Choudhary, Vibha R. Satsangi, Rohit Shrivastav, Sahab Dass, Enhancement of Photoelectric Conversion Properties of α-Fe_2O_3/Cu_2O Bilayered Photoanod, *International Journal of Materials, Mechanics and Manufacturing*, 2, pp. 51-55, 2014.

[57] S. Rai, A. Ikram, S. Sahai, S. Dass, R. Shrivastav, V.R. Satsangi, Photoactivity of MWCNTs modified α-Fe_2O_3 photoelectrode towards efficient solar water splitting, *Renewable Energy*, 83, pp. 447-454, 2015.

[58] P. Dias, T. Lopes, L. Andrade, A. Mendes, Temperature effect on water splitting using a Si-doped hematite photoanode, *Journal of Power Sources*, 272, pp. 567-580, 2014.

[59] K. Sivula, F. Le Formal, M. Grätzel, Solar Water Splitting: Progress Using Hematite (α-Fe_2O_3) Photoelectrodes, *ChemSusChem*, 4, pp. 432-449, 2011.

[60] B. Iandolo, B. Wickman, I. Zoric, A. Hellman, The rise of hematite: origin and strategies to reduce the high onset potential for the oxygen evolution reaction, *Journal of Materials Chemistry A*, 3, pp. 16896-16912, 2015.

[61] C. Acar, I. Dincer, A review and evaluation of photoelectrode coating materials and methods for photoelectrochemical hydrogen production, *International Journal of Hydrogen Energy*, 41, pp. 7950-7959, 2016.

[62] P. Dias, A. Vilanova, T. Lopes, L. Andrade, A. Mendes, Extremely stable bare hematite photoanode for solar water splitting, *Nano Energy*, 23, pp. 70-79, 2016.

[63] X. Chen, Z. Zhang, L. Chi, A.K. Nair, W. Shangguan, Z. Jiang, Recent Advances in Visible-Light-Driven Photoelectrochemical Water Splitting: Catalyst Nanostructures and Reaction Systems, *Nano-Micro Letters*, 8, pp. 1-12, 2016.

[64] Y. Ling, Y. Li, Review of Sn-Doped Hematite Nanostructures for Photoelectrochemical Water Splitting, *Particle & Particle Systems Characterization*, 31, pp. 1113-1121, 2014.

[65] A. Hankin, F.E. Bedoya-Lora, C.K. Ong, J.C. Alexander, F. Petter, G.H. Kelsall, From millimetres to metres: the critical role of current density distributions in photo-electrochemical reactor design, *Energy & Environmental Science*, 10, pp. 346-360, 2017.

[66] R.H. Coridan, A.C. Nielander, S.A. Francis, M.T. McDowell, V. Dix, S.M. Chatman, N.S. Lewis, Methods for comparing the performance of energy-conversion systems for use in solar fuels and solar electricity generation, *Energy & Environmental Science*, 8, pp. 2886-2901, 2015.

[67] J. Turner, G. Sverdrup, M.K. Mann, P.-C. Maness, B. Kroposki, M. Ghirardi, R.J. Evans, D. Blake, Renewable hydrogen production, *International Journal of Energy Research*, 32, pp. 379-407, 2008.

[68] D.N. Borton, W.E. Rogers, Solar Dissociation Of Hydrogen Sulfide: A First Step In Producing A Renewable Fuel, Energy Conversion Engineering Conference, 1990. IECEC-90. Proceedings of the 25th Intersociety, 1990, pp. 315-319.

[69] J. Zaman, A. Chakma, Production of hydrogen and sulfur from hydrogen sulfide, *Fuel Processing Technology*, 41, pp. 159-198, 1995.

[70] D.L. Pringle, The nature of the polysulfide anion, Chemistry, Iowa State University, 1967.

[71] R.H. Arntson, F.W. Dickson, G. Tunell, Saturation Curves of Orthorhombic Sulfur in the System S-Na_2S-H_2O at 25 and 50 °C, *Science*, 128, pp. 716, 1958.

[72] W.F. Giggenbach, Equilibriums involving polysulfide ions in aqueous sulfide solutions up to 240.deg, *Inorganic Chemistry*, 13, pp. 1724-1730, 1974.

[73] G.H. Kelsall, I. Thompson, Redox chemistry of H_2S oxidation by the British Gas Stretford Process. Part I: Thermodynamics of sulphur-water systems at 298 K, *Journal of Applied Electrochemistry*, 23, pp. 279-286, 1993.

[74] F. Bedoya-Lora, A. Hankin, G.H. Kelsall, Photo-electrochemical hydrogen sulfide splitting using Sn^{IV}-doped hematite photo-anodes, *Electrochemistry Communications*, 68, pp. 19-22, 2016.

[75] V. Preethi, S. Kanmani, Photocatalytic hydrogen production, *Materials Science in Semiconductor Processing*, 16, pp. 561-575, 2013.

[76] W.M. Haynes, Handbook of chemistry and physics, CRC Press, Boca Raton, United States of America, 2013.

[77] M. Gratzel, Molecular Engineering in Photoconversion Systems, Academic Press, Inc., New York, 1983.

[78] S. Licht, G. Hodes, J. Manassen, Numerical analysis of aqueous polysulfide solutions and its application to cadmium chalcogenide/polysulfide photoelectrochemical solar cells, *Inorganic Chemistry*, 25, pp. 2486-2489, 1986.

[79] R.C. Kainthla, J.O.M. Bockris, Photoelectrolysis of H_2S using an n-CdSe photoanode, *International Journal of Hydrogen Energy*, 12, pp. 23-26, 1987.

[80] R. Brahimi, Y. Bessekhouad, A. Bouguelia, M. Trari, Visible light induced hydrogen evolution over the heterosystem Bi_2S_3/TiO_2, *Catalysis Today*, 122, pp. 62-65, 2007.

[81] U.V. Kawade, R.P. Panmand, Y.A. Sethi, M.V. Kulkarni, S.K. Apte, S.D. Naik, B.B. Kale, Environmentally benign enhanced hydrogen production via lethal H_2S under natural sunlight using hierarchical nanostructured bismuth sulfide, *RSC Advances*, 4, pp. 49295-49302, 2014.

[82] X. Zong, J. Han, B. Seger, H. Chen, G. Lu, C. Li, L. Wang, An Integrated Photoelectrochemical–Chemical Loop for Solar-Driven Overall Splitting of Hydrogen Sulfide, *Angewandte Chemie*, 126, pp. 4488-4492, 2014.

[83] K. Natarajan, M. Saraf, S.M. Mobin, Visible-Light-Induced Water Splitting Based on a Novel α-Fe_2O_3/CdS Heterostructure, *ACS Omega*, 2, pp. 3447-3456, 2017.

[84] K. Rajeshwar, Materials aspects of photoelectrochemical energy conversion, *Journal of Applied Electrochemistry*, 15, pp. 1-22, 1985.

[85] O. Khaselev, J.A. Turner, A Monolithic Photovoltaic-Photoelectrochemical Device for Hydrogen Production via Water Splitting, *Science*, 280, pp. 425-427, 1998.

[86] S. Licht, B. Wang, S. Mukerji, T. Soga, M. Umeno, H. Tributsch, Efficient Solar Water Splitting, Exemplified by RuO_2-Catalyzed AlGaAs/Si Photoelectrolysis, *The Journal of Physical Chemistry B*, 104, pp. 8920-8924, 2000.

[87] J. Jia, L.C. Seitz, J.D. Benck, Y. Huo, Y. Chen, J.W.D. Ng, T. Bilir, J.S. Harris, T.F. Jaramillo, Solar water splitting by photovoltaic-electrolysis with a solar-to-hydrogen efficiency over 30%, *Nature Communications*, 7, pp. 13237, 2016.

[88] B.D. Alexander, P.J. Kulesza, I. Rutkowska, R. Solarska, J. Augustynski, Metal oxide photoanodes for solar hydrogen production, *Journal of Materials Chemistry*, 18, pp. 2298-2303, 2008.

[89] C.K. Ong, S. Dennison, S. Fearn, K. Hellgardt, G.H. Kelsall, Behaviour of Titanium-based Fe_2O_3 Photo-Anodes in Photo-Electrochemical Reactors for Water Splitting, *Electrochimica Acta*, 125, pp. 266-274, 2014.

[90] S. Sahai, A. Ikram, S. Rai, S. Dass, R. Shrivastav, V.R. Satsangi, CdSe quantum dots sensitized nanoporous hematite for photoelectrochemical generation of hydrogen, *International Journal of Hydrogen Energy*, 39, pp. 11860-11866, 2014.

[91] L. Steier, J. Luo, M. Schreier, M.T. Mayer, T. Sajavaara, M. Grätzel, Low-Temperature Atomic Layer Deposition of Crystalline and Photoactive Ultrathin Hematite Films for Solar Water Splitting, *ACS Nano*, 9, pp. 11775-11783, 2015.

[92] O. Zandi, A.R. Schon, H. Hajibabaei, T.W. Hamann, Enhanced Charge Separation and Collection in High-Performance Electrodeposited Hematite Films, *Chemistry of Materials*, 28, pp. 765-771, 2016.

[93] J.Y. Kim, D.H. Youn, J.H. Kim, H.G. Kim, J.S. Lee, Nanostructure-Preserved Hematite Thin Film for Efficient Solar Water Splitting, *ACS Applied Materials & Interfaces*, 7, pp. 14123-14129, 2015.

[94] M. Forster, R.J. Potter, Y. Ling, Y. Yang, D.R. Klug, Y. Li, A.J. Cowan, Oxygen deficient Fe_2O_3 photoelectrodes: a balance between enhanced electrical properties and trap-mediated losses, *Chemical Science*, 6, pp. 4009-4016, 2015.

[95] A. Koca, M. Şahin, Photocatalytic hydrogen production by direct sun light from sulfide/sulfite solution, *International Journal of Hydrogen Energy*, 27, pp. 363-367, 2002.

[96] M. Matsumura, S. Furukawa, Y. Saho, H. Tsubomura, Cadmium sulfide photocatalyzed hydrogen production from aqueous solutions of sulfite: effect of crystal structure and preparation method of the catalyst, *The Journal of Physical Chemistry*, 89, pp. 1327-1329, 1985.

[97] E. Borgarello, K. Kalyanasundaram, M. Grätzel, E. Pelizzetti, Visible Light Induced Generation of Hydrogen from H_2S in CdS-Dispersions, Hole Transfer Catalysis by RuO_2, *Helvetica Chimica Acta*, 65, pp. 243-248, 1982.

[98] S.P.a.H.K. Chullae Cho, Photocatalytic Hydrogen Evolution with Platinum Loaded Cadmium-Iron-Sulfide Mixed Crystal Powders in Aqueous Media, *Bulletin-Korean Chemical Society*, 21, pp. 805, 2000.

[99] M. Sharon, K. Basavaswaran, Photoelectrochemical behaviour of tin monosulphide, *Solar Cells*, 25, pp. 97-107, 1988.

[100] R.K. Arya, Photoelectrochemical hydrogen production using visible light *International Journal of Renewable Energy Research*, 2, pp., 2012.

[101] Z. Chen, A.J. Forman, T.F. Jaramillo, Bridging the Gap Between Bulk and Nanostructured Photoelectrodes: The Impact of Surface States on the Electrocatalytic and Photoelectrochemical Properties of MoS_2, *The Journal of Physical Chemistry C*, 117, pp. 9713-9722, 2013.

[102] T.F. Jaramillo, J.D. Benck, J. Kibsgaard, Z. Chen, B.N. Reinecke, (673d) Molybdenum Sulfides Materials As Hydrogen Evolution Catalysts and Surface Protecting Layers for Highly Active and Stable Silicon-Based Water Splitting Photocathodes, American Institue of Chemical Engineers Annual Meeting San Francisco, United States, 2013.

[103] Y. Bessekhouad, M. Mohammedi, M. Trari, Hydrogen photoproduction from hydrogen sulfide on Bi_2S_3 catalyst, *Solar Energy Materials and Solar Cells*, 73, pp. 339-350, 2002.

[104] B.F. Giannetti, S.H. Bonilla, C.F. Zinola, T. Rabóczkay, A study of the main oxidation products of natural pyrite by voltammetric and photoelectrochemical responses, *Hydrometallurgy*, 60, pp. 41-53, 2001.

[105] A. Ennaoui, S. Fiechter, W. Jaegermann, H. Tributsch, Photoelectrochemistry of Highly Quantum Efficient Single-Crystalline n - FeS_2 (Pyrite), *Journal of The Electrochemical Society*, 133, pp. 97-106, 1986.

[106] A. Ennaoui, S. Fiechter, H. Goslowsky, H. Tributsch, Photoactive Synthetic Polycrystalline Pyrite (FeS2) *Journal of The Electrochemical Society*, 132, pp. 1579-1582, 1985.

[107] A.K. Raturia, S. Waitab, B. Adudab, T. Nyangondab, Photoactive iron pyrite films for photoelectrochemical (PEC) cells, *Renewable Energy*, 20, pp. 37-43, 2000.

[108] B. Chakraborty, B. Show, S. Jana, B.C. Mitra, S.K. Maji, B. Adhikary, N. Mukherjee, A. Mondal, Cathodic and anodic deposition of FeS_2 thin films and their application in electrochemical reduction and amperometric sensing of H_2O_2, *Electrochimica Acta*, 94, pp. 7-15, 2013.

[109] J.-Y. Lin, J.-H. Liao, S.-W. Chou, Cathodic electrodeposition of highly porous cobalt sulfide counter electrodes for dye-sensitized solar cells, *Electrochimica Acta*, 56, pp. 8818-8826, 2011.

[110] F.A. Lowenheim, Modern Electroplating, John Wiley & Sons, 1963.

[111] R.S. Patil, Electrosynthesis of the molybdenum disulphide thin films and characterization, *Thin Solid Films*, 340, pp. 11-12, 1999.

[112] K.-T. Lee, S.-Y. Lu, Porous FTO thin layers created with a facile one-step Sn^{4+}-based anodic deposition process and their potential applications in ion sensing, *Journal of Materials Chemistry*, 22, pp. 16259-16268, 2012.

[113] Y. Wang, J.F. Huang, L.Y. Cao, H. Zhu, H.Y. He, J.P. Wu, Synthesis and characterisation of oriented Bi_2S_3 thin films by novel ultrasonic assisted cathodic electrodeposition route, *Surface Engineering*, 27, pp. 37-40, 2011.

[114] C.K. Ong, Design and Performance of Photo-electrochemical Reactors with Fe_2O_3 Photo-anodes for Water Splitting, Department of Chemical Engineering, Imperial College London, London, 2013.

[115] J. Jin, K. Walczak, M.R. Singh, C. Karp, N.S. Lewis, C. Xiang, An experimental and modeling/simulation-based evaluation of the efficiency and operational performance characteristics of an integrated, membrane-free, neutral pH solar-driven water-splitting system, *Energy & Environmental Science*, 7, pp. 3371-3380, 2014.

[116] S. Hu, C. Xiang, S. Haussener, A.D. Berger, N.S. Lewis, An analysis of the optimal band gaps of light absorbers in integrated tandem photoelectrochemical water-splitting systems, *Energy & Environmental Science*, 6, pp. 2984-2993, 2013.

[117] M.R. Singh, C. Xiang, N.S. Lewis, Evaluation of flow schemes for near-neutral pH electrolytes in solar-fuel generators, *Sustainable Energy & Fuels*, pp., 2017.

[118] I. Holmes-Gentle, F. Hoffmann, C.A. Mesa, K. Hellgardt, Membrane-less photoelectrochemical cells: product separation by hydrodynamic control, *Sustainable Energy & Fuels*, pp., 2017.

[119] A. Berger, R.A. Segalman, J. Newman, Material requirements for membrane separators in a water-splitting photoelectrochemical cell, *Energy & Environmental Science*, 7, pp. 1468-1476, 2014.

[120] J. Newman, Scaling with Ohm's Law; Wired vs. Wireless Photoelectrochemical Cells, *Journal of The Electrochemical Society*, 160, pp. F309-F311, 2013.

[121] H. Gerischer, The impact of semiconductors on the concepts of electrochemistry, *Electrochimica Acta*, 35, pp. 1677-1699, 1990.

[122] S. Haussener, C. Xiang, J.M. Spurgeon, S. Ardo, N.S. Lewis, A.Z. Weber, Modeling, simulation, and design criteria for photoelectrochemical water-splitting systems, *Energy & Environmental Science*, 5, pp. 9922-9935, 2012.

[123] M.A. Butler, Photoelectrolysis and physical properties of the semiconducting electrode WO_2, *Journal of Applied Physics*, 48, pp. 1914-1920, 1977.

[124] W.W. Gärtner, Depletion-Layer Photoeffects in Semiconductors, *Physical Review*, 116, pp. 84-87, 1959.

[125] R. Memming, Chapter 8: Processes at Semiconductor Electrodes, in: B.E. Conway, J.O.M. Bockris, E. Yeager, S.U.M. Khan, R.E. White (Eds.) Comprehensive Treatise of Electrochemistry, Springer, US, pp. 529 – 592 1983.

[126] J.M. Chin Kwie Joe, L.J.J. Janssen, S.J.D. van Strelen, J.H.G. Verbunt, W.M. Sluyter, Bubble parameters and efficiency of gas bubble evolution for a chlorine-, a hydrogen- and an oxygen-evolving wire electrode, *Electrochimica Acta*, 33, pp. 769-779, 1988.

[127] H. Vogt, The rate of gas evolution of electrodes—I. An estimate of the efficiency of gas evolution from the supersaturation of electrolyte adjacent to a gas-evolving electrode, *Electrochimica Acta*, 29, pp. 167-173, 1984.

[128] H. Vogt, On the gas-evolution efficiency of electrodes I – Theoretical, *Electrochimica Acta*, 56, pp. 1409-1416, 2011.

[129] P. Painmanakul, J. Wachirasak, M. Jamnongwong, G. Hebrard, Theoretical Prediction of Volumetric Mass Transfer Coefficient (k_{La}) for Designing an Aeration Tank, *Engineering Journal*, 13, pp. 16, 2009.

[130] T. Bosserez, L. Geerts, J. Rongé, F. Ceyssens, S. Haussener, R. Puers, J.A. Martens, Minimization of Ionic Transport Resistance in Porous Monoliths for Application in Integrated Solar Water Splitting Devices, *The Journal of Physical Chemistry C*, 120, pp. 21242-21247, 2016.

[131] S. Tembhurne, S. Haussener, Integrated Photo-Electrochemical Solar Fuel Generators under Concentrated Irradiation: I. 2-D Non-Isothermal Multi-Physics Modeling, *Journal of The Electrochemical Society*, 163, pp. H988-H998, 2016.

[132] Y.K. Gaudy, S. Haussener, Utilizing modeling, experiments, and statistics for the analysis of water-splitting photoelectrodes, *Journal of Materials Chemistry A*, 4, pp. 3100-3114, 2016.

[133] S.Y. Reece, J.A. Hamel, K. Sung, T.D. Jarvi, A.J. Esswein, J.J.H. Pijpers, D.G. Nocera, Wireless Solar Water Splitting Using Silicon-Based Semiconductors and Earth-Abundant Catalysts, *Science*, 334, pp. 645-648, 2011.

[134] K. Schulz, R. Schmack, H.W. Klemm, A. Kabelitz, T. Schmidt, F. Emmerling, R. Kraehnert, Mechanism and Kinetics of Hematite Crystallization in Air: Linking Bulk and Surface Models via Mesoporous Films with Defined Nanostructure, *Chemistry of Materials*, 29, pp. 1724-1734, 2017.

[135] M. Li, J. Deng, A. Pu, P. Zhang, H. Zhang, J. Gao, Y. Hao, J. Zhong, X. Sun, Hydrogen-treated hematite nanostructures with low onset potential for highly efficient solar water oxidation, *Journal of Materials Chemistry A*, 2, pp. 6727-6733, 2014.

[136] K. Sivula, R. Zboril, F. Le Formal, R. Robert, A. Weidenkaff, J. Tucek, J. Frydrych, M. Grätzel, Photoelectrochemical Water Splitting with Mesoporous Hematite Prepared by a Solution-Based Colloidal Approach, *Journal of the American Chemical Society*, 132, pp. 7436-7444, 2010.

[137] Y. Ling, G. Wang, D.A. Wheeler, J.Z. Zhang, Y. Li, Sn-Doped Hematite Nanostructures for Photoelectrochemical Water Splitting, *Nano Letters*, 11, pp. 2119-2125, 2011.

[138] K.H. P. Kofstad, Investigation on the Oxidation Mechanism of Titanium, *Acta Chemica Scandinavica*, 12, pp. 239-266, 1958.

[139] J. Frydrych, L. Machala, J. Tucek, K. Siskova, J. Filip, J. Pechousek, K. Safarova, M. Vondracek, J.H. Seo, O. Schneeweiss, M. Gratzel, K. Sivula, R. Zboril, Facile fabrication of tin-doped hematite photoelectrodes - effect of doping on magnetic properties and performance for light-induced water splitting, *Journal of Materials Chemistry*, 22, pp. 23232-23239, 2012.

[140] P.S. Bassi, L. Xianglin, Y. Fang, J.S.C. Loo, J. Barber, L.H. Wong, Understanding charge transport in non-doped pristine and surface passivated hematite (Fe_2O_3) nanorods under front and backside illumination in the context of light induced water splitting, *Physical Chemistry Chemical Physics*, 18, pp. 30370-30378, 2016.

[141] R. Milan, S. Cattarin, N. Comisso, C. Baratto, K. Kaunisto, N.V. Tkachenko, I. Concina, Compact hematite buffer layer as a promoter of nanorod photoanode performances, 6, pp. 35049, 2016.

[142] U. Bjoerksten, J. Moser, M. Graetzel, Photoelectrochemical Studies on Nanocrystalline Hematite Films, *Chemistry of Materials*, 6, pp. 858-863, 1994.

[143] C.K. Ong, S. Dennison, K. Hellgardt, G. Kelsall, Evaluation and Modeling of a Photo-Electrochemical Reactor for Hydrogen Production Operating under High Photon Flux, *ECS Transactions*, 35, pp. 11-19, 2011.

[144] V.M. Aroutiounian, V.M. Arakelyan, G.E. Shahnazaryan, H.R. Hovhannisyan, H. Wang, J.A. Turner, Photoelectrochemistry of tin-doped iron oxide electrodes, *Solar Energy*, 81, pp. 1369-1376, 2007.

[145] H.K. Dunn, J.M. Feckl, A. Muller, D. Fattakhova-Rohlfing, S.G. Morehead, J. Roos, L.M. Peter, C. Scheu, T. Bein, Tin doping speeds up hole transfer during light-driven water oxidation at hematite photoanodes, *Physical Chemistry Chemical Physics*, 16, pp. 24610-24620, 2014.

[146] K.G. Upul Wijayantha, S. Saremi-Yarahmadi, L.M. Peter, Kinetics of oxygen evolution at Fe_2O_3 photoanodes: a study by photoelectrochemical impedance spectroscopy, *Physical Chemistry Chemical Physics*, 13, pp. 5264-5270, 2011.

[147] L.M. Peter, Energetics and kinetics of light-driven oxygen evolution at semiconductor electrodes: the example of hematite, *Journal of Solid State Electrochemistry*, 17, pp. 315-326, 2013.

[148] W.P. Gomes, F. Cardon, Electron energy levels in semiconductor electrochemistry, *Progress in Surface Science*, 12, pp. 155-215, 1982.

[149] Y. Ma, S.R. Pendlebury, A. Reynal, F. Le Formal, J.R. Durrant, Dynamics of photogenerated holes in undoped $BiVO_4$ photoanodes for solar water oxidation, *Chemical Science*, 5, pp. 2964-2973, 2014.

[150] B. Hirschorn, M.E. Orazem, B. Tribollet, V. Vivier, I. Frateur, M. Musiani, Determination of effective capacitance and film thickness from constant-phase-element parameters, *Electrochimica Acta*, 55, pp. 6218-6227, 2010.

[151] B. Klahr, S. Gimenez, F. Fabregat-Santiago, T. Hamann, J. Bisquert, Water Oxidation at Hematite Photoelectrodes: The Role of Surface States, *Journal of the American Chemical Society*, 134, pp. 4294-4302, 2012.

[152] H. Uchiyama, M. Yukizawa, H. Kozuka, Photoelectrochemical Properties of Fe_2O_3–SnO_2 Films Prepared by Sol–Gel Method, *The Journal of Physical Chemistry C*, 115, pp. 7050-7055, 2011.

[153] S. Rühle, D. Cahen, Electron Tunneling at the TiO_2/Substrate Interface Can Determine Dye-Sensitized Solar Cell Performance, *The Journal of Physical Chemistry B*, 108, pp. 17946-17951, 2004.

[154] M.V. Diamanti, S. Codeluppi, A. Cordioli, M.P. Pedeferri, Effect of thermal oxidation on titanium oxides' characteristics, *Journal of Experimental Nanoscience*, 4, pp. 365-372, 2009.

[155] Y. Ling, G. Wang, J. Reddy, C. Wang, J.Z. Zhang, Y. Li, The Influence of Oxygen Content on the Thermal Activation of Hematite Nanowires, *Angewandte Chemie International Edition*, 51, pp. 4074-4079, 2012.

[156] B. Amami, M. Addou, F. Millot, A. Sabioni, C. Monty, Self-diffusion in α-Fe_2O_3 natural single crystals, *Ionics*, 5, pp. 358-370, 1999.

[157] I. Cesar, K. Sivula, A. Kay, R. Zboril, M. Grätzel, Influence of Feature Size, Film Thickness, and Silicon Doping on the Performance of Nanostructured Hematite Photoanodes for Solar Water Splitting, *The Journal of Physical Chemistry C*, 113, pp. 772-782, 2009.

[158] F.A. Benko, J. Longo, F.P. Koffyberg, A Comparison of Photochemical Properties of Amorphous and Polycrystalline Fe_2O_3, *Journal of The Electrochemical Society*, 132, pp. 609-613, 1985.

[159] R.A. Lunt, A.J. Jackson, A. Walsh, Dielectric response of Fe_2O_3 crystals and thin films, *Chemical Physics Letters*, 586, pp. 67-69, 2013.

[160] M.A. Butler, D.S. Ginley, M. Eibschutz, Photoelectrolysis with $YFeO_3$ electrodes, *Journal of Applied Physics*, 48, pp. 3070-3072, 1977.

[161] D.L.A. de Faria, S. Venâncio Silva, M.T. de Oliveira, Raman microspectroscopy of some iron oxides and oxyhydroxides, *Journal of Raman Spectroscopy*, 28, pp. 873-878, 1997.

[162] T. Ohsaka, F. Izumi, Y. Fujiki, Raman spectrum of anatase, TiO_2, *Journal of Raman Spectroscopy*, 7, pp. 321-324, 1978.

[163] S.P.S. Porto, P.A. Fleury, T.C. Damen, Raman Spectra of TiO_2, MgF_2 ZnF_2 FeF_2, and MnF_2, *Physical Review*, 154, pp. 522-526, 1967.

[164] X. Yang, R. Liu, Y. Lei, P. Li, K. Wang, Z. Zheng, D. Wang, Dual Influence of Reduction Annealing on Diffused Hematite/FTO Junction for Enhanced Photoelectrochemical Water Oxidation, *ACS Applied Materials & Interfaces*, 8, pp. 16476-16485, 2016.

[165] R. Morrish, M. Rahman, J.M.D. MacElroy, C.A. Wolden, Activation of Hematite Nanorod Arrays for Photoelectrochemical Water Splitting, *ChemSusChem*, 4, pp. 474-479, 2011.

[166] R.B. Beall, J.B. Clegg, J.J. Harris, Migration of Si in δ-doped GaAs, *Semiconductor Science and Technology*, 3, pp. 612, 1988.

[167] D. Briggs, M.P. Seah, Practical Surface Analysis, Auger and X-ray Photoelectron Spectroscopy, Wiley, 1990.

[168] B.V. King, I.S.T. Tsong, The depth resolution of sputter profiling, *Ultramicroscopy*, 14, pp. 75-78, 1984.

[169] M.J. Katz, S.C. Riha, N.C. Jeong, A.B.F. Martinson, O.K. Farha, J.T. Hupp, Toward solar fuels: Water splitting with sunlight and "rust"?, *Coordination Chemistry Reviews*, 256, pp. 2521-2529, 2012.

[170] B. Turan, J.-P. Becker, F. Urbain, F. Finger, U. Rau, S. Haas, Upscaling of integrated photoelectrochemical water-splitting devices to large areas, *Nature Communications*, 7, pp. 12681, 2016.

[171] A. Landman, H. Dotan, G.E. Shter, M. Wullenkord, A. Houaijia, A. Maljusch, G.S. Grader, A. Rothschild, Photoelectrochemical water splitting in separate oxygen and hydrogen cells, *Nature Materials*, advance online publication, pp., 2017.

[172] Q. Wang, T. Hisatomi, Q. Jia, H. Tokudome, M. Zhong, C. Wang, Z. Pan, T. Takata, M. Nakabayashi, N. Shibata, Y. Li, I.D. Sharp, A. Kudo, T. Yamada, K. Domen, Scalable water splitting on particulate photocatalyst sheets with a solar-to-hydrogen energy conversion efficiency exceeding 1%, *Nature Materials*, 15, pp. 611-615, 2016.

[173] M.D. Bhatt, J.S. Lee, Recent theoretical progress in the development of photoanode materials for solar water splitting photoelectrochemical cells, *Journal of Materials Chemistry A*, 3, pp. 10632-10659, 2015.

[174] S.P. Berglund, F.F. Abdi, P. Bogdanoff, A. Chemseddine, D. Friedrich, R. van de Krol, Comprehensive Evaluation of $CuBi_2O_4$ as a Photocathode Material for Photoelectrochemical Water Splitting, *Chemistry of Materials*, 28, pp. 4231-4242, 2016.

[175] A. Paracchino, V. Laporte, K. Sivula, M. Grätzel, E. Thimsen, Highly active oxide photocathode for photoelectrochemical water reduction, *Nature Materials*, 10, pp. 456-461, 2011.

[176] D.M.F. Santos, C.A.C. Sequeira, J.L. Figueiredo, Hydrogen production by alkaline water electrolysis, *Química Nova*, 36, pp. 1176-1193, 2013.

[177] A. Berger, J. Newman, An Integrated 1-Dimensional Model of a Photoelectrochemical Cell for Water Splitting, *Journal of The Electrochemical Society*, 161, pp. E3328-E3340, 2014.

[178] C. Carver, Z. Ulissi, C.K. Ong, S. Dennison, K. Hellgardt, G.H. Kelsall, Modeling and Evaluation of a Photoelectrochemical Reactor for H_2 Production, *ECS Transactions*, 28, pp. 103-117, 2010.

[179] A.J. Leenheer, H.A. Atwater, Water-Splitting Photoelectrolysis Reaction Rate via Microscopic Imaging of Evolved Oxygen Bubbles, *Journal of The Electrochemical Society*, 157, pp. B1290-B1294, 2010.

[180] H. Dotan, K. Sivula, M. Gratzel, A. Rothschild, S.C. Warren, Probing the photoelectrochemical properties of hematite electrodes using hydrogen peroxide as a hole scavenger, *Energy & Environmental Science*, 4, pp. 958-964, 2011.

[181] L.M. Peter, CHAPTER 1 Photoelectrochemistry: From Basic Principles to Photocatalysis, Photocatalysis: Fundamentals and Perspectives, The Royal Society of Chemistry, pp. 1-28, 2016.

[182] H. Vogt, On the gas-evolution efficiency of electrodes. II – Numerical analysis, *Electrochimica Acta*, 56, pp. 2404-2410, 2011.

[183] H. Vogt, The rate of gas evolution at electrodes—II. An estimate of the efficiency of gas evolution on the basis of bubble growth data, *Electrochimica Acta*, 29, pp. 175-180, 1984.

[184] N. Frossling, Uber die Verdunstung Fallender Tropfen (The Evaporation of Falling Drops), *Gerlands Beitrage zur Geophysik*, 52, pp. 107-216, 1938.

[185] G. Marrucci, L. Nicodemo, Coalescence of gas bubbles in aqueous solutions of inorganic electrolytes, *Chemical Engineering Science*, 22, pp. 1257-1265, 1967.

[186] D.F. McGinnis, J.C. Little, Predicting diffused-bubble oxygen transfer rate using the discrete-bubble model, *Water Research*, 36, pp. 4627-4635, 2002.

[187] A. Wüest, N.H. Brooks, D.M. Imboden, Bubble plume modeling for lake restoration, *Water Resources Research*, 28, pp. 3235-3250, 1992.

[188] W.D. Deckwer, Bubble Column Reactions, John Wiley, Chichester, 1992.

[189] W.D. Deckwer, R. Burckhart, G. Zoll, Mixing and mass transfer in tall bubble columns, *Chemical Engineering Science*, 29, pp. 2177-2188, 1974.

[190] J.B. Joshi, M.M. Sharma, A circulation model for bubble columns, *Transactions of the Institute of Chemical Engineers*, 57, pp. 244-251, 1979.

[191] W. Sheng, H.A. Gasteiger, Y. Shao-Horn, Hydrogen Oxidation and Evolution Reaction Kinetics on Platinum: Acid vs Alkaline Electrolytes, *Journal of The Electrochemical Society*, 157, pp. B1529-B1536, 2010.

[192] R.W. Powell, R.P. Tye, The thermal and electrical conductivity of titanium and its alloys, *Journal of the Less Common Metals*, 3, pp. 226-233, 1961.

[193] Y. Sone, P. Ekdunge, D. Simonsson, Proton Conductivity of Nafion 117 as Measured by a Four-Electrode AC Impedance Method, *Journal of The Electrochemical Society*, 143, pp. 1254-1259, 1996.

[194] A.T. Haug, R.E. White, Oxygen Diffusion Coefficient and Solubility in a New Proton Exchange Membrane, *Journal of The Electrochemical Society*, 147, pp. 980-983, 2000.

[195] Z. Ogumi, T. Kuroe, Z.i. Takehara, Gas Permeation in SPE Method: II . Oxygen and Hydrogen Permeation Through Nafion, *Journal of The Electrochemical Society*, 132, pp. 2601-2605, 1985.

[196] S.H. Lee, Molecular Dynamics Simulation Study for Hydroxide Ion in Supercritical Water using SPC/E Water Potential, *Bulletin of the Korean Chemical Society*, 34, pp. 2925-2930, 2013.

[197] R. De Gryse, W.P. Gomes, F. Cardon, J. Vennik, On the Interpretation of Mott-Schottky Plots Determined at Semiconductor/Electrolyte Systems, *Journal of The Electrochemical Society*, 122, pp. 711-712, 1975.

[198] S. Shibata, The Concentration of Molecular Hydrogen on the Platinum Cathode, *Bulletin of The Chemical Society of Japan*, 36, pp. 53-57, 1963.

[199] S. Shibata, Supersaturation of oxygen in acidic solution in the vicinity of an oxygen-evolving platinum anode, *Electrochimica Acta*, 23, pp. 619-623, 1978.

[200] Y. Tachibana, L. Vayssieres, J.R. Durrant, Artificial photosynthesis for solar water-splitting, *Nature Photon*, 6, pp. 511-518, 2012.

[201] N.A. Kelly, T.L. Gibson, Design and characterization of a robust photoelectrochemical device to generate hydrogen using solar water splitting, *International Journal of Hydrogen Energy*, 31, pp. 1658-1673, 2006.

[202] R.E. Rocheleau, E.L. Miller, A. Misra, High-Efficiency Photoelectrochemical Hydrogen Production Using Multijunction Amorphous Silicon Photoelectrodes, *Energy & Fuels*, 12, pp. 3-10, 1998.

[203] T. Lopes, P. Dias, L. Andrade, A. Mendes, An innovative photoelectrochemical lab device for solar water splitting, *Solar Energy Materials and Solar Cells*, 128, pp. 399-410, 2014.

[204] C. Xiang, A.Z. Weber, S. Ardo, A. Berger, Y. Chen, R. Coridan, K.T. Fountaine, S. Haussener, S. Hu, R. Liu, N.S. Lewis, M.A. Modestino, M.M. Shaner, M.R. Singh, J.C. Stevens, K. Sun, K. Walczak, Modeling, Simulation, and Implementation of Solar-Driven Water-Splitting Devices, *Angewandte Chemie International Edition*, 55, pp. 12974-12988, 2016.

[205] S.K. Shoor, Solubility of nonpolar gases in potassium hydroxid solutions, University of Florida, Florida, US, 1968.

[206] D. Tromans, Temperature and pressure dependent solubility of oxygen in water: a thermodynamic analysis, *Hydrometallurgy*, 48, pp. 327-342, 1998.

[207] R.E. Davis, G.L. Horvath, C.W. Tobias, The solubility and diffusion coefficient of oxygen in potassium hydroxide solutions, *Electrochimica Acta*, 12, pp. 287-297, 1967.

[208] H. Vogt, On the various types of uncontrolled potential increase in electrochemical reactors—The anode effect, *Electrochimica Acta*, 87, pp. 611-618, 2013.

[209] ASTM, G173-03 Standard Tables for Reference Solar Spectral Irradiances: Direct Normal and Hemispherical on 37 ° Tilted Surface, 2012.

[210] W. Giggenbach, Optical spectra and equilibrium distribution of polysulfide ions in aqueous solution at 20.deg, *Inorganic Chemistry*, 11, pp. 1201-1207, 1972.

[211] N. Li, Z. Weng, Y. Wang, F. Li, H.-M. Cheng, H. Zhou, An aqueous dissolved polysulfide cathode for lithium-sulfur batteries, *Energy & Environmental Science*, 7, pp. 3307-3312, 2014.

[212] W.E. Kleinjan, A.d. Keizer, A.J.H. Janssen, Kinetics of the chemical oxidation of polysulfide anions in aqueous solution, *Water Research*, 39, pp. 4093-4100, 2005.

[213] G. Schwarzenbach, A. Fischer, Die Acidität der Sulfane und die Zusammensetzung wässeriger Polysulfidlösungen, *Helvetica Chimica Acta*, 43, pp. 1365-1390, 1960.

[214] G. Le Guillanton, Q.T. Do, D. Elothmani, Determination of Mixtures of Polysulfides by Cyclic Voltammetry, *Journal of The Electrochemical Society*, 143, pp. L223-L225, 1996.

[215] A. Kamyshny, I. Ekeltchik, J. Gun, O. Lev, Method for the Determination of Inorganic Polysulfide Distribution in Aquatic Systems, *Analytical Chemistry*, 78, pp. 2631-2639, 2006.

[216] S. Licht, J. Davis, Disproportionation of Aqueous Sulfur and Sulfide: Kinetics of Polysulfide Decomposition, *The Journal of Physical Chemistry B*, 101, pp. 2540-2545, 1997.

[217] S.A. Khan, UV-ATR Spectroscopy Study of the Speciation in Aqueous Polysulfide Electrolyte Solutions, *International Journal of Electrochemical Science*, 7, pp. 561 - 568, 2012.

[218] A. Kamyshny, A. Goifman, J. Gun, D. Rizkov, O. Lev, Equilibrium Distribution of Polysulfide Ions in Aqueous Solutions at 25 °C: A New Approach for the Study of Polysulfides' Equilibria, *Environmental Science & Technology*, 38, pp. 6633-6644, 2004.

[219] P. Lessner, J. Winnick, F.R. McLarnon, E.J. Cairns, Kinetics of Aqueous Polysulfide Solutions: II . Electrochemical Measurement of the Rates of Coupled Electrochemical and Chemical Reactions by the Potential Step Method, *Journal of The Electrochemical Society*, 133, pp. 2517-2522, 1986.

[220] J.A. Tossell, Calculation of the visible-UV absorption spectra of hydrogen sulfide, bisulfide, polysulfides, and As and Sb sulfides, in aqueous solution, *Geochemical Transactions*, 4, pp. 28-33, 2003.

[221] X.S. Chai, J. Li, J.Y. Zhu, Simultaneous and rapid analysis of hydroxide, sulfide, and carbonate in kraft liquors by attenuated total reflection UV spectroscopy, *Journal of pulp and paper science*, 28, pp. 105-109, 2002.

[222] G.H. Kelsall, I. Thompson, Redox chemistry of H_2S oxidation by the British Gas Stretford Process. Part. II: Electrochemical behaviour of aqueous hydrosulphide (HS^-) solutions, *Journal of Applied Electrochemistry*, 23, pp. 287-295, 1993.

[223] R. Steudel, G. Holdt, R. Nagorka, On the Autoxidation of Aqueous Sodium Polysulfide [1], Zeitschrift für Naturforschung B, 1986, pp. 1519.

[224] T.G. Pearson, P.L. Robinson, CLXXXIX.-The polysulphides of the alkali metals. Part I. Sodium (i), *Journal of the Chemical Society (Resumed)*, pp. 1473-1497, 1930.

[225] W.F. Giggenbach, Kinetics of the polysulfide-thiosulfate disproportionation up to 240.deg, *Inorganic Chemistry*, 13, pp. 1730-1733, 1974.

[226] R. Ramachandran, R.K. Menon, An overview of industrial uses of hydrogen, *International Journal of Hydrogen Energy*, 23, pp. 593-598, 1998.

[227] M.L. Vrinat, The kinetics of the hydrodesulfurization process - a review, *Applied Catalysis*, 6, pp. 137-158, 1983.

[228] W. Villasmil, A. Steinfeld, Hydrogen production by hydrogen sulfide splitting using concentrated solar energy – Thermodynamics and economic evaluation, *Energy Conversion and Management*, 51, pp. 2353-2361, 2010.

[229] S.A. Naman, S.M. Aliwi, K. Al-Emara, Hydrogen production from the splitting of H_2S by visible light irradiation of vanadium sulfides dispersion loaded with RuO_2, *International Journal of Hydrogen Energy*, 11, pp. 33-38, 1986.

[230] P.K. Dutta, K. Rabaey, Z. Yuan, J. Keller, Spontaneous electrochemical removal of aqueous sulfide, *Water Research*, 42, pp. 4965-4975, 2008.

[231] Z. Mao, A. Anani, R.E. White, S. Srinivasan, A.J. Appleby, A Modified Electrochemical Process for the Decomposition of Hydrogen Sulfide in an Aqueous Alkaline Solution, *Journal of The Electrochemical Society*, 138, pp. 1299-1303, 1991.

[232] X. Zong, H. Chen, B. Seger, T. Pedersen, M.S. Dargusch, E.W. McFarland, C. Li, L. Wang, Selective production of hydrogen peroxide and oxidation of hydrogen sulfide in an unbiased solar photoelectrochemical cell, *Energy & Environmental Science*, 7, pp. 3347-3351, 2014.

[233] D.C. Crowe, D. Tromans, The Silver Sulfide Reference Electrode for Use in Alkaline Sulfide Solutions, *Corrosion*, 42, pp. 409-415, 1986.

[234] G. Segev, H. Dotan, K.D. Malviya, A. Kay, M.T. Mayer, M. Grätzel, A. Rothschild, High Solar Flux Concentration Water Splitting with Hematite (α-Fe_2O_3) Photoanodes, *Advanced Energy Materials*, 6, pp. 1500817-n/a, 2016.

[235] B. Klahr, S. Gimenez, O. Zandi, F. Fabregat-Santiago, T. Hamann, Competitive Photoelectrochemical Methanol and Water Oxidation with Hematite Electrodes, *ACS Applied Materials & Interfaces*, 7, pp. 7653-7660, 2015.

[236] T. Lopes, L. Andrade, F. Le Formal, M. Gratzel, K. Sivula, A. Mendes, Hematite photoelectrodes for water splitting: evaluation of the role of film thickness by impedance spectroscopy, *Physical Chemistry Chemical Physics*, 16, pp. 16515-16523, 2014.

[237] M.D. Lay, K. Varazo, J.L. Stickney, Formation of Sulfur Atomic Layers on Gold from Aqueous Solutions of Sulfide and Thiosulfate: Studies Using EC-STM, UHV-EC, and TLEC, *Langmuir*, 19, pp. 8416-8427, 2003.

[238] B.G. Ateya, F.M. AlKharafi, A.S. Al-Azab Electrodeposition of Sulfur from Sulfide Contaminated Brines, *Electrochemical and Solid-State Letters*, 6, pp. C137-C140, 2003.

Appendices

2. Chapter 2: Effects of annealing on the performance of tin-doped hematite photo-anodes

2.1 Linearity of photocurrent densities with light intensity

Photo-response was measured for unannealed Ti|Sn^{IV}-Fe_2O_3 samples at different intensities of light. Photocurrent densities were normalized by light intensity as in Figure S2-1(a), which shows that linearity of photocurrent response with light intensity was preserved across the electrode potential range investigated. Furthermore, the R-squared in Figure S2-1(b) shows almost perfect linearity in the range from 400 to 2500 W m^{-2}. Most experiments were conducted under high light intensity to enable greater insight into the photo-response behaviour, especially for PEIS measurements.

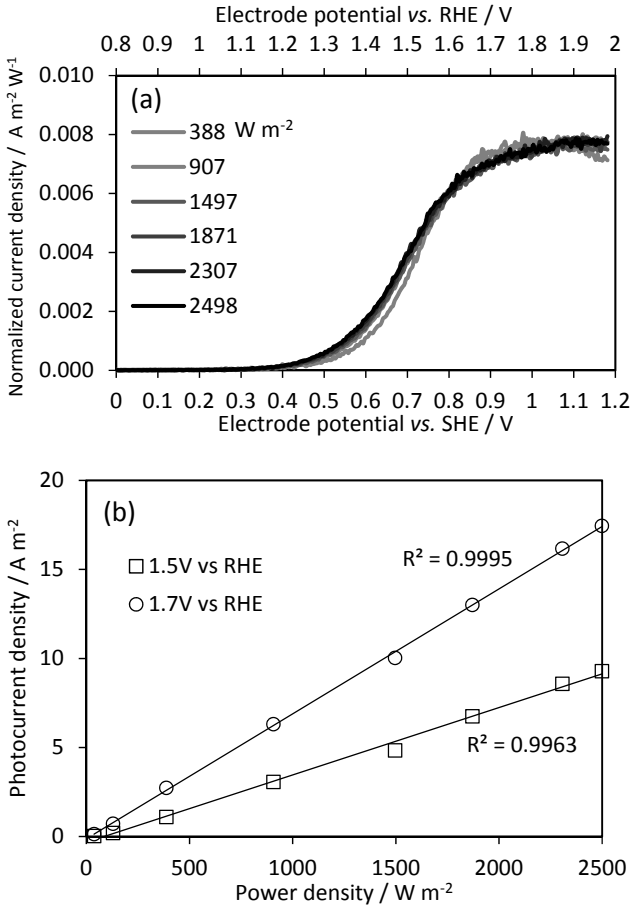


Figure S2-1. Photo-response of Sn^{IV}-doped α-Fe_2O_3 | 1 mol dm^{-3} NaOH under different light intensities. (a) Cyclic (photo-) voltammograms, scan rate 10 mV s^{-1}. (b) Linear effect of light intensities on photocurrent densities after 100 s under specified applied potentials.

2.2 Charge transfer efficiency of Sn^{IV}-doped and undoped Fe_2O_3 on FTO

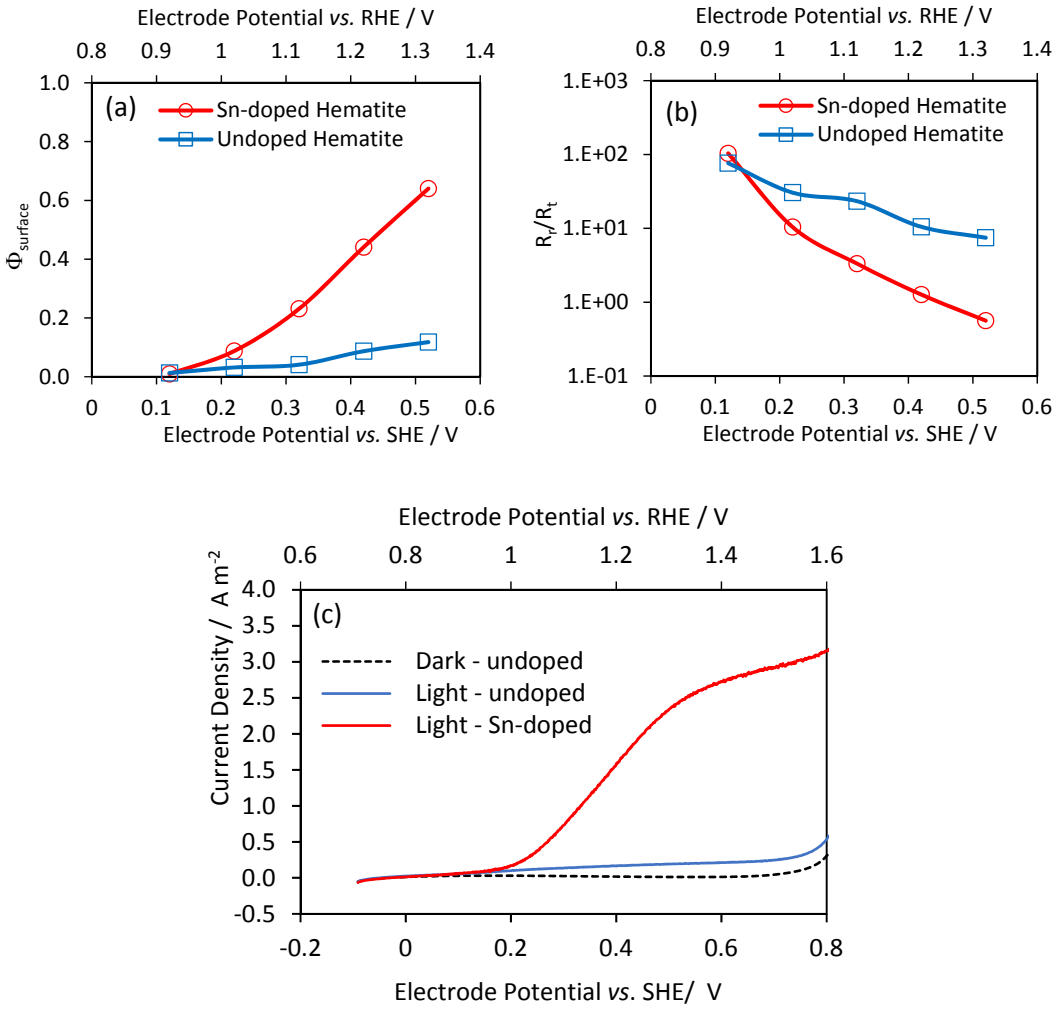


Figure S2-2. Effects of electrode potential and Sn^{IV} doping on (a) charge transfer efficiency, (b) recombination/charge transfer resistance ratio and (c) photocurrent of Sn^{IV}-doped and undoped α-Fe_2O_3 on FTO annealed at 500 °C for 60 minutes. Measurements performed by Dr. Anna Hankin.

2.3 Normalized IPCE spectra of Ti|Sn^{IV}-doped and FTO|Sn^{IV}-doped α-Fe_2O_3

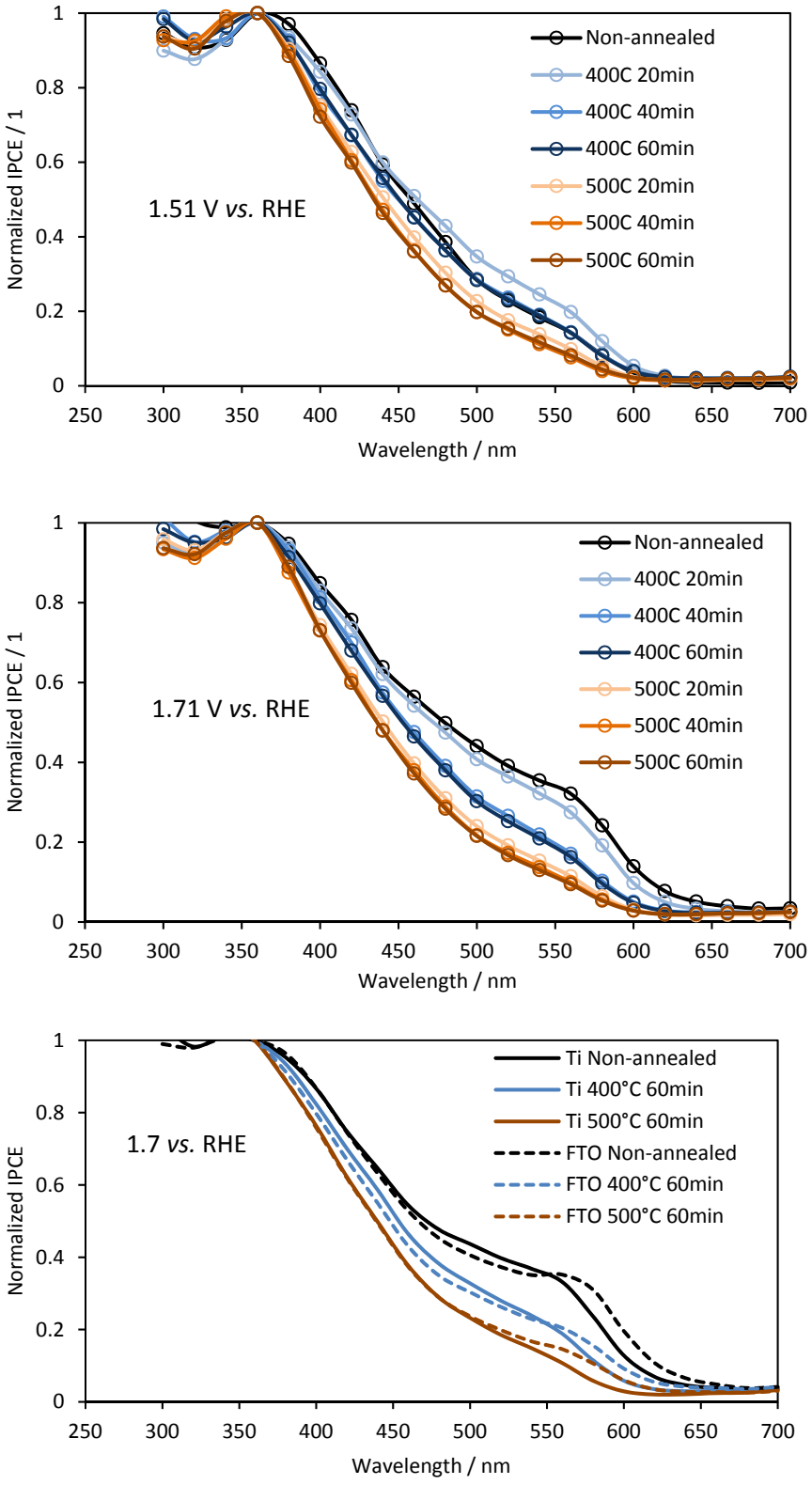


Figure S2-3. IPCE spectra normalized with respect to maximum (360 nm) of Ti|Sn^{IV}-doped and FTO|Sn^{IV}-doped α-Fe_2O_3 | 1 mol dm^{-3} NaOH at 1.5 and 1.7 V vs RHE.

2.4 Integrated IPCE and estimation of photocurrent densities

IPCEs, determined under monochromatic irradiation for a set of wavelengths, were integrated subsequently and summed to give estimates of total current densities, according to the following equation:

$$j_{\mathrm{ph}} = \int_{300\ \mathrm{nm}}^{700\ \mathrm{nm}} [\mathrm{ICPE}(\lambda)E(\lambda)d\lambda]_{1.71\mathrm{V\ vs\ RHE}}$$

Where E is the irradiance of the light source at a given wavelength, λ. Photocurrent densities so evaluated were compared to photocurrent densities measured by cyclic (photo-)voltammetry at 10 mV s^{-1} as show in figure 8.

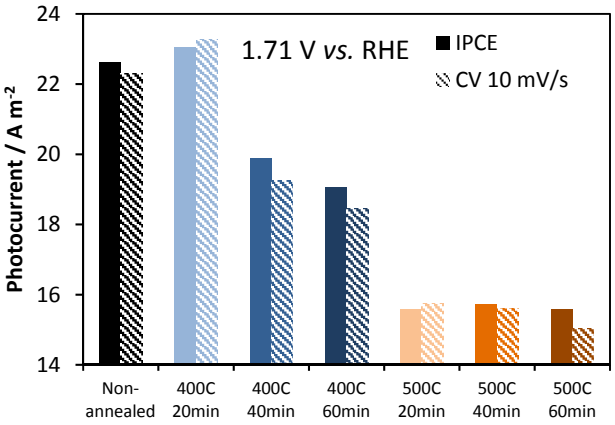


Figure S2-4. Integrated current density from IPCE measurements compared to cyclic voltammograms Ti|Sn^{IV}-doped α-Fe_2O | 1 mol dm^{-3} NaOH at 10 mV s^{-1} and 3000 W m^{-2} Xe arc lamp.

2.5 XPS analyses

Figure S2-5(a) shows the survey spectra of all four samples with all core and Auger lines indicated. The O 1*s* spectrum, Figure S2-5(b), is consistent for all four samples. Small amounts of N and Cl were found for all samples, see Figure S2-5(c) and (d). Whilst the N is comparable between all samples remaining at a level of around 3 rel. at% of N compared to Fe on the film surface, the Cl reduces significantly after annealing.

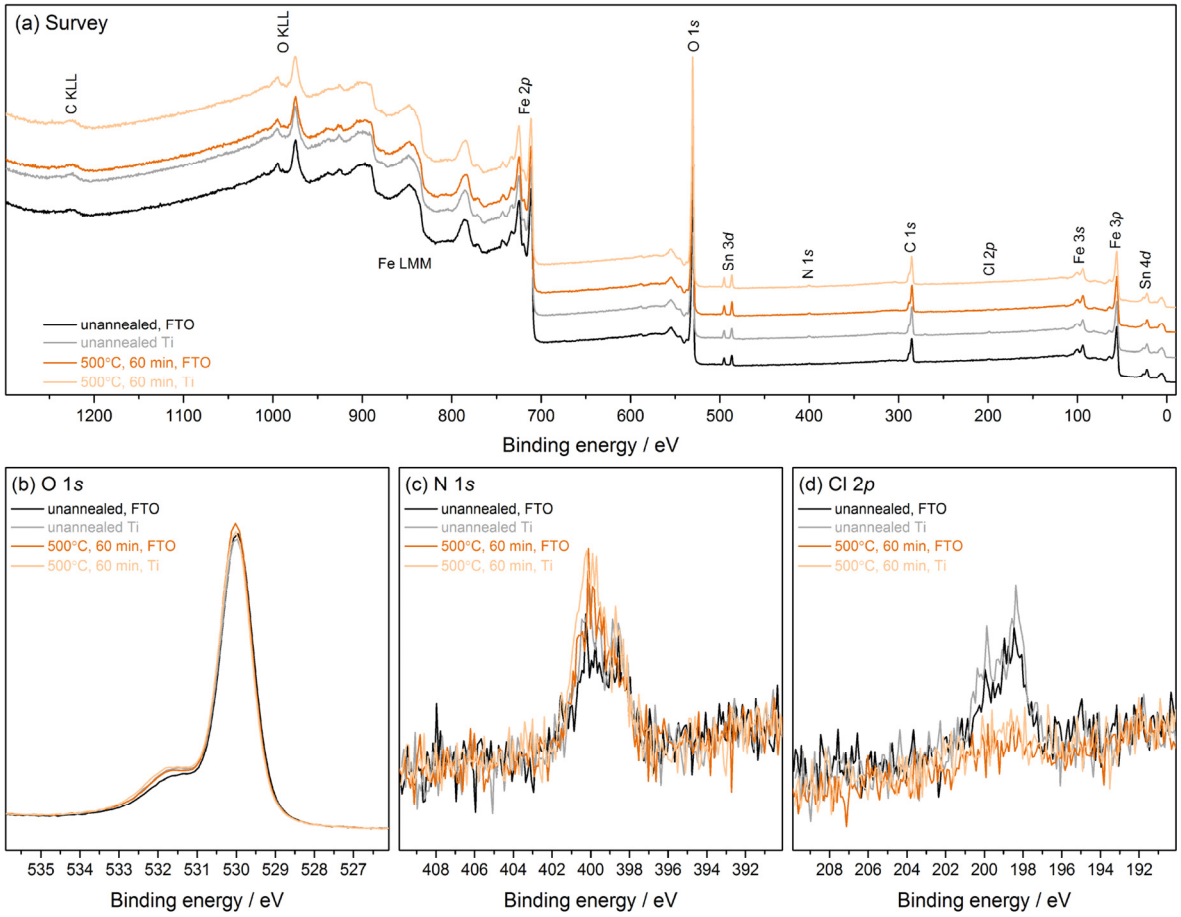


Figure S2-5. XPS measurements of Sn^{IV}-doped α-Fe_2O_3 on FTO and titanium unannealed and after annealing at 500 °C for 60 minuntes, including (a) survey spectra, and (b) O1*s*, (c) N 1*s*, and (d) Cl 2*p* core level spectra. Measurements performed by Dr. Anna Regoutz.

2.6 Flat band potential determination by the Gärtner-Butler (squared photocurrent extrapolation) method

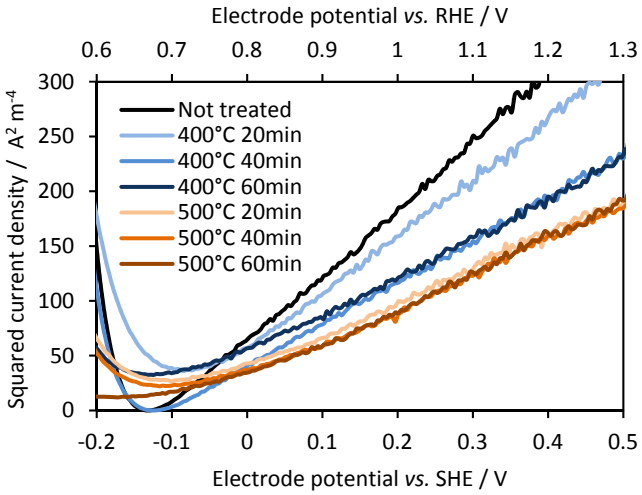


Figure S2-6. Effects of annealing temperature and time on squared photocurrent (evaluated by subtracting the dark current from the current measured under illumination) of Ti|Sn^{IV}-doped α-Fe_2O_3 | 1 mol dm^{-3} NaOH+0.5 mol dm^{-3} H_2O_2; 3000 W m^{-2} Xe arc lamp.

2.7 Raman spectra of Ti|Sn^{IV}-doped α-Fe_2O_3

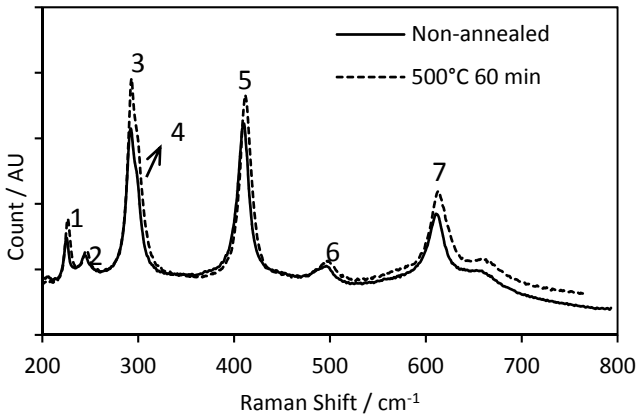


Figure S2-7. Raman spectra of Ti|Sn^{IV}-doped α-Fe_2O_3 unannealed, and annealed at 500 °C for 60 min. Measurements perforemed by Alessandra Vichi.

Table S2-1. Expected Raman peaks for hematite[1], anatase[2] and rutile[3] compared to experimental peaks for unannealed and annealed samples at 500 °C for 60 minutes.

Phase	Peak	Mode	Expected peak cm^{-1}	Unannealed cm^{-1}	500 °C 60min cm^{-1}
Hematite	1	A_{1g}	226	225.6	226.0
	2	E_g	245	244.6	245.6
	3	E_g	292	292.1	293.0
	4	E_g	299	298.5	300.0
	5	E_g	411	410.5	411.4
	6	A_{1g}	497	496.1	498.2
	7	E_g	612	611.9	613.5
Anatase		E_g	144		
		E_g	197		
		B_{1g}	399		
		A_{1g}	513		
		B_{1g}	519		
		E_g	639		
Rutile	7	B_{1g}	143		
		E_g	447		
		A_{1g}	612	611.9	613.5
		B_{2g}	826		

2.8 Absorbance and band gap of FTO|Sn^{IV}-doped α-Fe_2O_3

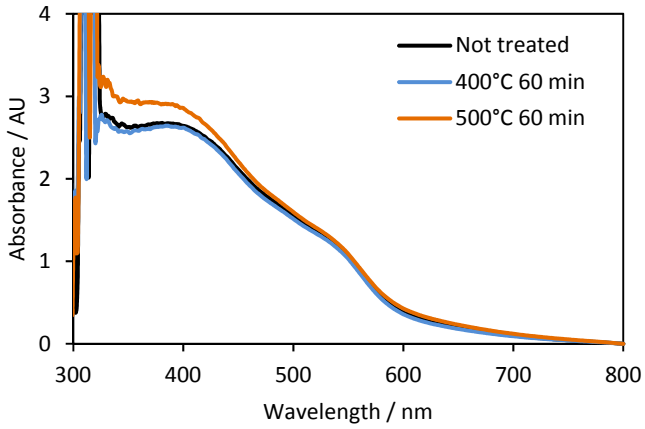


Figure S2-8. Absorbance spectra corrected for reflectance of FTO|Sn^{IV}-doped α-Fe_2O_3 unannealed, 400 °C and 500 °C annealing for 60 min. Measurements performed with the help of Mr. Camilo Mesa

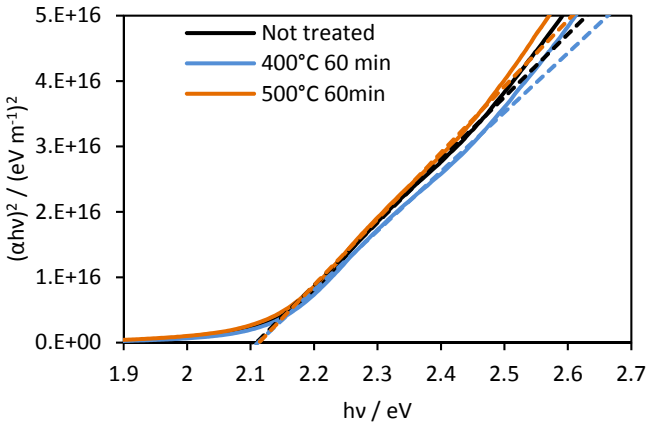


Figure S2-9. Tauc plot for direct band gap of Sn^{IV}-doped α-Fe_2O_3 on FTO: unannealed, 400 °C and 500 °C annealing for 60 min. Hematite film thickness 47 nm.

2.9 AFM analysis

Table S2-2. Surface area analysis and mean roughness calculated from AFM data for Sn^{IV}-doped α-Fe_2O_3 samples on FTO and titanium after different conditions of annealing.

FTO|Sn^{IV}-doped α-Fe_2O_3			
Sample	Surface vs projected area / %	Surface area vs unannealed / %	Mean roughness / nm
Unannealed	16.6	0.0	26.3
400 °C 20 min	22.0	4.6	31.2
400 °C 40 min	7.1	-8.1	13.8
400 °C 60 min	14.6	-1.7	27.1
500 °C 20 min	3.5	-11.3	12.7
500 °C 40 min	3.0	-11.6	14.2
500 °C 60 min	5.0	-10.0	16.9

Ti|SnIV-doped α-Fe_2O_3			
Sample	Surface vs projected area / %	Surface area vs Unannealed / %	Mean roughness / nm
Unannealed	10.2	0.0	10.6
400 °C 20 min	12.1	1.7	19.1
400 °C 40 min	6.3	-3.5	9.48
400 °C 60 min	2.9	-6.6	16.6
500 °C 20 min	1.8	-7.6	6.62
500 °C 40 min	4.6	-5.1	13.7
500 °C 60 min	2.1	-7.4	5.6

3. Chapter 3: Model of PEC systems: photocurrent and H_2 yield predictions

3.1 Comparison of two models for efficiency of gas evolution

3.1.1 Vogt's model

According to Vogt [4], the efficiency of gas evolution, f_G, depends on the fractional surface coverage (θ), current density and concentration difference between the interface and bulk of the solution.

$$f_G = 1 + K_2 - [K_2(2 + K_2) + K_3^2]^{0.5}$$

$$K_2 = 1.53 \frac{D}{d} \frac{RT}{P} \theta^{0.5}(1 - \theta^{0.5}) \Delta c^2 \frac{nF}{j}$$

$$K_3 = k_{Ec'}(1 - \theta) \Delta c \frac{nF}{j}$$

The term K_2 is related to the microconvection and K_3 represents the fraction transferred by macroconvection, being $k_{Ec'}$ the mass transfer coefficient due to macroconvection and estimated by the same author for oxygen (1×10^{-5} m s^{-1}) and hydrogen (2×10^{-5} m s^{-1}) gas evolution. Small variances in the efficiency of gas evolution are achieved when a surface coverage between 0.08 and 0.5 is used. Then, it is safe to assume a surface coverage of 0.1 for low current densities ($10 - 100$ A m^{-2}). The bubble size was assumed as $d = 50 \mu m$. The concentration of hydrogen and oxygen, at the interface of the cathode and anode respectively, was estimated from the figures reported by Shibata. [5, 6] Said experimental points were fitted to a 5 parameter logistic (5-PL) equation in order to obtain the concentration of oxygen or hydrogen as a function of the current density.

$$C_{o_2,H_2} = A + \frac{B - A}{\left(1 + \left(\frac{log\, j_{a,c}}{C}\right)^D\right)^E}$$

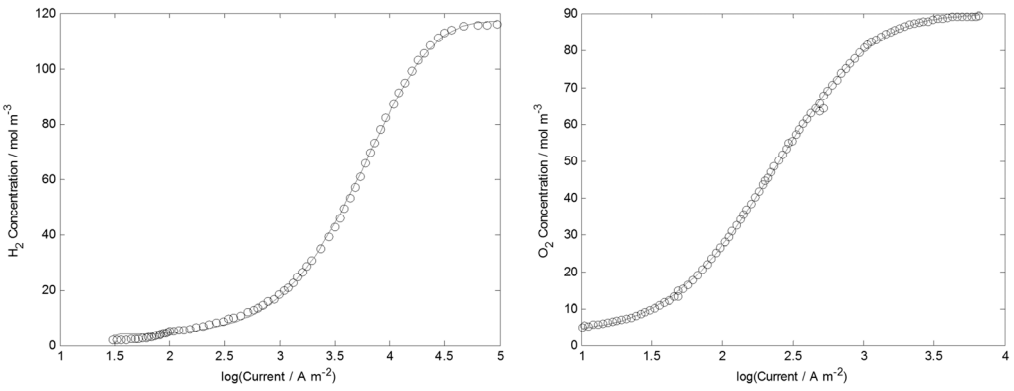


Figure S3-1. H_2 and O_2 concentration at cathode or anode/electrolyte interface vs current density and fitted data.

Table S3-1. Fitting coefficients for hydrogen and oxygen concentration as a function of current density.

Constant	H_2	O_2
A	117.98	89.859
B	4.2617	3.7964
C	7.9697	3.7662
D	5.6489	5.0145
E	303.50	7.6856

3.1.2 Kwie's model

A simpler relationship for oxygen and hydrogen gas evolution in alkaline conditions is proposed by Kwie et al.[7] It is only a function of current density and ad-hoc parameters found after fitting to experimental data, see Table S3-5.

$$\frac{f_G}{1-f_G} = aj^n$$

As it can be seen in Figure S3-2, both relationships are fairly similar. However, values estimated by Vogt fall into negatives values below current densities of ca. 10 A m^{-2}. This creates a discontinuity in the model which can be avoided if Kwie model is used. Both approaches were successfully used in the model presented to predict the behaviour of photo-electrochemical reactors. However, when using Vogt approach cumbersome restrictions must be applied and longer computing times were required.

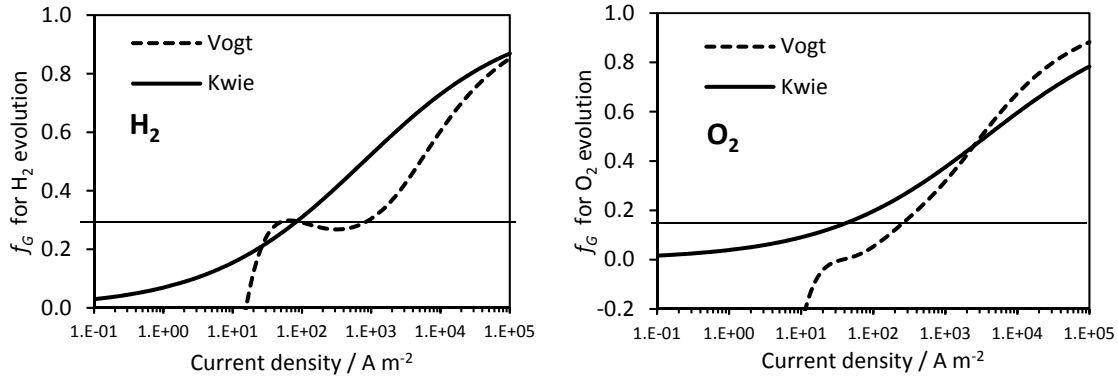


Figure S3-2. Efficiency of gas evolution for H_2 and O_2 estimated using Vogt (dashed) and Kwie (continuous) relationships

3.2 Volumetric mass transfer coefficient estimation for hydrogen and oxygen desorption in water

The volumetric absorption/desorption of gas in the liquid can be expressed in terms of the volumetric coefficient for liquid mass transfer:

$$\frac{dc_i}{dt} = N_{desorption} = K_L a(c_{sat,i} - c_i)$$

$K_L a$ is a function of the hydrodynamic properties of the fluid, diffusivity of the dissolved gas D_i, area of transfer per unit volume a, and characteristic length of the bubble, or in this case Sauter diameter d_B. K_L can be calculated using the Frossling correlation as a function of Re and Sc numbers

and the bubble slip velocity, v_B, which can be estimated from Wüest relationship. The area of transfer per unit volume can be estimated using Deckwer correlation in terms of the gas hold up, ε_G, which can be estimated from Joshi and Sharma's correlation.

Table S3-2. Estimation of volumetric coefficient for liquid mass transfer

Parameter	Symbol	Correlation	Value		Unit	Reference
			O_2	H_2		
Sauter diameter of bubble in saturated liquid	d_B		4.50×10^{-4}	4.50×10^{-4}	m	[8]
Diffusion coefficient of gas in electrolyte	D_i		1.59×10^{-9}	3.00×10^{-9}	$m^2\ s^{-1}$	[7]
Kinematic viscosity of electrolyte (water at 25 °C)	v		8.90×10^{-7}	8.90×10^{-7}	$m\ s^{-1}$	IAPWS
Bubble slip velocity (relative to liquid)	v_B	$4474\left(\frac{d_B}{2}\right)^{1.357}$	0.0502	0.0502	$m\ s^{-1}$	[9, 10]
Gas holdup	ε_G	$\frac{v_B}{0.3+2v_B}$	0.125	0.125	1	[11, 12]
Schmidt number	Sc	$\frac{v}{D_i}$	559.7	296.7	1	
Reynolds number	Re	$\frac{v_B d_B}{v}$	25.38	25.38	1	
Mass transfer coefficient	K_L	$\frac{D_i}{d_B}(2+0.6\mathrm{Re}^{\frac{1}{2}}\mathrm{Sc}^{\frac{1}{3}})$	9.51×10^{-5}	1.48×10^{-4}	$m\ s^{-1}$	[13]
Area of transfer per unit volume	a	$34.4v_B^{0.25}\varepsilon_G$	2.04	2.04	m^{-1}	[11, 14]
Volumetric coefficient for liquid mass transfer	K_La		1.94×10^{-4}	3.02×10^{-4}	s^{-1}	
Wüest correlation						
Volumetric coefficient for liquid mass transfer	K_La	$0.6\frac{d_B}{2}$	2.76×10^{-4}	2.76×10^{-4}	s^{-1}	[9, 10]
Deckwer correlation						
Volumetric coefficient for liquid mass transfer (absorption)	K_La	$0.0086(100\times v_B)^{0.884}$	3.58×10^{-2}	N/A	s^{-1}	[15]
Volumetric coefficient for liquid mass transfer (desorption)	K_La	$0.0274(100\times v_B)^{0.8}$	9.96×10^{-2}	N/A	s^{-1}	[15]

3.3 Summary of properties and parameter fed into the model

Table S3-3. Experimentally measured characteristics of photo-anode Ti|Sn^{IV}-Fe_2O_3

Parameter		Symbol	Value	Unit	Technique
Hematite film thickness		x	4.7×10^{-8}	m	Profilometry
Band gap		E_g	2.11	eV	Tauc-plot
Absorptivity		$\alpha_\lambda = f(\lambda)$		m^{-1}	Absorbance UV-Vis region
Relative permittivity		ε_r	38.2	1	Photo current/PEIS analysis[16]
Donor density		n_0	1.92×10^{25}	m^{-3}	Mott-Schottky (Dark)
Charge transfer resistance		$R_t = f(U_{applied})$		$\Omega\ m^{-2}$	PEIS
Surface recombination resistance		$R_r = f(U_{applied})$		$\Omega\ m^{-2}$	PEIS
Flat band	Unannealed	U_{fb}	0.711 *vs.* RHE	V	Squared photocurrent in 1 mol dm^{-3} NaOH + 0.5 mol dm^{-3} H_2O_2
	400 °C 60 min		0.675 *vs.* RHE	V	
	500 °C 60 min		0.725 *vs.* RHE	V	
Interfacial charge transfer efficiency		$\Phi_{surface} = f(A, B, \phi_{SC})$		1	Fitting of PEIS spectra
Fitting parameter A	Unannealed	A	2.547×10^{-6}	1	
	400 °C 60 min		1.059×10^{-4}	1	
	500 °C 60 min		1.079×10^{-2}	1	
Fitting parameter B	Unannealed	B	17.23	V^{-1}	
	400 °C 60 min		15.06	V^{-1}	
	500 °C 60 min		8.255	V^{-1}	
Bulk recombination	Unannealed	Φ_{bulk}	0.1108	1	Squared photocurrent in 1 mol dm^{-3} NaOH + 0.5 mol dm^{-3} H_2O_2
	400 °C 60 min		0.0888	1	
	500 °C 60 min		0.0702	1	
Exchange current	Unannealed	$j_{0,a}$	1.005×10^{-3}	$A\ m^{-2}$	Dark CV at 10 mV s^{-1}
	400 °C 60 min		1.337×10^{-3}	$A\ m^{-2}$	
	500 °C 60 min		8.029×10^{-3}	$A\ m^{-2}$	
Tafel slope	Unannealed	A_a	0.175	V dec^{-1}	Dark CV at 10 mV s^{-1}
	400 °C 60 min		0.224	V dec^{-1}	
	500 °C 60 min		0.454	V dec^{-1}	

Table S3-4. Properties of set up and spectrally resolve absorbed photon flux

Parameter		Symbol	Value	Unit	Technique
Temperature		T	298	K	Thermometer
pH		pH	13.6	1	pH-meter
Photon flux		I_0	6.02×10^{21}	$m^{-2}\ s^{-1}$	UV-Vis spectrophotometer
Absorbed photon flux	Unannealed	$\sum(I_0 - I_x)_\lambda$	2.97×10^{21}	$m^{-2}\ s^{-1}$	Integration of absorbance and photon flux
	400 °C 60 min		2.91×10^{21}	$m^{-2}\ s^{-1}$	
	500 °C 60 min		3.11×10^{21}	$m^{-2}\ s^{-1}$	
Absorbed photon flux times absorption coefficient	Unannealed	$\sum(I_0 - I_x)_\lambda \alpha_\lambda$	1.71×10^{29}	$m^{-3}\ s^{-1}$	Integration of absorbance and photon flux
	400 °C 60 min		1.70×10^{29}	$m^{-3}\ s^{-1}$	
	500 °C 60 min		1.72×10^{29}	$m^{-3}\ s^{-1}$	
Power intensity		P_0	3646	$W\ m^{-2}$	UV-Vis spectrophotometer
Conductivity of electrolyte (1 mol dm^{-3} NaOH)		$\sigma_{e,a}$ and $\sigma_{e,c}$	20.6	$S\ m^{-1}$	Conductivity Meter
Membrane thickness		l_m	3.30×10^{-4}	m	Taken from supplier

Table S3-5. Summary of parameter taken from literature or calculated from thermodynamic data

Parameter	Symbol	Value	Unit	Reference
Elementary charge	e	1.6022×10^{-19}	C	
Boltzmann constant	k_B	1.3806×10^{-23}	J K^{-1}	
Vacuum permittivity	ε_0	8.85×10^{-12}	F m^{-1}	
Speed of light	c	3.00×10^{8}	m s^{-1}	
Planck constant	h	6.626×10^{-34}	J s	
Faraday constant	F	96484.6	C mol^{-1}	
Gas constant	R	8.31445	J mol^{-1} K^{-1}	
Reversible potential of O_2 evolution (OER, pH 13.6)	$U_{O_2\|H_2O}$	1.229	V *vs.* RHE	
Reversible potential of H_2 evolution (HER, pH 13.6)	$U_{H_2O\|H_2}$	0	V *vs.* RHE	
Number of electrons transferred for O_2 evolution (OER)	n_{O_2}	4	1	
Number of electrons transferred for H_2 evolution (HER)	n_{H_2}	2	1	
Exchange current density cathode (Pt)	$j_{0,c}$	6.9	A m^{-2}	[17]
Transfer coefficient for oxidation (Pt)	$\alpha_{ox,c}$	0.5	1	[17]
Transfer coefficient for reduction (Pt)	$\alpha_{red,c}$	0.5	1	[17]
Conductivity of substrate (Ti)	σ_a and σ_c	1.8×10^{6}	S m^{-1}	[18]
Conductivity of membrane (Nafionff 117)	σ_m	10	S m^{-1}	[19]
Diffusion coefficient of O_2 in membrane (Nafionff 117)	$D_{O_2,m}$	6.2×10^{-11}	m^2 s^{-1}	[20]
Diffusion coefficient of H_2 in membrane (Nafionff 125)	$D_{H_2,m}$	8.02×10^{-11}	m^2 s^{-1}	[21]
Saturation concentration of O_2 in membrane (Nafionff 117)	$c_{O_2,sat,m}$	18.7	mol m^{-3}	[20]
Saturation concentration of H_2 in membrane (Nafionff 125)	$c_{H_2,sat,m}$	7.5	mol m^{-3}	[21]
Partition coefficient of O_2 membrane — electrolyte	$K_{O_2,m}$	21.01	1	[7, 20, 21]
Partition coefficient of H_2 membrane — electrolyte	$K_{H_2,m}$	14.42	1	[7, 20, 21]
Diffusion coefficient of O_2 in electrolyte (1 mol dm^{-3} KOH)	D_{O_2}	1.59×10^{-9}	m^2 s^{-1}	[7]
Diffusion coefficient of H_2 in electrolyte (1 mol dm^{-3} KOH)	D_{H_2}	3.0×10^{-9}	m^2 s^{-1}	[7]
Saturation concentration of O_2 in electrolyte (1 mol dm^{-3} KOH)	$c_{O_2,sat}$	0.89	mol m^{-3}	[7]
Saturation concentration of H_2 in electrolyte (1 mol dm^{-3} KOH)	$c_{H_2,sat}$	0.52	mol m^{-3}	[7]
Volumetric mass transfer coefficient of O_2 (water)	$k_L a_{O_2}$	1.94×10^{-4}	s^{-1}	[8, 11, 13]
Volumetric mass transfer coefficient of H_2 (water)	$k_L a_{H_2}$	3.02×10^{-4}	s^{-1}	[8, 11, 13]
Diffusion coefficient of OH^- in electrolyte (0.26 mol dm^{-3} NaOH)	D_{OH^-}	4.56×10^{-9}	m^2 s^{-1}	[22]
Proportionality factor of power law of O_2 bubble evolution (1 mol dm^{-3} KOH)	a_{G,O_2}	0.6	1	[7]
Exponent of power law of O_2 bubble evolution (1 mol dm^{-3} KOH)	n_{G,O_2}	0.39	1	[7]
Proportionality factor of power law of H_2 bubble evolution (1 mol dm^{-3} KOH)	a_{G,H_2}	1.1	1	[7]
Exponent of power law of H_2 bubble evolution (1 mol dm^{-3} KOH)	n_{G,H_2}	0.39	1	[7]

3.4 Donor density and flat band potential determination using Mott-Schottky

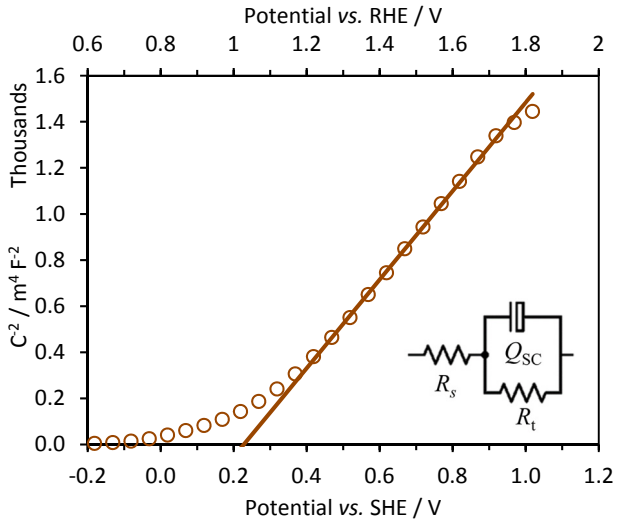


Figure S3-3. Mott-Schottky plots on Ti|Sn^{IV}-doped α-Fe_2O_3 in 1 mol dm^{-3} NaOH after annealing at 500 °C temperatures. Inset shows the equivalent electrical circuit used to fit the impedance spectra.

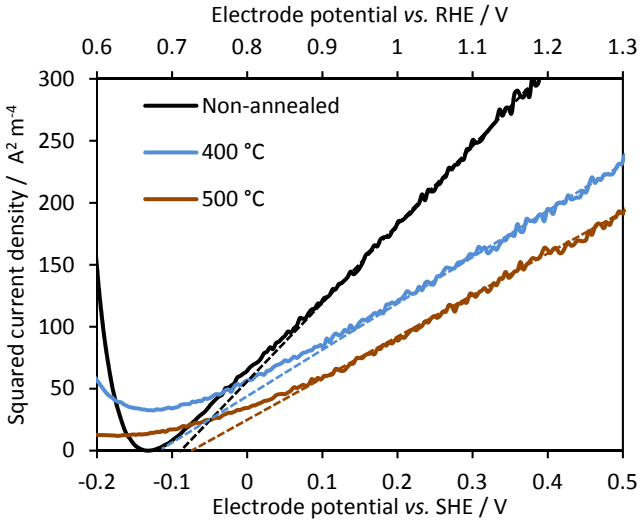


Figure S3-4. Squared photocurrent (evaluated by subtracting the dark current from the current measured under illumination) of Ti|Sn^{IV}-doped α-Fe_2O_3 after different temperature of annealing in presence of 0.5 mol dm^{-3} H_2O_2 and 3000 W m^{-2} Xe arc lamp.

Table S3-6. Effects of annealing temperature and time on flat band potential vs. RHE (V) for Ti|Sn^{IV}-doped α-Fe_2O_3 | 1 mol dm^{-3} NaOH estimated by different methods.

Sample	OCP(photo) 1 mol dm^{-3} NaOH	OCP(photo) 1 mol dm^{-3} NaOH + 0.5 mol dm^{-3} H_2O_2	j_{ph}^2
Unannealed	0.71	0.68	0.71
400 °C 60min	0.67	0.65	0.66
500 °C 60min	0.73	0.67	0.72

3.5 Absorbed photon flux determination

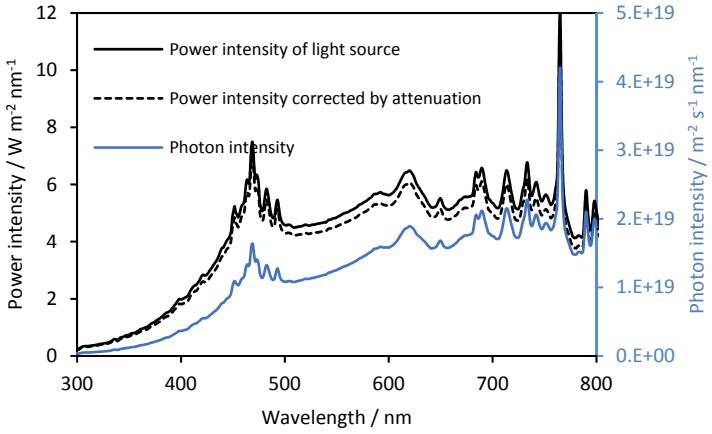


Figure S3-5. Power intensity before and after correction by electrolyte and quartz window attenuation of the 3600 W m^{-2} Xe arc lamp. Photon flux in the right axis.

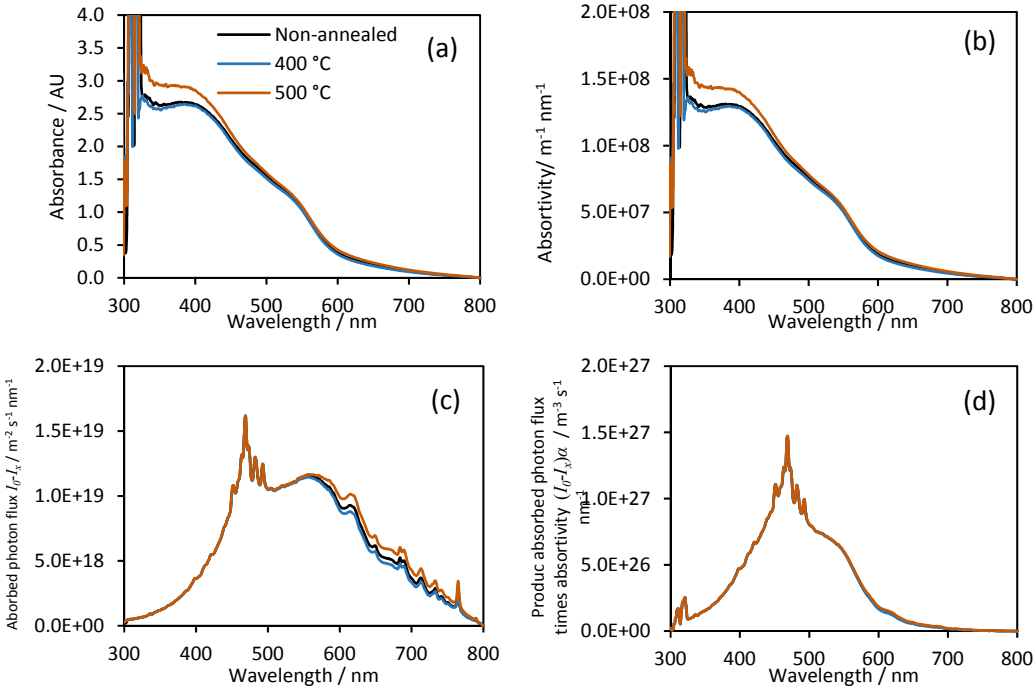


Figure S3-6. Optical properties of FTO|Sn^{IV}-doped α-Fe_2O_3 non-annealed, 400 °C and 500 °C annealing corrected by attenuation by electrolyte and quartz window. (a) absorbance spectra, (b) absorptivity, (c) absorbed photon flux and (d) product of photon flux and absorptivity.

3.6 Estimation of bulk recombination from photo-current in presence and absence of hole scavenger

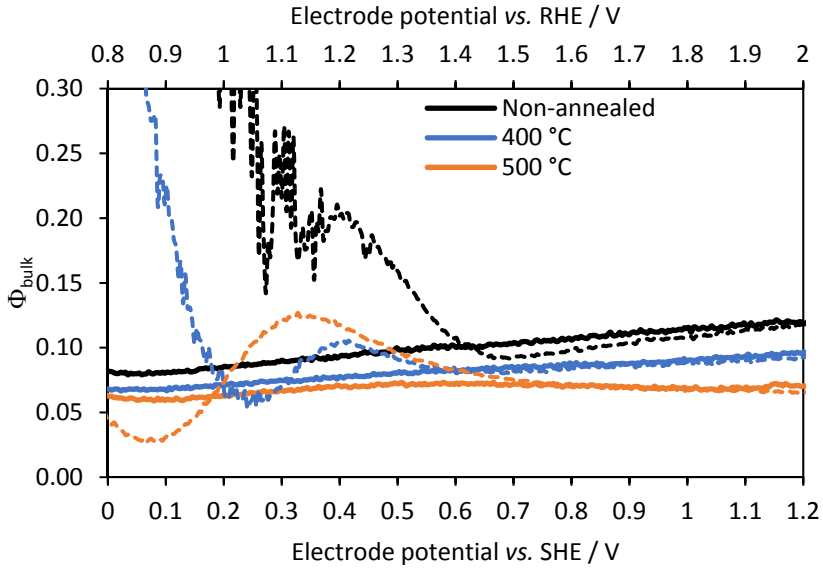


Figure S3-7. Bulk efficiency estimation using photoresponse in presence (continuous lines) and absence (dashed lines) of a hole-scavenger. The deviation at low potentials is due to very low currents densities measured in absence of hole scavenger. Photocurrents in 1 mol dm^{-3} NaOH only were corrected by surface recombination: dividing the photocurrent density by $\Phi_{surface}$ as a function of potential.

Table S3-7. Comparison of bulk recombination calculated from photoresponse in presence and absence of hole scavenger as an average between 1.4 and 2.0 V *vs.* RHE.

Sample	Φ_{bulk}	
	1 mol dm^{-3} NaOH + 0.5 mol dm^{-3} H_2O_2	1 mol dm^{-3} NaOH
Ti|Sn^{IV}-doped α-Fe_2O_3 unannealed	0.1107	0.1044
Ti|Sn^{IV}-doped α-Fe_2O_3 400 °C	0.0888	0.0862
Ti|Sn^{IV}-doped α-Fe_2O_3 500 °C	0.0702	0.0703

3.7 Efficiency of gas evolution (f_G) and gas desorption rate with the current density at the cathode and anode.

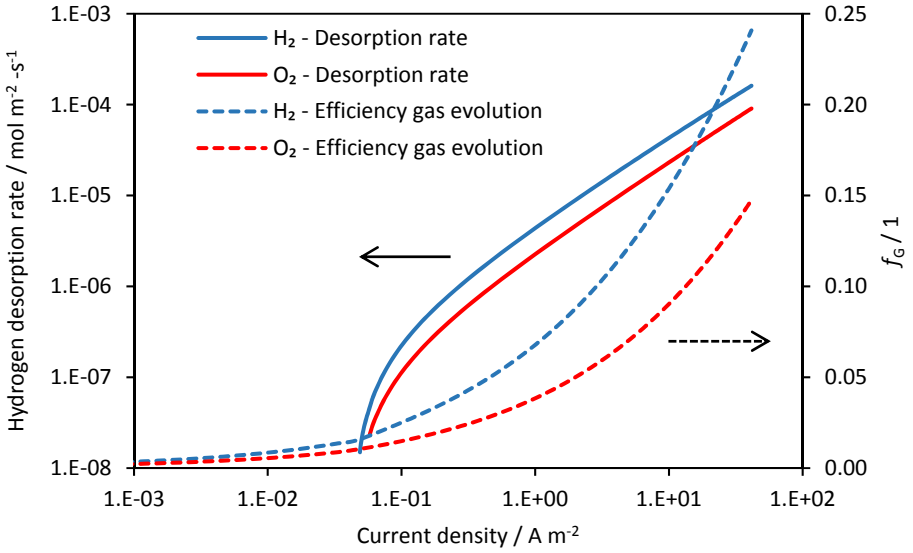


Figure S3-8. Dependence of efficiency of gas evolution f_G and gas desorption rate with current density at the cathode and anode for hydrogen and oxygen evolution respectively.

3.8 Properties of a hypothetical enhanced photo-anode

Table S3-8. Characterisation of hypothetical photo-anode

Parameter	Symbol	Value	Unit
Film thickness	x	4.7×10^{-8}	m
Band gap	E_g	1.7 729	eV nm
Absorptivity	α	1.47×10^{8}	m^{-1}
Relative permittivity	ε_r	40	1
Donor density	n_0	1×10^{25}	m^{-3}
Flat band	U_{fb}	0.1 *vs.* RHE	V
Interfacial charge transfer efficiency	$\Phi_{surface} = f(A, B, \phi_{SC})$		1
Fitting parameter A	A	1.059×10^{-4}	1
Fitting parameter B	B	15.06	V^{-1}
Bulk recombination	Φ_{bulk}	0.5	1
Exchange current	$j_{0,a}$	1.005×10^{-3}	A m^{-2}
Tafel slope	A_a	0.175	V dec^{-1}

Table S3-9. Properties of set up and absorbed photon flux for an enhanced photo-electrode

Parameter	Symbol	Value	Unit	Comments
Temperature	T	298	K	
pH	pH	13.6	1	
Photon flux	I_0	4.00×10^{21}	m^{-2} s^{-1}	Solar 1.5AM Direct
Absorbed photon flux	$\sum(I_0 - I_x)_\lambda$	1.21×10^{21}	m^{-2} s^{-1}	
Absorbed photon flux times absorption coefficient	$\sum(I_0 - I_x)_\lambda \alpha_\lambda$	1.78×10^{29}	m^{-3} s^{-1}	
Power intensity	P_0	900	W m^{-2}	Solar 1.5AM Direct
Conductivity of electrolyte (1 mol dm^{-3} NaOH)	σ_a and σ_c	20.6	S m^{-1}	

3.9 Fraction of hydrogen originated from desorption and gas evolution at the surface of the cathode.

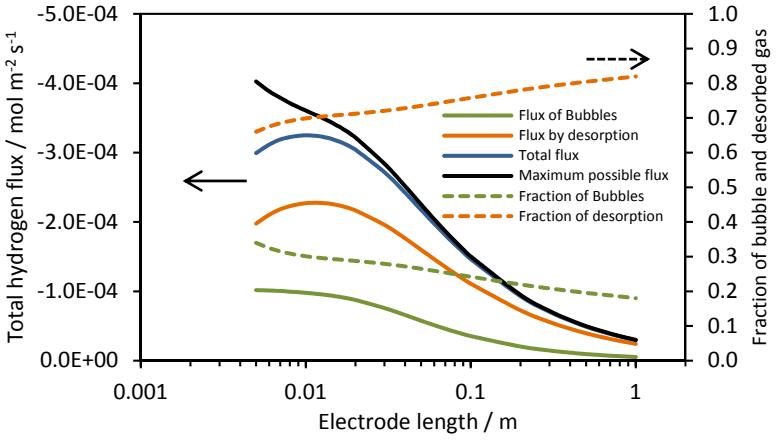


Figure S3-9. Hydrogen flux due to bubble at the electrode and desorption under supersaturated conditions (right axis). Fraction of bubble and desorption rates in the catholyte (left) for an enhanced electrode operating

Different definitions of efficiency were plotted in Figure S3-10. STH and ASTH follow the same trend as hydrogen yield. The difference between them is related to the electrical bias, which is accounted in ASTH efficiency definition.

$$\mathrm{STH} = \left[\frac{E_{\mathrm{H_2}} N_{\mathrm{H_2}}}{P^o}\right]_{\mathrm{AM\ 1.5G}}$$

$$\mathrm{ASTH} = \frac{E_{\mathrm{H_2}} N_{\mathrm{H_2}}}{\left(P^o + j_{ph}\Delta U_{\mathrm{bias}}\right)}$$

ABPE and AB-STH are more widely used definitions to compare systems under applied electrical bias in terms of the obtained current and not the hydrogen yield. The only difference between the two is that AB-STH accounts for faradaic efficiency effects, which, in the present case of study, is better to be replaced by crossover efficiency. Crossover efficiency, as defined in the main manuscript, accounts for combined faradaic and crossover losses. It can be seen how there is a compromise between the crossover efficiency and the total current density obtained from the system, resulting in a maximum at 0.02 m. This length is longer than the maximum obtained with ASTH, ca. 0.01 m, and it is related to the way ASTH accounts for electrical bias (denominator) compared to AB-STH (numerator). It is worth noticing that the total electrical bias applied to the system decreases with the length electrode, from 1.11 to 1.005 V.

$$\mathrm{ABPE} = \left[\frac{j_{\mathrm{ph}}(E^0 - |\Delta U_{\mathrm{bias}}|)}{P^o}\right]_{\mathrm{AM\ 1.5}}$$

$$\mathrm{AB-STH} = \frac{j_{\mathrm{ph}} \times \varepsilon_{H_2} \times (E^0 - \Delta U_{\mathrm{bias}})}{P^o}$$

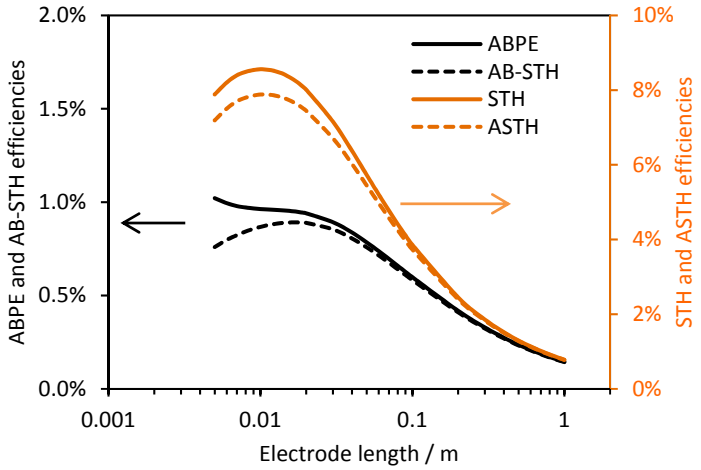


Figure S3-10. Comparison of different solar to hydrogen efficiencies estimated for for a hypothetical enhanced photo-electrode operating at 1 V *vs.* RHE.

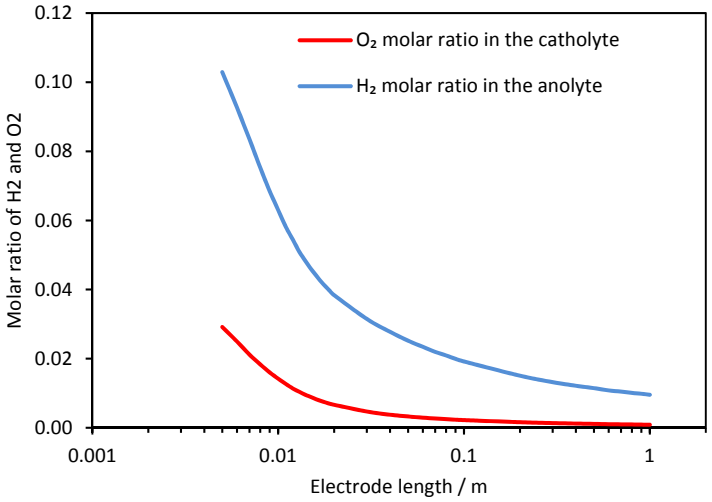


Figure S3-11. Molar fraction of H_2 and O_2 collected in the anode and cathode compartment respectively, values estimated for a hypothetical enhanced photo-electrode operating at 1 V *vs.* RHE.

3.10 Convergence and mesh study

The modelling was performed in COMSOL Multiphysics 5.2a with a Batteries and Fuel Cells module using an Intel Core™ i7-6700 CPU @ 3.40 GHz processor with a 40.0 GB RAM and 64-bit operating system. Conditions in bold were the ones used in the model.

3.10.1 Convergence study

Table S3-10. Convergence study for 2D model, anode potential: 1.6 V *vs.* RHE

Tolerance	Solution time / s	Dark current / A m^{-2}	Photocurrent / A m^{-2}	Hydrogen flux / mol m^{-2} s^{-1}
0.1	1	0.131	20.769	1.0791×10^{-4}
0.01	1	0.131	20.769	1.0791×10^{-4}
0.001	**1**	**0.131**	**20.769**	**1.0789×10^{-4}**
0.0001	1	0.131	20.769	1.0789×10^{-4}

Table S3-11. Convergence study for 2D model, anode potential = 1.6 V *vs.* RHE, electrode length = 0.1 m

Tolerance	Solution time / s	Dark current / A m^{-2}	Photocurrent / A m^{-2}	Hydrogen flux / mol m^{-2} s^{-1}
0.1	60	1.0585	65.048	3.3968×10^{-4}
0.01	62	1.0002	65.667	3.3241×10^{-4}
0.001	**62**	**1.0002**	**65.667**	$\mathbf{3.3241 \times 10^{-4}}$
0.0001	63	0.99839	65.676	3.3229×10^{-4}
0.00001	63	0.99839	65.676	3.3229×10^{-4}

3.10.2 Mesh study

Table S3-12. Mesh study for 2D model, anode potential: 1.6 V *vs.* RHE

Domain elements	Solution time / s	Dark current / A m^{-2}	Photocurrent / A m^{-2}	Hydrogen flux / mol m^{-2} s^{-1}
23	0.1	0.131	20.769	1.0789×10^{-4}
102	**1**	**0.131**	**20.769**	$\mathbf{1.0789 \times 10^{-4}}$
1001	1	0.131	20.769	1.0789×10^{-4}

Table S3-13. Mesh study for 2D model, anode potential = 1.6 V *vs.* RHE, electrode length = 0.1 m

Domain elements	Solution time / s	Dark current / A m^{-2}	Photocurrent / A m^{-2}	Hydrogen flux / mol m^{-2} s^{-1}
7882	8	1.1684	66.043	3.3273×10^{-4}
26799	18	1.0517	65.771	3.3225×10^{-4}
69530	**62**	**1.0002**	**65.667**	$\mathbf{3.3241 \times 10^{-4}}$
115305	87	0.97021	65.607	3.3224×10^{-4}
153344	119	0.96718	65.592	3.3220×10^{-4}
210500	193	0.95232	65.580	3.3241×10^{-4}

4. Chapter 4: Model of PER systems: up-scaled validation and geometrical optimisation

4.1 Map and characterisation of solar simulator

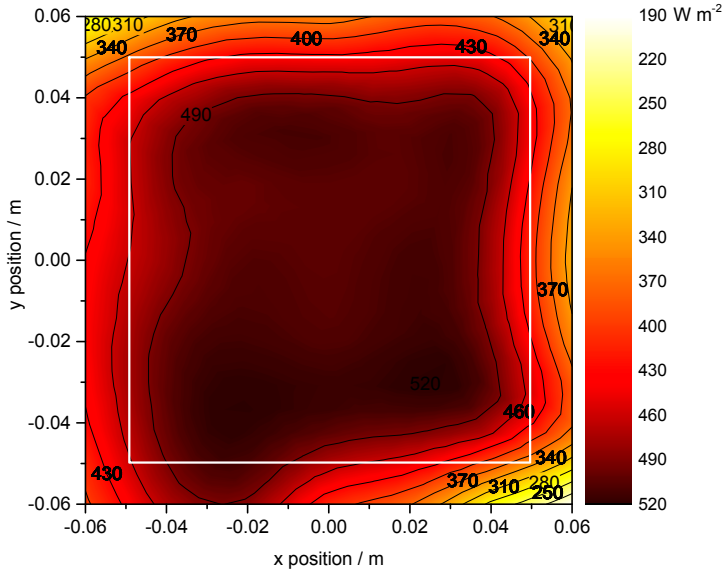


Figure S4-1. Power intensity of the solar simulator using a 550 W Xe arc lamp with a beam projected on an area of 0.12 × 0.12 m^2 and demarked (white square) power intensity for the 0.1 × 0.1 m^2 photo-anode with an average power intensity of 497 W m^{-2}.

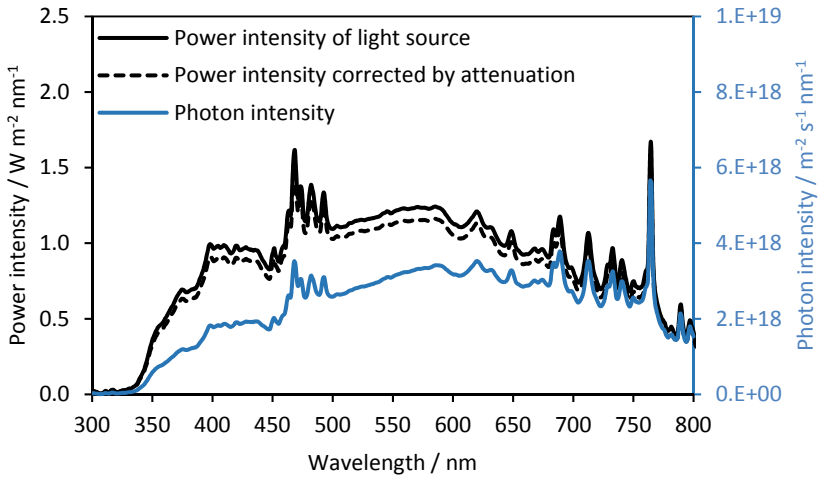


Figure S4-2. Average power intensity projected on an area of 0.1×0.1 m^2 before and after correction by electrolyte and quartz window attenuation of the 497 W m^{-2} solar simulator. Photon flux in the right axis.

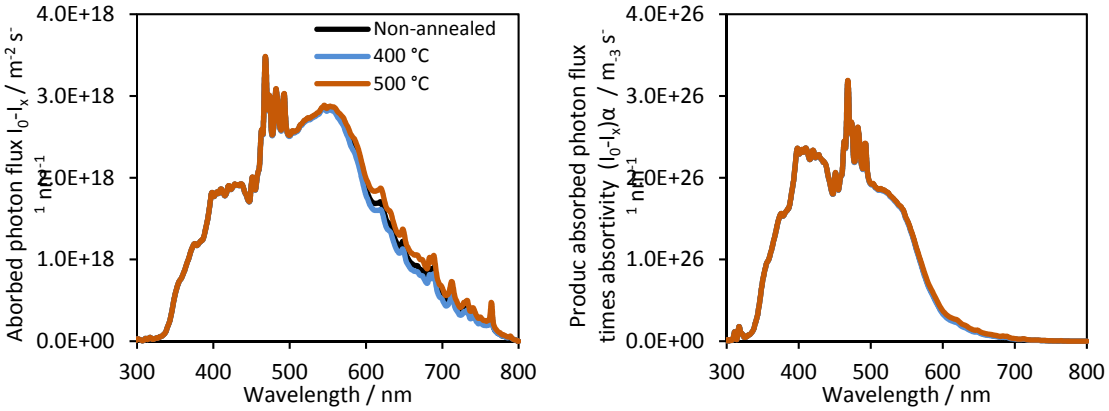


Figure S4-3. Average absorbed photon flux and product absorptivity × photon flux of Sn^{IV}-doped αFe_2O_3 samples after illumination with a solar simulator (497 W m^{-2} solar simulator).

4.2 Temperature history of the reactor upon illumination

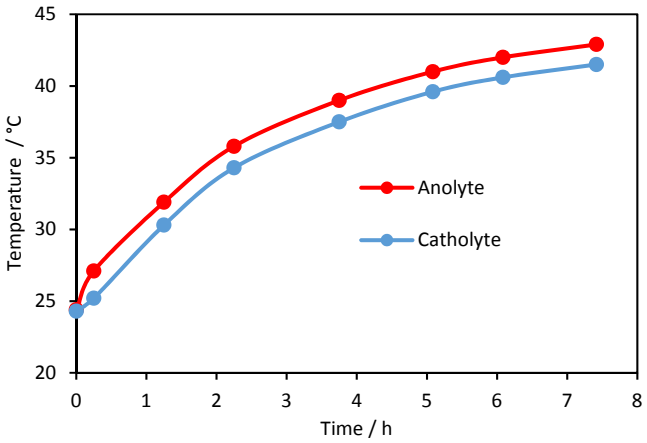


Figure S4-4. Temperature history of the reactor (2 dm^3) upon illumination with a solar simulator using a 550 W Xe arc lamp.

4.3 Effect of the temperature on diffusion parameters

4.3.1 Diffusion coefficient

Following Stokes-Einstein equation

$$\frac{D_1}{D_2} = \frac{T_1}{T_2}\frac{\mu_2}{\mu_1}$$

Table S4-1. Diffusion coefficients estimation of oxygen and hydrogen at 40 °C in 1 mol dm^{-3} KOH

		T_2	T_1	Units
Temperature	T	298	313	K
Water viscosity	μ	0.89	0.6527	mPa.s
O_2 in 1 mol dm^{-3} KOH	D_{O_2}	1.59×10^{-09}	2.28×10^{-09}	m^2 s^{-1}
H_2 in 1 mol dm^{-3} KOH	D_{H_2}	3.00×10^{-09}	4.30×10^{-09}	m^2 s^{-1}
OH^- in 0.26 mol dm^{-3} KOH	D_{OH^-}	4.56×10^{-09}	6.53×10^{-09}	m^2 s^{-1}

4.4 Concentration at saturation

Shoor [23] found the dependence of solubility in terms of activity coefficients referred to the ideal case for pure water, that is:

$$\gamma_i = x_i^o / x_i$$

Where x_i^o is the molar fraction (or concentration) in pure water and x_i is the molar fraction in presence of KOH. Assuming the concentration of gas is small compared to the concentration of KOH (4 orders of magnitude), we can assume that the total concentration of species in the solution is due to KOH only.

Table S4-2. Activity coefficients and saturated concentrations for oxygen and hydrogen in KOH solution at different temperatures

Activity coefficients of O_2				
[KOH] / mol dm^{-3}	Temperature / °C			
	25	40	60	80
0	1	1	1	1
0.92	1.531	1.535	1.445	1.345
2.67	3.06	2.87	2.58	2.5
5	8.15	7.24	6.3	5.73
1	1.601	1.596	1.497	1.398

Activity coefficients of H_2				
[KOH] / mol dm^{-3}	Temperature / °C			
	25	40	60	80
0	1	1	1	1
0.92	1.301	1.275	1.319	1.325
1.7	1.71	1.64	1.735	1.81
4.12	3.5	3.3	3.58	3.647
1	1.343	1.312	1.362	1.375

Saturated concentration / mol m^{-3}					
Solution	Gas	Temperature / °C			
		25	40	60	80
Pure water	O_2	1.246	1.049	0.875	0.775
Pure water	H_2	0.792	0.713	0.712	0.714
1 mol m^{-3} KOH	O_2	0.7783	0.6573	0.5845	0.5544
1 mol m^{-3} KOH	H_2	0.5897	0.5433	0.5229	0.5194

4.5 Estimation of volumetric mass transfer coefficients for hydrogen and oxygen desorption in water at 313 K

Following a similar procedure as reported in Chapter 3. $K_L a$ was recalculated for 313 K as follows:

Table S4-3. Estimation of volumetric coefficient for liquid mass transfer

Parameter	Symbol	Correlation	Value		Unit	Reference
			O_2	H_2		
Sauter diameter of bubble in saturated liquid	d_B		4.50×10^{-4}	4.50×10^{-4}	m	[8]
Diffusion coefficient of gas in electrolyte	D_i		2.28×10^{-9}	4.30×10^{-9}	$m^2\ s^{-1}$	Table S4-1
Kinematic viscosity of electrolyte (water at 25 °C)	υ		6.58×10^{-7}	6.58×10^{-7}	$m\ s^{-1}$	IAPWS
Bubble slip velocity (relative to liquid)	v_B	$4474\left(\frac{d_B}{2}\right)^{1.357}$	0.0502	0.0502	$m\ s^{-1}$	[9, 10]
Gas holdup	ε_G	$\frac{v_B}{0.3+2v_B}$	0.125	0.125	1	[11, 12]
Schmidt number	Sc	$\frac{\upsilon}{D_i}$	288.9	153.1	1	
Reynolds number	Re	$\frac{v_B d_B}{\upsilon}$	34.33	34.33	1	
Mass transfer coefficient	K_L	$\frac{D_i}{d_B}(2+0.6\mathrm{Re}^{\frac{1}{2}}\mathrm{Sc}^{\frac{1}{3}})$	1.28×10^{-4}	1.99×10^{-4}	$m\ s^{-1}$	[13]
Area of transfer per unit volume	a	$34.4v_B^{0.25}\varepsilon_G$	2.04	2.04	m^{-1}	[11, 14]
Volumetric coefficient for liquid mass transfer	$K_L a$		2.61×10^{-4}	4.05×10^{-4}	s^{-1}	

4.6 Photon flux map as a function of position

Experimentally measured power intensities and photon fluxes over an area of 0.12×0.12 m^2 were fitted into an exponential function with rotated coordinates.

$$I_0 = D_1 + D_2 \exp\left[-\left(x\cos\frac{\pi}{4} - y\sin\frac{\pi}{4}\right)^2\right] + D_3 \exp\left[-\left(x\sin\frac{\pi}{4} + y\cos\frac{\pi}{4}\right)^2\right]$$

$$I_0 - I_x = D_1 + D_2 \exp\left[-\left(x\cos\frac{\pi}{4} - y\sin\frac{\pi}{4}\right)^2\right] + D_3 \exp\left[-\left(x\sin\frac{\pi}{4} + y\cos\frac{\pi}{4}\right)^2\right]$$

$$(I_0 - I_x)\alpha = D_1 + D_2 \exp\left[-\left(x\cos\frac{\pi}{4} - y\sin\frac{\pi}{4}\right)^2\right] + D_3 \exp\left[-\left(x\sin\frac{\pi}{4} + y\cos\frac{\pi}{4}\right)^2\right]$$

Fitted parameters D_{1-3} are reported in table

Table S4-4. Fitted parameters of flux map as a function of position on the photo-anode surface

Parameter	I_0	$I_0 - I_x$	$(I_0 - I_x)\alpha$
D_1	-1.58×10^{23}	-9.84×10^{22}	-6.70×10^{30}
D_2	9.64×10^{22}	5.97×10^{22}	4.03×10^{30}
D_3	6.28×10^{22}	3.95×10^{22}	2.72×10^{30}
R^2	0.7320	0.7329	0.7342

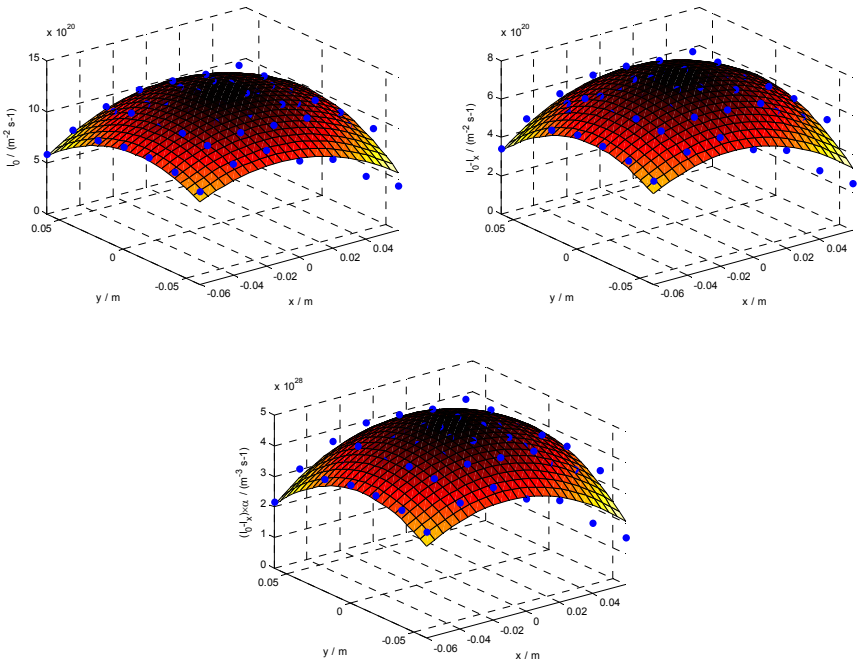


Figure S4-5. Experimental spectrally resolved values for I_0, $I_0 - I_x$ and $(I_0 - I_x)\alpha$ (dots) and fitted function.

4.7 Summary of properties and parameters fed into the model

Table S4-5. Experimentally measured characteristics of photo-anode Ti|Sn^{IV}-Fe_2O_3 without post-annealing.

Parameter	Symbol	Value	Unit	Technique
Hematite film thickness	x	4.7×10^{-8}	m	Profilometry
Band gap	E_g	2.11	eV	Tauc-plot
Absorptivity	$\alpha_\lambda = f(\lambda)$		m^{-1}	Absorbance UV-Vis region
Relative permittivity	ε_r	38.2	1	Photo current/PEIS analysis[16]
Donor density	n_0	1.92×10^{25}	m^{-3}	Mott-Schottky (Dark)
Charge transfer resistance	$R_t = f(U_{applied})$		$\Omega\ m^{-2}$	PEIS
Surface recombination resistance	$R_r = f(U_{applied})$		$\Omega\ m^{-2}$	PEIS
Flat band	U_{fb}	0.711 *vs.* RHE	V	Squared photocurrent in 1 mol dm^{-3} NaOH + 0.5 mol dm^{-3} H_2O_2
Interfacial charge transfer efficiency	$\Phi_{surface} = f(A, B, \phi_{SC})$		1	Fitting of PEIS spectra
Fitting parameter A	A	2.547×10^{-6}	1	
Fitting parameter B	B	17.23	V^{-1}	
Bulk recombination	Φ_{bulk}	0.1108	1	Squared photocurrent in 1 mol dm^{-3} NaOH + 0.5 mol dm^{-3} H_2O_2
Exchange current	$j_{0,a}$	1.005×10^{-3}	$A\ m^{-2}$	Dark CV at 10 mV s^{-1}
Tafel slope	A_a	0.175	V dec^{-1}	Dark CV at 10 mV s^{-1}

Table S4-6. Properties of set up and spectrally resolve absorbed photon flux for photo-anode Ti|Sn^{IV}-Fe_2O_3 without post-annealing and illuminated by 550 W Xe arc lamp solar simulator.

Parameter	Symbol	Value	Unit	Technique
Temperature	T	313	K	Thermometer
pH	pH	13.6	1	pH-meter
Photon flux	I_0	$f(x,y)$	$m^{-2}\ s^{-1}$	UV-Vis spectrophotometer
Absorbed photon flux	$\sum(I_0 - I_x)_\lambda$	$f(x,y)$	$m^{-2}\ s^{-1}$	Integration of absorbance and photon flux
Absorbed photon flux times absorption coefficient	$\sum(I_0 - I_x)_\lambda \alpha_\lambda$	$f(x,y)$	$m^{-3}\ s^{-1}$	Integration of absorbance and photon flux
Power intensity	P_0	497	$W\ m^{-2}$	UV-Vis spectrophotometer
Conductivity of electrolyte (1 mol dm^{-3} NaOH)	$\sigma_{e,a}$ and $\sigma_{e,c}$	20.6	$S\ m^{-1}$	Conductivity Meter
Membrane thickness	l_m	3.30×10^{-4}	m	Taken from supplier

Table S4-7. Summary of parameter taken from literature and corrected for 313 K.

Parameter	Symbol	313 K	Unit	Reference
Elementary charge	e	1.6022×10^{-19}	C	
Boltzmann constant	k_B	1.3806×10^{-23}	J K^{-1}	
Vacuum permittivity	ε_0	8.85×10^{-12}	F m^{-1}	
Speed of light	c	3.00×10^{8}	m s^{-1}	
Planck constant	h	6.626×10^{-34}	J s	
Faraday constant	F	96484.6	C mol^{-1}	
Gas constant	R	8.31445	J mol^{-1} K^{-1}	
Reversible potential of O_2 evolution (OER, pH 13.6)	$U_{O_2\|H_2O}$	1.229	V *vs.* RHE	
Reversible potential of H_2 evolution (HER, pH 13.6)	$U_{H_2O\|H_2}$	0	V *vs.* RHE	
Number of electrons transferred for O_2 evolution (OER)	n_{O_2}	4	1	
Number of electrons transferred for H_2 evolution (HER)	n_{H_2}	2	1	
Exchange current density cathode (Pt)	$j_{0,c}$	6.9	A m^{-2}	[17]
Transfer coefficient for oxidation (Pt)	$\alpha_{ox,c}$	0.5	1	[17]
Transfer coefficient for reduction (Pt)	$\alpha_{red,c}$	0.5	1	[17]
Conductivity of substrate (Ti)	σ_a , σ_c	1.8×10^{6}	S m^{-1}	[18]
Conductivity of membrane (Nafionff 117)	σ_m	10	S m^{-1}	[19]
Diffusion coefficient of O_2 in membrane (Nafionff 117)	$D_{O_2,m}$	6.2×10^{-11}	m^2 s^{-1}	[20]
Diffusion coefficient of H_2 in membrane (Nafionff 125)	$D_{H_2,m}$	8.02×10^{-11}	m^2 s^{-1}	[21]
Saturation concentration of O_2 in membrane (Nafionff 117)	$c_{O_2,sat,m}$	18.7	mol m^{-3}	[20]
Saturation concentration of H_2 in membrane (Nafionff 125)	$c_{H_2,sat,m}$	7.5	mol m^{-3}	[21]
Partition coefficient of O_2 membrane — electrolyte	$K_{O_2,m}$	28.46	1	[7, 20, 21]
Partition coefficient of H_2 membrane — electrolyte	$K_{H_2,m}$	13.81	1	[7, 20, 21]
Diffusion coefficient of O_2 in electrolyte (1 mol dm^{-3} KOH)	D_{O_2}	2.28×10^{-9}	m^2 s^{-1}	[7]
Diffusion coefficient of H_2 in electrolyte (1 mol dm^{-3} KOH)	D_{H_2}	4.30×10^{-9}	m^2 s^{-1}	[7]
Saturation concentration of O_2 in electrolyte (1 mol dm^{-3} KOH)	$c_{O_2,sat}$	0.657	mol m^{-3}	[7, 23]
Saturation concentration of H_2 in electrolyte (1 mol dm^{-3} KOH)	$c_{H_2,sat}$	0.543	mol m^{-3}	[7, 23]
Volumetric mass transfer coefficient of O_2 (water)	$k_La_{O_2}$	2.61×10^{-4}	s^{-1}	[8, 11, 13]
Volumetric mass transfer coefficient of H_2 (water)	$k_La_{H_2}$	4.05×10^{-4}	s^{-1}	[8, 11, 13]
Diffusion coefficient of OH^- in electrolyte (0.26 mol dm^{-3} NaOH)	D_{OH^-}	6.53×10^{-9}	m^2 s^{-1}	[22]
Proportionality factor of power law of O_2 bubble evolution (1 mol dm^{-3} KOH)*	a_{G,O_2}	0.6	1	[7]
Exponent of power law of O_2 bubble evolution (1 mol dm^{-3} KOH)*	n_{G,O_2}	0.39	1	[7]
Proportionality factor of power law of H_2 bubble evolution (1 mol dm^{-3} KOH)	a_{G,H_2}	1.1	1	[7]
Exponent of power law of H_2 bubble evolution (1 mol dm^{-3} KOH)	n_{G,H_2}	0.39	1	[7]

*Resulting gas evolution efficiency was multiplied by a factor of 2 to account for higher temperatures.

4.8 Spectrally resolve photon flux for sunlight 1.5AM

Table S4-8. Properties of set up for 3D symmetrical model and spectrally resolve absorbed photon flux for photo-anode Ti|Sn^{IV}-Fe_2O_3 without post-annealing and illuminated by natural sunlight 1.5AM Global tilt.

Parameter	Symbol	Value	Unit	Technique
Temperature	T	298	K	Thermometer
pH	pH	13.6	1	pH-meter
Photon flux	I_0	1.57×10^{-21}	m^{-2} s^{-1}	ASTM G173-03 (280 to 800 nm)[24] corrected by attenuation of electrolyte and quartz window
Absorbed photon flux	$\sum(I_0 - I_x)_\lambda$	8.91×10^{-20}	m^{-2} s^{-1}	Integration of absorbance and photon flux
Absorbed photon flux times absorption coefficient	$\sum(I_0 - I_x)_\lambda\alpha_\lambda$	5.87×10^{-28}	m^{-3} s^{-1}	Integration of absorbance and photon flux
Power intensity	P_0	1001	W m^{-2}	ASTM G173-03 (whole spectrum)[24]
Conductivity of electrolyte (1 mol dm^{-3} NaOH)	$\sigma_{e,a}$ and $\sigma_{e,c}$	20.6	S m^{-1}	Conductivity Meter

4.9 Comparison of reactor model with and without membrane

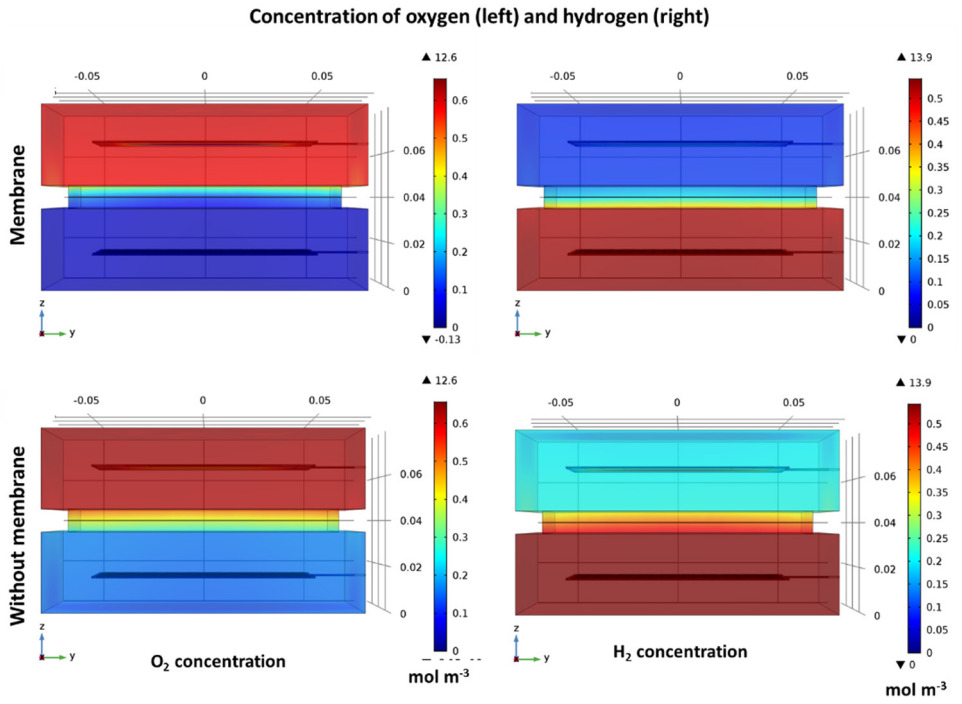


Figure S4-6. Oxygen and hydrogen concentration for up-scaled reactor operating at 40 °C and 1.51 V *vs.* RHE under steady state with (top) and without a membrane (bottom).

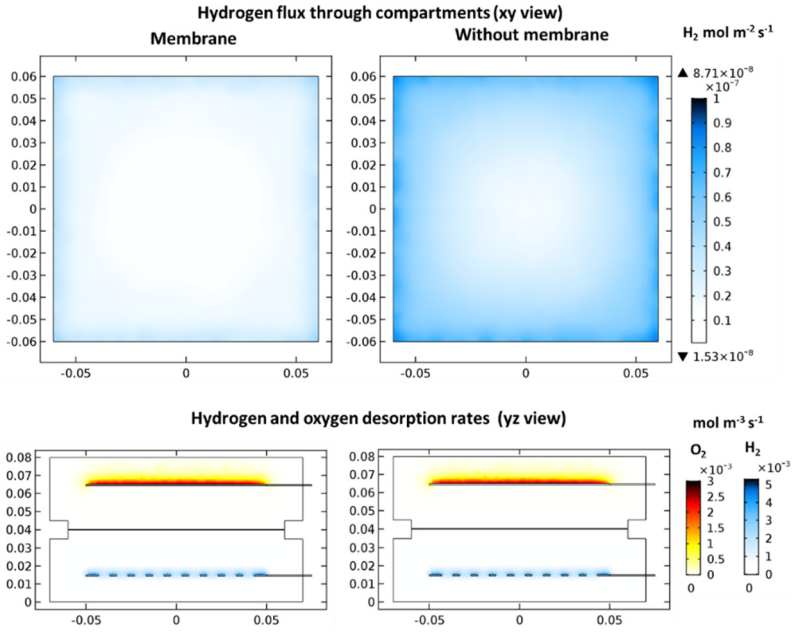


Figure S4-7. (top) Hydrogen flux between compartments and (bottom) desorption rates for hydrogen and oxygen for up-scaled reactor operating at 40 °C and 1.51 V vs. RHE under steady state with and without a membrane.

4.10 Hexagonal *vs.* square perforation distribution

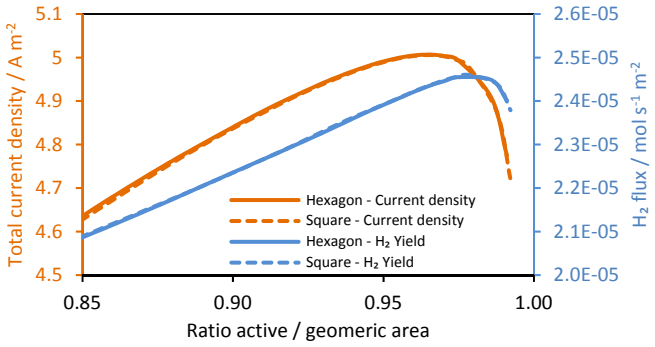


Figure S4-8. Total current density and hydrogen flux for a symmetrical 3D model. Comparison between square and hexagonal distribution of perforations as a function of the fraction of active area relative to the geometrical area. Wired setup without membrane in 1 mol dm^{-3} NaOH and 1.51 V *vs.* RHE.

4.11 Effect of donor density and electrolyte conductivity in net hydrogen fluxes

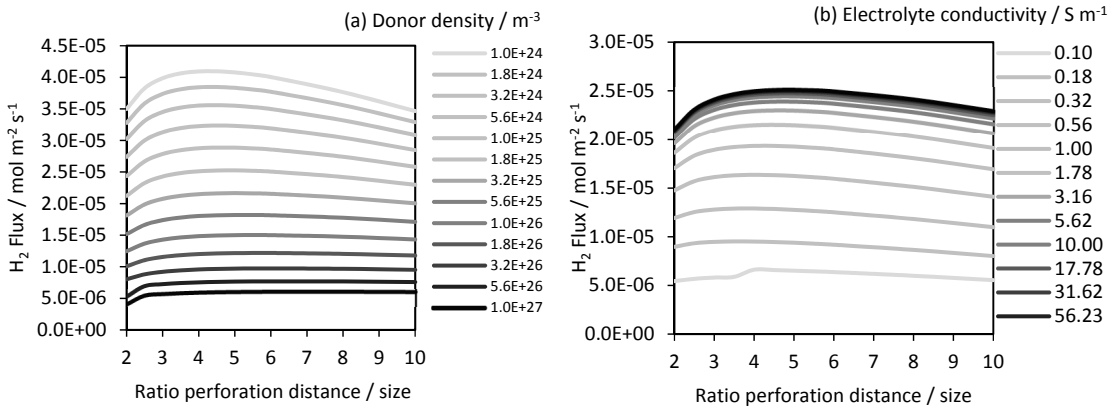


Figure S4-9. Hydrogen fluxes as a function of l_d/l_p for $l_p = 50\ \mu m$ for different (a) donor densities and (a) electrolyte conductivity. Wired symmetrical 3D model with perforations in a square and hexagonal distribution. 1 mol dm^{-3} NaOH and 1.51 V *vs.* RHE.

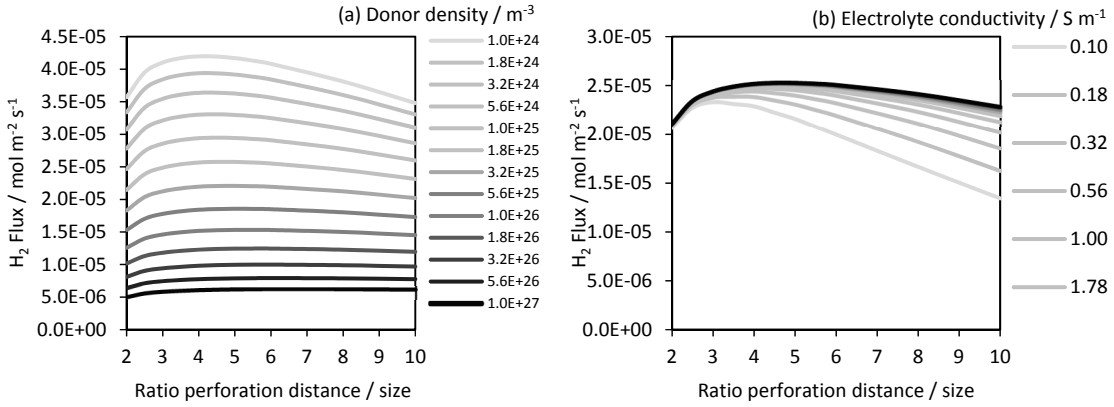


Figure S4-10. Hydrogen fluxes as a function of l_d/l_p for $l_p = 50\ \mu m$ for different (a) donor densities and (a) electrolyte conductivity. Wireless symmetrical 3D model with perforations in a square and hexagonal distribution. 1 mol dm^{-3} NaOH and 1.51 V *vs.* RHE.

5. Chapter 5: In situ determination of polysulfide ions in alkaline hydrogen sulfide solution

5.1 Effects of different variables on the absorbance of polysulfide solutions

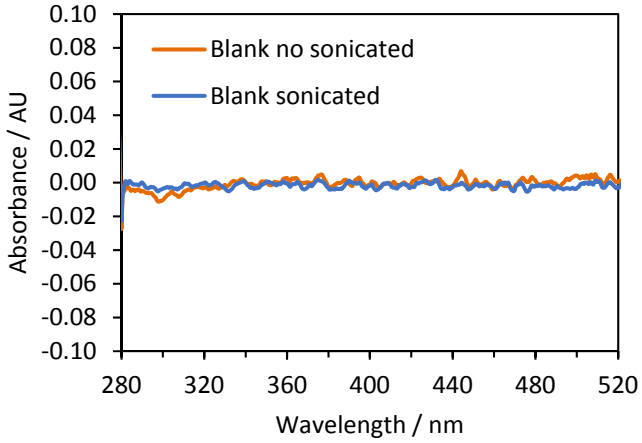


Figure S5-1. Absorbance spectra of blank solution (1 mol dm^{-3} NaOH and 0.5 mol dm^{-3} Na_2S) before and after sonication for 1h.

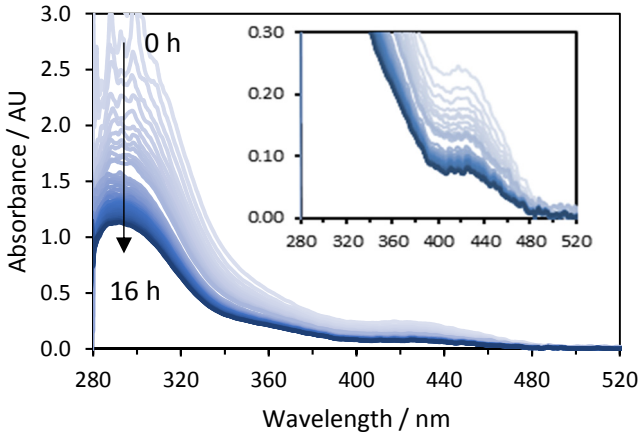


Figure S5-2. Absorbance spectra of 3 mmol dm^{-3} 'S' in 1 mol dm^{-3} NaOH and 0.5 mol dm^{-3} Na_2S with time. Solution was constantly bubbled with zero grade nitrogen with oxygen impurity removed.

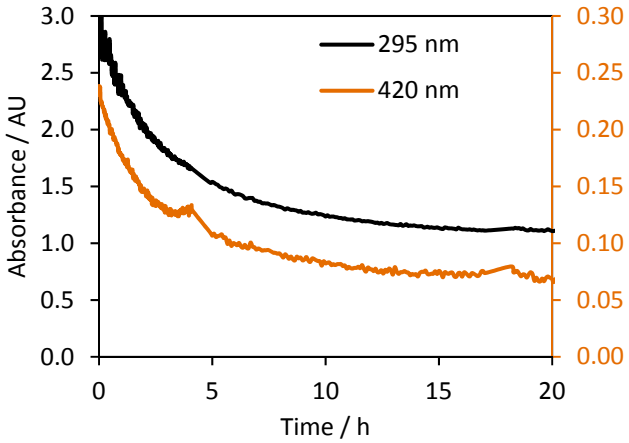


Figure S5-3. Absorbance of 3 mmol dm^{-3} 'S' in 1 mol dm^{-3} NaOH and 0.5 mol dm^{-3} Na_2S with time at 295 and 420 nm. Solution was constantly bubbled with zero grade nitrogen with oxygen impurity removed.

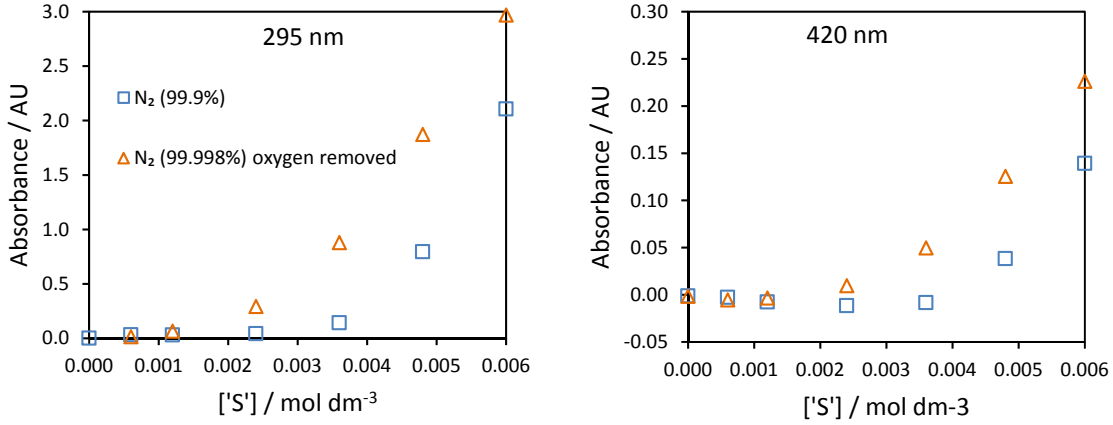


Figure S5-4. Calibration curves for different solutions purged with different grades of nitrogen.

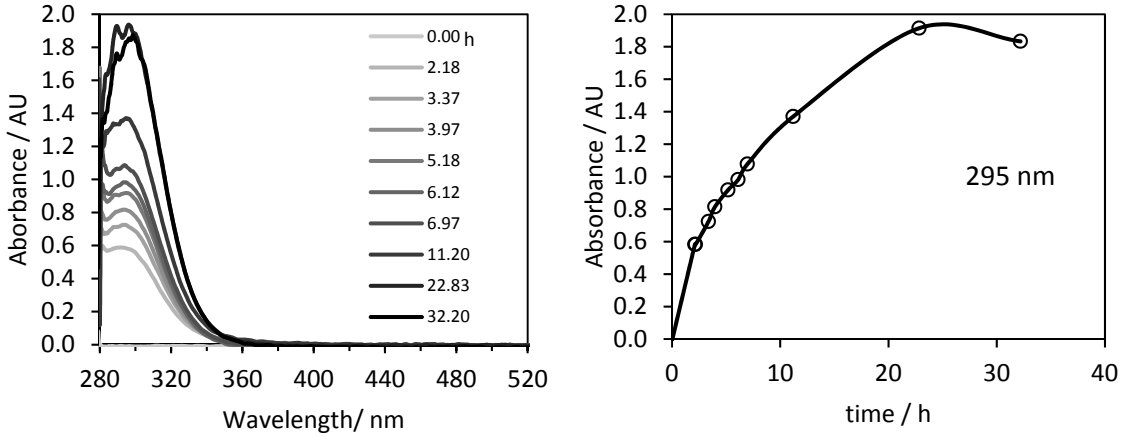


Figure S5-5. Absorbance of blank after bubbling air continuously for 35 hours.

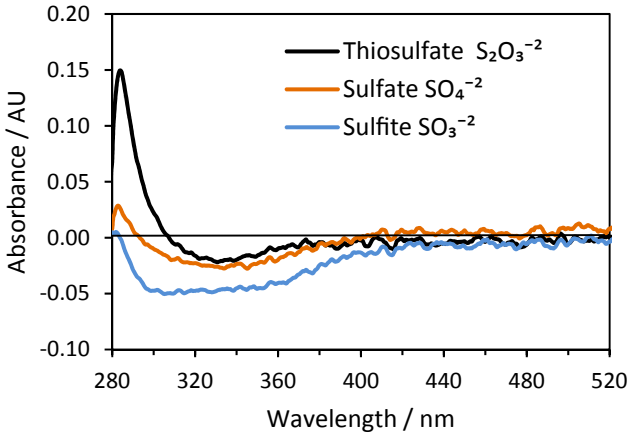


Figure S5-6. Effect of the presence of different sulfur oxoacids at 0.1 mol dm^{-3} on the absorbance spectra of blank solution, 1 mol dm^{-3} NaOH and 0.5 mol dm^{-3} Na_2S.

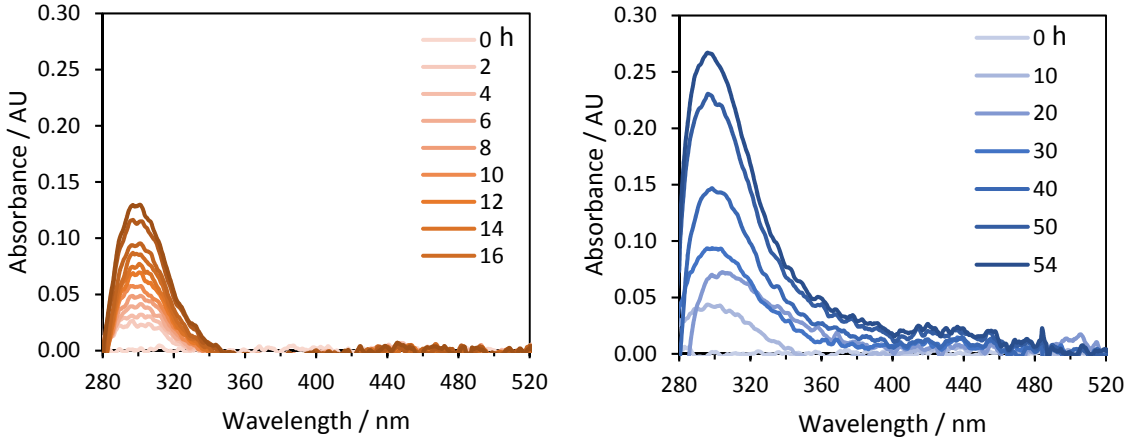


Figure S5-7. Absorbance spectra as a function of time for polysulfide evolution via oxidation of HS^- in 1 mol dm^{-3} NaOH and 0.5 mol dm^{-3} Na_2S in two different conditions in a lab-scale 0.1 dm^{-3} electrochemical reactor.

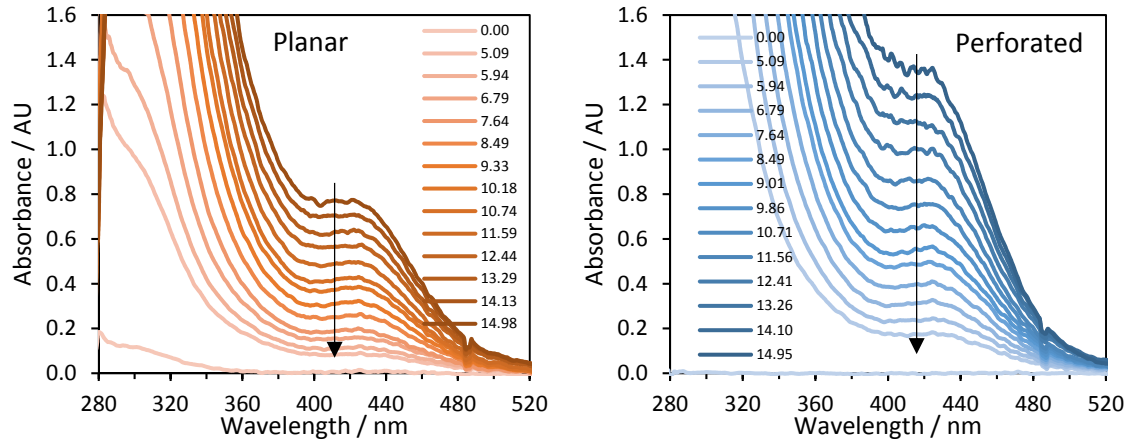


Figure S5-8. Absorbance spectra as a function of time for polysulfide evolution via oxidation of HS^- in 1 mol dm^{-3} NaOH and 0.5 mol dm^{-3} Na_2S for a planar and perforated electrode in a 0.8 dm^{-3} electrochemical reactor.

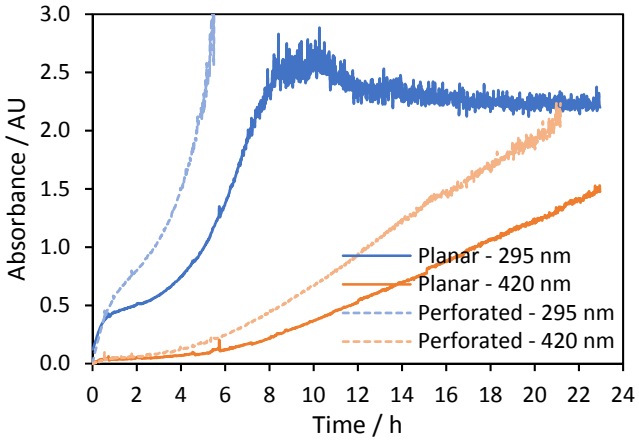


Figure S5-9. Absorbance at 295 and 420 nm as a function of time for polysulfide evolution via oxidation of HS^- in 1 mol dm^{-3} NaOH and 0.5 mol dm^{-3} Na_2S for a planar and perforated electrode in a 0.8 dm^{-3} electrochemical reactor.

5.2 Polysulfide activity-potential speciation

The distribution of polysulfide species was predicted using the approach reported by Kelsall and Thompson [25]. Electrochemical reactions from $n = 2$ to 5 can be represented as:

$$S_n^{2-} + nH^+ + 2(n-1)e^- \Leftrightarrow nHS^-$$

Homogeneous reactions for hydrogen sulfide dissolution in alkaline conditions as:

$$HS^- \Leftrightarrow S^{2-} + H^+$$

Mass balance:

$$['S'] = [HS^-] + \sum_1^5 [S_n^{2-}]$$

The electrochemical reactions follow the Nernst equation:

$$U = U^0 + \ln 10 \frac{RT}{\nu_e F} \log \prod [a]^{\nu_a}$$

Where E^0 is the equilibrium potential calculated from the standard Gibbs energy of formation, ν_a is the stoichiometry constant of species a, negative for reactants and positive for products, and ν_e is the charge number for the reaction. The Nernst equation can be rewritten as:

$$U = U^0 - 0.0591 \frac{\nu_{H^+}}{\nu_e} pH + 0.0591 \frac{\nu_{red}}{\nu_e} \log[red] + 0.0591 \frac{\nu_{ox}}{\nu_e} \log[ox]$$

The homogeneous reaction can be solved using the equilibrium constant for hydrogen sulfide ions in alkaline conditions (pH > 14) where the dissolved H_2S is insignificant, and only HS^- and S^{2-} ions are present.

$$K = \frac{[S^{2-}][H^+]}{[HS^-]} = 10^{-18.51}$$

MATLAB code:

```
clear all
clc
pH = 14;
S_total = 0.5;
E = linspace(-0.58,-0.2,50);
x0 = [0.9;1e-4;1e-6;1e-9;1e-11;1e-5]*S_total;

for i=1:length(E)
    options = optimoptions('fsolve','Display','off','Algorithm','trust-region-dogleg');
    x(:,i) = fsolve(@myfun,x0,options,S_total,pH,E(i));
    x0 = [x(:,i)];
end

function F = myfun(x,S_total,pH,E)
% x(1): HS-
% x(2): S2^(-2)
% x(3): S3^(-2)
% x(4): S4^(-2)
% x(5): S5^(-2)
% x(6): S^(-2)

F = [x(1) + 2.*x(2) + 3.*x(3) + 4.*x(4) + 5.*x(5) + x(6) - S_total;
     0.287090252108773 - 0.0591584736486536.*pH + 0.0295792368243268.*log10(x(2)) - 0.0591584736486536.*log10(x(1)) - E;
     0.097035468785862 - 0.0443688552364902.*pH + 0.0147896184121634.*log10(x(3)) - 0.0443688552364902.*log10(x(1)) - E;
     0.035929465967885 - 0.0394389824324357.*pH + 0.0098597456081089.*log10(x(4)) - 0.0394389824324357.*log10(x(1)) - E;
     0.007060658276140 - 0.0369740460304085.*pH + 0.0073948092060817.*log10(x(5)) - 0.0369740460304085.*log10(x(1)) - E;
     x(6)-10.^(-18.395).*10.^pH.*x(1)];
```

5.3 Polysulfide equilibria speciation: Licht[26, 27]

Dissolution reactions

$$H_2S \overset{K_1}{\Leftrightarrow} HS^- + H^+ \qquad HS^- \overset{K_2}{\Leftrightarrow} S^{2-} + H^+ \qquad H_2O \overset{K_w}{\Leftrightarrow} OH^- + H^+$$

$$K_1 = \frac{[H^+][HS^-]}{[H_2S]} \qquad K_2 = \frac{[H^+][S^{2-}]}{[HS^-]} \qquad K_w = [H^+][OH^-]$$

Polysulfide disproportionation

$$S_3^{2-} + HS^- + OH^- \overset{K_A}{\Leftrightarrow} 2S_2^{2-} + H_2O \qquad 2S_4^{2-} + HS^- + OH^- \overset{K_B}{\Leftrightarrow} 3S_3^{2-} + H_2O \qquad 3S_5^{2-} + HS^- + OH^- \overset{K_C}{\Leftrightarrow} 4S_4^{2-} + H_2O$$

$$K_A = \frac{[S_2^{2-}]^2}{[HS^-][OH^-][S_3^{2-}]} \qquad K_B = \frac{[S_3^{2-}]^3}{[HS^-][OH^-][S_4^{2-}]^2} \qquad K_C = \frac{[S_4^{2-}]^4}{[HS^-][OH^-][S_5^{2-}]^3}$$

Mass balance

$$\sum_1^5 [S_n^{2-}] + [H_2S] + [HS^-] = [Na_2S]$$

$$\sum_1^5 (n-1)[S_n^{2-}] = ['S']$$

Ionic strength, I, for species a with a charge number z can be calculated as:

$$I = 0.5 \sum z_a^2 [a]$$

The equilibrium constants are reported as a function of temperature and ionic strength, summarised by Licht:

$$pK = \frac{a}{T} + bT + c + dI^{0.5}$$

Table 5-1. Equilibrium constants for the aqueous polysulfide system.

pK	a	b	c	d
pK_1	2830.4	0.02083	-8.7289	
pK_2	28646	0.2657	-158.255	
pK_w	3927.1	0.01223	2.8334	
pK_A			4.20	-0.35
pK_B			1.75	-0.35
pK_C			-5.08	-0.35

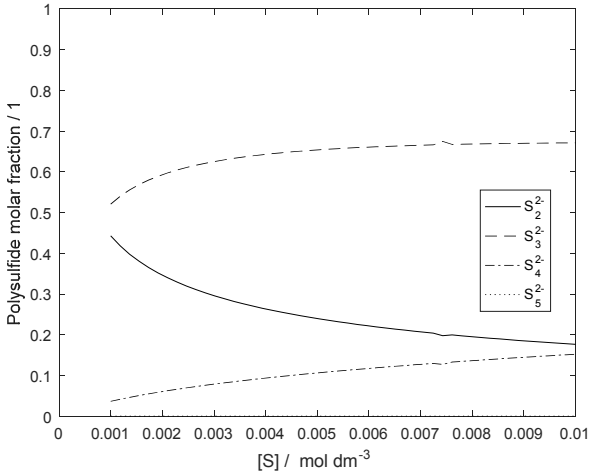


Figure S5-10. Polysulfide molar fraction as a function of zerovalent sulfur in 1 mol dm^{-3} NaOH and 0.5 mol dm^{-3} Na_2S.

MATLAB code:

```
clear all
clc

% x(1): H2S
% x(2): HS-
% x(3): S^2-
% x(4): S2^2-
% x(5): S3^2-
% x(6): S4^2-
% x(7): S5^2-

%Lower range of zerovalent sulfur

C_NaOH = 1; %M
C_Na2S = 0.5; %M
C_S = linspace(0.001,0.01,50); %M
IS = 2.08; %Ionic strength
T = 298.15; %K
pK_1 = 2830.4./T + 0.02083.*T - 8.7289;
pK_2 = 28646./T + 0.2657.*T - 158.255;
pK_w = 3927.1./T + 0.01223.*T - 2.8334;
K_1 = 10.^(-pK_1);
K_2 = 10.^(-pK_2);
K_w = 10.^(-pK_w);

pH = linspace(14,14.5,10);
C_H = 10.^(-pH);
C_OH = K_w./C_H;

x0 = [1e-6 0.5 0.0005 0.00001 0.00002 0.00001 1e-9]';
lb = [0 0 0 0 0 0 0];
ub = [2 2 2 2 2 2 2];

options = optimoptions('lsqnonlin','Display','off','Algorithm','trust-region-reflective');
options.TolFun = 1e-8;
options.TolX = 1e-8;

for j=1:length(C_S)
    for i=1:length(pH)
        x(i,:) = lsqnonlin(@myfun2,x0,[],[],options,C_Na2S,C_NaOH,C_S(j),IS,pH(i),T);
        C_OH_new(i) = C_NaOH + C_Na2S + x(i,1) + C_H(i) - (x(i,3) + x(i,4) + x(i,5) + x(i,6) + x(i,7));
        IS_new(i) = 0.5.*(C_H(i) + C_OH(i) + x(i,2) + 4.*(x(i,3) + x(i,4) + x(i,5) + x(i,6) + x(i,7)) + C_NaOH + 2.*C_Na2S);
    end

    pH_final = intersections(pH,C_OH,pH,C_OH_new,1); % Function taken from MATLAB REPOSITORY
    C_H_final = 10.^(-pH_final);

    IS_final = IS;
    tol = 1;
    while tol > 0.0001
        xx = lsqnonlin(@myfun2,x0,[],[],options,C_Na2S,C_NaOH,C_S(j),IS_final,pH_final,T);
```

```
        F = myfun2(xx,C_Na2S,C_NaOH,C_S(j),IS_final,pH_final,T);
        C_OH_final = C_NaOH + C_Na2S + xx(1) + C_H_final - (xx(3) + xx(4) + xx(5) + xx(6) + xx(7));
        IS_final_test = 0.5.*(C_H_final + C_OH_final + xx(2) + 4.*(xx(3) + xx(4) + xx(5) + xx(6) + xx(7)) + C_NaOH + 2.*C_Na2S);
        tol = abs(IS_final_test - IS_final);
        IS_final = IS_final_test;
    end

    xx_s(j,:) = xx;
    pH_s(j,:) = pH_final;
    C_H_s(j,:) = C_H_final;
    C_OH_s(j,:) = C_OH_final;
    IS_s(j,:) = IS_final;

    for i = 1:4
        u(j,i) = i*xx(i+3)/C_S(j);
        v(j,i) = xx(i+3)/C_S(j);
    end
end

% Polysulfide fraction
xx_total = xx_s(:,4) + xx_s(:,5) + xx_s(:,6) + xx_s(:,7);
w2 = xx_s(:,4)./xx_total;
w3 = xx_s(:,5)./xx_total;
w4 = xx_s(:,6)./xx_total;
w5 = xx_s(:,7)./xx_total;

function F = myfun2(x,C_Na2S,C_NaOH,C_S,IS,pH,T)
% x(1): H2S
% x(2): HS-
% x(3): S^2-
% x(4): S2^2-
% x(5): S3^2-
% x(6): S4^2-
% x(7): S5^2-

pK_1 = 2830.4./T + 0.02083.*T - 8.7289;
pK_2 = 28646./T + 0.2657.*T - 158.255;
pK_w = 3927.1./T + 0.01223.*T - 2.8334;
pK_A = 4.20 - 0.35.*IS;
pK_B = 1.75 - 0.35.*IS;
pK_C = -5.08 - 0.35.*IS;

K_1 = 10.^(-pK_1);
K_2 = 10.^(-pK_2);
K_w = 10.^(-pK_w);
K_A = 10.^(-pK_A);
K_B = 10.^(-pK_B);
K_C = 10.^(-pK_C);

C_H = 10.^(-pH);
C_OH = K_w./C_H;

F = [pK_1 - pH + log10(x(2)) - log10(x(1))
     pK_2 - pH + log10(x(3)) - log10(x(2))
     pK_A + 2.*log10(x(4)) - log10(x(2)) - log10(C_OH) - log10(x(5))
     pK_B + 3.*log10(x(5)) - log10(x(2)) - log10(C_OH) - 2.*log10(x(6))
     pK_C + 4.*log10(x(6)) - log10(x(2)) - log10(C_OH) - 3.*log10(x(7))
     sum(x) - C_Na2S
     1.*x(4) + 2.*x(5) + 3.*x(6) + 4.*x(7) - C_S];
```

5.4 Polysulfide equilibria speciation: Giggenbach [28]

Following the same reactions presented in Licht model, and assuming a constant concentration of OH^- (1 mol dm^{-3}), HS^- (0.5 mol dm^{-3}) and ionic strength of 2, a simplified model was developed using Giggenbach methodology but keeping the updated values of the equilibrium constant found by him few years later and presented in Table 5-1.[29] In order to simplify calculations, the fraction of elemental sulfur on each polysulfide (S_n^{2-}) was defined as u_{n-1} and a parameter B involving the product of hydrogen sulfide and hydroxide ion concentrations:

$$u_{n-1} = \frac{(n-1)[S_n^{2-}]}{S} \qquad B = \frac{[HS^-][OH^-]}{['S']}$$

The equilibrium was calculated at different values of B after solving the following equations

$$K_A = \frac{2[u_1]^2}{B[u_2]} \qquad K_B = \frac{9[u_2]^3}{8B[u_3]^2} \qquad K_C = \frac{64[u_3]^4}{81B[u_4]^3} \qquad K_C = \frac{64[u_3]^4}{81B[u_4]^3} \qquad K_C = \frac{64[u_3]^4}{81B[u_4]^3}$$

And mass balance:

$$\sum_{n=2}^{5} u_{n-1} = 1$$

However, from Licht model, it is known that [S_5^{2-}] is very low compared to the lower polysulfides orders. Thus, the mass balance can be rewritten in terms of u_1:

$$3u_1^3 + 2u_1^2(K_A K_B)^{0.5} - (1-u_1)B^2 K_A (K_A K_B)^{0.5} = 0$$

The results of the model were compared with the experimental data provided by Giggenbach, showing good agreement and demonstrating its suitability to be used to estimate the concentrations of polysulfide under the studied conditions. The distribution of polysulfides differed slightly from the predicted values compared to the predictions using a full mass balance at high concentration of zero-valent sulfur, with a significant deviation for S_2^{-2}. However, this was expected due to the assumptions considered in here are only valid for very low concentrations.

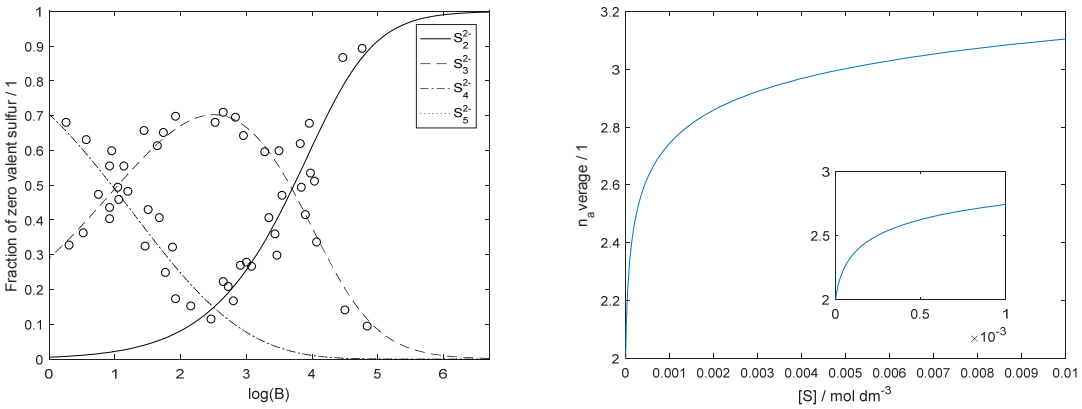


Figure S5-11. (Left) Fraction of zero-valent sulfur content in each polysulfide as a function of B and (right) average order of polysulfide as a function of zero-valent sulfur.

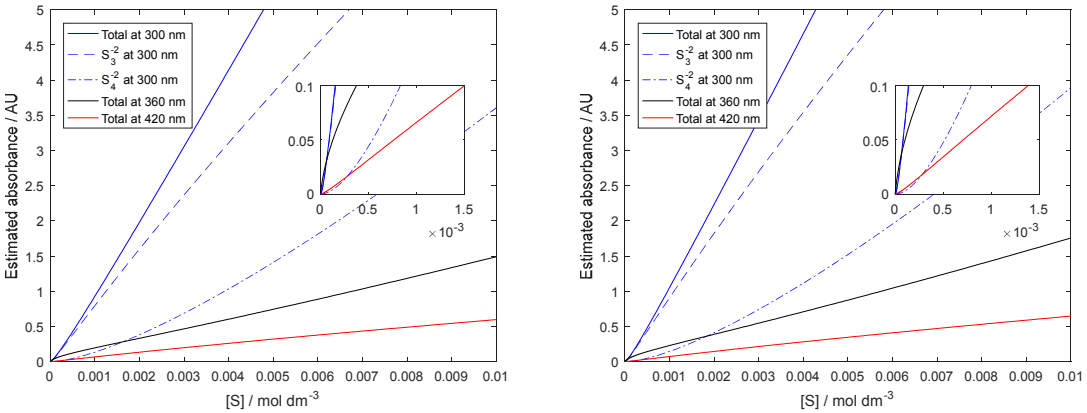


Figure S5-12. Estimated absorbance of polysulfide ions and contributions of S_3^{2-} and S_4^{2-} at 300 nm according to (left) Giggenbach and (right) Licht.

MATLAB code:

```
clc
clear all

%New Litch and Giggenbach estimations for K...
K12 = 1.9728e-04;
K23 = 0.0556;
K34 = 3.7590e+05;

%Asuming 1M NaOH and 0.5M Na2S
C_S = logspace(-7,log10(0.5),1000);
C_OH = 1;
C_SH = 0.5;
B = C_OH.*C_SH./(C_S);

x0 = 0.5; % initial point
for i=1:length(C_S)
        fun = @(x) f(x,B(i),K12,K23); % function
        u1(i) = fzero(fun,x0);
end

% u defined as [polysulfide].*n/C_S
u2 = 2.*u1.^2./(K12.*B);
u3 = (9.*u2.^3./(8.*K23.*B)).^(1/2);
u4 = (64.*u3.^4./(81.*K34.*B)).^(1/3);
ut = u1+u2+u3;

%Concentrations
S2 = u1.*C_S./1;
S3 = u2.*C_S./2;
S4 = u3.*C_S./3;
S5 = u4.*C_S./4;
C_OH = C_OH - S2 - S3 - S4 - S5;
C_SH = C_SH - S2 - S3 - S4 - S5;

% Polysulfide fraction
S_total = S2 + S3 + S4 + S5;
w2 = S2./S_total;
w3 = S3./S_total;
w4 = S4./S_total;
w5 = S5./S_total;

n_average = (2.*S2 + 3.*S3 + 4.*S4 + 5.*S5)./S_total;
data_c=[C_S' S2' S3' S4' S5'];
data_w=[C_S' w2' w3' w4' w5'];

% Molar absortivity [295 ;360(420nm for S3)] nm
a2=[0;850];
a3=[2280;190];
a4=[3420;960];
a5=[8000;2560];

abs_295 = l.*(a2(1).*S2 + a3(1).*S3 + a4(1).*S4 + a5(1).*S5);
abs_normalized_295 = l.*(a2(1).*w2 + a3(1).*w3 + a4(1).*w4 + a5(1).*w5);

abs_360 = l.*(a2(2).*S2 + a4(2).*S4 + a5(2).*S5);
abs_normalized_360 = l.*(a2(2).*w2 + a4(2).*w4 + a5(2).*w5);

abs_420 = l.*(a3(2).*S3);
abs_normalized_420 = l.*(a3(2).*w3);

% Target function
function y = f(x,B,K12,K23)
y = 3.*x.^3 + 2.*x.^2.*B.*(K12.*K23).^0.5 - (1-x).*(B.^2).*K12.*(K12.*K23).^0.5;
```

6. Chapter 6: Photo-assisted hydrogen sulfide splitting using tin-doped hematite

6.1 Mott-Schottky (MS) analysis

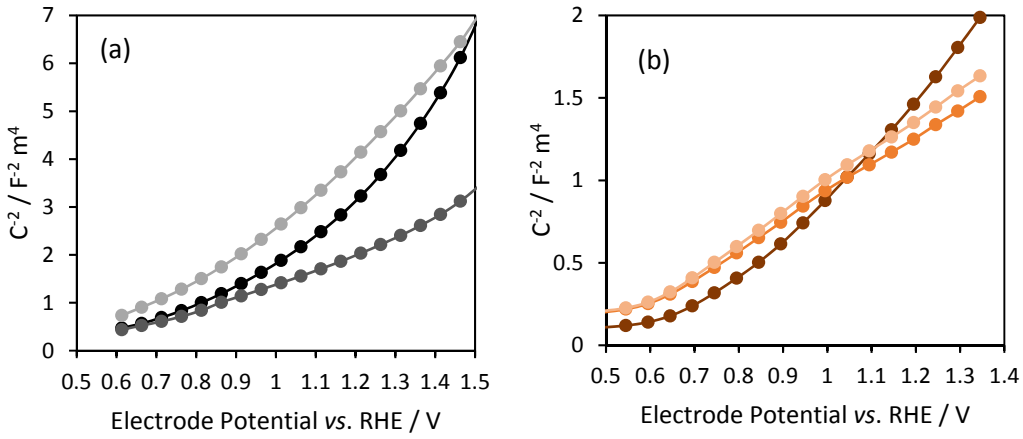


Figure S6-1. Mott-Schottky analysis of Ti|Sn^{IV}-doped α-Fe_2O_3 in (a) 1 mol dm^{-3} NaOH and (b) 1 mol dm^{-3} NaOH + 0.5 mol dm^{-3} Na_2S.

Table S6-1. Flat band potential and electron donor density values of Ti|Sn^{IV}-doped α-Fe_2O_3 in 1 mol dm^{-3} NaOH ± 0.5 mol dm^{-3} Na_2S determined from Mott-Schottky plots in Figure S6-1.

	1 mol dm^{-3} NaOH			1 mol dm^{-3} NaOH + 0.5 mol dm^{-3} Na_2S		
Sample	Flat band *vs.* SHE / V	Donor density / m^{-3}	Flat band *vs.* RHE / V	Flat band *vs.* SHE / V	Donor density / m^{-3}	Flat band *vs.* RHE / V
115	0.214	2.62E+27	1.01	-0.114	1.19E+28	0.690
402	-0.213	1.12E+28	0.591	-0.361	2.12E+28	0.443
702	-0.119	4.68E+27	0.685	-0.355	1.95E+28	0.449

6.2 Effect of the number of layers during spray pyrolysis on hydrogen sulfide and water splitting.

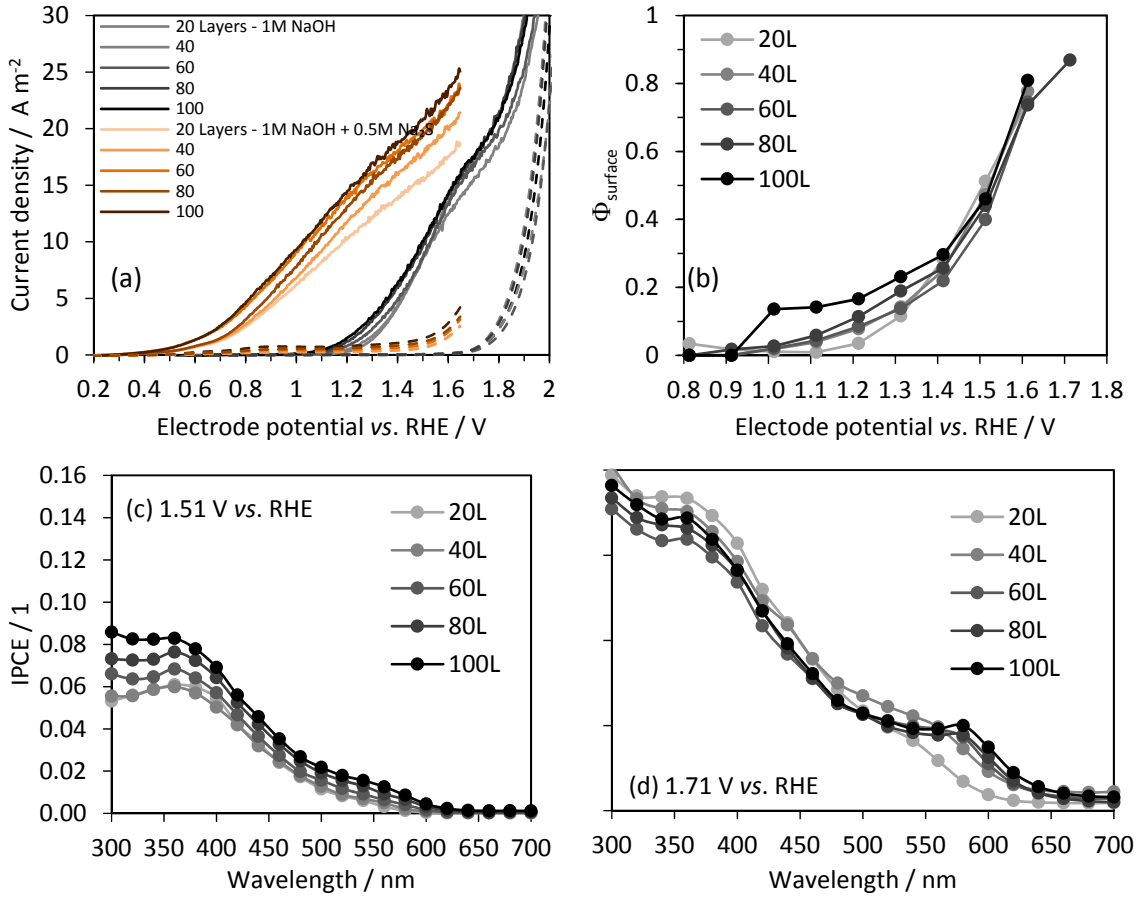


Figure S6-2. Effect of the number of layers during spray pyrolysis on the photo-response of Ti|Sn^{IV}-doped α-Fe_2O_3 photo-anodes. (a) Current density as a function of potential in 1 mol dm^{-3} NaOH ± 0.5 mol dm^{-3} Na_2S. (b) Interfacial charge transfer efficiencies obtained from PEIS spectra as a function of potential. IPCE at (c) 1.51 and (d) 1.71 V *vs.* RHE in 1 mol dm^{-3} NaOH.

Table S6-2. Flat band potentials measured with different techniques for Ti|Sn^{IV}-doped α-Fe_2O_3 with different numbers of Fe_2O_3 layers during spray pyrolysis.

	Flat band potential *vs.* RHE / V			
Sample	MS	PEIS	OCP under high intensity illumination	Onset in voltamogram (Approx.)
20L	0.549	0.302	0.735	0.704
40L	0.562	0.382	0.759	0.704
60L	0.557	0.377	0.722	0.704
80L	0.541	0.400	0.740	0.704
100L	0.535	0.382	0.725	0.704

6.3 Effect of post-annealing of Ti|Sn^{IV}-doped α-Fe_2O_3 photo-anodes on hydrogen sulfide splitting

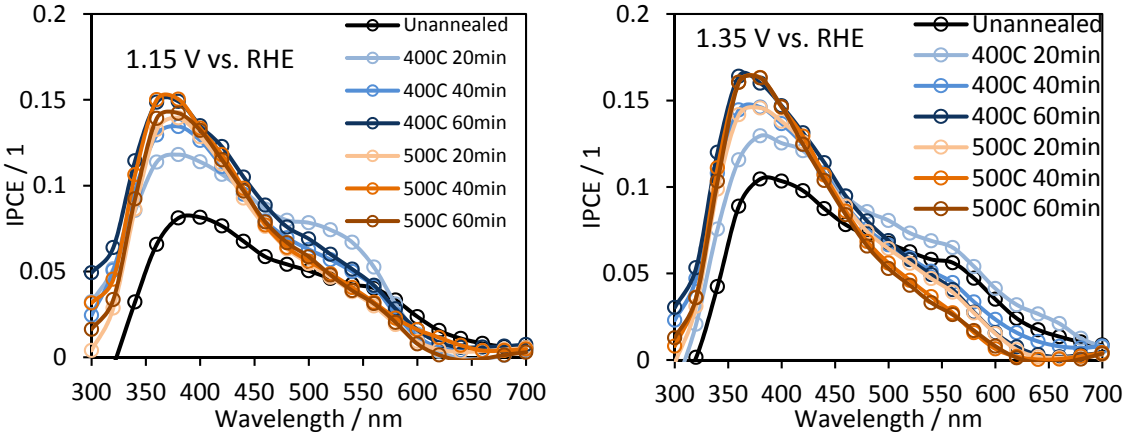


Figure S6-3. IPCE of Ti|Sn^{IV}-doped α-Fe_2O_3 annealed at different conditions in 1 mol dm^{-3} NaOH ± 0.5 mol dm^{-3} Na_2S at (a) 1.15 and 1.35 V *vs.* RHE.

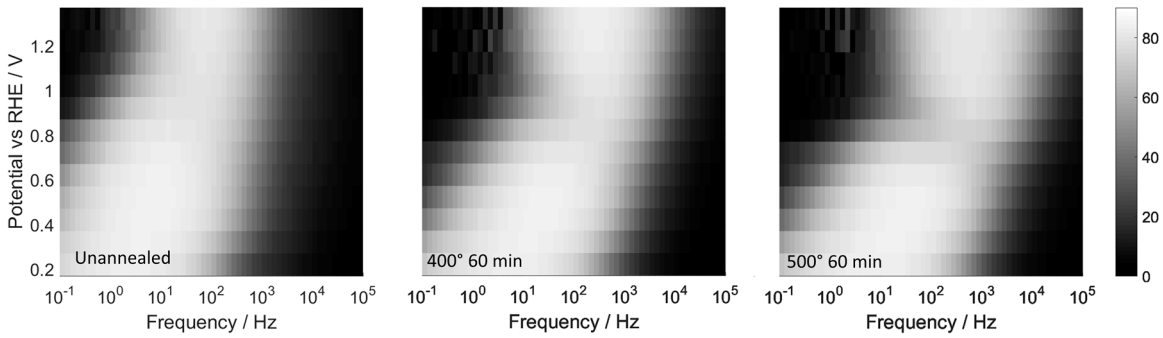


Figure S6-4. Phase shift obtained from PEIS spectra for Ti|Sn^{IV}-doped α-Fe_2O_3 annealed at different conditions and studied in 1 mol dm^{-3} NaOH ± 0.5 mol dm^{-3} Na_2S as a function of potential.

6.4 Study of effect of hydrogen sulfide concentration on photo-assisted electrolysis using Ti | Sn^{IV}-doped α-Fe_2O_3

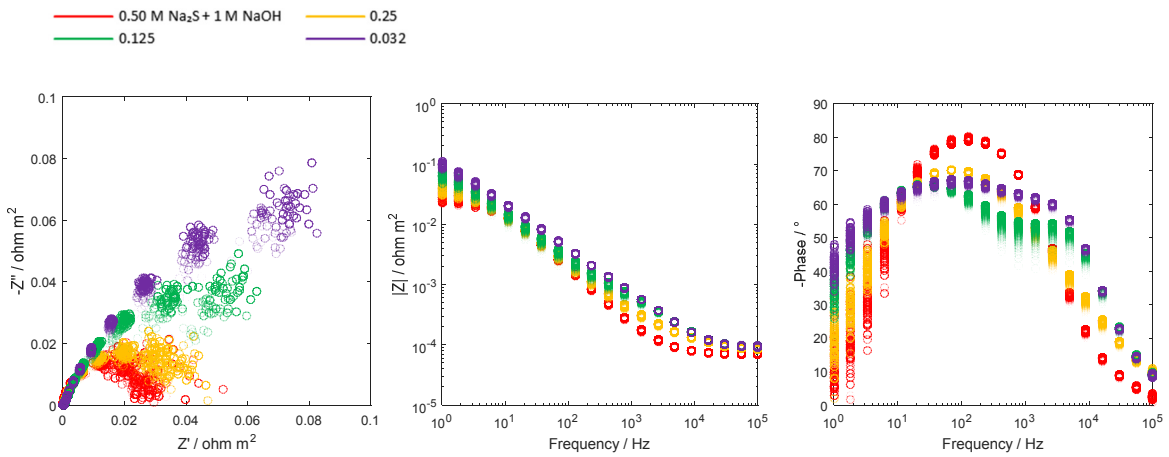


Figure S6-5. PEIS spectra: Nyquist, Bode and phase plots of Ti | Sn^{IV}-doped α-Fe_2O_3 | 1 mol dm^{-3} NaOH + 0.5 mol dm^{-3} Na_2S | Pt | Ti at photo-anode potential of 1.15 V *vs.* RHE and different concentrations of hydrogen sulfide ions during 1.7 hours of photo-assisted hydrogen sulfide splitting, transparency to colour corresponds to increasing time. Xenon arc lamp irradiance 2 670 W m^{-2}.

6.5 Effect of stirring on hydrogen sulfide splitting using Ti | Sn^{IV}-doped α-Fe_2O_3

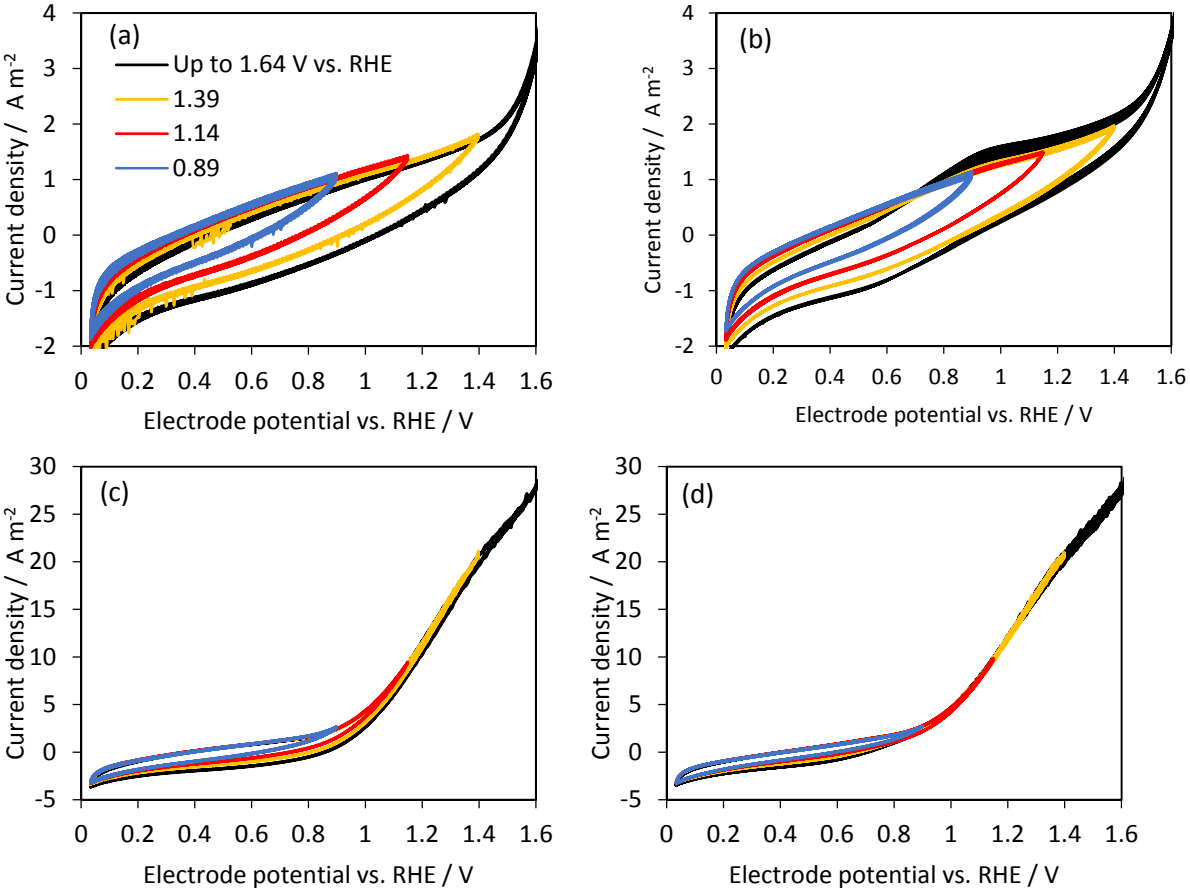


Figure S6-6. Cyclic voltammograms (20 cycles) under (a) dark and stirred electrolyte, (b) dark and quiescent electrolyte, (c) illuminated and stirred and (d) illuminated and quiescent conditions for Ti | Sn^{IV}-doped α-Fe_2O_3 | 1 mol dm^{-3} NaOH + 0.5 mol dm^{-3} Na_2S | Pt | Ti with different electrode potential upper limits and 50 mV s^{-1} scan rate. Xenon arc lamp irradiance 2 900 W m^{-2}.

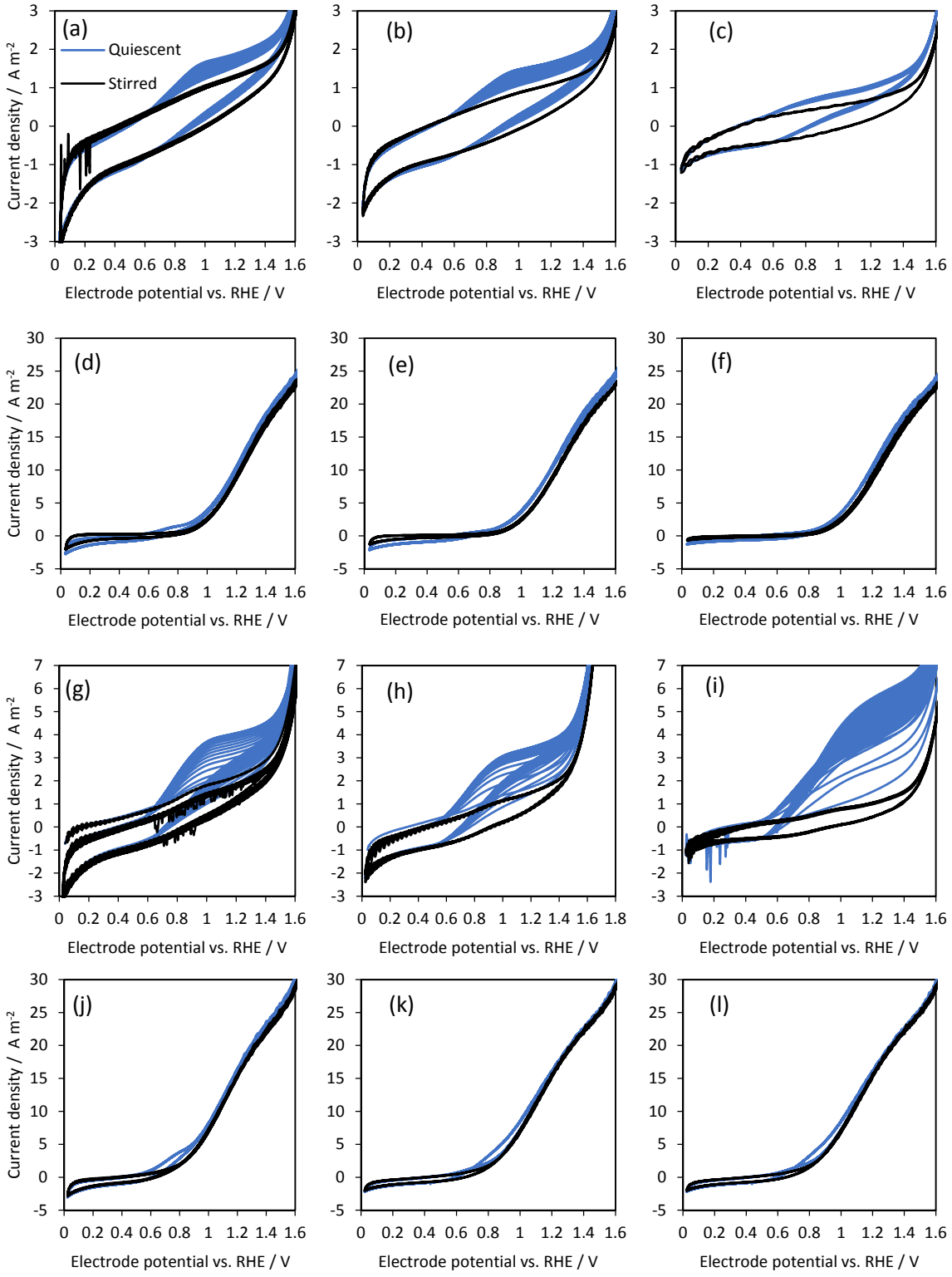


Figure S6-7. Cyclic voltammograms (> 10 cycles) of Ti | Sn^{IV}-doped α-Fe_2O_3 | 1 mol dm^{-3} NaOH + X mol dm^{-3} Na_2S | Pt | Ti with different hydrogen sulfide concentration (a - f) 0.5 mol dm^{-3} and (g - k) 1 mol dm^{-3} Na_2S, under (a,b,c,g,h,i) dark and (d,e,f,j,k,l) illumination conditions and scan rate (a,d,g,j) 100 (b,e,h,k) 50 and (c,f,i,j) 10 mV s^{-1} scan rate under stirred and quiescent electrolyte. Xenon arc lamp irradiance 2 900 W m^{-2}.

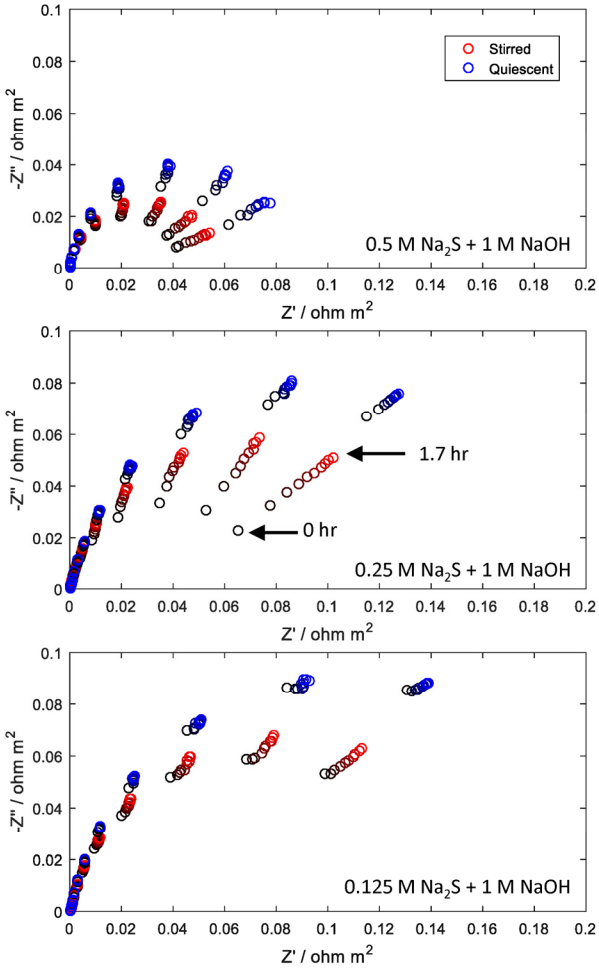


Figure S6-8. Nyquist plots of impedance spectra of photo-anode at 1.65 V *vs.* RHE in cell: Ti | Sn^{IV}-doped α-Fe_2O_3 | 1 mol dm^{-3} NaOH + X mol dm^{-3} Na_2S | Pt | Ti at different concentrations of hydrogen sulfide ions, different times from 0 to 1.7 hours of hydrogen sulfide splitting under stirred and quiescent conditions, and without illumination.

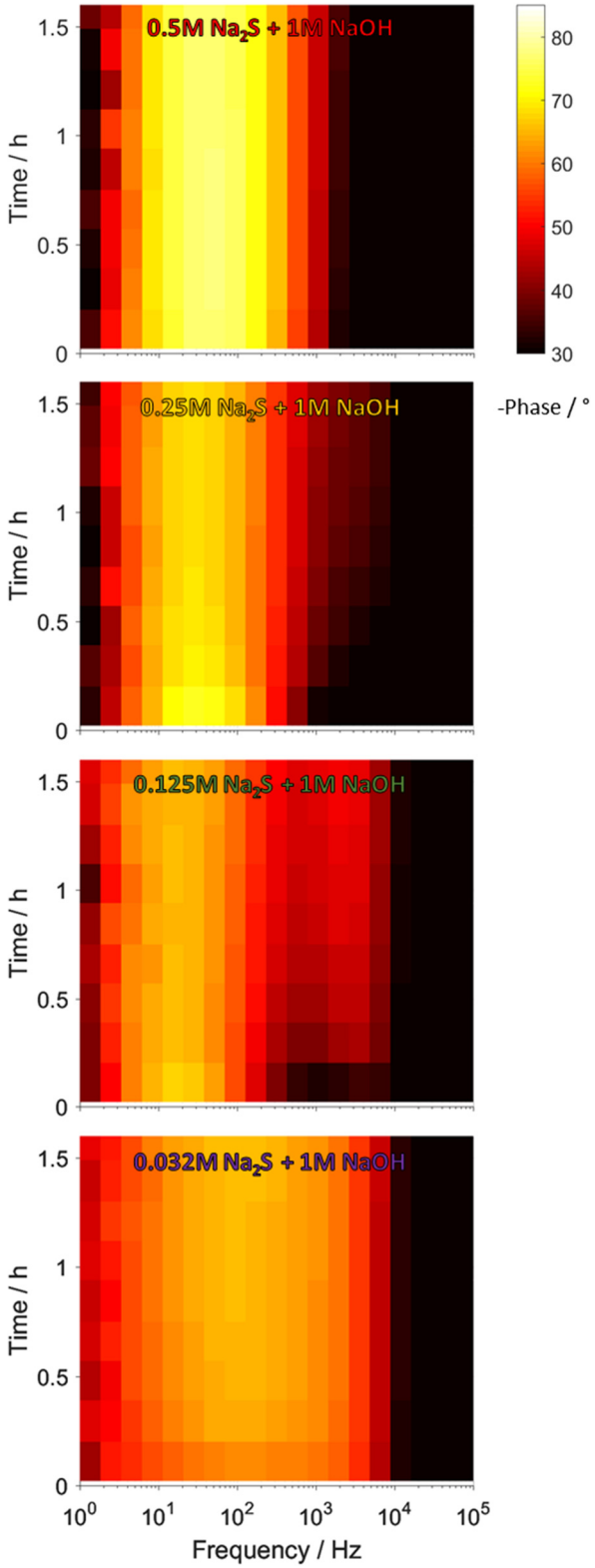


Figure S6-9. Phase shift of PEIS spectra as a function of time for photo-anode at 1.15 V *vs.* RHE in cell: Ti | Sn^{IV}-doped α-Fe_2O_3 | 1 mol dm^{-3} NaOH + X mol dm^{-3} Na_2S | Pt | Ti at different concentrations of hydrogen sulfide ions for photo-assisted hydrogen sulfide splitting with xenon arc lamp irradiance 2 670 W m^{-2}.

6.6 Studies of photo-assisted hydrogen sulfide splitting using Ti | Sn^{IV}-doped α-Fe_2O_3 in an up-scaled reactor (PER).

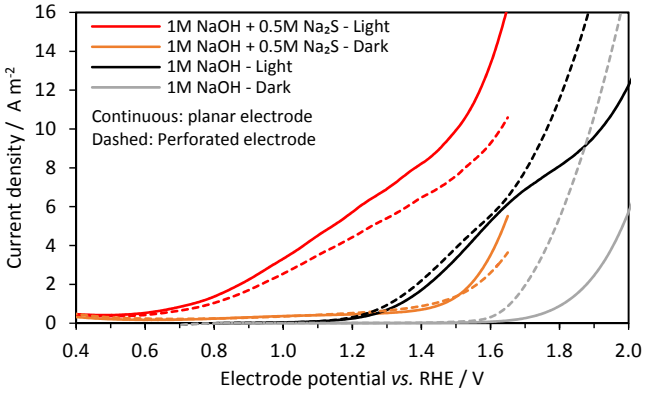


Figure S6-10. Linear sweep voltammograms of a planar and perforated 0.1×0.1 m^2 photo-anodes in Ti | Sn^{IV}-doped α-Fe_2O_3 | 1 mol dm^{-3} NaOH ± 0.5 mol dm^{-3} Na_2S (pH = 14) | Pt | Ti under dark and illuminated conditions in a PER; 50 mV s^{-1} scan rate. Xenon arc lamp irradiance 457 W m^{-2}.

6.7 Photographs of Sn^{IV}-doped α-Fe_2O_3 samples.

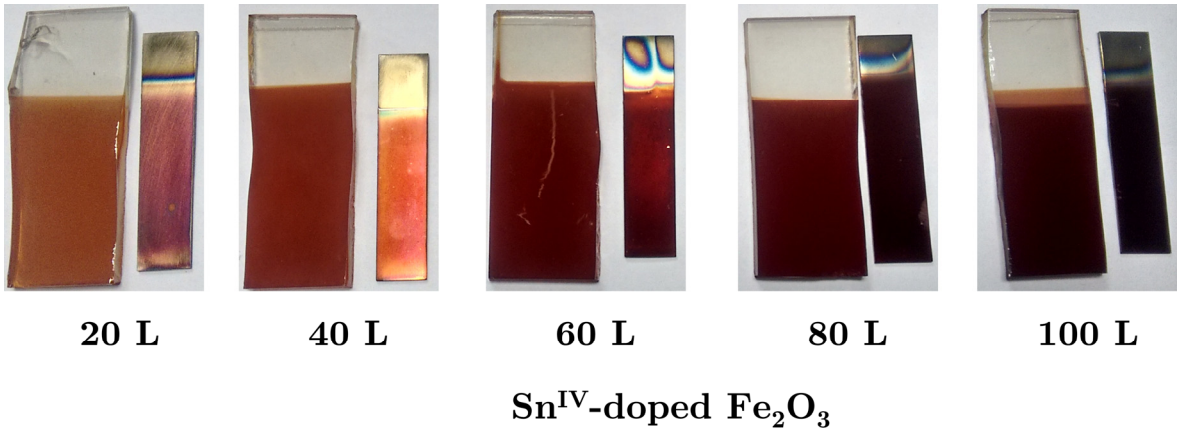


Figure S6-11. Sn^{IV}-doped α-Fe_2O_3 samples on FTO (left) and Ti (right) substrates produced with different passes of precursors during spray pyrolysis.

7. Copyrights permissions

Element	Source of work	Copyright holder	Granted
Figure 1-1	T. Bak, et al. International Journal of Hydrogen Energy, 27 (2002) 991-1022.	Elsevier	Yes
Figure 1-2 Table 1-2	S. Koumi Ngoh, D. Njomo, Renewable and Sustainable Energy Reviews, 16 (2012) 6782-6792.	Elsevier	Yes
Figure 1-3	A.S. Joshi, I. Dincer, B.V. Reddy, International Journal of Hydrogen Energy, 35 (2010) 4901-4908.	Elsevier	Yes
Figure 1-4	T. Lopes, et al. International Journal of Hydrogen Energy, 35 (2010) 11601-11608.	Elsevier	Yes
Figure 1-5 Figure 1-10	J.W. Ager, et al. Energy & Environmental Science, 8 (2015) 2811-2824.	Royal Society of Chemistry	Yes
Figure 1-6	B.A. Pinaud, et al. Energy & Environmental Science, 6 (2013) 1983-2002.	Royal Society of Chemistry	Yes
Figure 1-8	V. Preethi, S. Kanmani, Materials Science in Semiconductor Processing, 16 (2013) 561-575.	Elsevier	Yes
Figure 1-12	Z. Chen, et al. Journal of Materials Research, 25 (2010) 3-16.	Cambridge University Press	Yes

References

[1] D.L.A. de Faria, S. Venâncio Silva, M.T. de Oliveira, Raman microspectroscopy of some iron oxides and oxyhydroxides, *Journal of Raman Spectroscopy*, 28, pp. 873-878, 1997.

[2] T. Ohsaka, F. Izumi, Y. Fujiki, Raman spectrum of anatase, TiO_2, *Journal of Raman Spectroscopy*, 7, pp. 321-324, 1978.

[3] S.P.S. Porto, P.A. Fleury, T.C. Damen, Raman Spectra of TiO_2, MgF_2 ZnF_2 FeF_2, and MnF_2, *Physical Review*, 154, pp. 522-526, 1967.

[4] H. Vogt, The rate of gas evolution of electrodes—I. An estimate of the efficiency of gas evolution from the supersaturation of electrolyte adjacent to a gas-evolving electrode, *Electrochimica Acta*, 29, pp. 167-173, 1984.

[5] S. Shibata, The Concentration of Molecular Hydrogen on the Platinum Cathode, *Bulletin of The Chemical Society of Japan*, 36, pp. 53-57, 1963.

[6] S. Shibata, Supersaturation of oxygen in acidic solution in the vicinity of an oxygen-evolving platinum anode, *Electrochimica Acta*, 23, pp. 619-623, 1978.

[7] J.M. Chin Kwie Joe, L.J.J. Janssen, S.J.D. van Strelen, J.H.G. Verbunt, W.M. Sluyter, Bubble parameters and efficiency of gas bubble evolution for a chlorine-, a hydrogen- and an oxygen-evolving wire electrode, *Electrochimica Acta*, 33, pp. 769-779, 1988.

[8] G. Marrucci, L. Nicodemo, Coalescence of gas bubbles in aqueous solutions of inorganic electrolytes, *Chemical Engineering Science*, 22, pp. 1257-1265, 1967.

[9] D.F. McGinnis, J.C. Little, Predicting diffused-bubble oxygen transfer rate using the discrete-bubble model, *Water Research*, 36, pp. 4627-4635, 2002.

[10] A. Wüest, N.H. Brooks, D.M. Imboden, Bubble plume modeling for lake restoration, *Water Resources Research*, 28, pp. 3235-3250, 1992.

[11] P. Painmanakul, J. Wachirasak, M. Jamnongwong, G. Hebrard, Theoretical Prediction of Volumetric Mass Transfer Coefficient (k_{La}) for Designing an Aeration Tank, *Engineering Journal*, 13, pp. 16, 2009.

[12] J.B. Joshi, M.M. Sharma, A circulation model for bubble columns, *Transactions of the Institute of Chemical Engineers*, 57, pp. 244-251, 1979.

[13] N. Frossling, Uber die Verdunstung Fallender Tropfen (The Evaporation of Falling Drops), *Gerlands Beitrage zur Geophysik*, 52, pp. 107-216, 1938.

[14] W.D. Deckwer, Bubble Column Reactions, John Wiley, Chichester, 1992.

[15] W.D. Deckwer, R. Burckhart, G. Zoll, Mixing and mass transfer in tall bubble columns, *Chemical Engineering Science*, 29, pp. 2177-2188, 1974.

[16] A. Hankin, F.E. Bedoya-Lora, C.K. Ong, J.C. Alexander, F. Petter, G.H. Kelsall, From millimetres to metres: the critical role of current density distributions in photo-electrochemical reactor design, *Energy & Environmental Science*, 10, pp. 346-360, 2017.

[17] W. Sheng, H.A. Gasteiger, Y. Shao-Horn, Hydrogen Oxidation and Evolution Reaction Kinetics on Platinum: Acid vs Alkaline Electrolytes, *Journal of The Electrochemical Society*, 157, pp. B1529-B1536, 2010.

[18] R.W. Powell, R.P. Tye, The thermal and electrical conductivity of titanium and its alloys, *Journal of the Less Common Metals*, 3, pp. 226-233, 1961.

[19] Y. Sone, P. Ekdunge, D. Simonsson, Proton Conductivity of Nafion 117 as Measured by a Four-Electrode AC Impedance Method, *Journal of The Electrochemical Society*, 143, pp. 1254-1259, 1996.

[20] A.T. Haug, R.E. White, Oxygen Diffusion Coefficient and Solubility in a New Proton Exchange Membrane, *Journal of The Electrochemical Society*, 147, pp. 980-983, 2000.

[21] Z. Ogumi, T. Kuroe, Z.i. Takehara, Gas Permeation in SPE Method: II . Oxygen and Hydrogen Permeation Through Nafion, *Journal of The Electrochemical Society*, 132, pp. 2601-2605, 1985.

[22] S.H. Lee, Molecular Dynamics Simulation Study for Hydroxide Ion in Supercritical Water using SPC/E Water Potential, *Bull. Korean Chem. Soc.*, 34, pp. 2925-2930, 2013.

[23] S.K. Shoor, Solubility of nonpolar gases in potassium hydroxid solutions, University of Florida, Florida, US, 1968.

[24] ASTM, G173-03 Standard Tables for Reference Solar Spectral Irradiances: Direct Normal and Hemispherical on 37fl Tilted Surface, 2012.

[25] G.H. Kelsall, I. Thompson, Redox chemistry of H2S oxidation by the British Gas Stretford Process. Part I: Thermodynamics of sulphur-water systems at 298 K, *J Appl Electrochem*, 23, pp. 279-286, 1993.

[26] S. Licht, G. Hodes, J. Manassen, Numerical analysis of aqueous polysulfide solutions and its application to cadmium chalcogenide/polysulfide photoelectrochemical solar cells, *Inorganic Chemistry*, 25, pp. 2486-2489, 1986.

[27] S. Licht, J. Davis, Disproportionation of Aqueous Sulfur and Sulfide: Kinetics of Polysulfide Decomposition, *The Journal of Physical Chemistry B*, 101, pp. 2540-2545, 1997.

[28] W. Giggenbach, Optical spectra and equilibrium distribution of polysulfide ions in aqueous solution at 20.deg, *Inorganic Chemistry*, 11, pp. 1201-1207, 1972.

[29] W.F. Giggenbach, Equilibriums involving polysulfide ions in aqueous sulfide solutions up to 240.deg, *Inorganic Chemistry*, 13, pp. 1724-1730, 1974.